DETERMINATION OF THE NEUTRON AND GAMMA FLUX

DISTRIBUTION IN THE PRESSURE VESSEL AND CAVITY

OF A BOILING WATER REACTOR

A Thesis

Submitted to the Graduate Faculty of the
Louisiana State University and
Agricultural and Mechanical College
in partial fulfillment of the
requirements for the degree of
Master of Science in Nuclear Engineering

in

The Department of Nuclear Science

by
Mehdi Asgari
B.S., Louisiana State University, 1984

May, 1989

Dedicated to
my family

ACKNOWLEDGEMENTS

TABLE OF CONTENTS

TABLE OF CONTENTS (continued)

TABLE OF CONTENTS (continued)

LIST OF TABLES

LIST OF TABLES (continued)

LIST OF FIGURES

LIST OF FIGURES (continued)

LIST OF FIGURES (continued)

LIST OF FIGURES (continued)

ABSTRACT

The Grand Gulf Boiling Water Reactor (BWR/6) owned and operated by Mississippi Power & Light Company has been analyzed to determine the neutron and gamma energy spectrum and flux levels in regions from the reactor vessel throughout the concrete shield wall. One major task of this study is to perform neutron and gamma transport calculations; another is to experimentally analyze the neutron dosimeters which were placed in the reactor cavity by MP&L.

Several two-dimensional and one-dimensional transport calculations were performed for the Grand Gulf reactor configuration. The results from these calculations were synthesized to obtain the three-dimensional neutron flux spectra and dosimeter activity. The results from the transport calculations indicate the flux above 1 MeV peaks near the axial mid-plane and azimuthal angle between 40^0 and 45^0 depending upon the radial locations. The peak flux above 1 MeV incident on the vessel and at mid-cavity is about 1.82E9 and 1.07E8 $n.cm^{-2}.s^{-1}$, respectively. The vessel fluence accumulated during cycle-2 and after 32 effective full power years is about 4.41E16 and 1.84E18 $n.cm^{-2}$, respectively.

The results from the analysis of the activated wires of the neutron dosimetry experiment reveal about a 5 foot discrepancy in the location of the peak in the axial activity distribution as compared with that of the transport calculation. It was concluded that such behavior in the experimental results is inconsistant with the source distribution and that the location of the dosimeters placed in the cavity is most likely displaced from the locations originally reported in the design of the experiment. Thus the experimental results were shifted by 5 feet, based

on the calculated distribution. The comparison of the experimental and
calculated relative axial distribution and absolute dosimeter foils
activity after the axial shift are much more consistent and show
acceptable agreement.

CHAPTER 1

INTRODUCTION

The huge initial capital investment in the construction of a
nuclear power plant requires that utility companies operate the plant as
long as possible before permanent shutdown in order to recover the
invested capital and to provide the public with low utility rates. An
important factor impacting the operating lifetime of a nuclear power
reactor is the integrity of the reactor pressure vessel (RPV). The RPV
is a large steel tank containing the reactor core in which heat is
generated by fission. The RPV is subject to radiation embrittlement due
to the continual neutron bombardment during reactor operation. This
damage mechanism reduces the ability of the steel tank to withstand
severe stresses. This reduced integrity could result in the reactor
vessel failure under certain accident conditions in which low
temperature, emergency coolant is injected into the RPV. The rapid
change in temperature could cause a large thermal stress in the
embrittled RPV, resulting in the propagation of a flaw through the
vessel wall.

The U. S. Nuclear Regulatory Commission, NRC, has placed strict
limits on the amount of radiation damage that an RPV can receive and
still remain in operation. The NRC also requires that each utility
company operating a nuclear reactor maintain an RPV surveillance program
to monitor the RPV neutron fluence exposure during reactor lifetime
operation. Thus, several surveillance capsules containing both
metallurgical specimens of the material used in weldments and RPV, as
well as dosimetry foils of different activation cross-section

thresholds, have been incorporated into the design of nuclear reactors. These capsules are periodically removed and analyzed during the reactor lifetime operation. Unfortunately, the dosimeter data only provides limited information at a few selected points within the reactor. Thus, to obtain a detailed knowledge about the intensity and energy distribution of the neutron flux bombarding the RPV, it is necessary to perform neutron transport calculations in addition to the dosimetry analysis. The transport calculations provide extensive data at all points in the reactor vessel, as well as within the cavity where radiation damage to support structures may be a concern. The accuracy of the transport calculations is governed by the accuracy of the reactor model and the fundamental nuclear cross-section data.

The primary objectives of this study are as follows:

a. To develop an appropriate transport model for the Grand Gulf BWR/6 reactor configuration,

b. To perform R-θ, R-Z and 1-D (R) radiation transport calculations for this model using the discrete ordinates code called DOT-IV,

c. To synthesize the R-θ, R-Z and 1-D fluxes in order to obtain the three-dimensional flux distribution and activity within the reactor and the cavity regions,

d. To use the transport calculation results in estimating the neutron and gamma ray field at any location throughout the vessel, reactor cavity and biological concrete shield wall,

e. To determine the cumulative fluence incident on and within the RPV during Grand Gulf cycle-2,

f. To estimate the cumulative fluence after 32 effective

full power years of the reactor lifetime operation,

g. To perform an experimental measurement to obtain dosimeter

foils activations in the reactor cavity region, and

h. To use the experimental measurements to benchmark the

accuracy of the calculated results.

The cavity dosimetry experiment began in November of 1986, based upon a previous agreement between Mississippi Power & Light Company, Middle South Utilities and the LSU Nuclear Science Center. The Grand Gulf management appointed a team to perform this experiment. In this experiment, three sets of approximately 50 foot long wires along with dosimeter foils were installed from three azimuthal locations in the reactor cavity of the Grand Gulf BWR/6 during cycle-2. The wires were to provide the relative axial distribution at different azimuthal locations, while the dosimeter foils were to benchmark the accuracy of the absolute results obtained in the transport calculations.

The cavity dosimetry is not required at present by the NRC, but provides an important supplement to in-vessel dosimetry. The following are some of the advantages of cavity dosimetry over in-vessel dosimetry.

1- It is more readily accessible and cheaper to analyze.

2- It provides information about ex-vessel radiation environment.

3- It can be implemented easily in the latter years of reactor

lifetime when there is no more in-vessel dosimetry.

4- It provides "insurance" against unforeseen future requirements.

The cavity dosimetry has already been implemented in several BWR and PWR reactors such as Browns Ferry[1] and Arkansas Nuclear One[2].

CHAPTER 2

THEORETICAL BACKGROUND

2.1 Introduction to transport theory

Transport calculations are commonly used for determining the
neutron and gamma flux distributions beyond the reactor core. The
computational costs for such calculations are relatively high despite
the continuous developments in computer technology. In this section,
the principle features of transport theory as employed in this work will
be briefly discussed, and a description of the mathematics, physics and
numerical methods will be provided.

Neutron transport, or generally speaking, particle transport
involves treatment of the flow of particles in phase space (space,
energy, direction) as influenced by interaction with the matter along
the flow path. The neutron transport equation is simply a mathematical
balance of the physical neutron production and losses. The general form
of the transport equation has seven independent variables; three
spatial, energy or speed, two direction, and one time variable.
Although the general transport equation often can be simplified to a
form involving fewer independent variables, the computational solution
is still fairly expensive.

2.2 The steady state Boltzmann transport equation[3]

The Boltzmann transport equation is the mathematical expression
describing the physical neutron production and losses in phase space
(space, energy, and direction). The neutron balance is applied to the
neutron density within a small volume (dV) about V, energy interval dE
about E, and direction $d\Omega$ about Ω, as shown in figure 2.1. Neutron

production can be due to neutrons born from fission, in-scatter from other energies and directions or external neutron sources. On the other hand, neutron losses can be due to absorption, out-scatter and leakage. The mathematical expression for each term in the neutron balance equation are as follows:

2.2.1 Production terms:

The number of neutrons per second produced in $dVdEd\Omega$ due to fission is

$$\chi(E)\int_{E'}\int_{4\pi}d\hat{\Omega}'\left[\vartheta\Sigma_f(\hat{r},E')\Psi(\hat{r},E',\hat{\Omega}')dE'dEd\hat{\Omega}dV\right] .$$

The number of neutrons per second in dV that scatter from energy E' to dE and from direction $\hat{\Omega}'$ to $d\hat{\Omega}$ is

$$\int_{E'}\int_{4\pi}d\hat{\Omega}'\left[\Sigma_s(\hat{r},E'\rightarrow E,\hat{\Omega}'\rightarrow\hat{\Omega})\Psi(\hat{r},E',\hat{\Omega}')dE'dEd\hat{\Omega}dV\right] .$$

The number produced by external source in $dVdEd\Omega$:

$$Q(\hat{r},E,\hat{\Omega})dEdVd\hat{\Omega}$$

2.2.2 Losses terms:

The number of neutrons per second lost from $dVdEd\Omega$ by scatter and absorption is

$$\Sigma_T(\hat{r},E)\Psi(\hat{r},E,\hat{\Omega})dVdEd\hat{\Omega}$$

2.2.3 Leakage:

The net leakage of neutrons in $dEd\hat{\Omega}$ through the small volume dV, figure 2.1, can be obtained by summing the leakage through all six faces of the volume dV. The sum of the leakage through all surfaces can be written as

$$\hat{i}\cdot\hat{\Omega}\frac{\delta\Psi}{\delta X}dVdEd\hat{\Omega} + \hat{j}\cdot\hat{\Omega}\frac{\delta\Psi}{\delta Y}dVdEd\hat{\Omega} + \hat{k}\cdot\hat{\Omega}\frac{\delta\Psi}{\delta Z}dVdEd\hat{\Omega}$$
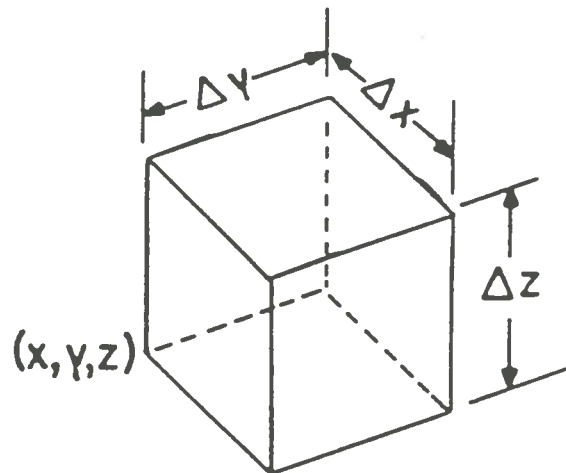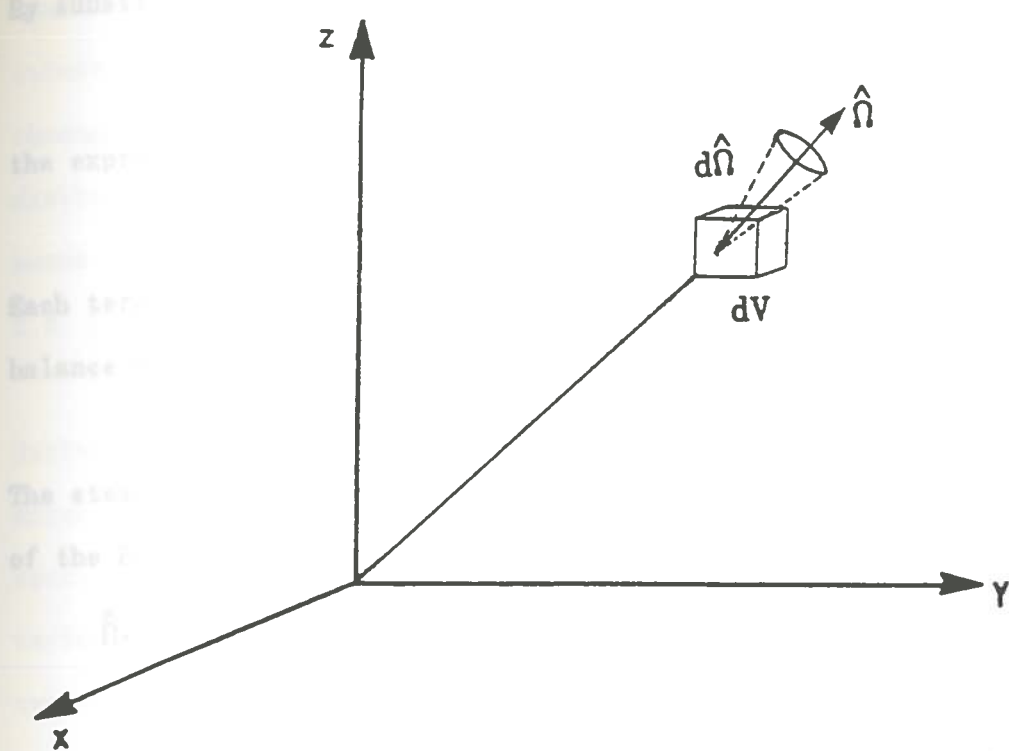
Fig. 2.1   Incremental volume in cartesian coordinate system used to describe the neutron balance equation

By substituting the gradient operator (∇)

$$\nabla = \hat{i}\frac{\delta}{\delta X} + \hat{j}\frac{\delta}{\delta Y} + \hat{k}\frac{\delta}{\delta Z} ,$$

the expression for net leakage through dV can be obtained as follows:

$$\nabla \cdot \hat{\Omega}\Psi(\hat{r},E,\hat{\Omega})dVdEd\hat{\Omega}$$

Each term can now be substituted in the following steady state neutron balance equation,

$$\text{Production in } dVdEd\Omega = \text{Losses in } dVdEd\Omega$$

The steady state, time independent, integro-differential equation form of the Boltzmann transport equation can thus be written as:

$$\hat{\Omega} \cdot \nabla\Psi(\hat{r},E,\hat{\Omega}) + \Sigma_T(\hat{r},E)\Psi(\hat{r},E,\hat{\Omega}) = \int_{E'}\int_{4\pi}\Big[\chi(E)\vartheta\Sigma_F(\hat{r},E') +$$

$$\Sigma_s(\hat{r},E'\rightarrow E,\hat{\Omega}'\rightarrow\hat{\Omega})\Big]\Psi(\hat{r},E',\hat{\Omega}')dE'd\hat{\Omega}' + Q(\hat{r},E,\hat{\Omega}) \qquad (2.1)$$

where in the above equations

$\Sigma_f(\hat{r},E')$ = macroscopic fission cross-section

$\Sigma_T(\hat{r},E)$ = total macroscopic cross-section (absorption and scatter)

$\Sigma_s(\hat{r},E'\rightarrow E,\hat{\Omega}'\rightarrow\hat{\Omega})$ = macroscopic double-differential scattering

cross-section for scattering from energy

E' to E and from direction Ω' to Ω

$\Psi(\hat{r},E,\hat{\Omega})$ = angular flux

$Q(\hat{r},E,\hat{\Omega})$ = external fixed source

$\chi(E)$ = fission spectrum

ϑ = average number of neutrons born due to fission

The divergence term in the Boltzmann transport equation will take different forms for different geometry coordinate systems. In neutronic calculations, this equation together with the appropriate boundary conditions, describing the distribution of neutrons at the exterior

boundaries, makes up a mathematical problem with a unique solution. The solution will correspond to the expected distribution of neutron flux throughout the phase space. The Boltzmann transport equation in discretized form along with the boundary conditions can be solved by means of several computer codes such as DOT.

2.3 Coordinate systems and divergence operator

The term $\hat{\Omega} \cdot \nabla \Psi(\hat{r}, E, \hat{\Omega})$ in equation (2.1) represents the direction derivative of the neutron angular flux along the streaming path in the direction of motion $\hat{\Omega}$. The neutron streaming path can be described by specifying the three spatial and two direction variables. These variables depend upon the geometrical and angular direction coordinate system to be used. The following are the three commonly used coordinate systems in deterministic transport codes along with the mathematical expansion of $\hat{\Omega} \cdot \nabla \Psi(\hat{r}, E, \hat{\Omega})$ term for each coordinate system. Note that in each coordinate system, the direction $\hat{\Omega}$ in the angular direction coordinate system can be described in terms of polar and azimuthal angles. Figure 2.2 represents the typical three-dimensional rectangular and cylindrical, along with the angular direction coordinate systems to define the direction $\hat{\Omega}$. In the following equations symbol $\hat{e}$ denotes a unit vector.

2.3.1 Rectangular coordinates (X,Y,Z)[4]

In this system, a point at space is described by its coordinates $\hat{r} = (X, Y, Z)$. The differential volume element is given by $dV = dXdYdZ$. The direction vector $\hat{\Omega}$ can be expressed

$$\hat{\Omega} = \hat{e}_x \Omega_x + \hat{e}_y \Omega_y + \hat{e}_z \Omega_z \text{ where}$$

$$\Omega_x = \hat{e}_x \cdot \hat{\Omega} = \cos\Psi = \mu$$
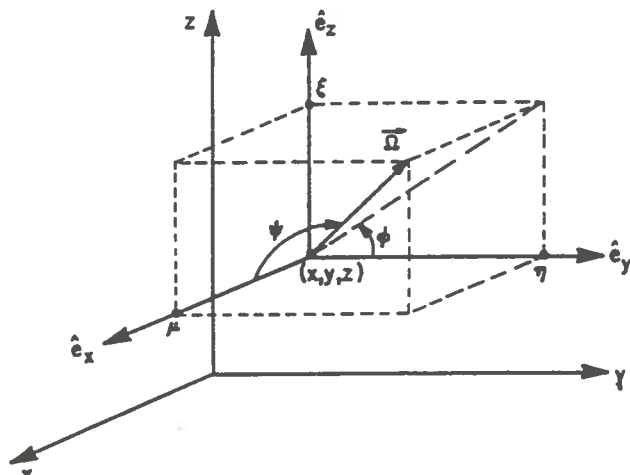
Cartesian
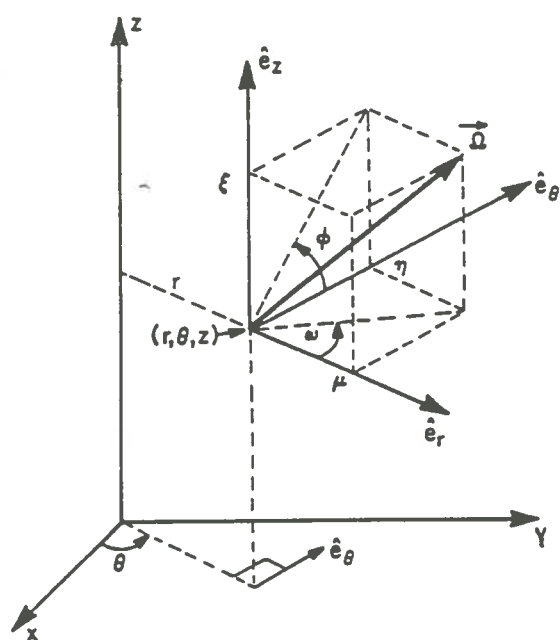
Cylindrical

Fig. 2.2 Three-dimensional spatial and directional coordinate
systems[4]

$$\Omega_y = \hat{e}_y \cdot \hat{\Omega} = Sin\Psi Cos\emptyset = \sqrt{1-\mu^2} Cos\emptyset = \eta$$

$$\Omega_z = \hat{e}_z \cdot \hat{\Omega} = Sin\Psi Sin\emptyset = \sqrt{1-\mu^2} Sin\emptyset = \xi$$

Therefore

$$\hat{\Omega} \cdot \nabla \Psi(\hat{r}, E, \hat{\Omega}) = \mu \frac{\delta}{\delta X} \Psi(\hat{r}, E, \hat{\Omega}) + \eta \frac{\delta}{\delta Y} \Psi(\hat{r}, E, \hat{\Omega}) + \xi \frac{\delta}{\delta Z} \Psi(\hat{r}, E, \hat{\Omega}) \quad (2.2)$$

For two-dimensional systems of (X,Y) coordinates the term $\frac{\delta \Psi}{\delta Z} = 0$; and for a one-dimensional system slab, both $\frac{\delta \Psi}{\delta Z} = \frac{\delta \Psi}{\delta Y} = 0$.

2.3.2 Cylindrical coordinates (R,θ,Z)[4]

In this system a point in space is described by its coordinates $\hat{r} = (R,\theta,Z)$. The differential volume element is given by $dV = RdRd\theta dZ$. The direction vector $\hat{\Omega}$ is

$$\hat{\Omega} = \hat{e}_r \Omega_r + \hat{e}_\theta \Omega_\theta + \hat{e}_z \Omega_z$$

where

$$\Omega_r = \hat{e}_r \cdot \hat{\Omega} = \sqrt{1-\xi^2} Cos\omega = \mu$$

$$\Omega_\theta = \hat{e}_\theta \cdot \hat{\Omega} = \sqrt{1-\xi^2} Sin\omega = \eta$$

$$\Omega_z = \hat{e}_z \cdot \hat{\Omega} = \xi$$

The "conservative" form of the divergence term for the geometry is:

$$\Omega \cdot \nabla \Psi(\hat{r}, E, \hat{\Omega}) = \frac{\mu}{R} \frac{\delta}{\delta R}(R\Psi(\hat{r}, E, \hat{\Omega})) + \frac{\eta}{R} \frac{\delta}{\delta\theta} \Psi(\hat{r}, E, \hat{\Omega}) - \frac{1}{R} \frac{\delta}{\delta\omega}(\eta\Psi(\hat{r}, E, \hat{\Omega})) +$$

$$\xi \frac{\delta}{\delta Z} \Psi(\hat{r}, E, \hat{\Omega}) \quad (2.3)$$

It is often useful to consider two-dimensional sub-spaces of the general three-dimensional cylindrical system. For two-dimensional systems of (R,Z) or (R,θ) cylindrical coordinates the general equation will reduce to

$$(R,Z): \quad \hat{\Omega} \cdot \nabla \Psi(\hat{r}, E, \hat{\Omega}) = \frac{\mu}{R} \frac{\delta}{\delta R}(R\Psi(\hat{r}, E, \hat{\Omega})) - \frac{1}{R} \frac{\delta}{\delta \omega}(\eta \Psi(\hat{r}, E, \hat{\Omega})) + \xi \frac{\delta}{\delta Z}\Psi(\hat{r}, E, \hat{\Omega})$$

$$(2.4)$$

$$(R,\theta): \quad \hat{\Omega} \cdot \nabla \Psi(\hat{r}, E, \hat{\Omega}) = \frac{\mu}{R} \frac{\delta}{\delta R}(R\Psi(\hat{r}, E, \hat{\Omega})) + \frac{\eta}{R} \frac{\delta}{\delta \theta}\Psi(\hat{r}, E, \hat{\Omega}) - \frac{1}{R} \frac{\delta}{\delta \omega}(\eta \Psi(\hat{r}, E, \hat{\Omega}))$$

$$(2.5)$$

$$(1-D): \quad \hat{\Omega} \cdot \nabla \Psi(\hat{r}, E, \hat{\Omega}) = \frac{\mu}{R} \frac{\delta}{\delta R}(R\Psi(\hat{r}, E, \hat{\Omega})) - \frac{1}{R} \frac{\delta}{\delta \omega}(\eta \Psi(\hat{r}, E, \hat{\Omega}))$$

$$(2.6)$$

2.4 Discrete ordinates technique for solving the transport equation

There have been several methods introduced[5] for solving the transport equation, such as, the spherical-harmonics method, the Fourier-transform approach, the Monte Carlo method, and the discrete ordinates technique. Two of the most commonly used methodologies used to solve the transport equation for RPV analysis are the Monte Carlo method and the discrete ordinates method. The first is based on random statistical simulation of the neutrons path, and the latter is based on expressing the continuous form of the Boltzmann transport equation in terms of discrete variables. The discrete ordinates technique is by for the most favored method for RPV calculations in the U. S., and will be the focus of discussion in this chapter.

In discretizing the continuous form of transport equation, the spatial variables are expressed as finite intervals, the energy variable as energy groups, and the direction variables as discrete directions. Generally, the discrete ordinates equation is a representation of neutron balance over a finite-sized interval in phase space, whereas; the continuous form of the Boltzmann equation is a representation of neutron balance over a differential phase space interval.

2.5 DOT-IV transport code

At present, there are several computer codes available which use the discrete ordinates technique for solving the Boltzmann transport equation. Probably the most commonly used code, especially by nuclear industries for reactor pressure vessel fluence calculation is called DOT. The DOT-IV code is the latest in the series of DOT codes developed at Oak Ridge National Laboratory. In this code, like other discrete ordinates codes, the discrete abscissas that define the finite intervals, energy intervals, and discrete directions are called mesh points, group boundaries and the quadrature, respectively. DOT-IV has the capability of solving the transport equation in two-dimensional coordinate systems such as X-Y, R-Z, R-θ, and also in one-dimensional geometries. However, three-dimensional problems cannot be addressed. DOT-IV also has an input option for representing the mesh cells in a fixed or variable mesh. The structure of the required input and output for the DOT-IV code is shown in figure 2.3. For a detailed discussion and input description, refer to a DOT-IV documentation or to reference (6).

2.6 Spatial discretization

As mentioned earlier, the discrete ordinates transport code, DOT-IV, is limited to only one- or two-dimensional coordinate systems. After the selection of the coordinate system for a given problem, the spatial discretization is performed by simply dividing the geometry into the desired discrete mesh intervals. These discrete mesh intervals are defined by specifying the corners of the finite intervals constituting the mesh cells. For example, two arrays representing the location of
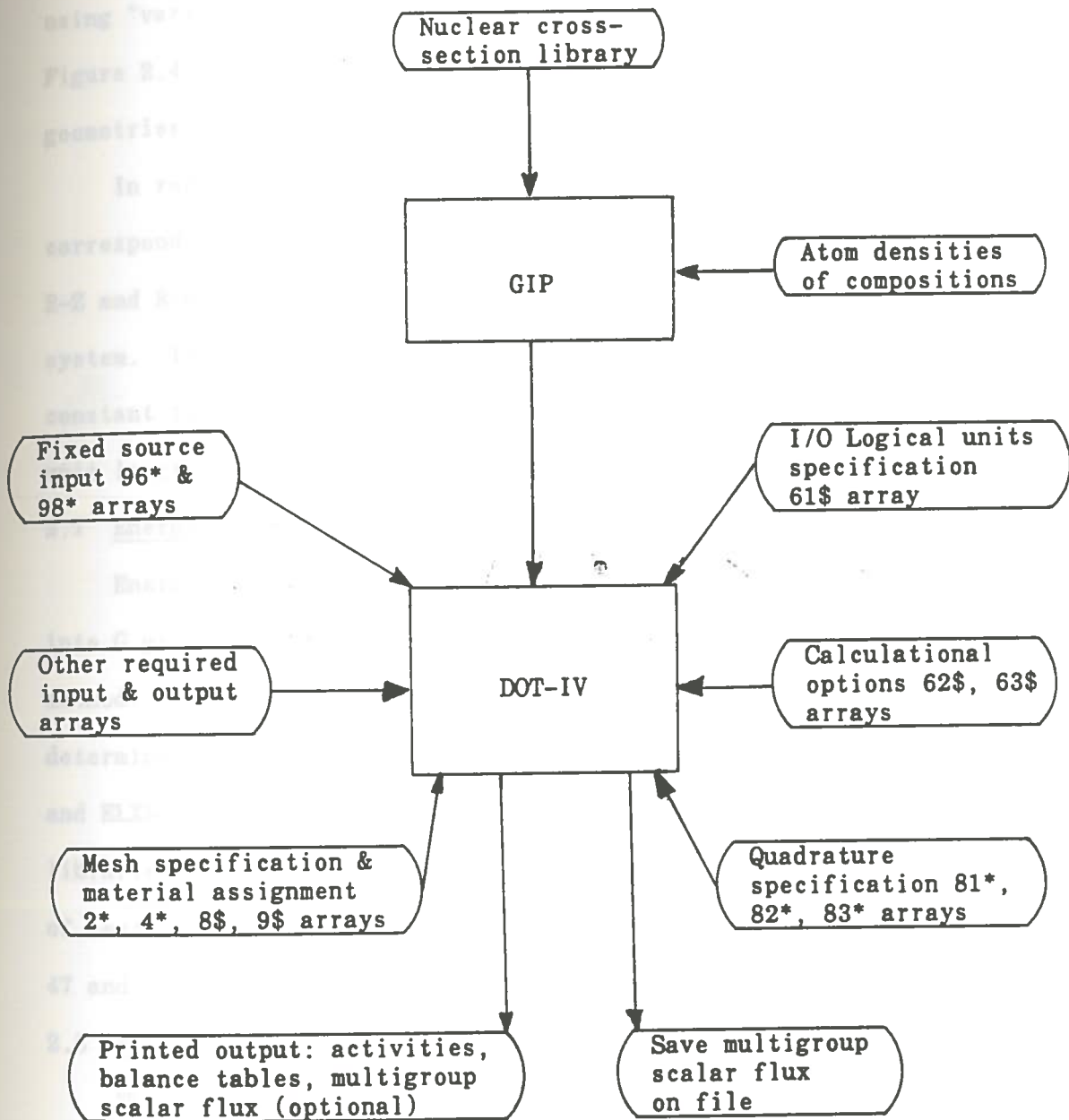
Fig. 2.3 Block diagram of DOT-IV input and output

finite intervals in both dimensions are required to be input in DOT-IV. The discrete ordinates transport code, DOT-IV, has the capability of using "variable mesh" or "mixed mesh" for defining the mesh cells. Figure 2.4 represents three basic mesh cells for three commonly used geometries, X-Y, R-Z and R-θ, in pressure vessel calculations.

In rectangular coordinate systems, the X-Y coordinate system can correspond to any two of the three coordinate axes in 3-D, X-Y-Z. The R-Z and R-θ geometries are subsets of a 3-D cylindrical coordinate system. In all two-dimensional calculations, the flux is assumed to be constant in the third dimension. The flux calculated by DOT-IV is per unit length of the unspecified third dimension.

2.7 Energy discretization

Energy discretization is performed by dividing the energy domain into G groups. This method of discretization is called multi-group method. The number and structure of the energy groups are essentially determined by the cross-section library input into DOT-IV. SAILOR[7] and ELXSIR[8] cross-section libraries are two of several cross-section libraries commonly used for discrete ordinates calculations. The number of neutron energy groups used in these two cross-section libraries are 47 and 56, respectively.

2.8 Angular discretization

The angular discretization in discrete ordinates calculation is performed by representing the infinite number of directions for neutron motion with a finite set of directions, $\hat{\Omega}_n$, n=1, M, where M is the total number of the discrete finite directions. As shown in figure 2.5, each of the discrete directions $\hat{\Omega}_n$ intersects the surface of a unit

XY
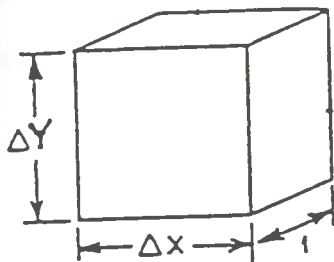
Volume = $\Delta X \Delta Y$

RZ
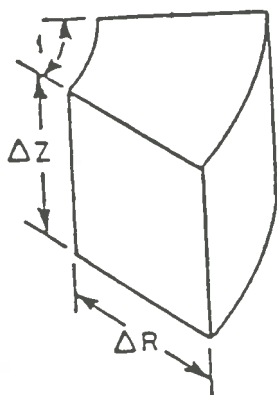
Volume = $2\pi R \Delta \bar{R} \Delta Z$

Rθ
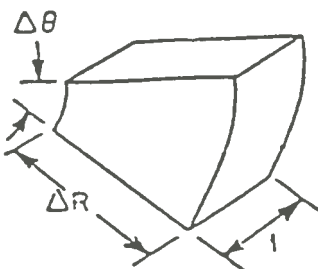
Volume = $2\pi R \Delta \bar{R} \Delta \theta$

Fig. 2.4 Two-dimensional mesh elements used in DOT-IV
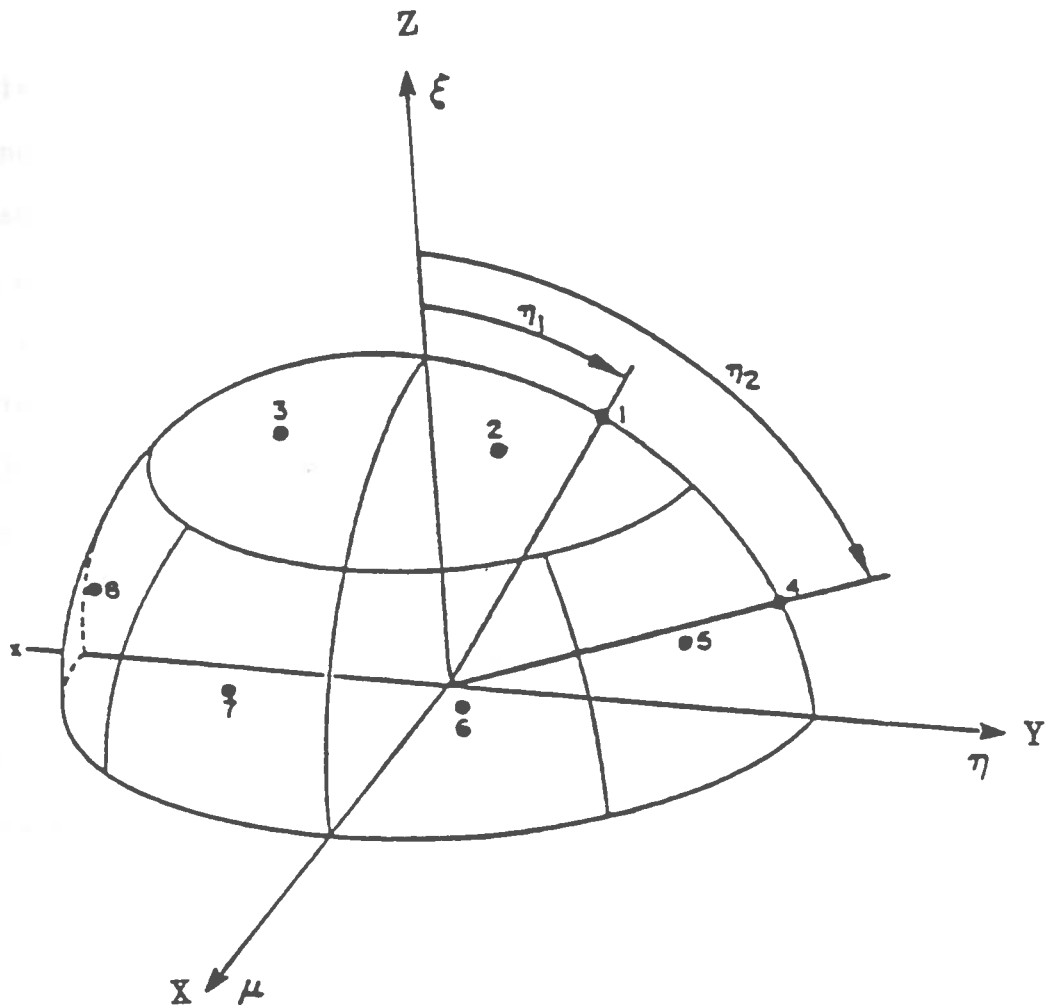
Fig. 2.5 Angular discretization of the direction variable "$\hat{\Omega}$"
(only an upper quadrant of a S_4 quadrature shown)

sphere at a particular point dividing the surface of the sphere into several discrete areas ΔA_n. For each discrete direction $\hat{\Omega}_n$ the associated solid angle interval $\Delta\hat{\Omega}_n$ about $\hat{\Omega}_n$ is proportional to the corresponding discrete area ΔA_n.

$$\Delta\hat{\Omega}_n = \frac{\Delta A_n}{4\pi R^2} \tag{2.7}$$

where R is the radius of the unit sphere. The solid angle intervals in DOT are not measured in steradian units, but in units which are a factor of $\frac{1}{4\pi}$ smaller. The discrete ordinates angular flux at some particular location and energy group $(\Psi(\hat{\Omega}_n))$ corresponding to the direction $\hat{\Omega}_n$ is equal to the number of neutrons per second per cm^2 which pass through the finite area ΔA_n, per unit solid angle. The discrete ordinates scalar flux is simply the sum of all the neutrons passing through the unit sphere or

$$\Phi = \sum_{n=1}^{M} \Psi_n(\hat{\Omega}_n)\Delta\hat{\Omega}_n \tag{2.8}$$

Due to the units of the solid angle, there is a factor of 4π difference between values of angular flux calculated by DOT-IV and the angular flux per steradian, i.e.

$$\Psi_{DOT}(\hat{\Omega}_n) = 4\pi\Psi(\hat{\Omega}_n),$$

where Ψ is the flux per steradians. The expression used to compute the scalar flux in DOT-IV is

$$\Phi = \sum_{n=1}^{M} \Psi_{DOT}(\Omega_n)W_n \tag{2.9}$$

Where

$$W_n = \frac{\Delta\Omega_n}{4\pi} \tag{2.10}$$

The parameter W_n is called directional "weight" and has a value between 0 and 1. Thus

$$\sum_{n=1}^{M} W_n = 1.0$$

The set of discrete directions Ω_n and their associated "weight" W_n are known as a discrete ordinates "quadrature set".

In DOT-IV the direction vector Ω_n is specified by giving the two components of Ω_n along the directional coordinate axis $\Omega_n = (\mu, \eta)$, as shown in the three-dimensional cartesian coordinate of figure 2.2. In terms of spherical coordinates, these direction cosines are:

$$\mu = Cos\Psi$$

$$\eta = Sin\Psi\ Cos\emptyset$$

In DOT-IV, a quadrature set is defined by specifying three input arrays, each containing M numbers of μ, η, ω_n. The η values determine latitude levels on the unit direction sphere and the number of latitude lines is called "S_n order" of the quadrature. Each latitude is divided into discrete μ values. Figure 2.6 represents the arrangement of the directions in an S_6 quadrature set, within one octant of the unit sphere. The total number of directions in a quadrature set of order n for a two-dimensional geometry is equal to

$$N = \frac{n(n+4)}{2}$$

Thus an S_6 quadrature set has 30 directions. (Note: In two-dimensional geometries the angular flux is symmetrical in the left and right hemisphere of the unit sphere, so that the quadrature directions are
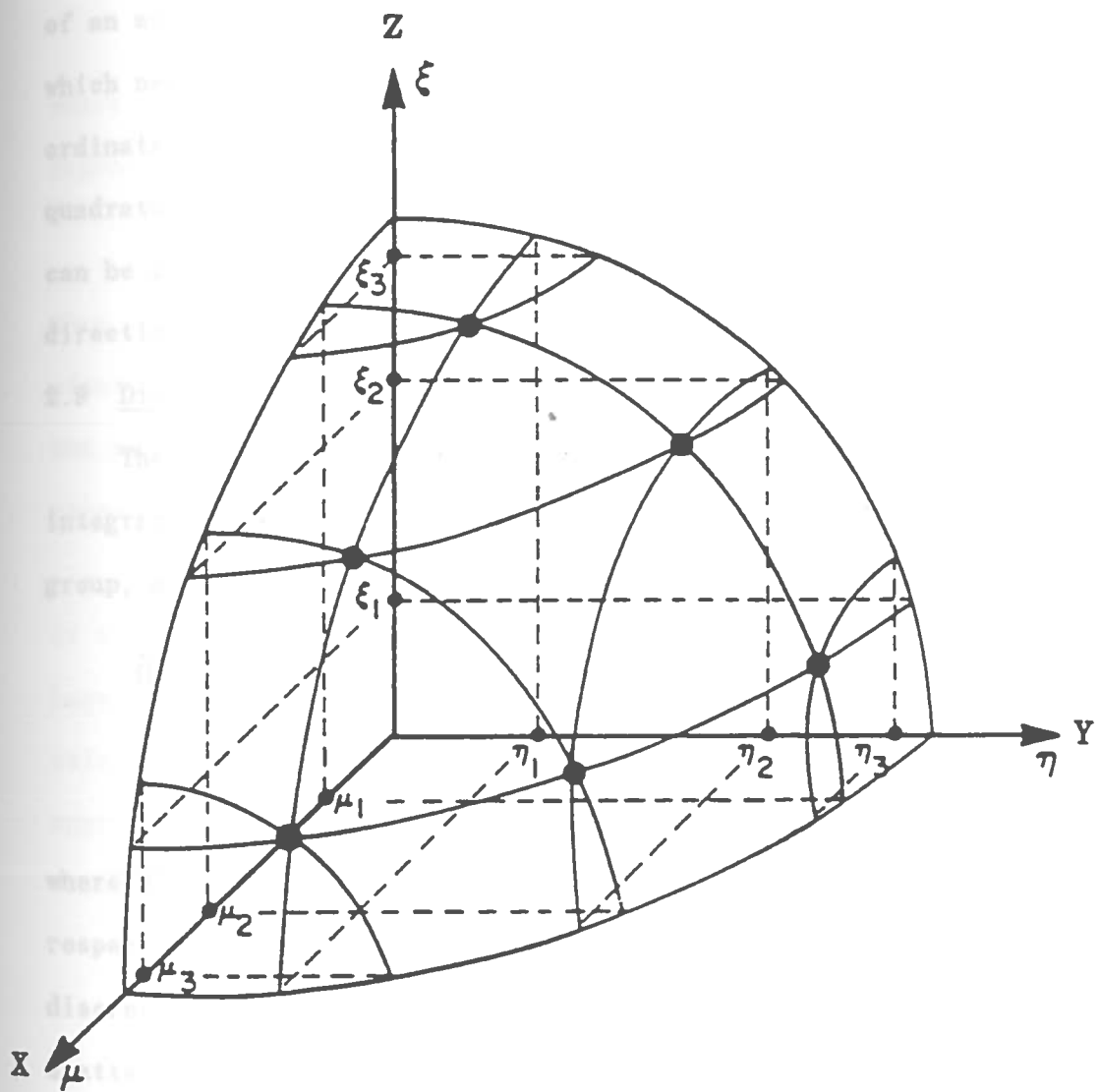
Fig. 2.6 An S_6 quadrature set arrangement[4]

given for only a single hemisphere.)

A quadrature set must be adequate to represent the flow of neutrons within the system and also serves as a numerical quadrature for computing the direction integral in the scatter source. The selection of an accurate quadrature set becomes very important in problems in which neutron streaming plays a major role. In such cases, the discrete ordinates transport calculation will perform very poorly if a low order quadrature set is used. In most cases, the neutron streaming problem can be avoided by employing more discrete directions biased in the direction of streaming.

2.9 Discretized Boltzmann Transport equation

The discretized Boltzmann Transport equation can be obtained by integrating equation (2.1) over each discrete finite mesh cell, energy group, and direction interval. Thus, equation (2.1) can be written as:

$$\hat{\Omega}_n \cdot \nabla \Psi_g(i,j,\hat{\Omega}_n) + \Sigma_{tg}(i,j)\Psi_g(i,j,\hat{\Omega}_n) = \sum_{n=1}^{M} \Delta\hat{\Omega}_n \sum_{g'=1}^{G} \left[\chi_{g'} \vartheta\Sigma_{fg'}(i,j) + \right.$$

$$\left. \Sigma_{s,g' \to g}(i,j,\hat{\Omega}_{n'} \to \hat{\Omega}_n) \right] \Psi_{g'}(i,j,\hat{\Omega}_{n'}) + Q_g(i,j,\hat{\Omega}_n) \qquad (2.11)$$

where M and G are maximum number of directions and energy groups, respectively. It should be noted that this equation is not the final discretized form of the transport equation, since the differential scatter cross-section is usually expressed as a Legendre expansion. The flux is calculated at the mid point of the mesh cell and can be thought of as the average flux over the volume of the mesh cell.

2.10 Treatment of Anisotropic Scatter

In the Boltzmann transport equation, the double differential scattering cross-section $\Sigma_s(r,E' \to E, \Omega' \to \Omega)$ represents the probability of

scatter of neutrons from an energy E' and direction Ω' to an energy of E and direction Ω. As shown in figure 2.7, when a neutron undergoes a collision, the direction of motion after the collision depends upon the angle between the final and initial directions,

$$Cos\theta_0 = \Omega' \cdot \Omega \equiv \mu_0$$

where μ_0 is equal to the cosine of the scattering angle. The angle dependant double differential scatter cross-section can be written as

$$\Sigma_s(r, E' \rightarrow E, \mu_0) \ (cm)^{-1}(ev)^{-1}(solid\ angle)^{-1}$$

When the incoming neutrons scatter uniformly in all outgoing directions after collision, then the scattering is said to be isotropic, otherwise; the scattering is anisotropic. In reality, most scattering is anisotropic in the laboratory system of coordinates.

In the discrete ordinates DOT-IV code, the anisotropic scattering is treated by expanding the double differential scattering cross in Legendre polynomials of the scatter cosine μ_0. In most transport calculations, the 3rd order polynomial expansion is a sufficient approximation. The 3rd order "P3 expansion" of the differential scatter cross-section is as follows:

$$\Sigma_s(r, E' \rightarrow E, \mu_0) = \Sigma_0(r, E' \rightarrow E)P_0 + \Sigma_1(r, E' \rightarrow E)P_1(\mu_0) +$$

$$\Sigma_2(r, E' \rightarrow E)P_2(\mu_0) + \Sigma_3(r, E' \rightarrow E)P_3(\mu_0) \qquad (2.12)$$

The coefficients of the Legendre polynomials are called the "cross-section moments", and the Legendre Polynomials are given by

$$P_0 = 1$$

$$P_1 = \mu_0$$
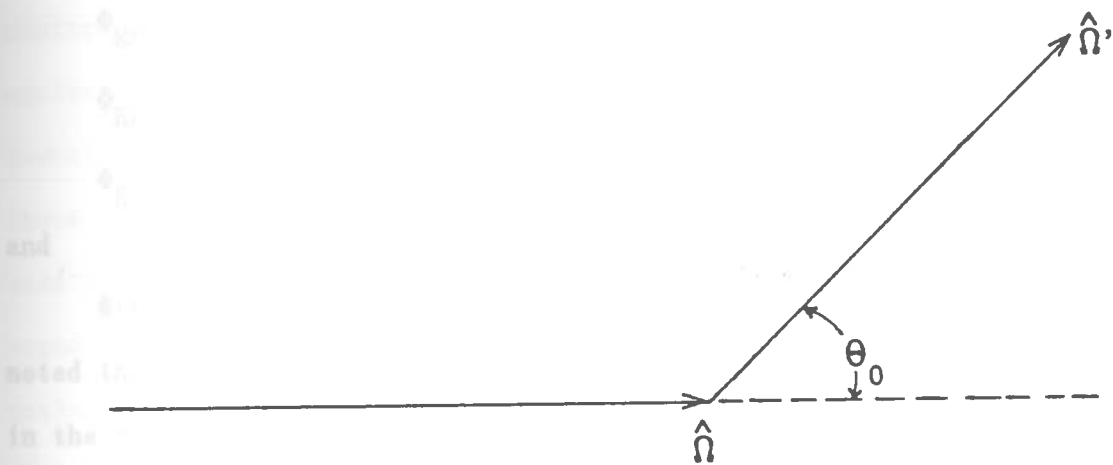
Fig. 2.7 Representation of neutron scattering ($\hat{\Omega}$ and $\hat{\Omega}'$ are the before and after scatter direction, respectively and θ_0 is scattering angle)

are defined as follows:

$$\Phi_{R\theta}(R,\theta) = \int_{-\infty}^{\infty} \Phi(R,\theta,Z)\ dZ \qquad (2.13)$$

$$\Phi_{RZ}(R,Z) = \int_{0}^{2\pi} \Phi(R,\theta,Z)\ d\theta \qquad (2.14)$$

$$\Phi_{R}(R) \quad = \int_{-\infty}^{\infty} \int_{0}^{2\pi} \Phi(R,\theta,Z)\ d\theta dZ \qquad (2.15)$$

where

$\Phi_{R\theta}(R,\theta) = (R-\theta)$ channel flux

$\Phi_{RZ}(R,Z) = (R-Z)$ channel flux

$\Phi_{R}(R) \quad = (R)$ channel flux

and

$\Phi(R,Z,\theta)$ is assumed to be in the true 3-D flux. It should be noted that the channel fluxes for each group are related to each other in the following relation:

$$\int_{0}^{2\pi} \Phi_{R\theta}(R,\theta)\ d\theta = \int_{-\infty}^{\infty} \Phi_{RZ}(R,Z)\ dZ = \Phi_{R}(R) \qquad (2.16)$$

Now the "synthesized flux" as a function of (R,θ,Z) variables can be defined by the following relation:

$$\Phi_{syn}(R,\theta,Z) = \frac{\Phi_{R\theta}(R,\theta) \cdot \Phi_{RZ}(R,Z)}{\Phi_{R}(R)} \qquad (2.17)$$

Although equation (2.17) is an approximate expression, it has been shown[9] that it is an exact 3-D distribution if the flux is separable either azimuthally or axially. In the case where the flux is not separable, equation (2.17) always gives the exact axial and azimuthal integrated values of the flux at all radial points[9]. It can also be

shown that the R-θ, R-Z, 1-D channel fluxes obey an equation which has an identical form as the standard R-θ, R-Z and 1-D equations solved by the transport code DOT-IV.

2.12 RPV fluence determination

The U.S. Nuclear Regulatory Commission, NRC, requires that each utility company operating a nuclear reactor maintain a RPV surveillance program to monitor the RPV neutron fluence exposure. Thus, several surveillance capsules containing both metallurgical specimens and neutron dosimeter foils have been incorporated into the design of the nuclear power reactors. These capsules are usually located in the downcomer region of the reactors. Periodic removal and analysis of these surveillance capsules provide very vital information which can be used in assessing the integrity of the RPV. Currently most organizations use a combination of transport calculation and measured dosimeter activities to obtain the RPV fluence. The analysis of the irradiated neutron dosimeter foils provide measured activities for each dosimeter material at the location of surveillance capsules. The transport calculation provides information in much more detail about the fluence rate and the energy spectrum of the neutron flux at all locations in the reactor. In this section, a brief description of the methodology used in combining the transport calculation and the measured dosimeter activities is presented.

The measured "saturated activity", A_{sat}, of a particular dosimeter foil sample is the activity corresponding to the steady state in which the rate of production by neutron reactions is equal to the rate of loss by radioactive decay. Thus, in general, the saturation activity per

atom of the sample in terms of "time of removal activity", A_{tor}, which is the activity of the sample at the end of the irradiation period, is calculated as follows:

$$A_{sat} = A_{tor} / h(t)N_0 \qquad (2.18)$$

and

$$h(t) = \sum_{j=1}^{J} P_j (1-e^{-\lambda T_j}) e^{-\lambda(T-t_j)} \qquad (2.19)$$

where A_{tor} = time of removal activity (Bq)

A_{sat} = saturation activity (per target atom)

$h(t)$ = non-saturation factor

N_0 = number of target atoms in dosimeter foil

P_J = fraction of full power during period j

λ = decay constant (d^{-1})

T_j = length of time (d) for irradiation interval j

T = time (d) from beginning of irradiation to time of removal

t_j = elapsed time (d) from beginning of irradiation to end of interval j

J = number of irradiation intervals

Also the "saturated activity", A_{sat}, can be defined as follows:

$$(A_{sat})_{meas} = \int_0^\infty \Phi(E)\sigma(E)dE = \frac{\int_0^\infty \Phi(E)\sigma(E)dE}{\int_{E_t}^\infty \Phi(E)dE} \int_{E_t}^\infty \Phi(E)dE \qquad (2.20)$$

and therefore

$$(A_{sat})_{meas} = \bar{\sigma}_{E_t} \Phi(E>E_t)_{meas} \qquad (2.21)$$

where

$\bar{\sigma}_{E_t}$ = the effective spectrum-averaged one group cross-section (barn)

and

$\phi(E>E_t)$ = the fluence rate of the neutrons with energies greater than the dosimeter threshold energy, E_t, $(n.cm^{-2}.s^{-1})$. From equation (2.21),

$$\Phi(E>E_t)_{meas} = \frac{(A_{sat})_{meas}}{\bar{\sigma}_{E_t}}$$

(2.22)

In equation (2.22), the $(A_{sat})_{meas}$ can be obtained from the measured dosimeter activation and $\bar{\sigma}_{E_t}$ can be obtained from the transport calculation. Thus, defining the calculated "saturated activity" A_{cal} in a similar way:

$$(A_{sat})_{cal} = \bar{\sigma}_{E_t} \Phi(E>E_t)_{cal}$$

(2.23)

Equation (2.0) can be re-written as

$$\Phi(E>E_t)_{meas} = \frac{(A_{sat})_{meas}}{(A_{sat})_{cal}} \Phi(E>E_t)_{cal}$$

(2.24)

Equation (2.24) shows that if the calculation-to-experiment activity ratio $(C/E) = (A_{sat})_{meas}/(A_{sat})_{cal}$ is near unity, then the calculated flux will be close to the true flux. The total fluence is given by

$$\Phi(E>E_t) = \Phi(E>E_t) \sum_{j=1}^{J} P_j T_j$$

(2.25)

Finally, the "lead factor" LF, is another terminology commonly used in RPV fluence analysis and defined as:

$$LF = \frac{\text{neutron fluence rate } (E>E_t) \text{ at the surveillance capsule center}}{\text{maximum neutron-fluence rate at any location of interest}}$$

$$= \frac{\Phi(E>E_t)_{sc}}{\Phi(E>E_t)_L} \tag{2.26}$$

where both fluxes can be obtained from the transport calculation. The LF is most often defined for the peak flux incident on the vessel.

CHAPTER 3

MULTI-DIMENSIONAL DISCRETE ORDINATES TRANSPORT CALCULATIONS

Several discrete ordinates transport calculations using the DOT-IV code were performed to obtain the channel fluxes that describe radial, azimuthal, and axial flux distribution inside the reactor vessel and the reactor cavity of the Grand Gulf BWR/6 Nuclear Power Plant. In this chapter, a description of the reactor considered in the analysis and the transport calculations of the reactor model will be presented.

3.1 Description of the reactor

This study has been performed for the Grand Gulf BWR/6 boiling water reactor owned by Mississippi Power & Light Company, which is located in Port Gibson, Mississippi. The BWR/6 is the latest BWR product line designed by the General Electric Corporation. These reactors have output power capabilities ranging from 600 to 1400 MW electric. Some of the BWR/6 principle design features as compared to earlier BWR's are more fuel bundles, smaller diameter fuel rods, longer active fuel length and 8 X 8 fuel bundle arrangement.

Figure 3.1 represents a typical boiling water reactor and its internal components. Some of the major components, as shown in figure 3.1, are reactor vessel, core and internal, shroud top guide assembly, core plate assembly, steam separator and dryer, and jet pumps. The typical plan view of the core arrangement and the lattice configuration of a boiling water reactor are shown in figure 3.2. The Grand Gulf nuclear reactor core consists of 800 fuel assemblies, each of which contains 64 fuel pins which are spaced and supported in a square 8 X 8 array by lower and upper tie plates. Figure 3.3 represents a typical

VENT AND HEAD SPRAY

STEAM OUTLET

CORE SPRAY INLET

LOW PRESSURE COOLANT INJECTION INLET

CORE SPRAY SPARGER

JET PUMP ASSEMBLY

FUEL ASSEMBLIES

JET PUMP/RECIRCULATION WATER INLET

VESSEL SUPPORT SKIRT

CONTROL ROD DRIVES

IN-CORE FLUX MONITOR

STEAM DRYER LIFTING LUG

STEAM DRYER ASSEMBLY

STEAM SEPARATOR ASSEMBLY

FEEDWATER INLET

FEEDWATER SPARGER

CORE SPRAY LINE

TOP GUIDE

CORE SHROUD

CONTROL BLADE

CORE PLATE

RECIRCULATION WATER OUTLET

SHIELD WALL

CONTROL ROD DRIVE HYDRAULIC LINES

Fig. 3.1   Cut-away view of a boiling water reactor (BWR/6)[10]

Core arrangement
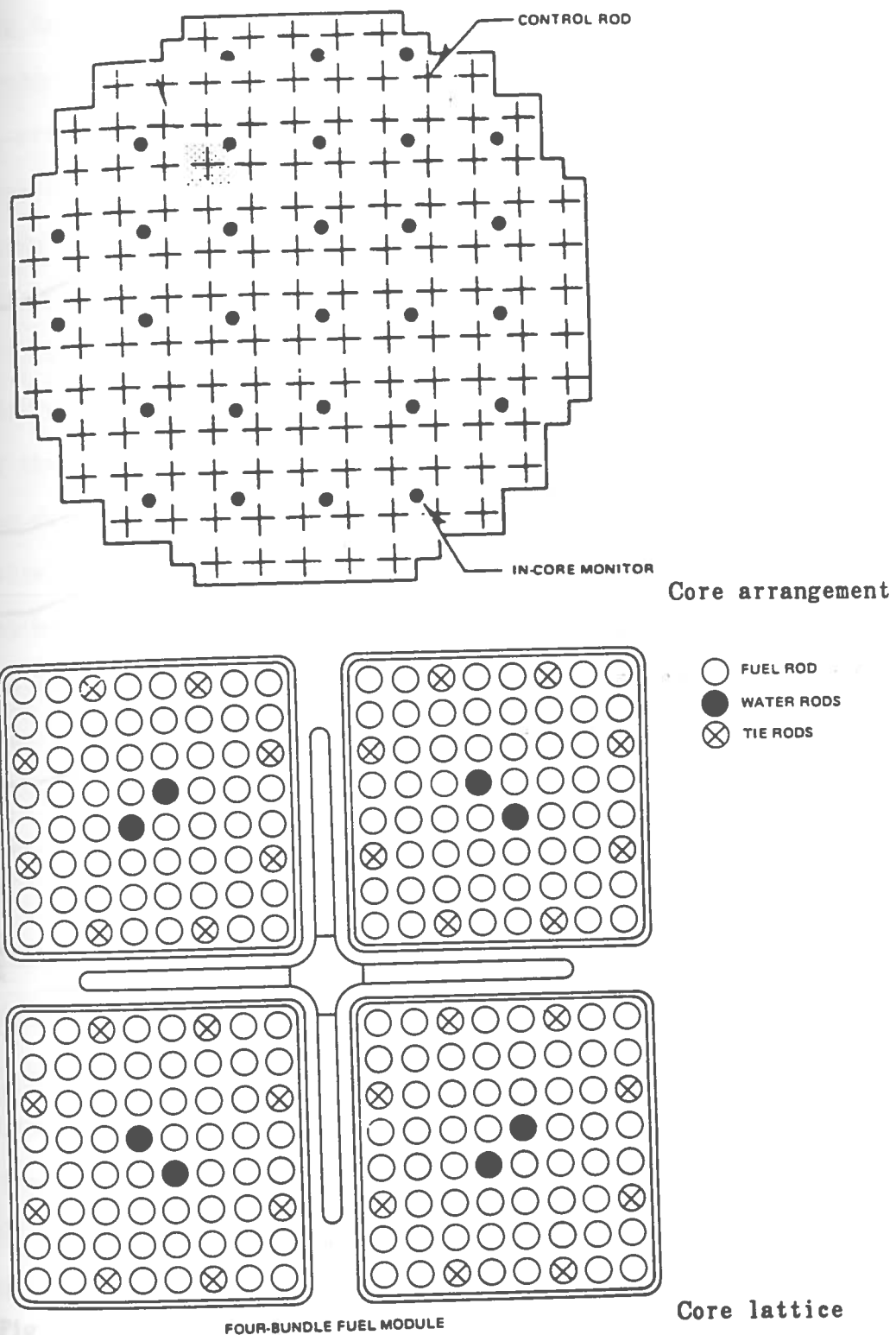
Core lattice

Fig. 3.2 Cross-sectional view of a typical BWR/6 core arrangement and core lattice[10]
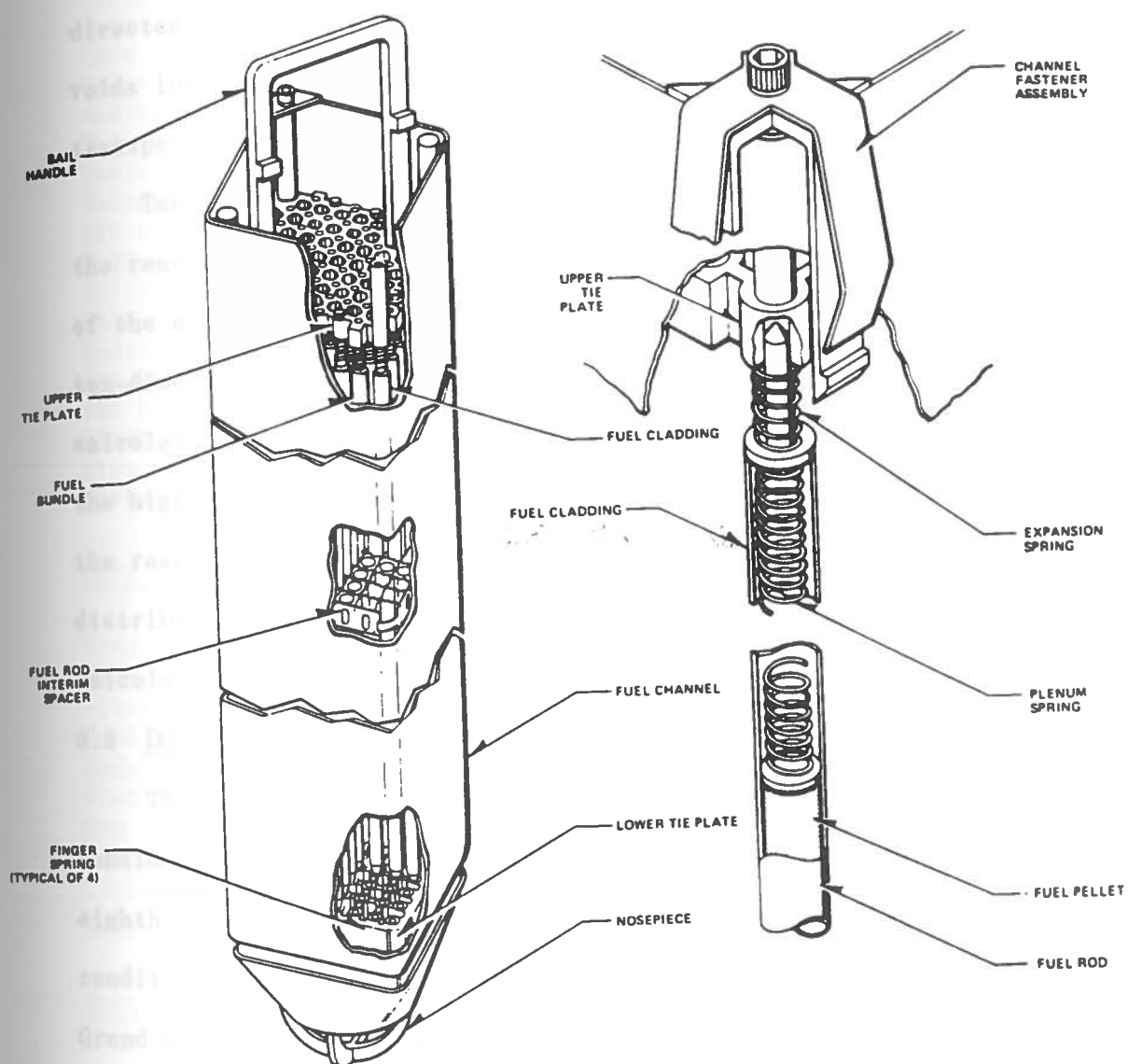
Fig. 3.3 Cut-away view of a typical BWR/6 fuel assembly[10]

BWR fuel assembly. Water is circulated through the reactor core producing saturated steam. The steam is then separated from the re-circulated water and dried in the top of the vessel, and then directed to the steam turbine-generator to generate electricity. The voids introduced in the core coolant by boiling affects the neutron transport, and must be included in the transport model.

Table 3.1 represents some of the core design data used in modeling the reactor for analysis. It should be noted that a simplified version of the actual reactor must be used in the calculation models, since only two-dimensional geometries can be represented in the DOT transport calculations. Also, only the nuclides which could effect the leakage of the high energy neutrons from the core were included in the modeling of the reactor core. As discussed in the previous section, the 3-D flux distribution is synthesized from the results of DOT R-θ, R-Z, and R calculations, respectively.

3.2 DOT-IV R-θ calculation

The symmetrical fuel loading pattern in the core enables one to consider only one eighth of the core for the R-θ calculation. The one eighth core model corresponds to a 45^0 slice with reflected boundary conditions at 0^0 and 45^0. Figure 3.4 represents an octal section of the Grand Gulf reactor at the horizontal mid-plane from the center of the core to beyond the biological concrete shield around the reactor cavity. The model used in the DOT-IV R-θ calculation is made up of 60 angular (θ) mesh intervals with a variable number of radial (R) mesh points for each θ coordinate, ranging from 144-165 radial intervals per θ. The recommended methodology described in reference (11) was followed in

Table 3.1 Core Design Data for Grand Gulf Nuclear Reactor

Reactor

Design Reactor thermal power	3833	MW
Core inlet temperature	278.9	Degrees C
Core operating pressure	1044	psig
Outer core diameter	486.41	cm
Radius of the shroud inner face	270.256	cm
Shroud thickness	5.08	cm
Radius of the liner of the RPV wall	321.31	cm
Thickness of the liner	0.476	cm
RPV wall thickness	16.392	cm
Radius of the insulation liner	351.79	cm
Thickness of the insulation liner	0.159	cm
Thickness of the insulation	8.571	cm
Radius of the concrete shield wall	436.88	cm
Jet Pump ID	18.212	cm
Jet Pump OD	20.752	cm
Riser ID	25.40	cm
Riser OD	28.245	cm
Surveillance capsule total width/thickness	8.38/3.10	cm

Core and Fuel Assemblies

Total number of fuel assemblies	800	
Number of fuel rods per assembly	64	
Pitch to pitch	15.199	cm
Fuel volume fraction in the core	22.7 %	
Moderator volume fraction in the core	61.3 %	
Cladding & channel volume fraction in the core	15 %	
Gap volume fraction	1 %	
Cladding material	Zircaloy-4	
Fuel material	UO_2	
Active core length	381	cm

Heat Transfer and Fluid Flow

Core saturated temperature	287.7	Degrees C
Total core flow	117.0	mlbs/hr
Core channel flow	103.0	mlbs/hr
Void fraction at the core mid-plane	40.50 %	
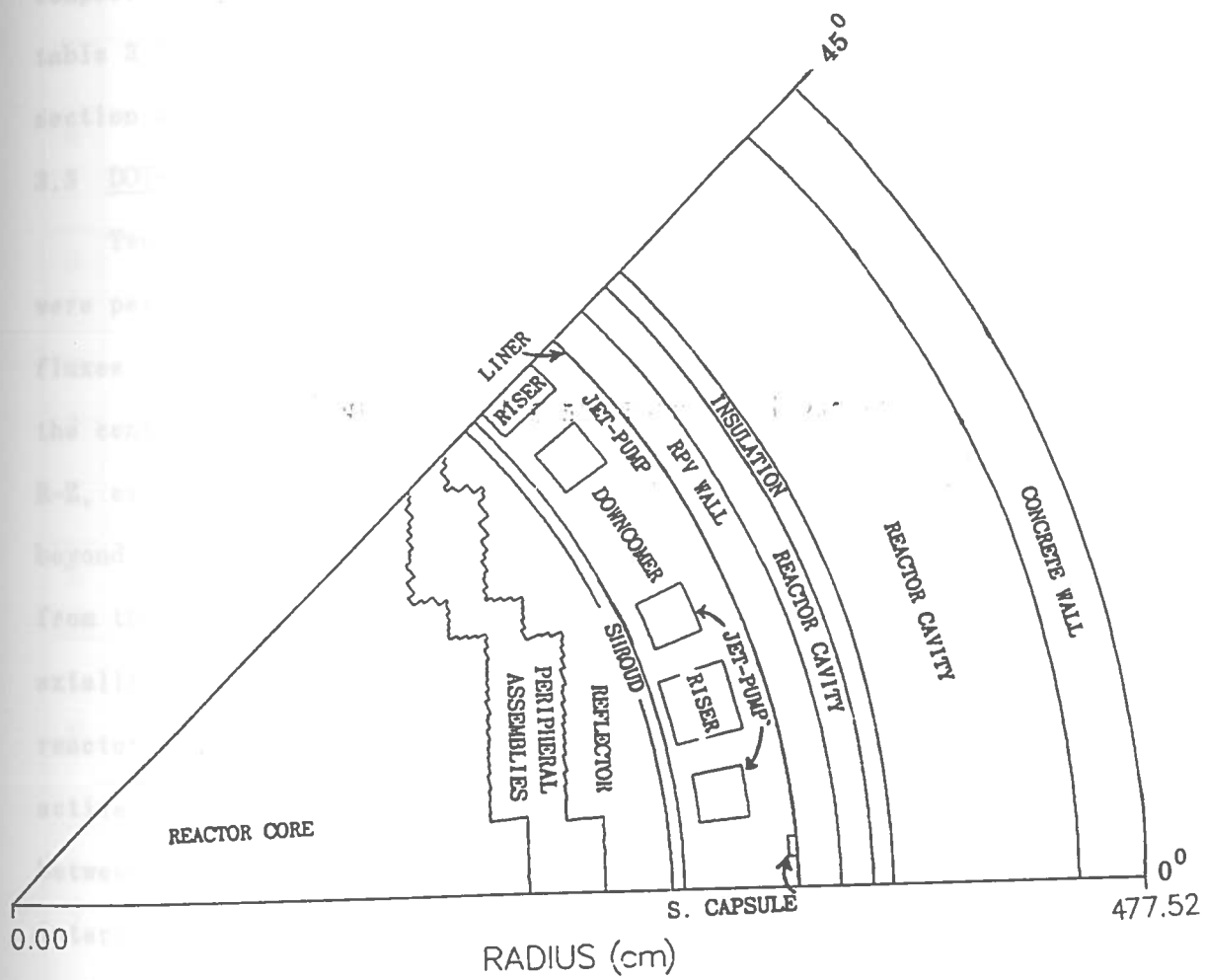
Fig. 3.4 1/8th slice of the Grand Gulf reactor model used in DOT–IV R–θ calculation

discretizing this model. The cross-sectional models of jet pumps, risers, and the surveillance capsules are included in the DOT-IV R-θ calculation to account for the significant flux perturbation effects from the presence of these reactor components. As shown in figure 3.4, the reactor model is made up of 14 different regions. The material composition for these regions used in the R-θ calculation are given in table 3.2. In this calculation, a P_3 expansion of scattering cross-section and an S_6 angular quadrature is used.

3.3 DOT-IV R-Z calculation

Two different "in-vessel and ex-vessel" R-Z transport calculations were performed to determine the axial variation of neutron and gamma fluxes. The first R-Z calculation, in-vessel, models the reactor from the center of the core to the outer surface of the RPV wall. The second R-Z, ex-vessel, model extends from the inner liner of the RPV wall to beyond the shield wall. The second R-Z calculation was "bootstrapped" from the first by coupling at the inner surface of the RPV. Both models axially have the same height, which is the exact dimensions of the reactor from approximately fifty centimeters below the bottom of the active fuel up to the outlet nozzle elevation. The main difference between these two runs is the order of quadrature and the axial mesh intervals. In order to accurately treat axial streaming in the cavity region, a larger quadrature biased in the upward and downward directions was used in the second DOT-IV R-Z calculation. The boundary fluxes at the inner face of the RPV wall calculated in the first R-Z run were interpolated to coincide with the quadrature set and axial mesh used in the second R-Z calculation. These reformated boundary fluxes were used

Table 3.2 R–θ Material Zones and Material Densities

No	Material Zone	Material/ Nuclide	Atom Densities (Atom/barn.cm)	SAILOR ID No.	Description
1	Inner-Core	H O U-235 U-238 Zr	1.8307E-02 1.9569E-02 9.4546E-05 5.1120E-03 6.4800E-03	235-238 59-62 43-46 47-50 27-30	Note (2) Note (1) " " "
2	Outer-Core	H O U-235 U-238 Zr	1.8307E-02 1.9569E-02 9.4546E-05 5.1120E-03 6.4800E-03	235-238 59-62 43-46 47-50 27-30	Note (2) Note (1) " " "
3	Reflector	H O	4.9284E-02 2.4642E-02	235-238 59-62	Note (2) Note (1)
4	Shroud (SS 304)	Cr Mn Ni Fe C Si	1.7400E-02 1.5200E-03 8.5500E-03 5.8300E-02 2.3700E-04 8.9300e-04	239-242 243-246 247-250 255-258 79-82 107-110	Note (2) " " " " Note (1)
5	Downcomer	H O	5.0455E-02 2.5228E-02	235-238 59-62	Note (2) Note (1)
6	Jet-Pump	H O Cr Fe Ni	4.1394E-02 2.0697E-02 2.7867E-03 1.1456E-02 1.2385E-03	235-238 59-62 239-242 259-262 247-250	Note (2) Note (1) Note (2) " "
7	Riser	H O Cr Fe Ni	4.2876E-02 2.1438E-02 2.3302E-03 9.5801E-03 1.0357E-03	235-238 59-62 239-242 259-262 247-250	Note (2) Note (1) Note (2) " "
8	S. Capsule	Steel	1.0000E+00	—	Note (3)
9	RPV Liner	SS 304	1.0000E+00	—	Note (3)

Table 3.2 Continued

NO	Material Zone	Material/ Nuclide	Atom Densities (Atom/barn.cm)	SAILOR ID NO.	Description
10	RPV Wall (Steel)	Cr Mn Ni Fe C Si	1.2700E-04 1.1200E-03 4.4400E-04 8.1900E-02 9.8100E-04 3.7100e-04	239-242 251-254 247-250 259-262 139-142 107-110	Note (2) " " " " Note (1)
11	Cavity	AIR/O	9.6200E-06	59-62	—
12	Insulation Liner	SS 304	1.0000E+00	—	Note (3)
13	Insulation	Al	6.0603E-03	103-106	Note (1)
14	Shield Wall	Concrete	1.9481E+00	195-198	Note (1)

Note (1)   ID number is the same for original and modified SAILOR library

Note (2)   Only in modified SAILOR library

Note (3)   This material is defined in another zone

as a boundary source for the second R-Z calculations.

3.3.1 In-vessel R-Z model

The in-vessel R-Z model used for the DOT-IV calculation, as shown in figure 3.5, is made up of 99 and 146 axial and radial mesh intervals, respectively. Also shown in this figure are the different zones used in this calculation. The material composition for each zone is given in table 3.3. Since the axial power distribution in the assemblies is not symmetrical with respect to the mid-plane of the core, the entire length of the core must be modeled in the R-Z DOT run. In addition to the axial power variation, the void distribution due to boiling also varies axially along the active core length; therefore, it is necessary to account for the presence of space dependant voids in BWR transport calculations. In this calculation, the active core length has been divided into eight regions with a representative average moderator void fraction. Figure 3.6 compares the actual moderator void fraction distribution with model distribution used in an R-Z calculation as a function of active core height. In this calculation, a P_3 expansion of the scattering cross-section, a symmetrical S_6 angular quadrature set, 47 neutron energy groups, and 20 gamma energy groups were used.

3.3.2 Cavity, "ex-vessel", R-Z model

The calculation of the neutron and gamma flux in the Grand Gulf reactor cavity was performed using a somewhat simplified geometry. The cavity region is the void space between the RPV wall and the concrete shield wall. To treat the streaming effect in the cavity region, a somewhat finer axial mesh and quadrature have been used in this calculation. The cavity R-Z model consists of 198 axial, 40 radial mesh
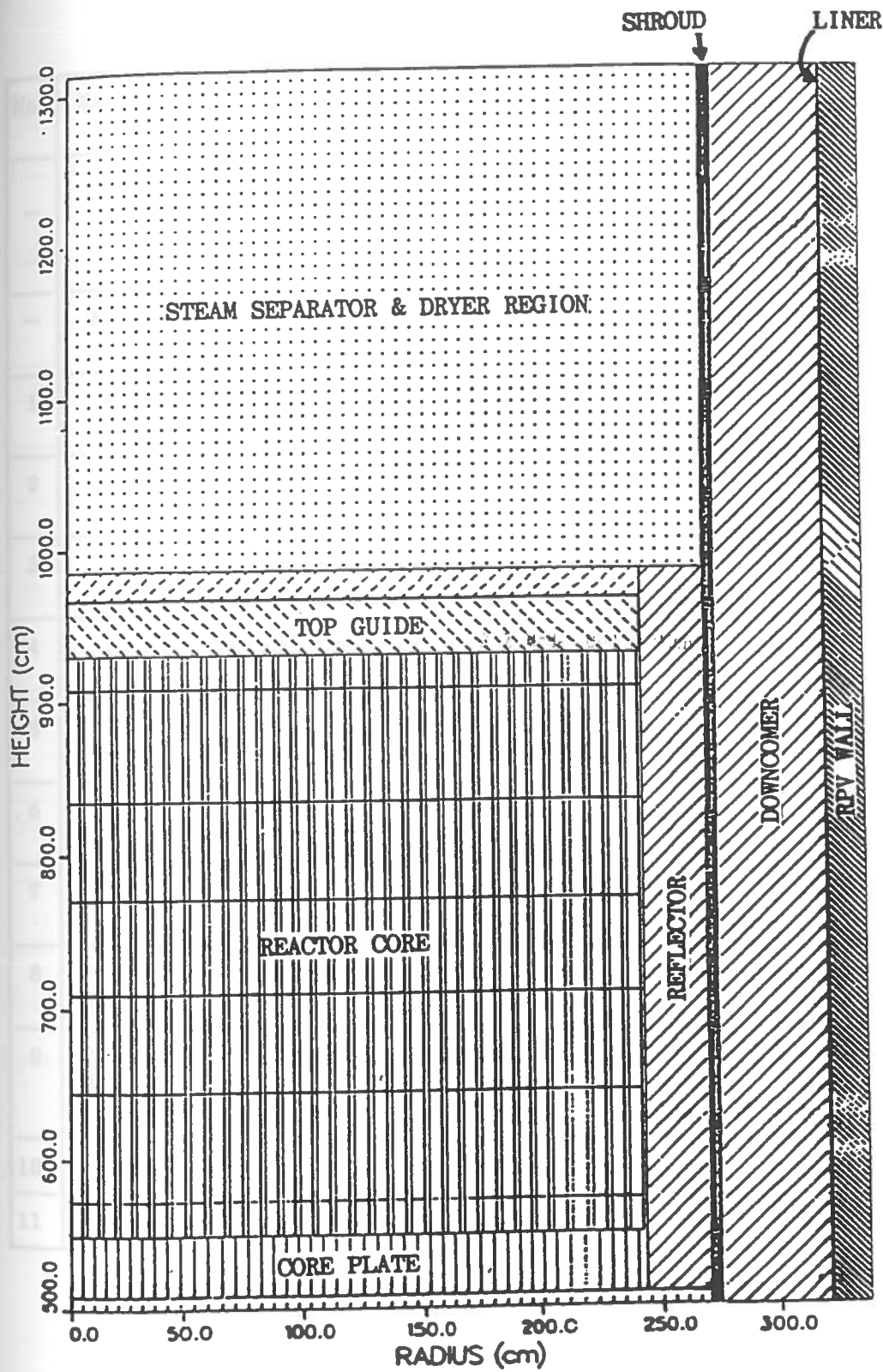
Fig. 3.5 In-vessel R-Z model used in DOT-IV calculation

Table 3.3 R-Z Material Zones and Material Densities

No	Material Zone	Material/ Nuclide	Atom Densities (Atom/barn.cm)	SAILOR ID No.	Description
–	Fuel	O U-235 U-238 Zr	1.0415E-02 9.4546E-05 5.1120E-03 6.4800E-03	59-62 43-46 47-50 27-30	Note (1) " " "
–	SAT.H2O	H O	4.9284E-02 2.4642E-02	235-238 59-62	Note (2) Note (1)
1	Core-1	Fuel SAT.H2O	1.0000E+00 6.1320E-01	— —	Note (3) "
2	Core-2	Fuel SAT.H2O	1.0000E+00 5.6300E-01	— —	Note (3) "
3	Core-3	Fuel SAT.H2O	1.0000E+00 4.2850E-01	— —	Note (3) "
4	Core-4	Fuel SAT.H2O	1.0000E+00 3.3030E-01	— —	Note (3) "
5	Core-5	Fuel SAT.H2O	1.0000E+00 2.6800E-01	— —	Note (3) "
6	Core-6	Fuel SAT.H2O	1.0000E+00 2.2560E-01	— —	Note (3) "
7	Core-7	Fuel SAT.H2O	1.0000E+00 2.0870E-01	— —	Note (3) "
8	70% Void H2O & Zr	SAT.H2O Zr	2.4660E-01 7.6896E-03	— 27-30	Note (3) Note (1)
9	70% VOID H2O & Zr & SS 304	SAT.H2O Zr SS 304	1.9930E-01 7.5125E-03 1.6180E-01	— 27-30 183-186	Note (3) Note (1) Note (4)
10	70% Void H2O	SAT.H2O	3.0000E-01	—	Note (3)
11	Reflector	SAT.H2O	1.0000E+00	—	Note (3)

Table 3.3 Continued

NO	Zone	Material/ Nuclide	Atom Densities (Atom/barn.cm)	SAILOR ID No.	Descrip- tion
12	Shroud (SS 304)	Cr Mn Ni Fe C Si	1.7400E-02 1.5200E-03 8.5500E-03 5.8300E-02 2.3700E-04 8.9300e-04	239-242 243-246 247-250 255-258 79-82 107-110	Note (2) " " " " Note (1)
13	Downcomer	H O	5.0455E-02 2.5228E-02	235-238 59-62	Note (2) Note (1)
14	RPV Liner	SS 304	1.0000E+00	—	Note (4)
15	RPV Wall (Steel)	Cr Mn Ni Fe C Si	1.2700E-04 1.1200E-03 4.4400E-04 8.1900E-02 9.8100E-04 3.7100e-04	239-242 251-254 247-250 259-262 139-142 107-110	Note (2) " " " " Note (1)
16	Inlet Region	SAT.H2O Zr SS 304	7.1860E-01 7.9747E-03 1.1350E-01	— 27-30 —	Note (3) Note (1) Note (4)
17	Core Plate	SAT.H2O SS 304	9.4640E-01 7.5600E-02	— —	Note (3) Note (4)

Note (1)   ID number is the same for original and modified SAILOR library

Note (2)   Only in modified SAILOR library

Note (3)   This material has already been defined to be mixed with other
material(s)

Note (4)   This material is defined in another zone
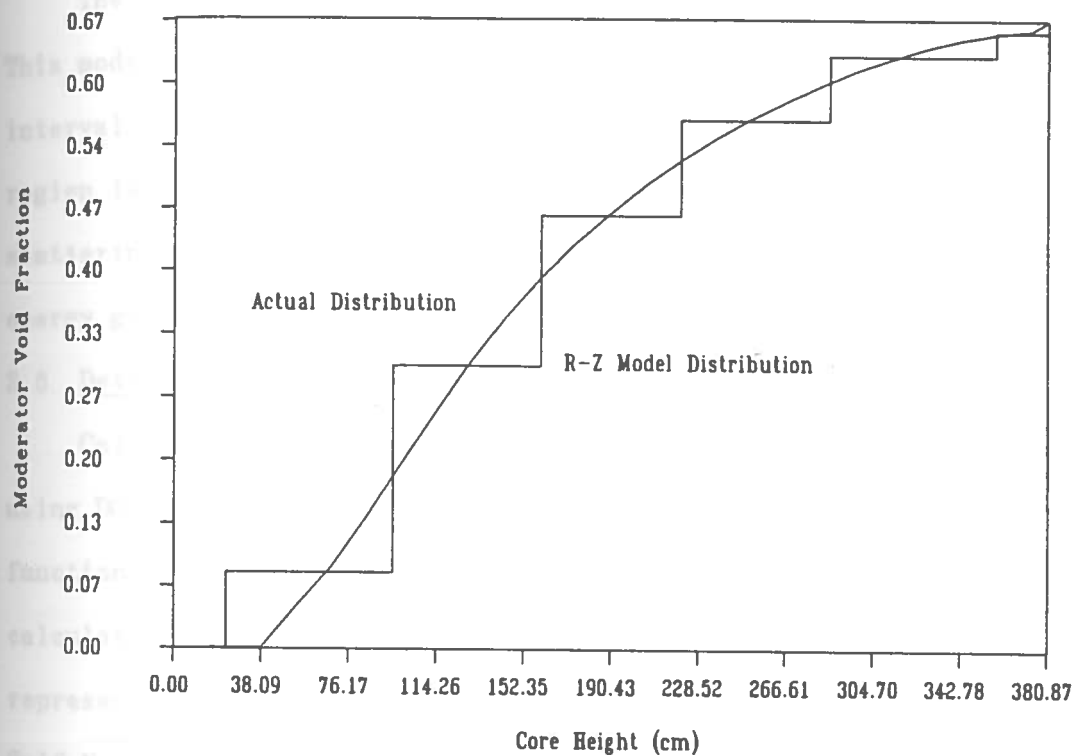
Fig. 3.6 Comparison of actual and modeled moderator void fraction distribution used in in-vessel R-Z calculation

intervals and 130 angular directions. The R-Z model used in this calculation is shown in figure 3.7. The material composition for each region is given in table 3.4. In this calculation, a P_3 expansion of scattering cross-section, 47 neutrons and 20 gamma energy groups were used.

3.4 DOT-IV 1-D calculation

The 1-D model used in this calculation is shown in figure 3.8. This model consists of 168 radial mesh intervals, one axial mesh interval and 10 material regions. The material composition of each region is given in table 3.5. In this calculation, the P_3 expansion of scattering cross-section, S_6 angular quadrature, 47 neutron and 20 gamma energy groups has been used.

3.5 Determination of neutron source

Calculation of neutron source for DOT-IV R-θ run was performed using DOTSOR[12] code, a module of the LEPRICON[11] system. The function of this code is to generate the R-θ source for DOT-IV transport calculation based on the given X-Y core power distribution. Table 3.6 represents the average assembly-wise power during cycle-2 of the Grand Gulf Nuclear Reactor. The 1/4 core X-Y power density values are converted to a neutron source density, and the X-Y source distribution is then mapped into the 1/8 core R-θ mesh used in the DOT-IV.

For the in-vessel R-Z calculation, the axial burnup distributions, as shown in table 3.7, are used to calculate the relative axial distribution. All the data presented in tables 3.6 and 3.7 were obtained from the Reactor Engineering Division[13] of the Grand Gulf Nuclear Station. Since the axial burnup distribution varies radially
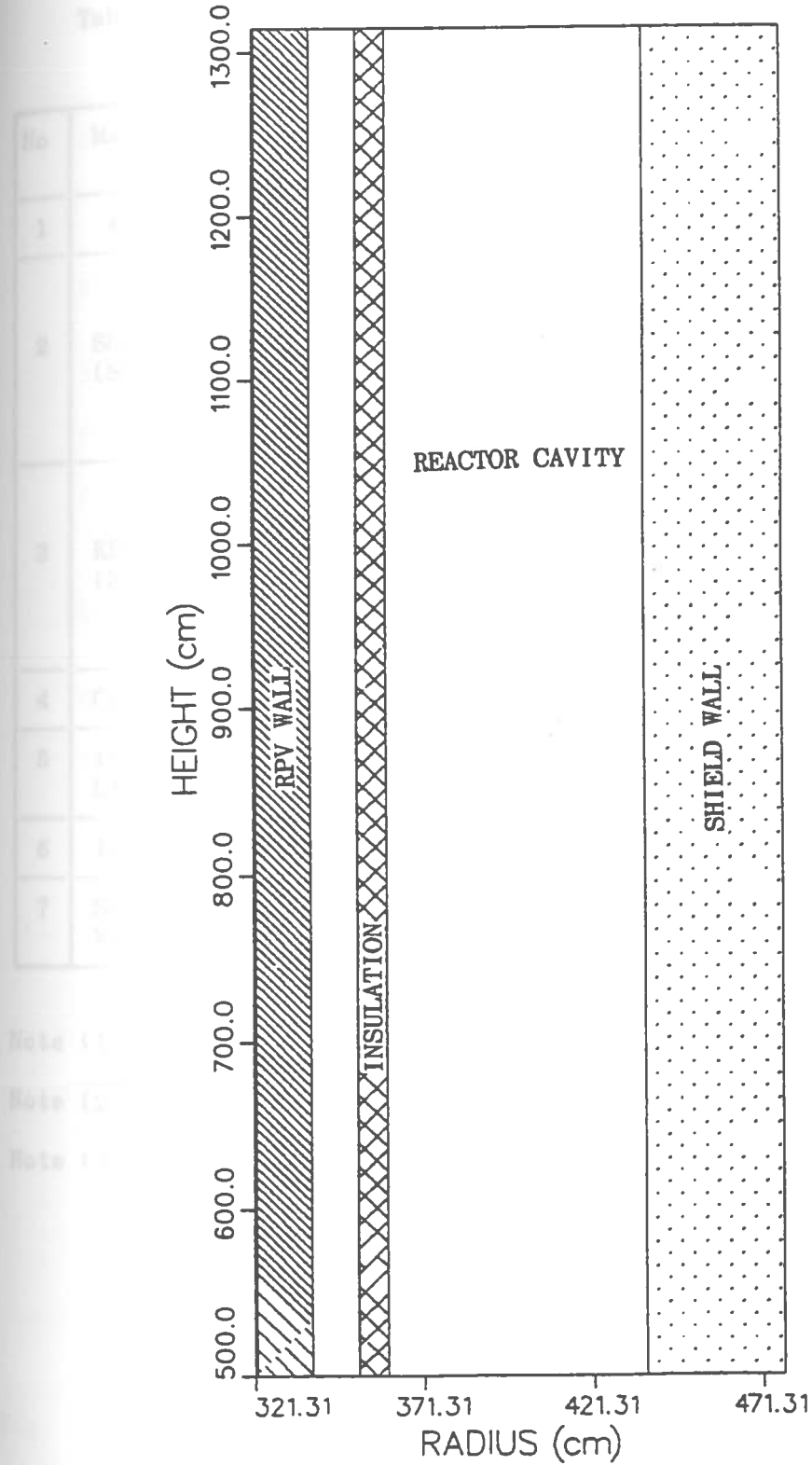
Fig. 3.7   Ex-vessel, cavity, R-Z model used in DOT-IV calculation

Table 3.4 Cavity R-Z Material Zones and Material Densities

No	Material Zone	Material/ Nuclide	Atom Densities (Atom/barn.cm)	SAILOR ID NO.	Description
1	Absorber	Absorber	1.0000E+06	—	—
2	Shroud (SS 304)	Cr	1.7400E-02	239-242	Note (2)
		Mn	1.5200E-03	243-246	"
		Ni	8.5500E-03	247-250	"
		Fe	5.8300E-02	255-258	"
		C	2.3700E-04	79-82	"
		Si	8.9300e-04	107-110	Note (1)
3	RPV Wall (Steel)	Cr	1.2700E-04	239-242	Note (2)
		Mn	1.1200E-03	251-254	"
		Ni	4.4400E-04	247-250	"
		Fe	8.1900E-02	259-262	"
		C	9.8100E-04	139-142	"
		Si	3.7100e-04	107-110	Note (1)
4	Cavity	AIR/O	9.6200E-06	59-62	Note (1)
5	Insulation LINER	SS 304	1.0000E+00	—	Note (3)
6	Insulation	Al	6.0603E-03	103-106	Note (1)
7	Shield Wall	Concrete	1.9481E+00	195-198	Note (1)

Note (1) ID number is the same for original and modified SAILOR library

Note (2) Only in modified SAILOR library

Note (3) This material is defined in another zone

Concrete shield wall ⟶ — 477.52

— 436.88

Reactor cavity ⟶

Insulation ⟶ — 360.68
— 351.79
Reactor cavity ⟶
— 338.18
RPV wall ⟶
— 321.31

Downcomer ⟶

Core shroud ⟶ — 275.34
— 270.26
Core reflector ⟶

— 242.56

Reactor core ⟶

— 0.00
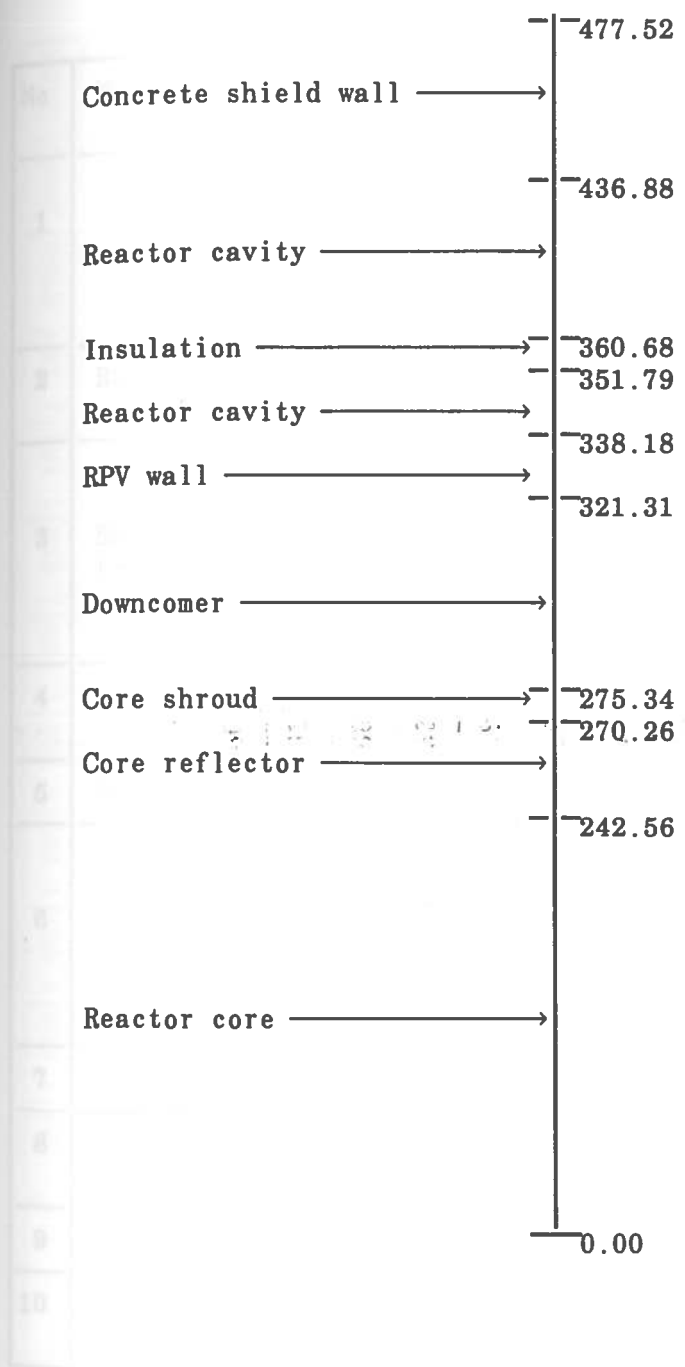
Fig. 3.8   One-dimensional model used in DOT-IV calculation (distance is in cm)

Table 3.5   1-D Material Zones and Material Densities

No	Material Zone	Material/ Nuclide	Atom Densities (Atom/barn.cm)	SAILOR ID NO.	Description
1	Core	H O U-235 U-238 Zr	1.8307E-02 1.9569E-02 9.4546E-05 5.1120E-03 6.4800E-03	235-238 59-62 43-46 47-50 27-30	Note (2) Note (1) " " "
2	Reflector	H O	4.9284E-02 2.4642E-02	235-238 59-62	Note (2) Note (1)
3	Shroud (SS 304)	Cr Mn Ni Fe C Si	1.7400E-02 1.5200E-03 8.5500E-03 5.8300E-02 2.3700E-04 8.9300e-04	239-242 243-246 247-250 255-258 79-82 107-110	Note (2) " " " " Note (1)
4	Downcomer	H O	5.0455E-02 2.5228E-02	235-238 59-62	Note (2) "
5	RPV Liner	SS 304	1.0000E+00	183-186	Note (3)
6	RPV Wall (Steel)	Cr Mn Ni Fe C Si	1.2700E-04 1.1200E-03 4.4400E-04 8.1900E-02 9.8100E-04 3.7100e-04	239-242 251-254 247-250 259-262 139-142 107-110	Note (2) " " " " Note (1)
7	Cavity	AIR/O	9.6200E-06	59-62	Note (1)
8	Insulation Liner	SS 304	1.0000E+00	—	Note (3)
9	Insulation	Al	6.0603E-03	103-106	Note (1)
10	Shield Wall	Concrete	1.9481E+00	195-198	Note (1)

Note (1)   ID number is the same for original and modified SAILOR library

Note (2)   Only in modified SAILOR library

Note (3)   This material is defined in another zone

.9965	1.026	.9875	1.017	1.003	1.037	1.251	1.103	1.131	1.128	1.314	1.098	1.191	.8670	.6450	.3170
1.027	1.081	.9590	1.192	1.041	1.138	1.002	1.272	1.126	1.291	1.115	1.268	1.033	1.006	.6255	.2665
.9945	.9590	.9565	1.057	1.236	.9980	1.167	1.106	1.153	1.126	1.285	1.089	1.166	.8350	.5190	
1.017	1.191	1.052	1.256	1.099	1.269	1.108	1.159	1.160	1.342	1.143	1.261	1.010	.9430	.4470	
1.003	1.039	1.234	1.097	1.105	1.118	1.152	1.157	1.363	1.176	1.320	1.089	1.116	.7670	.4070	
1.038	1.138	.9995	1.268	1.118	1.288	1.132	1.356	1.193	1.351	1.129	1.210	.9365	.8325	.3650	
1.253	1.002	1.168	1.108	1.151	1.128	1.314	1.168	1.357	1.158	1.261	1.000	.9700	.6020	.2660	
1.102	1.273	1.108	1.159	1.159	1.353	1.168	1.153	1.154	1.285	1.049	1.053	.7030	.3520		
1.131	1.125	1.153	1.160	1.361	1.188	1.353	1.149	1.289	1.077	1.109	.7975	.4645			
1.130	1.293	1.127	1.342	1.173	1.348	1.154	1.282	1.077	1.129	.8520	.6660	.3560			
1.316	1.117	1.288	1.145	1.320	1.127	1.259	1.047	1.107	.8510	.6945	.5165	.2400			
1.101	1.272	1.094	1.264	1.090	1.210	.9980	1.051	.7955	.6665	.5165	.3030				
1.195	1.036	1.169	1.012	1.118	.9370	.9700	.7015	.4640	.3560	.2400					
.8705	1.010	.8375	.9455	.7690	.8335	.6015	.3505								
.6465	.6275	.5205	.4475	.4090	.3655	.2670									
.3195	.2665														

Table 3.6 X-Y Relative Power Distribution at the Core Mid-plane

Table 3.7   R-Z Axial and Radial Burnup (MWD/MT) Distribution

Height[a] (cm)	Inner Core[b] Average	Adjacent to[c] Peripheral Average	Peripheral[d] Average
3.810	0.7635	0.5475	0.2875
11.430	2.4275	1.6985	0.8404
19.050	4.2285	2.9056	1.3712
26.480	5.5202	3.7752	1.7533
33.720	6.3026	4.3073	1.9864
40.960	6.9432	4.7555	2.1849
48.200	7.3665	5.0754	2.3302
55.440	7.7337	5.3671	2.4659
62.680	7.9636	5.5900	2.5784
69.910	8.1749	5.8010	2.6869
77.150	8.3051	5.9605	2.7792
84.390	8.4306	6.1158	2.8699
91.630	8.5024	6.2207	2.9432
98.850	8.5739	6.3253	3.0162
106.050	8.6205	6.3784	3.0673
113.240	8.6663	6.4299	3.1176
120.440	8.6907	6.4398	3.1502
127.640	8.7115	6.4426	3.1797
134.830	8.7014	6.4228	3.1924
142.030	8.6801	6.3948	3.1991
149.230	8.6434	6.3554	3.1975
156.420	8.5971	6.3091	3.1908
163.070	8.5526	6.2661	3.1838
169.160	8.5098	6.2268	3.1765
175.260	8.4670	6.1875	3.1692
181.360	8.4342	6.1518	3.1632
187.450	8.4014	6.1162	3.1572
193.550	8.3726	6.0828	3.1512
199.640	8.3478	6.0518	3.1452
205.740	8.3230	6.0208	3.1392
211.840	8.3090	5.9921	3.1335
217.930	8.2950	5.9635	3.1278
224.580	8.2795	5.9299	3.1191
231.780	8.2625	5.8913	3.1073
238.970	8.2397	5.8488	3.0929
246.170	8.2076	5.8000	3.0744
253.370	8.1730	5.7463	3.0530
260.560	8.1315	5.6791	3.0235
267.780	8.0842	5.6070	2.9908
274.960	8.0060	5.5092	2.9410
282.150	7.9256	5.4099	2.8903
289.370	7.7754	5.2626	2.8149
296.610	7.6249	5.1149	2.7393

Table 3.7 Continued

Height [a] (cm)	Inner Core [b] Average	Adjacent to [c] Peripheral Average	Peripheral [d] Average
303.850	7.3745	4.9075	2.6312
311.090	7.1156	4.6949	2.5204
318.330	6.7399	4.4215	2.3804
325.560	6.3386	4.1349	2.2341
332.800	5.8335	3.7917	2.0551
240.040	5.2862	3.4255	1.8627
347.280	4.6913	2.9865	1.6291
354.520	3.8744	2.4999	1.3686
361.950	2.8917	1.8529	1.0244
369.570	1.6712	1.0454	0.5964
377.190	0.5305	0.3208	0.1913

[a] Active core height in cm (0.0 cm = bottom of active core and 381 cm = top of active core)

[b] Averaged over inner core assemblies

[c] Averaged over row of assemblies adjacent to peripheral assemblies

[d] Averaged over peripheral assemblies

from the inner core assemblies to the peripheral assemblies, the average axial distributions at three regions (inner core, next to the last assembly, and peripheral assembly) were used to represent the burnup distribution for the reactor core. The 1-D source was obtained by integrating the R-Z source over Z. Figure 3.9 shows the power-time histogram of Grand Gulf during cycle-2 as provided by Mississippi Power & Light. This figure illustrates the monthly and cumulative thermal load factor for cycle-2. These load factors are the ratio of the actual thermal energy generated during the month or cycle over the energy that would have been generated by full power operation during the month or cycle. The monthly power-time history from this figure is tabulated in table 3.8.

3.6 Three-dimensional flux synthesis

Three-dimensional flux synthesis was performed by using another member of the LEPRICON system called DOTSYN[9]. This code is based on the "single-channel" synthesis method described earlier, which is one of the most commonly used methods for approximating the 3-D fluxes and dosimeter activities in RPV analysis. In this code, the 3-D flux is synthesized using the following expression previously discussed:

$$\Phi(R,\theta,Z) = \Phi_{R\theta}(R,\theta) \cdot \frac{\Phi_{RZ}(R,Z)}{\Phi_R(1-D)}$$

(3.1)

where

$\Phi(R,\theta,Z)$ = 3-D synthesized flux

$\Phi_{R\theta}(R,\theta)$ = Flux obtained from DOT R-θ calculation

$\Phi_{RZ}(R,Z)$ = Flux obtained from DOT R-Z calculation

$\Phi_R(1-D)$ = Flux obtained from DOT 1-D radial calculation
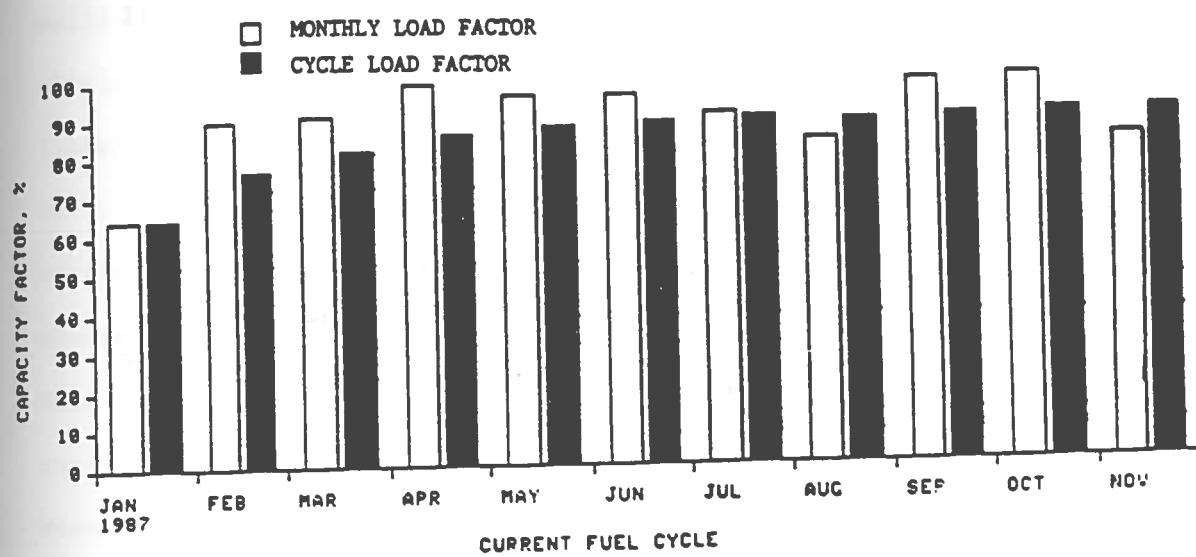
Fig. 3.9   Power-time histogram for Grand Gulf cycle-2

Table 3.8   Power-Time History of Grand Gulf Cycle-2

Month/year	Days of irradiation	Power fraction
1/87	31	0.640
2/87	28	0.890
3/87	31	0.900
4/87	30	0.990
5/87	31	0.960
6/87	30	0.960
7/87	31	0.900
8/87	31	0.820
9/87	30	0.990
10/87	31	0.990
11/87	7	0.820

The code also has the capability of calculating the 3-D fluxes and activities at any dosimeter locations.

3.7 Multi-group cross-section library

The nuclear cross-section library is one of the essential ingredients in nuclear analysis. The accuracy of the cross-section data is one of the primary factors that governs the accuracy of the analysis as compared with the experimental results. There are several multi-group cross-section libraries currently available for LWR shielding analysis. A new version of the SAILOR nuclear cross-section library has been used to obtain all the nuclear data necessary for the calculations in this study. The new SAILOR library is a modified version of the original SAILOR[7]. In the new SAILOR library, the thermal cross-section values for Cr, Mn, Ni and H is slightly different than that of the original SAILOR to incorporate a more realistic thermal spectrum. Also in this library the iron inelastic cross-section was based on a more recent, and much improved evaluation performed by Peter Fu of ORNL. The present analysis is one of the first to employ the new Fu iron cross-section data. This library, like the original SAILOR, consists of 47 neutron energy groups and 20 gamma energy groups. Table 3.9 shows the neutron and gamma energy group structure for this library. The different materials along with their SAILOR ID's are used to represent the material composition of different zones in the DOT-IV runs that are given in tables 3.2 to 3.5. The microscopic cross-section for these materials from the SAILOR library along with the atom densities were mixed in a code called GIP to obtain the macroscopic cross-sections used in the DOT-IV calculations. Reaction rates have been calculated

Table 3.9   SAILOR 47-Group Neutron and 20-Group Gamma Library
Energy Structure

Neutron Groups

Energy Group	Upper Limit (MeV)	Lower Limit (MeV)
1	1.733E+01	1.419E+01
2	1.419E+01	1.221E+01
3	1.221E+01	1.000E+01
4	1.000E+01	8.607E+00
5	8.607E+00	7.408E+00
6	7.408E+00	6.065E+00
7	6.065E+00	4.966E+00
8	4.966E+00	3.679E+00
9	3.679E+00	3.012E+00
10	3.012E+00	2.725E+00
11	2.725E+00	2.466E+00
12	2.466E+00	2.365E+00
13	2.365E+00	2.346E+00
14	2.346E+00	2.231E+00
15	2.231E+00	1.920E+00
16	1.920E+00	1.653E+00
17	1.653E+00	1.353E+00
18	1.353E+00	1.003E+00
19	1.003E+00	8.208E-01
20	8.208E-01	7.427E-01
21	7.427E-01	6.081E-01
22	6.081E-01	4.979E-01
23	4.979E-01	3.688E-01
24	3.688E-01	2.972E-01
25	2.972E-01	1.832E-01
26	1.832E-01	1.111E-01
27	1.111E-01	6.738E-02
28	6.738E-02	4.087E-02
29	4.087E-02	3.183E-02
30	3.183E-02	2.606E-02
31	2.606E-02	2.418E-02
32	2.418E-02	2.188E-02
33	2.188E-02	1.503E-02
34	1.503E-02	7.102E-03
35	7.102E-03	3.355E-03
36	3.355E-03	1.585E-03
37	1.585E-03	4.540E-04
38	4.540E-04	2.144E-04
39	2.144E-04	1.013E-04
40	1.013E-04	3.727E-05
41	3.727E-05	1.068E-05

Table 3.9 Continued

Energy Group	Upper Limit (MeV)	Lower Limit (MeV)
42	1.068E-05	5.043E-06
43	5.043E-06	1.855E-06
44	1.855E-06	8.764E-07
45	8.764E-07	4.140E-07
46	4.140E-07	1.000E-07
47	1.000E-07	1.000E-11

Gamma Groups

Energy Group	Upper Limit (MeV)	Lower Limit (MeV)
1	1.400E+01	1.000E+01
2	1.000E+01	8.000E+00
3	8.000E+00	7.000E+00
4	7.000E+00	6.000E+00
5	6.000E+00	5.000E+00
6	5.000E+00	4.000E+00
7	4.000E+00	3.000E+00
8	3.000E+00	2.000E+00
9	2.000E+00	1.500E+00
10	1.500E+00	1.000E-01
11	1.000E+00	8.000E-01
12	8.000E-01	7.000E-01
13	7.000E-01	6.000E-01
14	6.000E-01	4.000E-01
15	4.000E-01	2.000E-01
16	2.000E-01	1.000E-01
17	1.000E-01	6.000E-02
18	6.000E-02	3.000E-02
19	3.000E-02	2.000E-02
20	2.000E-02	1.000E-02

for the following selected dosimeter materials from the SAILOR "activity material".

$Fe^{54}(n,p)Mn^{54}$; $Ni^{58}(n,p)^{58}Co$; $Np^{237}(n,f)^{137}Cs$; $U^{238}(n,f)^{137}Cs$;

$Ti^{46}(n,p)^{46}Sc$; Total Flux ; Flux >1.0 MeV ; Flux >0.1 MeV ;

Flux <0.4 eV (Thermal Flux)

The $Cu^{63}(n,\alpha)^{60}Co$ activity cross-sections in the SAILOR library have been previously observed to produce poor results. In this analysis the $Cu^{63}(n,\alpha)$ cross-sections were obtained from a more accurate data set that was available at ORNL.

The cross-sections for the $Ta^{181}(n,\gamma)^{182}Ta$ activity calculation were obtained from the VELM22[14] multi-group cross-section library. This library contains 22 energy groups. The 47 group fluxes from DOT-IV calculations were collapsed to VELM22 group structure.

CHAPTER 4

GRAND GULF REACTOR CAVITY NEUTRON DOSIMETER EXPERIMENT

The neutron dosimeter experiment was performed using several dosimeter foils and wires representing a variety of reaction cross-section thresholds. The objective of this experiment was to estimate the intensity of the fast neutron flux at different azimuthal and axial locations in the cavity of the Grand Gulf Boiling Water Reactor shown in figure 4.1. The measured, absolute activity of these dosimeter foils will be used to compare with the calculated activities of the same dosimeters at the location of the irradiation, whereas the wires will provide the relative axial distribution.

Three sets of wires; Ni, Cu, Fe and ten sets of dosimeter packets were prepared at LSU to be activated in the reactor cavity of Grand Gulf during cycle-2. These wires and dosimeter foils, along with a written experimental procedure, was shipped to the Grand Gulf Nuclear Power Plant. Based on a previous agreement, the Grand Gulf management had assigned a team to conduct the experiment. The installation of the wires and dosimeter packets was completed by December 1986.

On November 7, 1987, at the end of the one year, cycle-2 period, the three sets of wires and dosimeter packets were removed from the cavity of the Grand Gulf Nuclear Power Plant. These wires and dosimeter packets passed through several stages of testing at the plant, counting for radioactivity and decontamination before being released for shipment back to the Nuclear Science Center at LSU. The preliminary counting of the radiation levels conducted by the Grand Gulf Health Physics department revealed that the γ-β contact dose to be 25 mR. The total
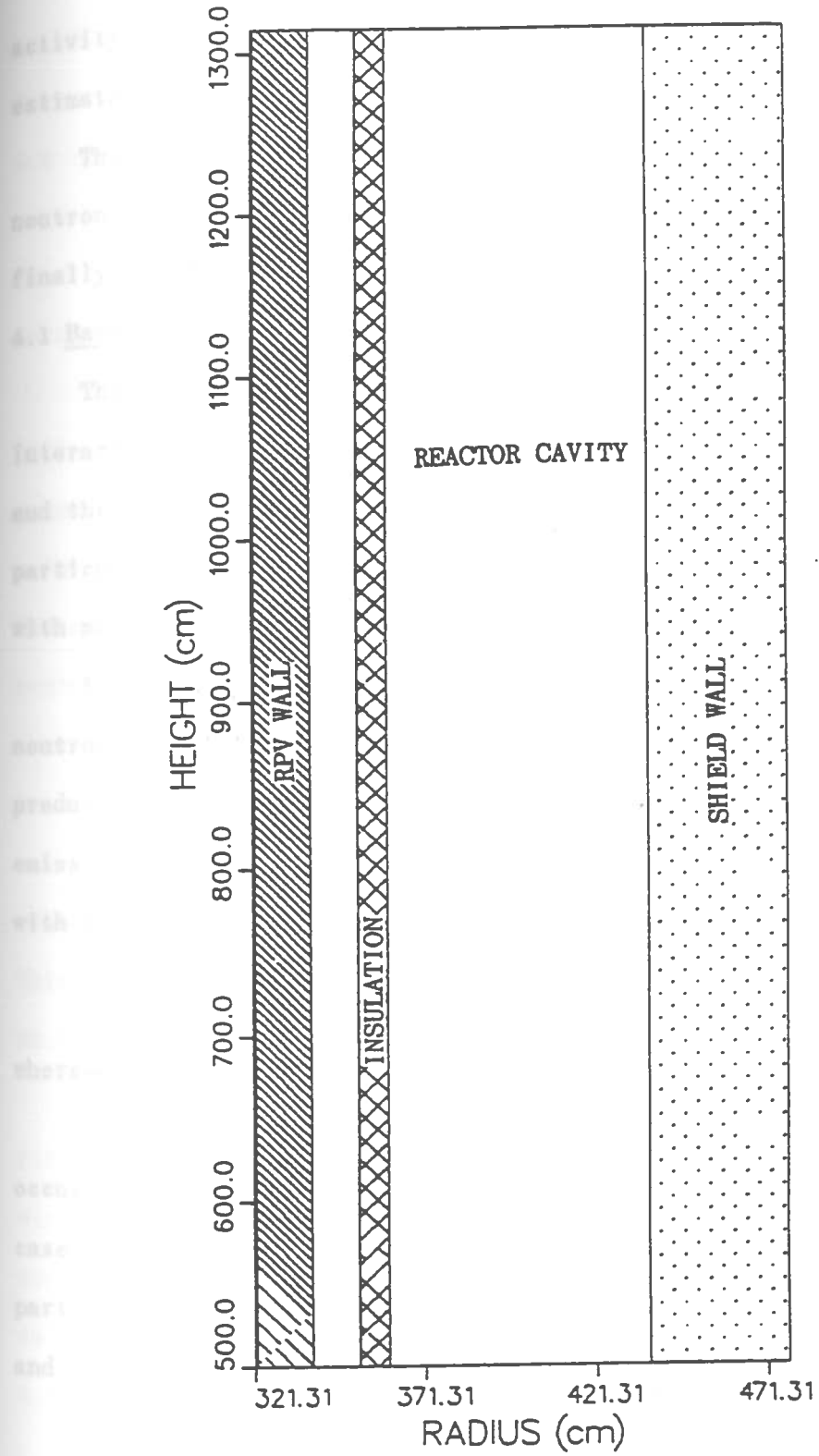
Fig. 4.1 Cavity R-Z model

activity of 0.22 mCi consisting of Co-60, Co-58, Ta-182, and Mn-54 was estimated.

This chapter will first present a brief theoretical background on neutron activation followed by material, experimental procedure and finally, the activation counting result.

4.1 Background

The activation of a material in the neutron field results from the interaction of the neutron with that matter. The energy of the neutron and the material cross-section are the key for the probability of the particular interaction to occur. The two types of neutron interaction with matter will be the emphasis of this discussion.

1) <u>Radioactive capture (n,γ)</u>. This interaction takes place when a neutron is absorbed in the nucleus of a matter. The result is the production of an excited compound nucleus which attains stability by emission of gamma radiation. This type of reaction is more probable with thermal and epithermal neutrons and can be written as:

$$_{Z}^{A}X + _{0}^{1}n \longrightarrow _{Z}^{A+1}Y + \gamma$$
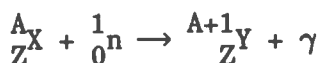
where X and n are the reactant and Y and γ are the product.

2) <u>Capture with particle emission</u>. Ejection of a charged particle occurs normally when a fast neutron interacts with matter. In this case, the resultant compound nucleus will decay by ejection of a charged particle. Two examples of this type of interaction are (n,p) and (n,α) and the process can be written as:

$$(n,P): \quad _{Z}^{A}X + _{0}^{1}n \longrightarrow _{Z-1}^{A}Y + _{1}^{1}P$$

$$(n,\alpha): \quad _{Z}^{A}X + _{0}^{1}n \longrightarrow _{Z-2}^{A-3}Y + _{2}^{4}\alpha$$
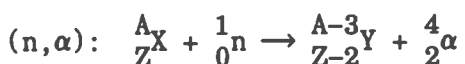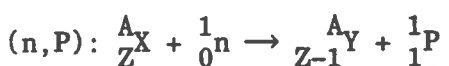
In this study the (n,P) and (n,α) reactions are used for fast neutron detection.

4.2 <u>Activation dosimeter foils and selection criteria</u>:

For the selection of the activation foil dosimeters used in this experiment, the guidelines described in reference (15) were followed in accordance with the availability and cost of the material constraints.

The neutron dosimeter packets included several types of activation foils with various threshold energies. Although this experiment primarily emphasized estimating the intensity of the fast neutron flux, a few foils with thermal energy range sensitivity were also included. The activation foils used for both fast and thermal neutron flux estimation along with the type of reactions, half-life, and threshold energy data are given in table 4.1. Mostly long half-life materials, except Al and Al Au alloy (Al-Au), were selected in case of any unexpected delay between the end of irradiation and counting time. Some of these foils, such as Fe, Ni, Cu, and Al, were purchased from Morton Thiokol, Inc. The percentage of purity of all the foils is roughly 99.99%.

Each set of wires used in this experiment included approximately fifty feet of three different wires of Ni, Cu, and Fe. Since these wires were used to estimate the relative axial distribution of fast neutrons, the purity of each wire was not a major criteria in the selection of the wires.

4.3 <u>Procedures</u>

4.3.1 <u>Preparation and installation of the dosimeters</u>

The three sets of wires and activation dosimeter foils were each

Table 4.1   Types of Neutron Dosimeter Foils Used in the Cavity
Experiment

Foils & reactions	Half-life	Threshold energy (MeV)
^{54}Fe(n,p)^{54}Mn	312 days	2.20
^{58}Ni(n,p)^{58}Co	71 days	1.60
^{63}Cu(n,α)^{60}Co	5.27 years	5.00
^{27}Al(n,α)^{24}Na	15.06 hours	7.20
^{181}Ta(n,γ)^{182}Ta	114 days	thermal
^{197}Au(n,γ)^{198}Au	2.69 days	thermal
^{59}Co(n,γ)^{60}Co	5.27 years	thermal

suspended at three different azimuthal locations in the reactor cavity, as shown in figure 4.2. Each set contained three different wires, corresponding to Ni, Cu, and Fe, respectively. The wires extended approximately 50 feet, from the bottom of the annulus to eight feet above the feed water nozzle. The installation diagram provided by Grand Gulf is shown in figure 4.3. The dosimeter packets which were attached to the wires at various elevations by the Grand Gulf team are also shown in figure 4.3. The dosimeter packets were made out of two (2"x2"x0.006") aluminum plates. Each packet contained four different activation foils wrapped in (0.002") thick aluminum foil to protect it from any cross contamination. Each foil was glued at each of the four corners of the aluminum plates and a second aluminum plate was placed on top and stapled on the edges to the first plate, constructing a dosimeter packet. Each packet was then wrapped in (0.002") thick aluminum foil to prevent any airborne contamination in the cavity region. Table 4.2 represents the types of activation foil dosimeters comprising each dosimeter packets.

4.3.2 Shipping and storage

On February 2, 1988, the neutron flux dosimeter packets and wires were shipped to the Nuclear Science Center at LSU in a certified type-A container under the supervision of the Grand Gulf Health Physics officials. The shipment was checked upon arrival by the Nuclear Science Center Radiation Protection officers and stored in room 52. This room is a long-term storage room for any radioactive material used in the Nuclear Science Center.
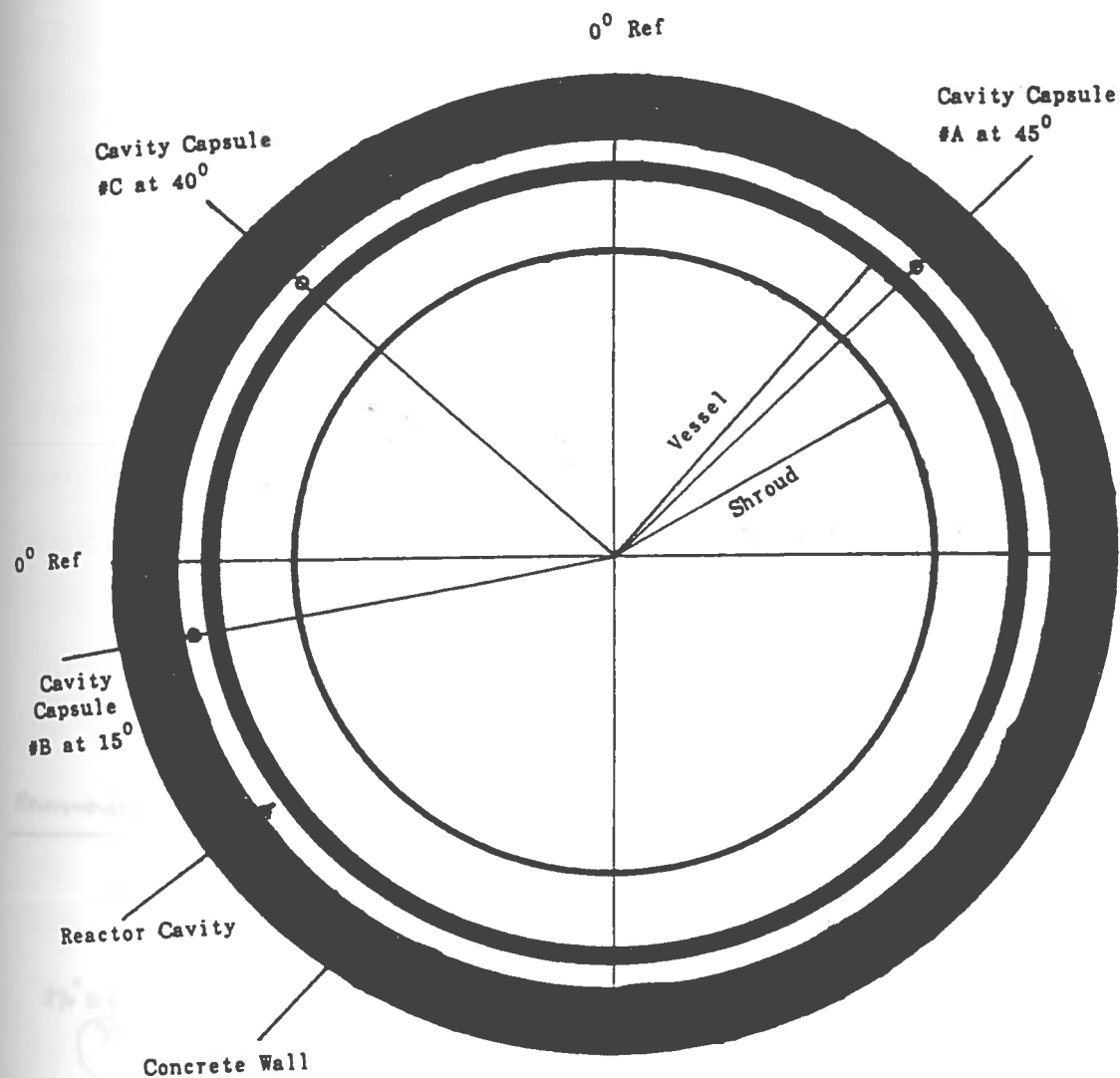
Fig. 4.2 Azimuthal location of the Grand Gulf neutron capsule in the reactor cavity
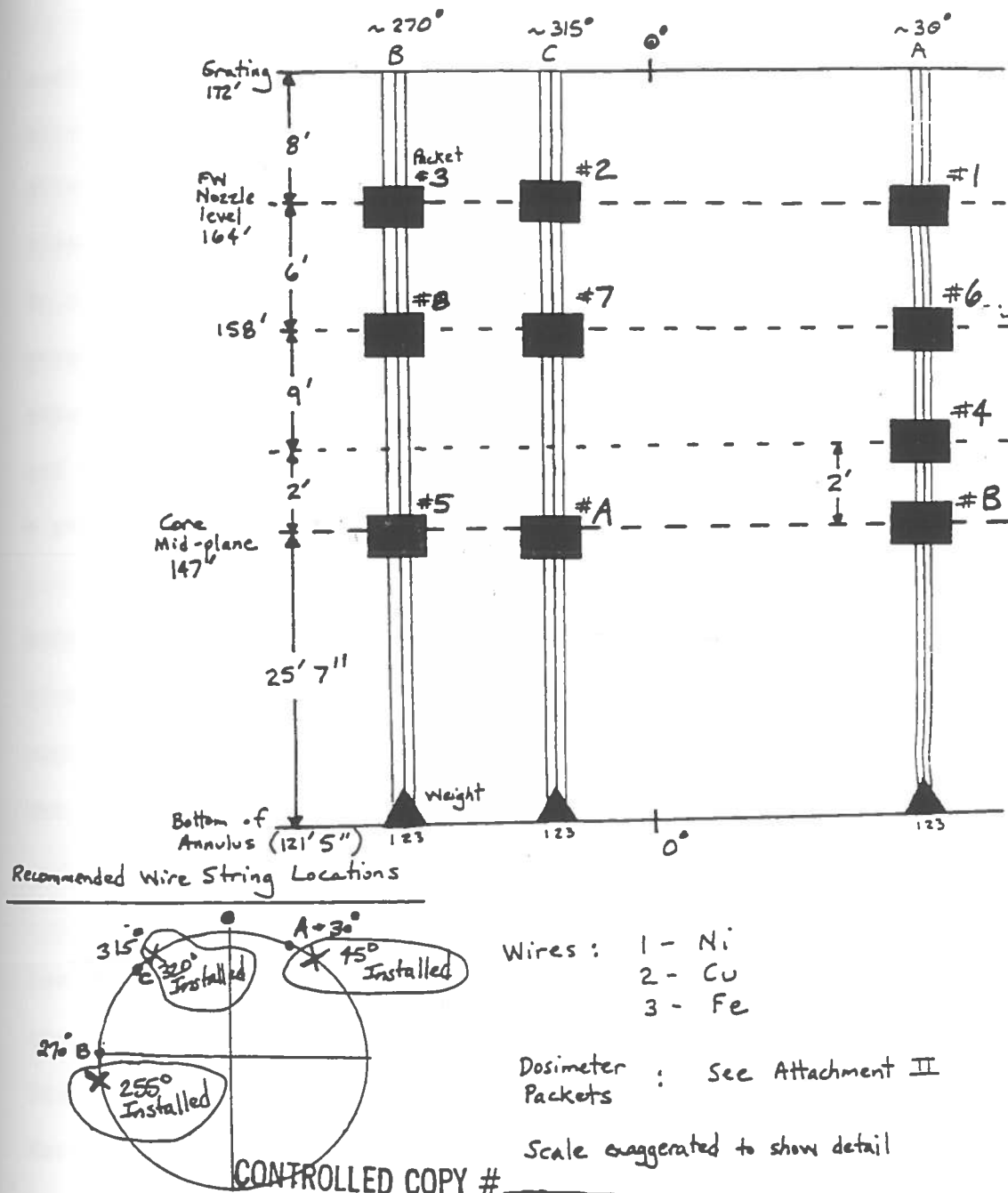
Fig. 4.3 Installation diagram of the neutron dosimeters[16]

Table 4.2 Neutron Dosimeter Foils With Corresponding Weights

Dosimeter capsule #	Foils	Weight (gm)
A	Au–Al	0.11389
	Cd–Au–Al	0.09860
	Cd–Co	0.20555
	Co	0.14379
B	Au–Al	0.12172
	Cd–Au–Al	0.10273
	Cd–Co	0.21534
	Co	0.14501
1	Fe	0.12665
	Ni	0.39125
	Cu	1.23430
	Ta	0.35514
2	Fe	0.13270
	Ni	0.34887
	Cu	1.35417
	Ta	0.36399
3	Fe	0.13140
	Ni	0.40869
	Cu	1.22105
	Ta	0.35781
4	Fe	0.12671
	Ni	0.36924
	Cu	1.19685
	Ta	0.34250
5	Fe	0.13278
	Ni	0.36664
	Cu	1.31235
	Ta	0.36440
6	Fe	0.13240
	Ni	0.39946
	Cu	1.28808
	Al	0.11587
7	Fe	0.13280
	Ni	0.37728
	Cu	1.23328
	Al	0.10829
8	Fe	0.13390
	Ni	0.35058
	Cu	1.18345
	Al	0.10956

4.3.3 Activated wires and foils handling procedure

Preliminary surveying of the three wire sets indicate that the γ-β contact dose varied within 20-30 mR. Based on this measurement the wires at 45^0 and 15^0 had the highest and lowest activity, respectively. After the separation of the wires, each wire was wiped off several times, first with clean dampened and then with clean dry rags, in order to clean any existing surface contamination before the wires were prepared for counting. In order to avoid any excess contact dose exposure from handling the wires and foils, the use of heavy duty gloves and tweezers or pliers were used. Each of the wires were wrapped around a pre-labeled spool and was stored in room 52.

Each dosimeter packet was cleaned following the same procedure mentioned above, before disassembling. All components of each packet, aluminum plates and foils were monitored and disposed of in the appropriate waste container. Each foil was cleaned and re-weighed, then was sealed in thin plastic and stored in pre-labeled envelopes.

4.3.4 Counting procedure

The LSU high purity Ge (HP Ge) Gamma Spectrometer has a relatively low counting efficiency which hampered counting some of the low activity samples. Therefore the dosimeter foils were shipped to the Louisiana Nuclear Energy Division Environmental Laboratory to be analyzed by Mr. Matt Schlenker. There, the foils were analyzed with a high efficiency high purity Ge (HP Ge) Gamma Spectrometer and Multi-Channel analyzer along with "Canberra Spectran-F V3.00" software. The software is an automated NRC standard methodology for gamma spectrum analysis.

The gamma spectrum of all activated wires were analyzed by using

the high purity Ge (HP Ge) Gamma Spectrometer and Multi-Channel analyzer
at LSU. Each wire was marked at every one foot interval along its
entire length. The activated wire was then passed over the detector
tube. Sufficient shielding materials were used to collimate the
detector in a way so that only a 3.5 inch segment (the detector tube
diameter) of the length of wire at each of the one foot intervals was
counted. Also the spools containing the remainder of the wires were
shielded from all sides by means of lead bricks to reduce the radiation
level below 2 mR and to avoid any excessive background counts increase.

4.4 Experimental results

Table 4.3 represents the results obtained from the analysis of the
activated dosimeter foils. In this table, the types of foils which were
activated in the reactor cavity, along with the activity of each nuclide
is listed. Because the delivery of the dosimeters were delayed for
about three months, the low half-life activated dosimeter foils such as
Al and Al-Au had decayed away prior to counting. Also, it should be
noted that because of lower levels of high energy neutron flux at the
upper elevation in the cavity, some of the foils and wires, with high
threshold energy, contained insufficient activities. The 3.5 inch
segment, of each wire was counted for every one foot interval along the
entire length and the obtained results are tabulated in tables 4.4
through 4.6. In these tables the counts per minute per 3.5" wire
segment and the associated percent standard deviations are obtained
using the following relations[17]:

$$r = x/t$$

where r is the net count rate (counts.min^{-1}) and x is the total net

Table 4.3 Measured Activity of the Dosimeter Foils at Several
Axial and Azimuthal Locations in the Reactor Cavity

15^0 Azimuth

Height[a]	Foils and reactions	$Ae^{[b]} \pm \%$ SD[c]
779.78	$^{58}Ni(n,p)^{58}Co$	2.15E+4±1.00%
	$^{54}Fe(n,p)^{54}Mn$	7.83E+2±5.75%
	$^{63}Cu(n,\alpha)^{60}Co$	2.38E+1±4.15%
	$^{181}Ta(n,\gamma)^{182}Ta$	2.54E+7±0.51%
1115.06	$^{58}Ni(n,p)^{58}Co$	5.35E+2±3.80%
	$^{54}Fe(n,p)^{54}Mn$	1.20E+1±16.1%
	$^{63}Cu(n,\alpha)^{60}Co$	No Activity
1297.94	$^{58}Ni(n,p)^{58}Co$	1.07E+2±8.10%
	$^{54}Fe(n,p)^{54}Mn$	1.33E+1±29.0%
	$^{63}Cu(n,\alpha)^{60}Co$	No Activity
	$^{181}Ta(n,\gamma)^{182}Ta$	4.17E+5±0.68%

40^0 Azimuth

Height[a]	Foils and reactions	$Ae^{[b]} \pm \%$ SD[c]
1115.06	$^{58}Ni(n,p)^{58}Co$	7.15E+2±3.20%
	$^{54}Fe(n,p)^{54}Mn$	1.58E+1±27.0%
	$^{63}Cu(n,\alpha)^{60}Co$	No Activity
1297.94	$^{58}Ni(n,p)^{58}Co$	2.25E+2±5.80%
	$^{54}Fe(n,p)^{54}Mn$	1.07E+1±18.0%
	$^{63}Cu(n,\alpha)^{60}Co$	No Activity
	$^{181}Ta(n,\gamma)^{182}Ta$	6.93E+5±0.80%

Table 4.3 Continued

45^0 Azimuth

Height[a]	Foils and reactions	Ae[b] ± % SD[c]
840.74	$^{58}Ni(n,p)^{58}Co$	8.76E+3±1.60%
	$^{54}Fe(n,p)^{54}Mn$	3.30E+2±8.20%
	$^{63}Cu(n,\alpha)^{60}Co$	9.20E+0±5.00%
	$^{181}Ta(n,\gamma)^{182}Ta$	2.28E+7±0.50%
1115.06	$^{58}Ni(n,p)^{58}Co$	4.62E+2±2.75%
	$^{54}Fe(n,p)^{54}Mn$	1.37E+1±16.0%
	$^{63}Cu(n,\alpha)^{60}Co$	No Activity
1297.94	$^{58}Ni(n,p)^{58}Co$	1.98E+2±5.80%
	$^{54}Fe(n,p)^{54}Mn$	6.90E+0±25.3%
	$^{63}Cu(n,\alpha)^{60}Co$	No Activity
	$^{181}Ta(n,\gamma)^{182}Ta$	6.26E+5±0.64%

[a] The height corresponds to the original axial locations of the dosimeters.

[b] Experimental measure activity (Bq/g)

[c] % Standard Deviation

Table 4.4 Measured Axial Activity in Counts per Minute per 3.5"
Wire Segments of Fe, Ni and Cu at 15^0 Azimuth

ELEVATION (cm)	$^{54}Fe(n,p)^{54}Mn$	$^{58}Ni(n,p)^{58}Co$ Counts/min(% SD[a])	$^{63}Cu(n,\alpha)^{60}Co$
35.56	19.0(8.00)	13.0(9.00)	10.0(9.00)
66.04	59.0(4.50)	14.0(9.00)	14.0(9.00)
96.52	20.0(7.50)	14.0(10.0)	32.0(5.50)
127.00	22.0(7.50)	16.0(9.00)	34.0(5.50)
157.48	59.0(4.50)	19.0(8.00)	30.0(6.00)
187.96	40.0(5.50)	26.0(7.00)	87.0(3.50)
218.44	60.0(4.50)	32.0(6.00)	49.0(4.50)
248.92	36.0(7.50)	49.0(4.50)	48.0(4.50)
279.40	108.0(4.50)	77.0(3.50)	41.0(5.00)
309.88	80.0(5.50)	122.0(3.00)	39.0(5.50)
340.36	126.0(4.50)	215.0(3.00)	45.0(5.00)
370.84	192.0(3.50)	360.0(3.00)	23.0(7.00)
401.32	314.0(2.00)	661.0(2.50)	33.0(6.00)
431.80	336.0(2.00)	950.0(2.50)	42.0(5.00)
462.28	435.0(1.50)	1340.0(2.00)	43.0(5.00)
492.76	547.0(1.50)	1522.0(1.00)	49.0(4.40)
523.24	570.0(1.50)	1723.0(1.00)	42.0(5.00)
553.72	624.0(1.50)	1947.0(1.00)	44.0(3.50)
584.20	663.0(1.50)	2047.0(0.50)	54.0(3.50)
614.68	676.0(1.00)	2070.0(0.50)	54.0(3.50)
645.16	630.0(1.50)	1985.0(0.50)	47.0(3.50)
675.64	583.0(1.50)	1850.0(0.50)	48.0(4.50)
706.12	513.0(1.50)	1698.0(1.00)	44.0(5.00)
736.60	409.0(1.50)	1377.0(1.00)	55.0(4.50)
767.08	282.0(2.00)	973.0(1.50)	28.0(6.50)
779.78	245.0(2.00)	811.0(1.50)	41.0(5.00)
810.26	161.0(2.50)	487.0(2.00)	42.0(5.00)
840.74	104.0(3.50)	287.0(3.00)	65.0(6.00)
871.22	71.0(4.00)	181.0(3.50)	37.0(7.50)
901.70	56.0(4.50)	129.0(4.00)	10.0(14.5)
932.18	42.0(7.50)	101.0(4.50)	9.0(16.0)
962.66	31.0(9.00)	84.0(5.00)	---------
993.14	---------	75.0(5.50)	No Counts
1023.62	No Counts	68.0(5.50)	---------
1054.10	---------	61.0(6.00)	---------
1084.58	---------	49.0(6.50)	---------
1120.14	---------	44.0(6.00)	---------
1150.62	---------	43.0(6.00)	---------
1181.10	---------	35.0(6.50)	---------

[a]% Standard Deviation in combined count rate and background

Table 4.5 Measured Axial Activity in Counts per Minute per 3.5"
Wire Segments of Fe, Ni and Cu at 40^0 Azimuth

ELEVATION (cm)	^{54}Fe(n,p)^{54}Mn	^{58}Ni(n,p)^{58}Co	^{63}Cu(n,α)^{60}Co
		Counts/min(% SD[a])	
25.40	No Counts	12.0(10.0)	No Counts
55.88	----------	15.0(8.50)	----------
86.36	----------	17.0(8.00)	----------
116.84	----------	18.0(8.50)	----------
147.32	----------	22.0(7.00)	----------
177.80	----------	24.0(7.00)	----------
208.28	----------	31.0(6.00)	----------
238.76	----------	37.0(5.50)	----------
269.24	----------	53.0(4.50)	----------
299.72	34.0(3.00)	163.0(3.50)	----------
330.20	80.0(2.00)	303.0(2.50)	----------
360.68	141.0(1.50)	554.0(3.50)	----------
391.16	232.0(1.00)	889.0(2.50)	14.0(9.00)
421.64	394.0(1.00)	1334.0(1.00)	20.0(7.50)
452.12	528.0(0.50)	1632.0(1.00)	32.0(6.00)
482.60	644.0(0.50)	1990.0(1.00)	38.0(5.50)
513.08	759.0(0.50)	2122.0(1.00)	45.0(5.00)
543.56	835.0(0.50)	2259.0(1.00)	47.0(5.00)
574.04	862.0(0.50)	2511.0(1.00)	48.0(4.00)
604.52	890.0(0.50)	2610.0(1.00)	55.0(3.50)
635.00	888.0(0.50)	2685.0(1.00)	55.0(3.50)
665.48	868.0(0.50)	2572.0(1.00)	46.0(4.00)
695.96	740.0(0.50)	2137.0(1.00)	43.0(4.00)
723.90	621.0(0.50)	1879.0(1.00)	36.0(5.50)
756.92	539.0(0.50)	1475.0(1.50)	31.0(6.00)
779.78	384.0(1.00)	1197.0(1.50)	22.0(7.00)
810.26	223.0(1.00)	611.0(4.00)	14.0(9.00)
840.74	121.0(1.50)	311.0(4.00)	7.0(13.5)
871.22	72.0(2.00)	179.0(4.00)	4.0(16.5)
901.70	44.0(2.50)	127.0(4.50)	--------
932.18	34.0(3.00)	87.0(5.00)	NO Counts
962.66	28.0(3.50)	66.0(5.50)	--------
993.14	----------	50.0(6.00)	--------
1023.62	No Counts	48.0(7.00)	--------
1054.10	----------	40.0(6.50)	--------
1084.58	----------	32.0(7.00)	--------
1120.14	----------	37.0(6.50)	--------
1150.62	----------	34.0(5.50)	--------
1181.10	----------	28.0(6.50)	--------

[a] % Standard Deviation in combined count rate and background

Table 4.6 Measured Axial Activity in Counts per Minute per 3.5"
Wire Segments of Fe, Ni and Cu at 45^0 Azimuth

ELEVATION (cm)	$^{54}Fe(n,p)^{54}Mn$	$^{58}Ni(n,p)^{58}Co$	$^{63}Cu(n,\alpha)^{60}Co$
		Counts/min(% SD[a])	
35.56	No Counts	10.0(11.0)	No Counts
66.04	----------	15.0(8.50)	----------
86.52	----------	17.0(9.00)	----------
127.00	----------	22.0(7.50)	----------
157.48	----------	28.0(6.50)	----------
187.96	----------	38.0(5.50)	----------
218.44	----------	53.0(4.50)	----------
248.92	24.0(7.50)	76.0(4.00)	----------
279.40	34.0(8.50)	119.0(3.00)	----------
309.88	71.0(4.00)	213.0(3.00)	----------
340.36	128.0(3.00)	402.0(2.50)	----------
370.84	236.0(2.00)	712.0(3.00)	12.0(9.50)
401.32	419.0(1.50)	1133.0(2.50)	26.0(6.50)
431.80	539.0(1.50)	1623.0(1.00)	30.0(6.50)
462.28	669.0(1.50)	1911.0(1.00)	40.0(5.00)
492.76	837.0(1.00)	2496.0(1.00)	49.0(4.50)
523.24	923.0(1.00)	2781.0(1.00)	54.0(4.50)
553.72	1000.0(1.00)	3130.0(1.00)	59.0(3.50)
584.20	1022.0(1.00)	3303.0(0.50)	60.0(3.50)
614.68	1091.0(1.00)	3439.0(0.50)	61.0(3.50)
645.16	1062.0(1.00)	3437.0(0.50)	59.0(3.50)
675.64	994.0(1.00)	3178.0(0.50)	54.0(3.50)
706.12	881.0(1.00)	2714.0(1.00)	46.0(4.00)
736.60	692.0(1.00)	2092.0(1.00)	38.0(4.00)
767.08	450.0(1.50)	1354.0(1.50)	23.0(5.50)
779.78	341.0(2.00)	1132.0(1.50)	18.0(6.00)
810.26	211.0(3.00)	671.0(2.00)	9.0(8.50)
840.74	108.0(3.00)	351.0(3.00)	9.0(8.50)
871.22	62.0(4.50)	207.0(4.00)	----------
901.70	36.0(6.00)	149.0(5.00)	No Counts
932.18	24.0(7.50)	107.0(4.50)	----------
962.66	19.0(8.50)	87.0(5.00)	----------
993.14	----------	80.0(5.00)	----------
1023.62	No Counts	68.0(5.50)	----------
1054.10	----------	62.0(5..0)	----------
1084.58	----------	54.0(5.50)	----------
1120.14	----------	54.0(5.50)	----------
1150.62	----------	49.0(7.00)	----------
1181.10	----------	46.0(7.00)	----------

[a] % Standard Deviation in combined count rate and background

counts (x=total counts - background) recorded over a time t (min). Thus, the standard deviation in the count rate is:

$$\sigma_r = \sigma_x \ / \ t = (\sigma_c^2 + \sigma_b^2)^{1/2} \ / \ t$$

where σ_r, σ_x, σ_c and σ_b are the associated standard deviatons in counts per minute. The percent standard deviation associated with net count rate (r) is simply:

$$\%SD = (\sigma_r \ / \ r) \bullet 100$$

The results from tables 4.4 through 4.6 are also plotted in figures 4.4 through 4.6 to obtain the relative axial distribution of activities as a function of cavity height. These results indicated that the wire set at the 45^0 and 15^0 azimuth locations had the highest and the lowest activity, respectively. Thus, the fast neutron flux in the reactor cavity peaked at 45^0 azimuth. The fluctuation in the ^{60}Co and ^{54}Mn counts of the neutron activated Cu and Fe wires located at the 15^0 azimuth revealed the presence of ^{60}Co and ^{54}Mn cross contamination of these wires especially for the bottom 15 feet. At such low elevation no activity in the Cu and Fe wires is expected due to the fact that the Cu and Fe have high activation threshold energy. This is the case for the Cu and Fe wires located at the 40^0 and 45^0 azimuth, as shown in tables 4.5 and 4.6. The ^{60}Co cross contamination could also be detected on the Ni wire at the 15^0 location. The possible explanation for the cross contamination is that perhaps the wires at this azimuth location were in contact with pipes or some other structural material in that vicinity. The data from Cu wire at 15^0 do not appear to be reliable and will be omitted.

By analyzing these data, several unexpected behaviors in the
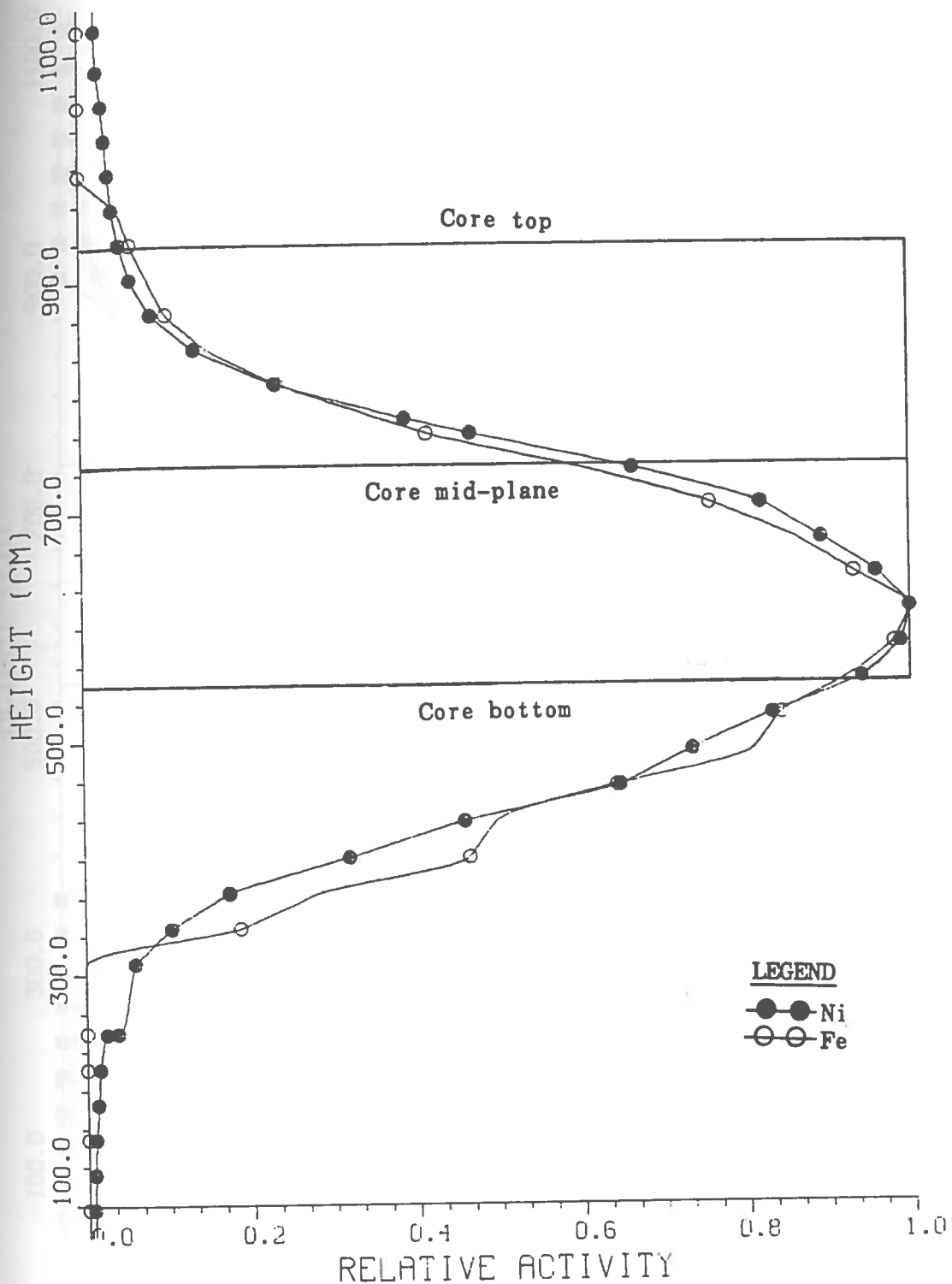
Fig. 4.4 The experimental relative axial activity distribution of the two wires, Ni and Fe at the 15° azimuth location
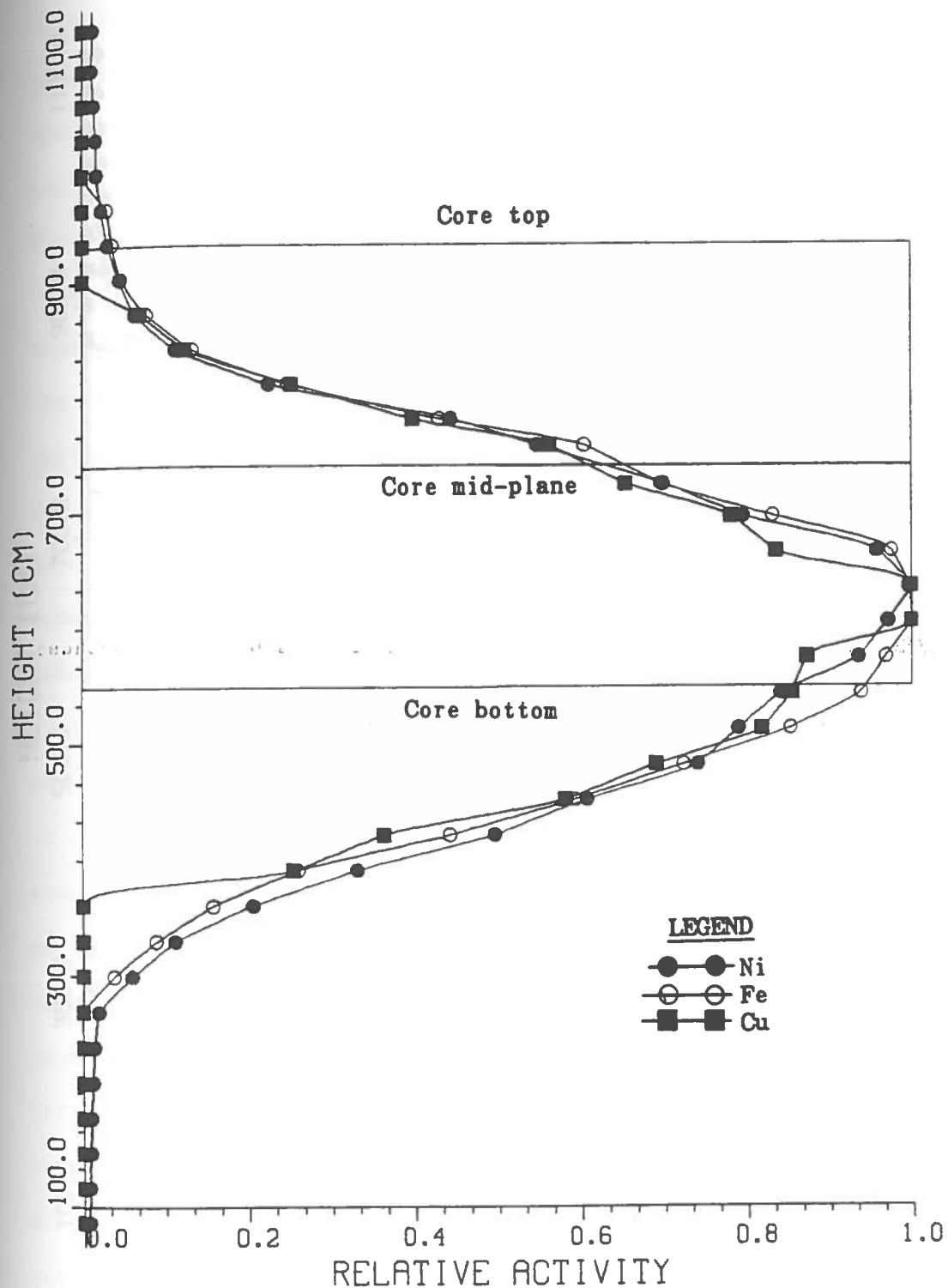
Fig. 4.5 The experimental relative axial activity distribution of the three wires, Ni, Cu, and Fe at the 40^0 azimuth location
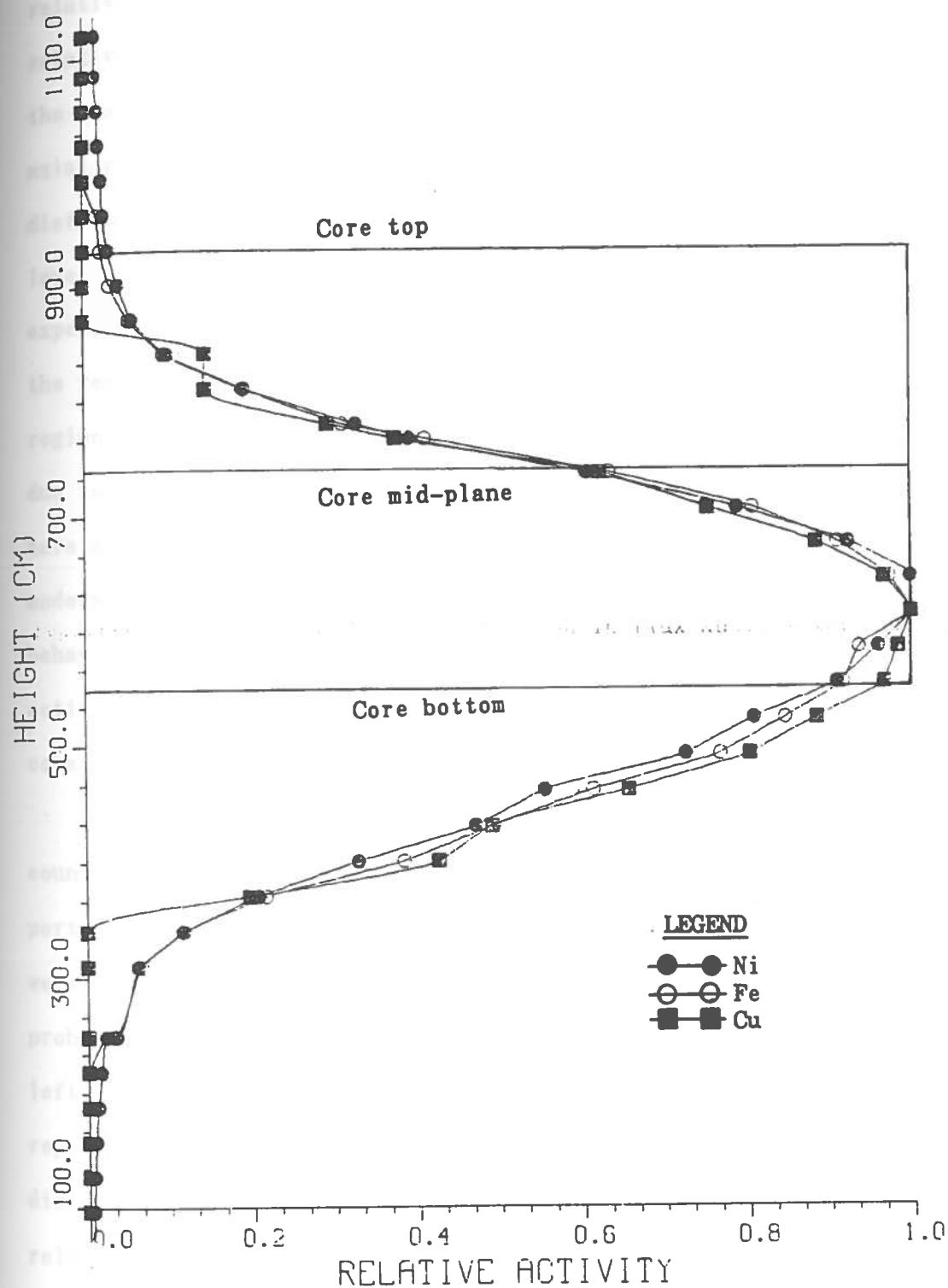
Fig. 4.6 The experimental relative axial activity distribution of the three wires, Ni, Cu, and Fe at the 45^0 azimuth location

relative axial activity distribution were noted. First, the peak of the relative axial activity distribution occurs far below the mid-plane of the reactor core as shown in figures 4.4 through 4.6. Although the axial power does peak below the mid-plane in a BWR, the source distribution does not explain how the wire activity can attain such high levels below the active core height in the cavity. Secondly, the experimental results for axial levels corresponding to the upper half of the reactor core indicate relatively low activity as compared to the region below the active core. This behavior does not appear reasonable due to the fact that the neutrons born in the upper half of the core have a better probability of escaping to the cavity, since the core moderator density is lower at that elevation. Looking at both behaviors, the question arises as to how there could be so little activity at elevations corresponding to the upper half of the active core, and so much below the bottom of the core.

Finally, during the preparation of the activated wires for counting, it was noted that approximately seven feet from the top portion of all wires were missing when they were shipped to LSU. There were several calls made to the Grand Gulf station inquiring about this problem, but unfortunately, the person in charge of this project had left Grand Gulf, and no one could resolve the discrepancy in the reported length and actual length of the wires. Considering the discrepancy in the length of the wires and the abnormal behavior of the relative axial activity distribution; it seems that the only explanation for the observed behavior is that there was a shift in the reported location where the wires were installed within the cavity.

Despite these problems with the experimental results, the measured relative activities of the wires will be compared with those from the transport calculations and the appropriate action will be taken in the next chapter to correct for the shift in the relative axial activity distribution.

CHAPTER 5

RESULTS

In this section, the description of the DOT-IV transport calculation results will be presented, followed by the analysis of results and finally their comparison with the experimental results.

5.1 Description of calculated results

Figures 5.1 through 5.3 represent the radial and azimuthal variation of the absolute calculated flux above 1 MeV, the DPA, and the thermal flux, respectively. Figures 5.1-a and 5.1-b show the same quantity at two different regions, inside the reactor pressure vessel and in the cavity vicinity, respectively. Figures 5.4 through 5.6 represent the radial and axial variation in flux above 1 MeV, DPA, and thermal flux, respectively, as obtained from in-vessel R-Z transport calculations. Figures 5.7 through 5.9 are similar type plots obtained from ex-vessel R-Z calculations for the cavity and concrete shield regions. Figures 5.10 and 5.11 are also based on ex-vessel R-Z calculations and show gamma heating and gamma dose contours, respectively, in the cavity.

Table 5.1 shows the calculated spectrum averaged cross-section for several reactions at the center of the 3^0 surveillance capsule at the axial core mid-plane and peak locations. Tables 5.2 and 5.3 show the calculated saturated activities within the 3^0 surveillance capsule at the axial core mid-plane and peak locations, respectively. Table 5.4 shows the calculated non-saturation factors for several dosimeters based on the cycle-2 power-time history. Table 5.5 shows the lead factors at various radial locations through the RPV wall and cavity region. Tables

5.6 and 5.7 show the relative azimuthal variation in flux above 1 MeV through the PV wall and cavity region, respectively. In tables 5.8 through 5.10 the radial variation total DPA, flux above 1 MeV thermal flux and thermal-to-fast flux ratio are tabulated at three axial locations of core mid-plane, peak and feed water nozzle elevation, respectively. Table 5.11 shows the peak cumulative total DPA and fluence based on axial and azimuthal peak flux above 1 MeV during cycle-2 and after 32 EFPY at different locations through the RPV wall. Table 5.12 shows the radial variation in gamma heating and gamma absorbed dose rate obtained in transport calculations at three axial locations of core mid-plane, peak and feed water nozzle elevation, respectively. Several more tables of calculation results are presented in Appendix A.

Figure 5.12 shows the absolute neutron spectrum outside the 3^0 surveillance capsule (SC) in the downcomer region and in the center of the SC at the axial peak location. Figures 5.13 through 5.15 represent the neutron spectrum at two radial locations of 1/4-T and 3/4-T of PV wall at axial core mid-plane, peak and feed water nozzle elevation, respectively. Figures 5.16 through 5.18 are similar type plots, except at the radial locations of reactor mid-cavity and 6" into the concrete shield wall. Figure 5.19 illustrates the variation of the neutron spectrum through the concrete shield wall at the core mid-plane. Figures 5.20 through 5.22 show the absolute gamma spectrum at four radial locations of 1/2-T, 3/4-T PV, reactor mid-cavity and 6" into the concrete shield wall at the axial core mid-plane, peak and feed water nozzle elevation, respectively. Figure 5.23 shows radial variation of

flux above 1 MeV at five axial locations of bottom, mid-plane, top of active core, peak, and feed water nozzle elevation. Finally, figure 5.24 shows axial variation of flux above 1 MeV at five radial locations of 1/4-T, 1/2-T, 3/4-T, 4/4-T of PV wall and mid-cavity.

5.2 Analysis of results

Based on R-θ transport calculations, the flux in the RPV of this BWR/6 reactor was found to peak at an azimuthal angle between 40° and 45° depending upon the radial location. Tables 5.7 and 5.8 illustrate the azimuthal variation of the flux above 1 MeV at several points through the PV wall and the cavity region at the core axial mid-plane. There is a factor of 1.76 variation in the azimuthal dependence of the flux above 1 MeV at 0-T of PV. This factor has a value of 1.67 at the reactor mid-cavity. As shown in these tables, the azimuthal variation of the flux above 1 MeV also depends slightly on the radial location. From the R-Z transport calculations, the flux was found to peak near, but slightly above the core mid-plane even though the source in the core peaked near the bottom of the core. The combined effects of a bottom peaked source distribution and a top peaked moderator void fraction is the cause for the location of the R-Z flux peak. Figure 5.24 illustrates the axial variation of the flux above 1 MeV at several points within the RPV wall and the cavity region. The flux above 1 MeV at the mid-cavity and at the elevation corresponding to the top of the core and the inlet feed water nozzle are factors of 2.74, 49.5 lower than the core mid-plane value, respectively.

The flux above 1 MeV incident on the vessel wetted surface at the peak azimuthal and axial location is about $1.819E9$ $n.cm^{-2}.s^{-1}$. The flux

(E>1 MeV) incident on the vessel at the peak azimuthal and core axial mid-plane is about 1.749E9 $n.cm^{-2}.s^{-1}$. The peak flux (E>1 MeV) is reduced to a value of 7.911E7 $n.cm^{-2}.s^{-1}$ at the front of the concrete shield wall. Based upon the calculated peak flux above 1 MeV, the total fluence due to 280.37 full power days of cycle-2 at wetted surface of RPV, is about 4.406E16 $n.cm^{-2}$. Based on this fluence rate the projected cumulative fluence after 32 effective full power years is about 1.838E18 $n.cm^{-2}$.

As shown in tables A.2-a through A.2-h of Appendix A, at the 0-T peak location about 81.1% of the total DPA, displacement per atom, is due to flux (E>1 MeV), 16.5% is due to flux (0.1<E<1.0 MeV) and less than 1% is due to thermal neutrons. At 3/4-T of the PV and mid-cavity, these values change to 52.9%, 41%, 0.0% and 48.8%, 45.8%, 0.3%, respectively. The thermal energy neutron flux contribution increases through the concrete shield wall. At the radial location corresponding to one foot into the concrete, where the thermal-to-fast flux ratio has a value of 24.8, about 14.3% of the total DPA is due to thermal flux. Tables A.3-a through A.3-h show that at 0-T, 3/4-T of the PV and axial feed water nozzle elevation, the percent of contribution of flux (E>1 MeV), flux (0.1<E<1 MeV) and thermal flux to the total DPA are 83.8, 13.8, 1.0 and 14.2, 69.7, 0.2, respectively. At one foot into the concrete, where the thermal-to-flux above 1 MeV ratio is 208.4 about 59% of the total DPA is due to thermal flux. It should be noted that the magnitude of the total DPA at this point is about 2.0E-05 times that at the peak 1/4-T value.

Figure 5.7 illustrates the axial streaming of the flux (E>1 MeV) in the cavity region. As seen in this figure, at the axial locations above

the top of the core, the high energy neutrons entering through the outer surface of the vessel and penetrating back into the RPV wall causes an increase in the flux above 1 MeV intransverse from inner to outer RPV wall. This effect can be easily seen in figure 5.23. In this figure at the axial elevation corresponding to the inlet feed water nozzle, the flux above 1 MeV actually increases through the RPV wall instead of decreasing, which can be seen at the axial active core elevation. The DPA contours, figure 5.8, show a similar behavior. Figure 5.9 shows the behavior of the thermal flux in the cavity and in the concrete shield wall regions. As seen in this figure, the fast neutrons leaking from the vessel are thermalized as they enter the concrete shield and generate a localized thermal source within the wall. The thermal neutrons emerging from the concrete shield travel across the cavity and strike the RPV wall at the outer surface causing a peak in the thermal flux in this vicinity. In the analysis of neutron spectrum, figure 5.12 clearly illustrates the change in neutron spectra due to the presence of the surveillance capsule. In this figure, at the outside of the surveillance capsule the neutron energy spectrum follows the same behavior as the MaxWellian distribution in thermal energy range, 1/E in the epithermal region and fission spectra at the high energy range. Whereas at the center of the surveillance capsule, this behavior is perturbed due to the iron presence in the SC. Thus, it is important to include the surveillance capsule in the reactor model when performing transport calculations to account for the flux perturbation.

The gamma calculation results have been presented in terms of gamma spectra, gamma heating source, and gamma absorbed dose rate throughout

LEGEND
□ = 1.00+13
○ = 1.00+12
△ = 1.00+11
+ = 1.00+10
× = 5.00+09
◇ = 1.00+09
⋇ = 6.00+08
⊞ = 3.00+08
⊠ = 1.00+08
⊿ = 1.00+07
⊕ = 1.00+06
⊘ = 1.00+05

45°

0°

0.00

477.52

RADIUS (cm)
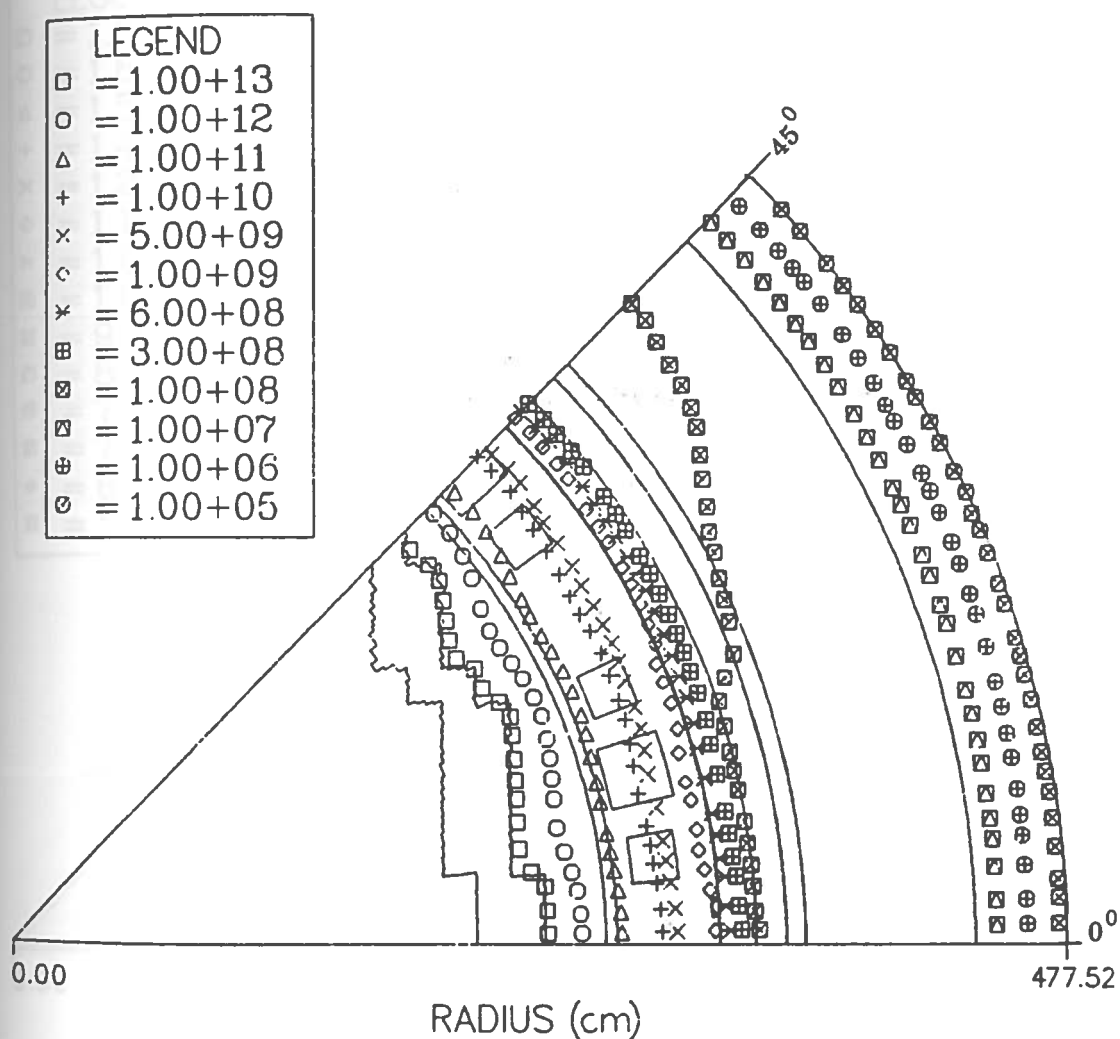
Fig. 5.1-a Neutron flux above 1.0 MeV [n.cm^{-2}.s^{-1}] contours within the reactor vessel and the concrete shield wall based upon DOT-IV R-θ calculation
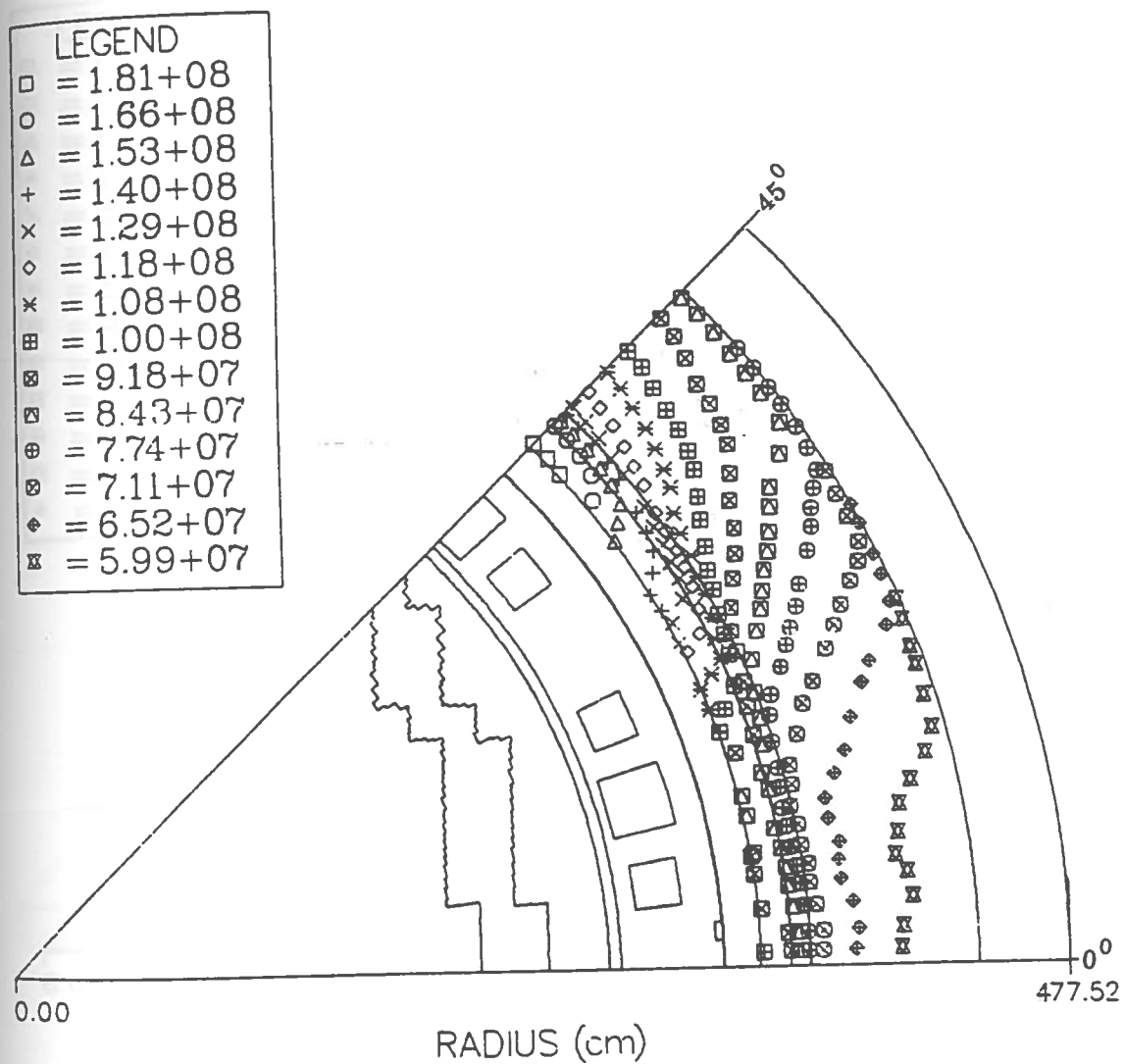
Fig. 5.1-b Neutron flux above 1.0 MeV [n.cm.$^{-2}$.s^{-1}] contours within the reactor cavity based upon DOT-IV R-θ calculation
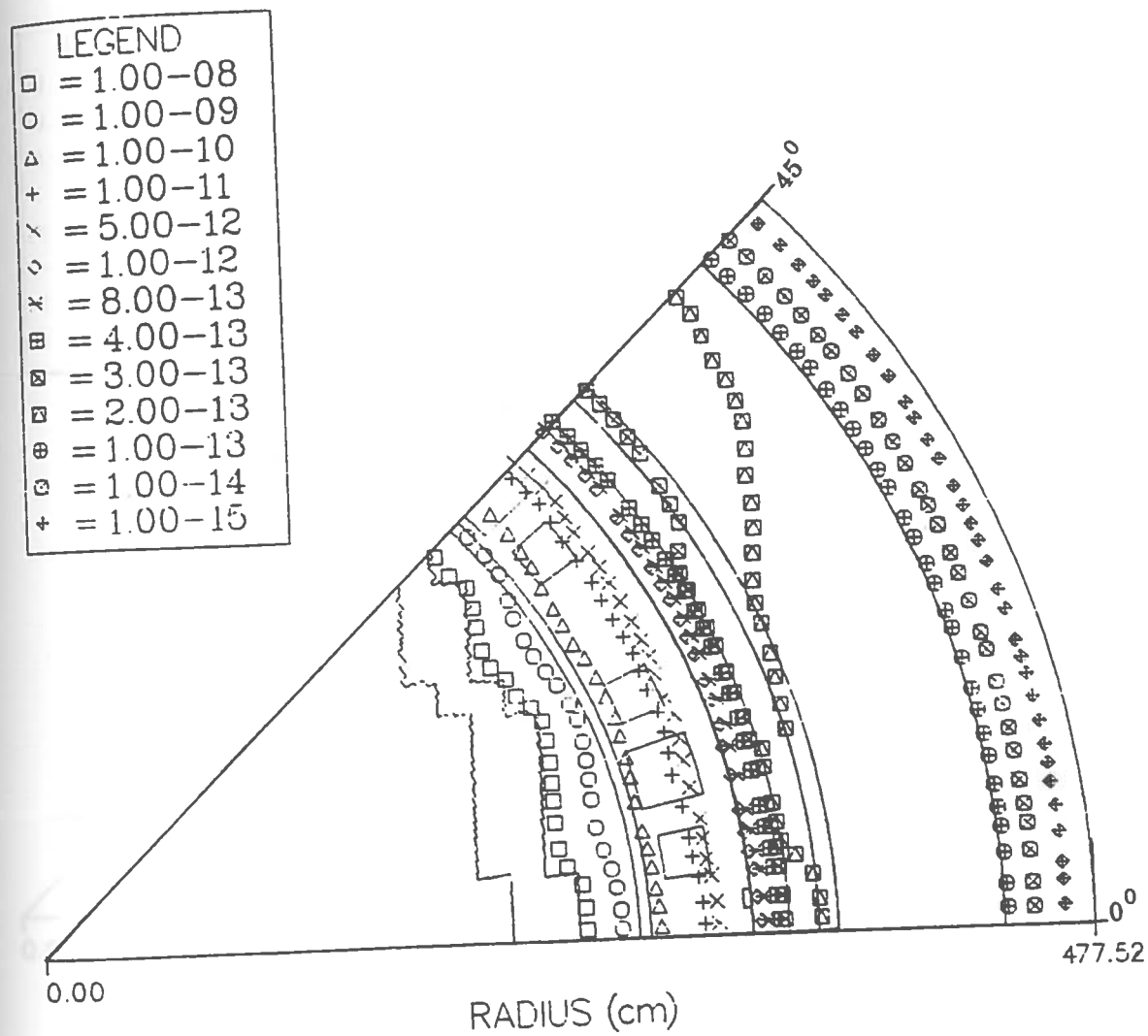
Fig. 5.2 Displacement per atom, DPA, [DPA.s^{-1}] contours based upon
DOT-IV R-θ calculation
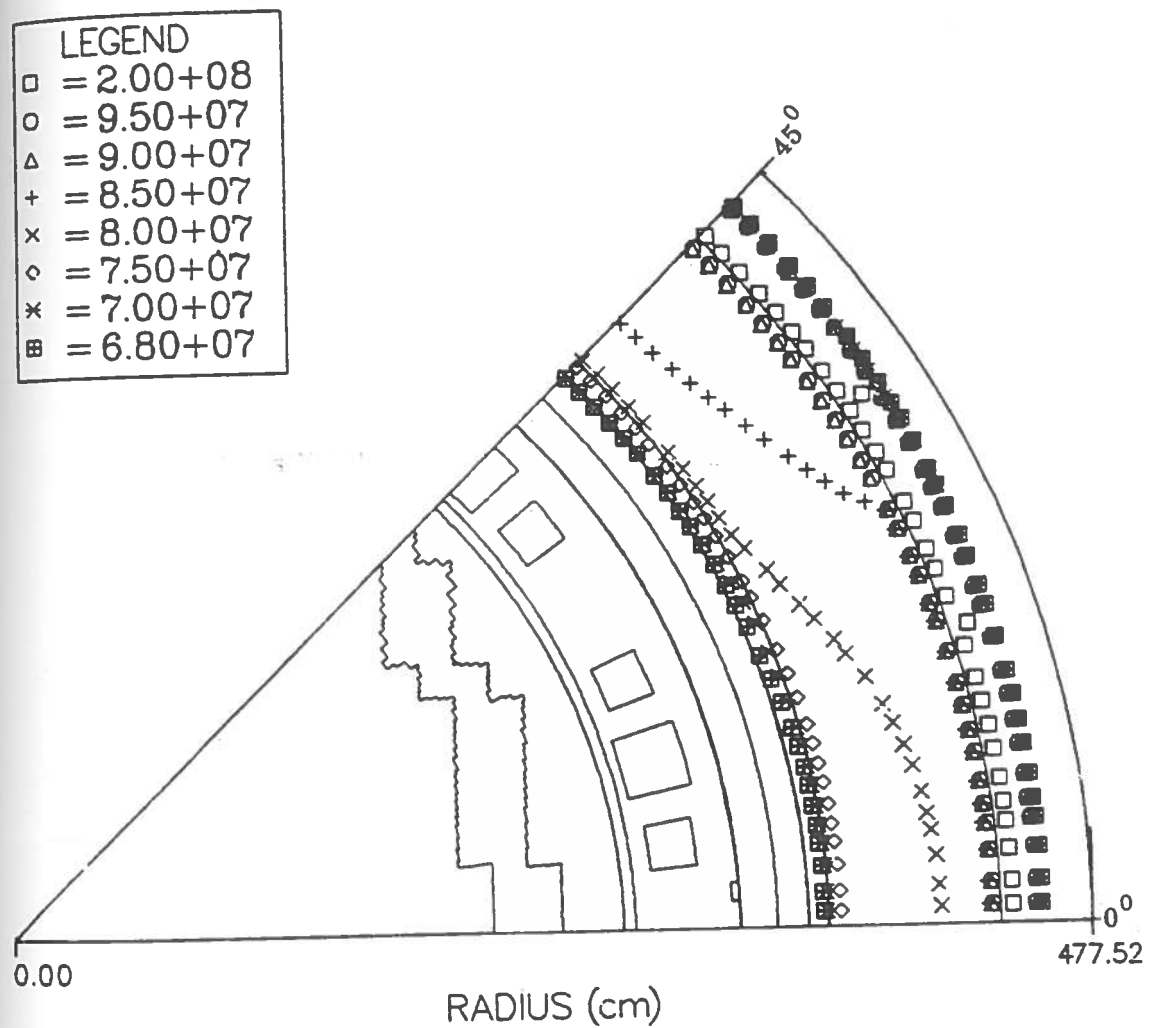
Fig. 5.3 Neutron flux below 0.4 eV [n.cm.$^{-2}$.s^{-1}] contours based upon DOT-IV R-θ calculation
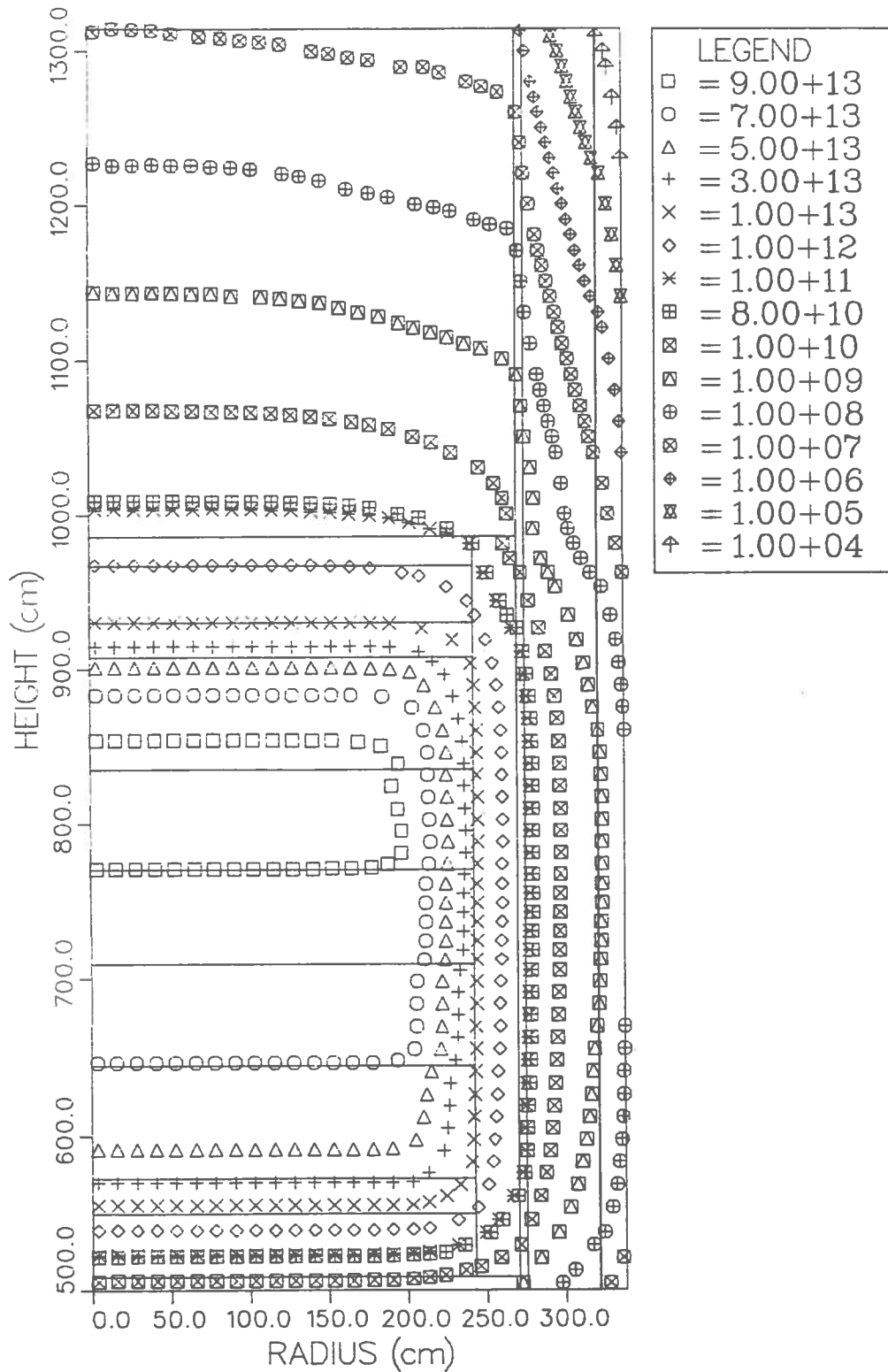
Fig. 5.4   Neutron flux above 1 MeV [n.cm.$^{-2}$.s^{-1}] contours based upon in-vessel DOT-IV R-Z calculation
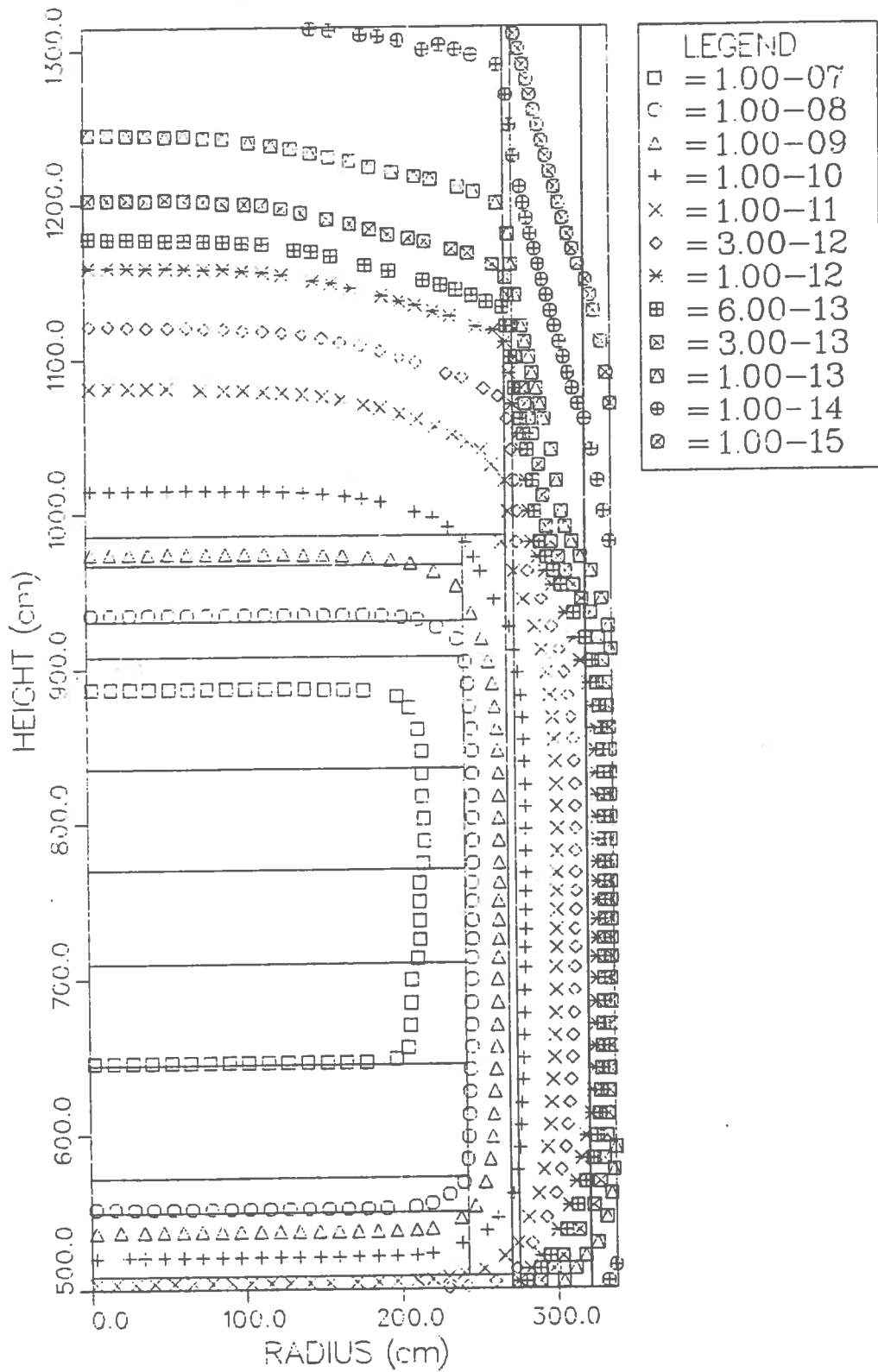
Fig. 5.5 Displacement per atom, DPA, [DPA.s^{-1}] contours based upon in-vessel DOT-IV R-Z calculation
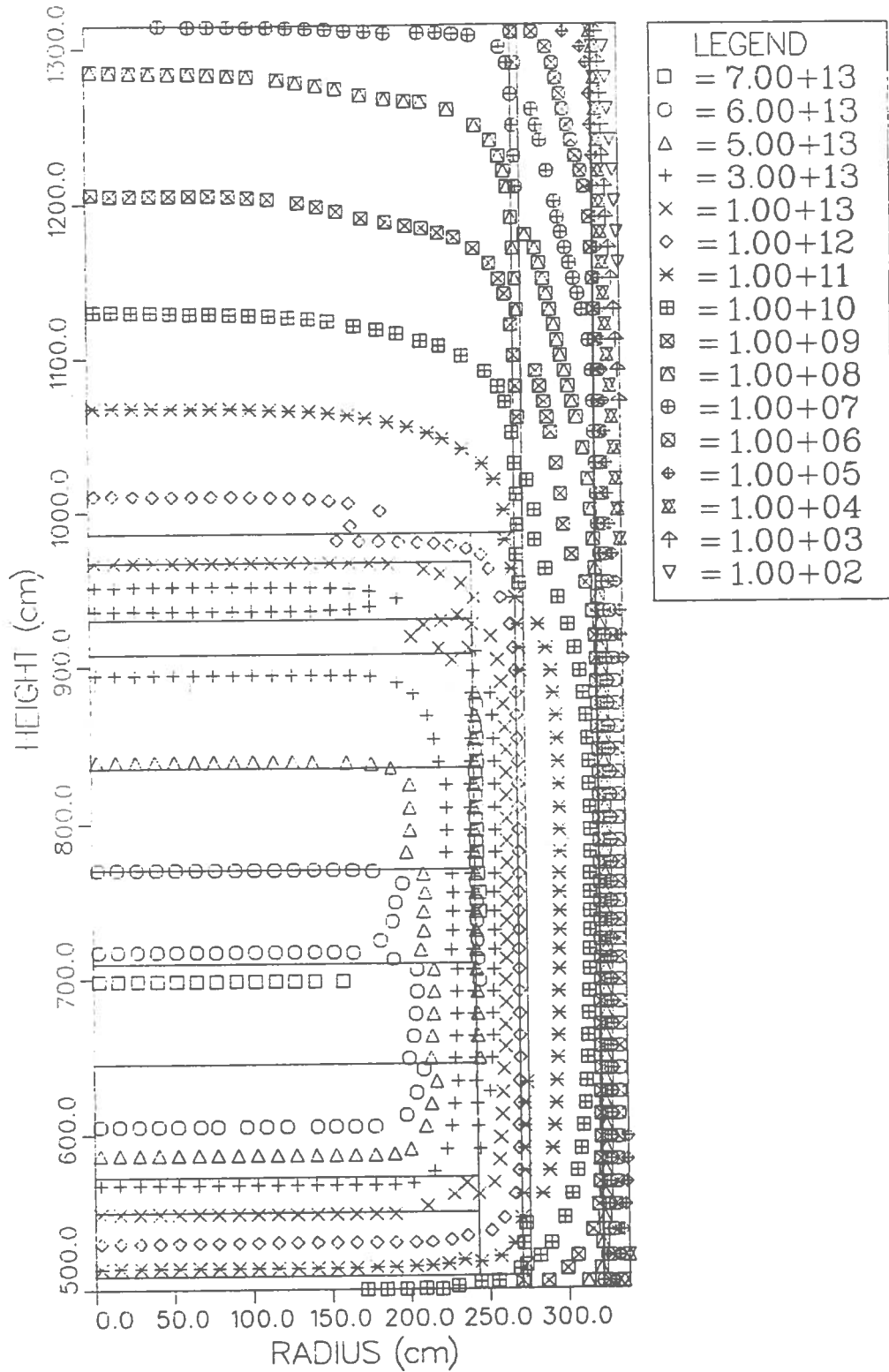
Fig. 5.6 Neutron flux below 0.4 eV [n.cm^{-2}.s^{-1}] contours based upon in-vessel DOT-IV R–Z calculation
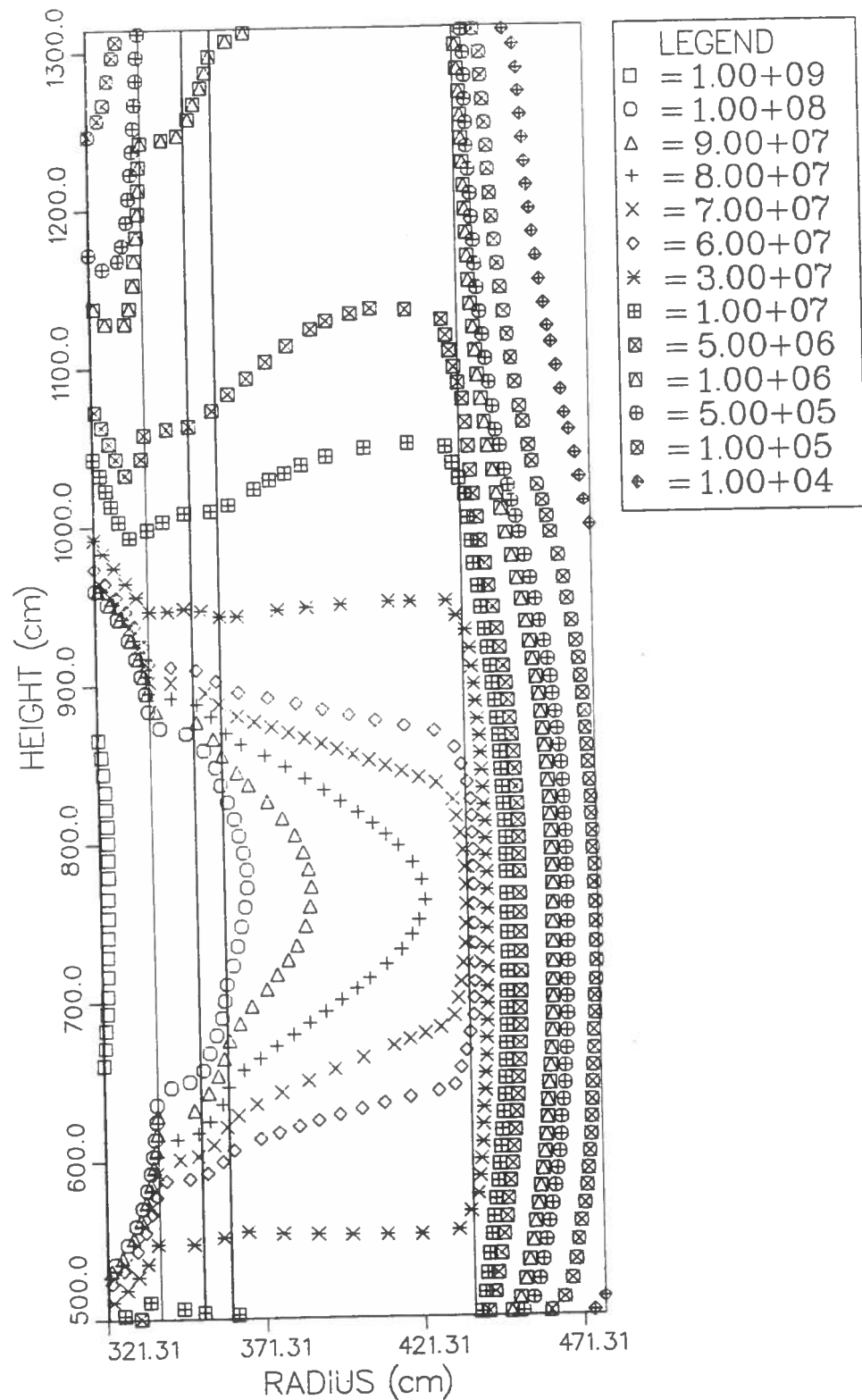
Fig. 5.7 Neutron flux above 1.0 MeV [n.cm^{-2}.s^{-1}] contours based upon ex-vessel (cavity) DOT-IV R-Z calculation
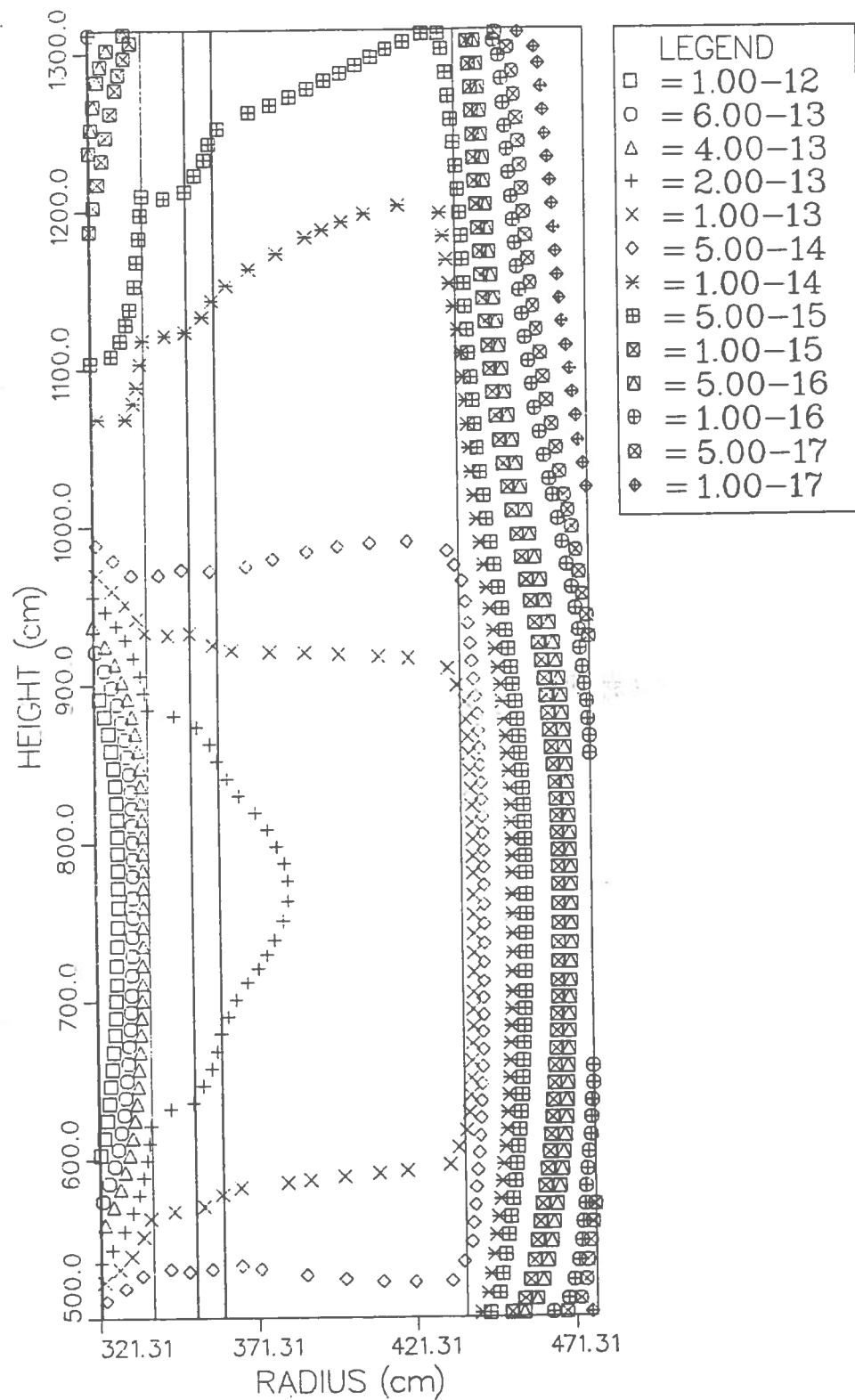
Fig. 5.8 Displacement per atom, DPA, [DPA.s^{-1}] contours based upon
ex-vessel (cavity) DOT-IV R-Z calculation
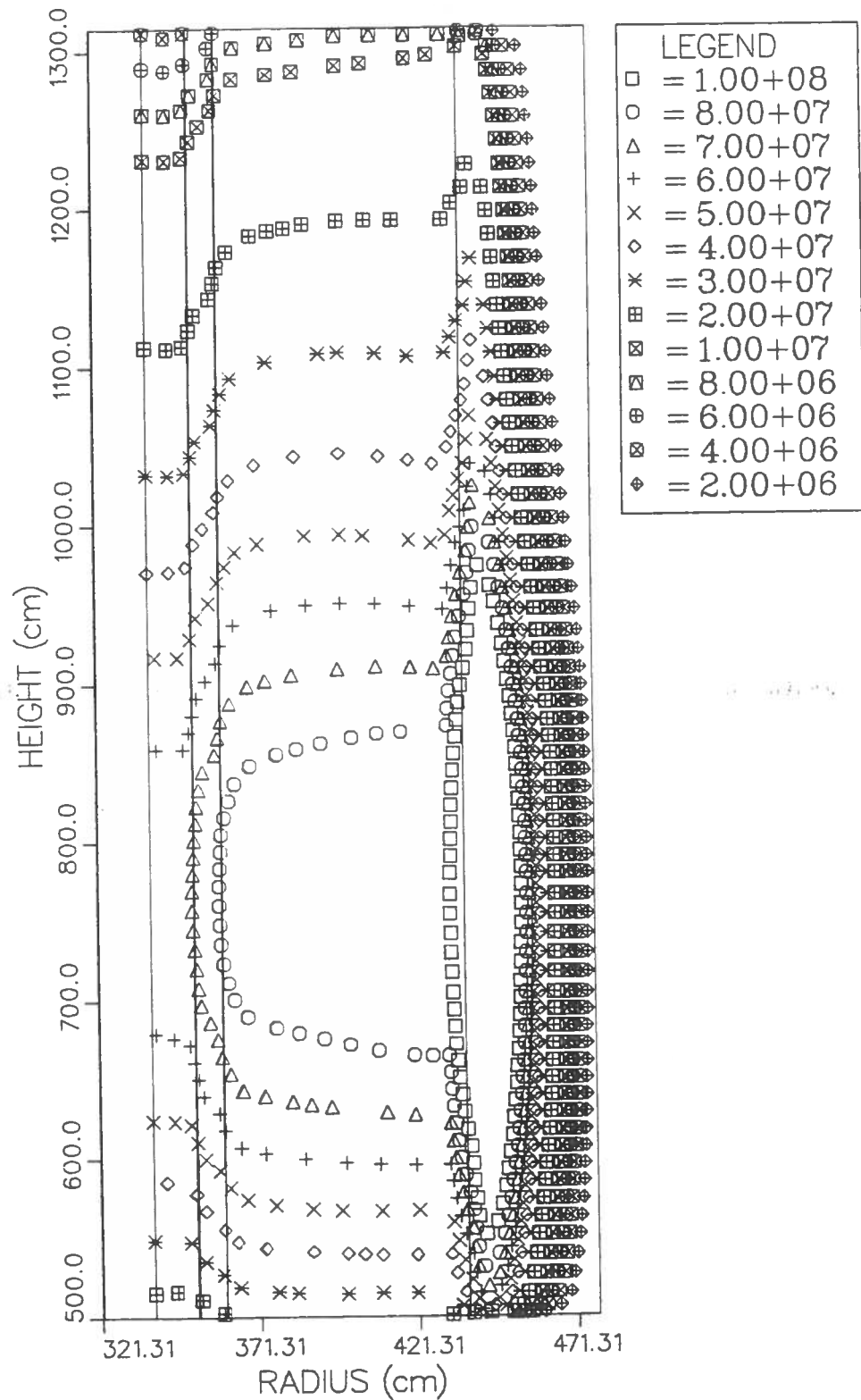
Fig. 5.9 Neutron flux below 0.4 eV [n.cm^{-2}.s^{-1}] contours based upon ex-vessel (cavity) DOT-IV R-Z calculation
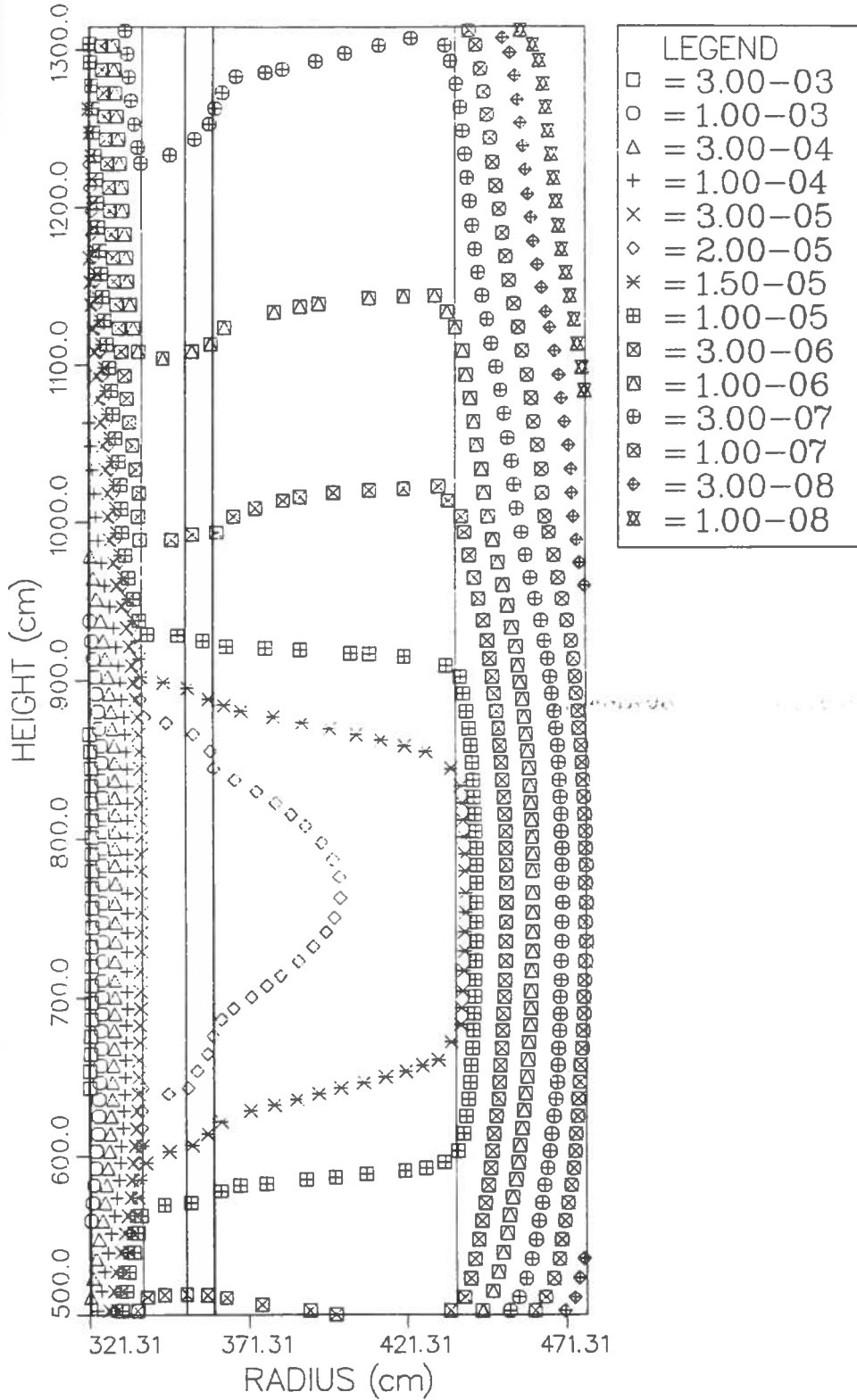
Fig. 5.10 Gamma heating [w/gm-SS 304] contours based upon ex-vessel
(cavity) DOT-IV R-Z calculation
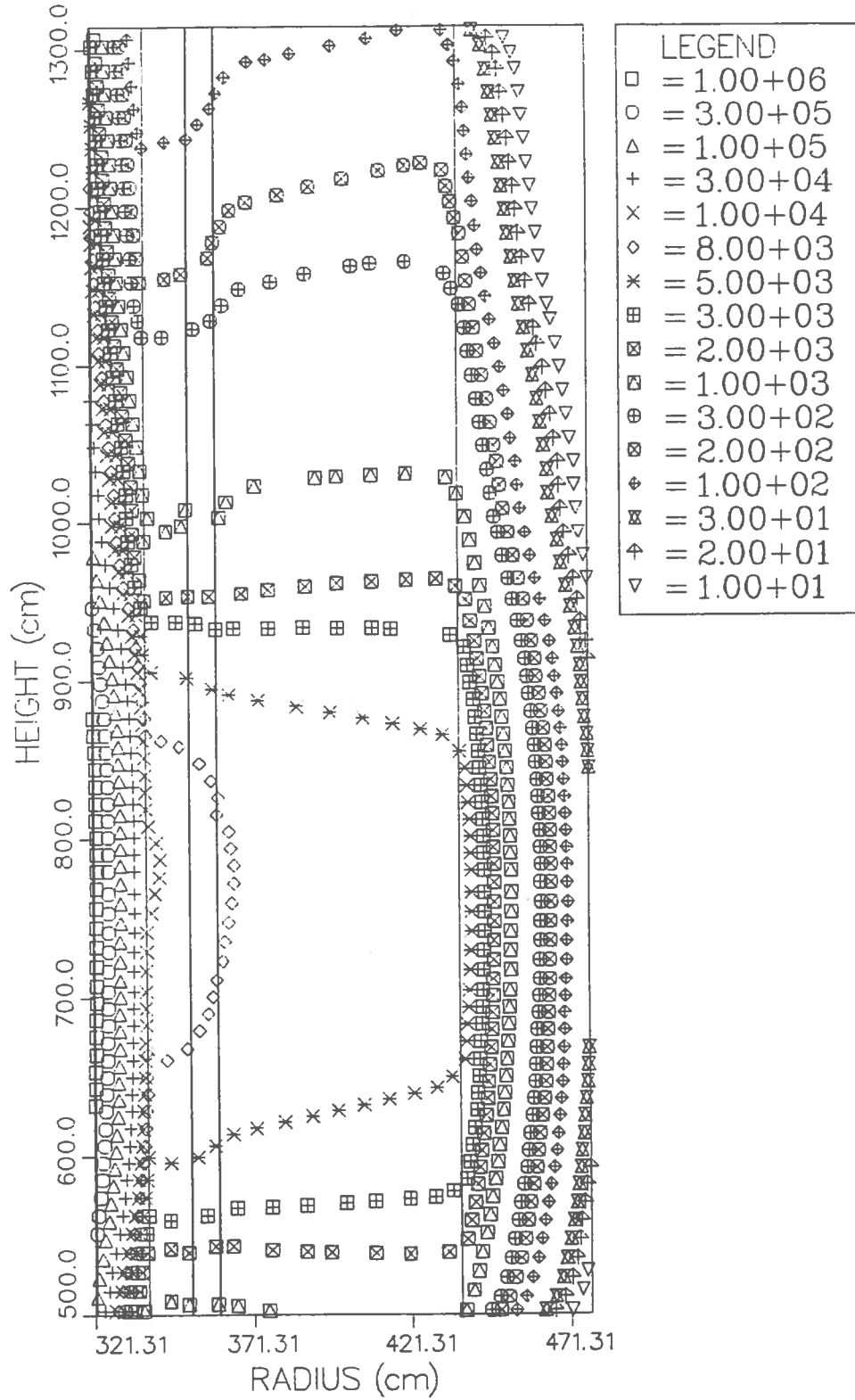
Fig. 5.11 Gamma absorbed dose [rad/hr] contours based upon ex-vessel (cavity) DOT-IV R-Z calculation

Table 5.1   Spectrum Averaged Cross-Section at Center of 3^0
Surveillance Capsule for Grand Gulf Cycle-2

Reaction	$\bar{\sigma}(b)$ @ Mid-Plane	$\bar{\sigma}(b)$ @ RZ Peak[a]
$^{54}Fe(n,p)^{54}Mn$	0.1762	0.1758
$^{58}Ni(n,p)^{58}Co$	0.2163	0.2159
$^{63}Cu(n,\alpha)^{60}Co$	0.0030	0.0030
$^{238}U(n,f)^{137}Cs$	0.4817	0.4813
$^{46}Ti(n,p)^{46}Sc$	0.0366	0.0365

[a] R-Z Φ > 1 MeV peaks 48.47 cm above the mid-plane (739.93 cm)

Table 5.2 Calculated Saturated Activities in the Grand Gulf 3^0
Surveillance Capsule at Mid-Plane (Cycle-2)

Dosimeter	Saturated Activities (Bq/g)		
	R=318.73 cm	R=319.76 cm	R=320.79 cm
$^{54}Fe(n,p)^{54}Mn$	1.331E+05	1.148E+05	9.719E+04
$^{58}Ni(n,p)^{58}Co$	1.821E+06	1.578E+06	1.341E+06
$^{63}Cu(n,\alpha)^{60}Co$	2.411E+04	2.063E+04	1.749E+04
$^{237}Np(n,f)^{137}Cs$	3.860E+05	3.633E+05	3.321E+05
$^{238}U(n,f)^{137}Cs$	8.470E+04	7.612E+04	6.643E+04
$^{46}Ti(n,p)^{46}Sc$	4.534E+04	3.882E+04	3.279E+04

Flux	$\Phi(E)$ n.cm^{-2}.s^{-1}		
$\Phi(E > 1.0$ MeV)	1.117E+09	1.041E+09	9.343E+08
$\Phi(E > 0.1$ MeV)	1.948E+09	1.937E+09	1.845E+09
$\Phi(E < 0.4$ eV)	1.278E+09	5.948E+08	3.164E+08

Table 5.3 Calculated Saturated Activities in the Grand Gulf 3^0
Surveillance Capsule at Axial Peak (Cycle-2)

Dosimeter	Saturated Activities (Bq/g)		
	R=318.73 cm	R=319.76 cm	R=320.79 cm
$^{54}Fe(n,p)^{54}Mn$	1.382E+05	1.191E+05	1.009E+05
$^{58}Ni(n,p)^{58}Co$	1.891E+06	1.638E+06	1.392E+06
$^{63}Cu(n,\alpha)^{60}Co$	2.493E+04	2.133E+04	1.808E+04
$^{237}Np(n,f)^{137}Cs$	4.019E+05	3.783E+05	3.458E+05
$^{238}U(n,f)^{137}Cs$	8.804E+04	7.912E+04	6.904E+04
$^{46}Ti(n,p)^{46}Sc$	4.700E+04	4.023E+04	3.398E+04

Flux	$\Phi(E)$ n.cm^{-2}.s^{-1}		
$\Phi(E > 1.0$ MeV$)$	1.162E+09	1.083E+09	9.718E+08
$\Phi(E > 0.1$ MeV$)$	2.027E+09	2.016E+09	1.919E+09
$\Phi(E < 0.4$ eV$)$	1.334E+09	6.204E+08	3.301E+08

Table 5.4 Non-Saturation Factors (h)

Dosimeter	$h^{(a)}$
$^{54}Fe(n,p)^{54}Mn$	0.45375
$^{58}Ni(n,p)^{58}Co$	0.88525
$^{63}Cu(n,\alpha)^{60}Co$	0.09566
$^{238}U(n,f)^{137}Cs$	0.01747
$^{46}Ti(n,p)^{46}Sc$	0.85613
$^{181}Ta(n,\gamma)^{182}Ta$	0.79033

$^{(a)}h = \sum_{j} P_j (1 - e^{-\lambda T_j}) e^{-\lambda(T - t_j)}$ refer to Chapter 2.12 for more details.

Table 5.5 Calculated Lead Factors at Various Radial Locations
Through the RPV Wall and Cavity of Grand Gulf Cycle-2

Location[a]	Lead Factor[b]
O-T	0.613
1/4-T	0.904
1/2-T	1.519
3/4-T	2.661
4/4-T	5.450
1/2-CW	9.702
1-CW	13.232

---

[a]Location within the RPV or in the cavity (i.e. 1/2-T = one-half RPV
wall thickness and 1/2-CW = one-half cavity width = middle of cavity,
etc.)

[b]Lead Factor $= \dfrac{\Phi_{sc}(>1)}{\Phi_1(>1)}$

where Φ_{sc} is the calculated flux at the center of the 3 surveillance
capsule, and Φ_1 is the maximum calculated flux incident at the indicated
locations.

Table 5.6 Relative Azimuthal Variation[a] in Φ(>1 MeV) Through
the RPV Wall of Grand Gulf Cycle-2

J	$\overline{\theta}$	O-T[b]	1/4-T[b]	1/2-T[b]	3/4-T[b]
1	1.1245E+00	0.5349	0.5317	0.5311	0.5335
2	2.4995E+00	0.4945	0.4831	0.4946	0.5055
3	3.0000E+00	0.4841	0.4634	0.4777	0.4911
4	3.5005E+00	0.4711	0.4576	0.4689	0.4812
5	4.3755E+00	0.4756	0.4649	0.4662	0.4736
6	5.2390E+00	0.4492	0.4522	0.4550	0.4629
7	5.9890E+00	0.4239	0.4334	0.4419	0.4529
8	6.7500E+00	0.4076	0.4183	0.4302	0.4437
9	7.1250E+00	0.4009	0.4118	0.4248	0.4391
10	7.3250E+00	0.3978	0.4084	0.4220	0.4365
11	7.5950E+00	0.3921	0.4032	0.4174	0.4324
12	8.1300E+00	0.3864	0.3972	0.4111	0.4261
13	8.5350E+00	0.3889	0.3970	0.4092	0.4235
14	8.7460E+00	0.3881	0.3963	0.4075	0.4214
15	9.2070E+00	0.3878	0.3953	0.4050	0.4180
16	1.0261E+01	0.3929	0.3965	0.4028	0.4141
17	1.1624E+01	0.3868	0.3901	0.3963	0.4082
18	1.3124E+01	0.3670	0.3774	0.3890	0.4044
19	1.4500E+01	0.3736	0.3838	0.3969	0.4135
20	1.5500E+01	0.3896	0.4010	0.4141	0.4303
21	1.6500E+01	0.4181	0.4290	0.4402	0.4541
22	1.7376E+01	0.4526	0.4598	0.4669	0.4774
23	1.8376E+01	0.4868	0.4878	0.4910	0.4990
24	1.9500E+01	0.4997	0.5013	0.5053	0.5140
25	2.0239E+01	0.4966	0.5026	0.5105	0.5213
26	2.1239E+01	0.4990	0.5088	0.5195	0.5324
27	2.2500E+01	0.5113	0.5236	0.5364	0.5507
28	2.3500E+01	0.5333	0.5455	0.5584	0.5722
29	2.4261E+01	0.5591	0.5683	0.5795	0.5922
30	2.4636E+01	0.5709	0.5798	0.5911	0.6035
31	2.5017E+01	0.5852	0.5920	0.6030	0.6151
32	2.5517E+01	0.6041	0.6099	0.6198	0.6313
33	2.5875E+01	0.6179	0.6245	0.6335	0.6441
34	2.6566E+01	0.6470	0.6511	0.6577	0.6665
35	2.7566E+01	0.6695	0.6775	0.6856	0.6942
36	2.8301E+01	0.6835	0.6934	0.7034	0.7129
37	2.8801E+01	0.6932	0.7035	0.7149	0.7251
38	2.9250E+01	0.7009	0.7119	0.7245	0.7353
39	2.9745E+01	0.7091	0.7208	0.7338	0.7454
40	3.0256E+01	0.7171	0.7296	0.7434	0.7551
41	3.0761E+01	0.7259	0.7382	0.7524	0.7641
42	3.1250E+01	0.7343	0.7468	0.7606	0.7720
43	3.1608E+01	0.7416	0.7537	0.7668	0.7776
44	3.2108E+01	0.7484	0.7599	0.7724	0.7832
45	3.3000E+01	0.7609	0.7707	0.7815	0.7916

Table 5.6 Continued

J	$\overline{\theta}$	O–T[b]	1/4–T[b]	1/2–T[b]	3/4–T[b]
46	3.3690E+01	0.7664	0.7759	0.7861	0.7964
47	3.4440E+01	0.7692	0.7792	0.7912	0.8030
48	3.5239E+01	0.7689	0.7825	0.7983	0.8123
49	3.6027E+01	0.7734	0.7923	0.8108	0.8263
50	3.7288E+01	0.8089	0.8292	0.8475	0.8616
51	3.8761E+01	0.8844	0.8983	0.9095	0.9167
52	3.9761E+01	0.9427	0.9482	0.9515	0.9527
53	4.0236E+01	0.9642	0.9678	0.9692	0.9688
54	4.0986E+01	1.0000	0.9952	0.9921	0.9890
55	4.1874E+01	0.9979	1.0000	1.0000	0.9987
56	4.2510E+01	0.9839	0.9937	0.9986	1.0000
57	4.3386E+01	0.9618	0.9782	0.9907	0.9974
58	4.4250E+01	0.9474	0.9654	0.9837	0.9949
59	4.4725E+01	0.9419	0.9603	0.9826	0.9956
60	4.4975E+01	0.9422	0.9640	0.9853	0.9982

[a] Peak values are normalized to unity

[b] Location within the RPV (i.e. 1/2–T = one-half RPV wall thickness)

Table 5.7   Relative Azimuthal Variation[a] in $\Phi(>1$ MeV) Through the Reactor Cavity of Grand Gulf Cycle-2

J	$\overline{\theta}$	0-CW[b]	1/2-CW[b]	1-CW[b]
1	1.1245E+00	0.5121	0.5986	0.6279
2	2.4995E+00	0.4973	0.5939	0.6095
3	3.0000E+00	0.4882	0.5950	0.6071
4	3.5005E+00	0.4806	0.5957	0.6130
5	4.3755E+00	0.4706	0.5939	0.6233
6	5.2390E+00	0.4654	0.5918	0.6215
7	5.9890E+00	0.4564	0.5896	0.6231
8	6.7500E+00	0.4532	0.5897	0.6161
9	7.1250E+00	0.4546	0.5898	0.6071
10	7.3250E+00	0.4591	0.5898	0.6051
11	7.5950E+00	0.4468	0.5899	0.6117
12	8.1300E+00	0.4395	0.5898	0.6158
13	8.5350E+00	0.4501	0.5901	0.6113
14	8.7460E+00	0.4400	0.5898	0.6131
15	9.2070E+00	0.4325	0.5891	0.6243
16	1.0261E+01	0.4289	0.5886	0.6369
17	1.1624E+01	0.4256	0.5932	0.6474
18	1.3124E+01	0.4256	0.5999	0.6560
19	1.4500E+01	0.4349	0.6120	0.6639
20	1.5500E+01	0.4485	0.6203	0.6682
21	1.6500E+01	0.4671	0.6287	0.6729
22	1.7376E+01	0.4834	0.6367	0.6774
23	1.8376E+01	0.5010	0.6479	0.6892
24	1.9500E+01	0.5135	0.6626	0.6991
25	2.0239E+01	0.5250	0.6735	0.7057
26	2.1239E+01	0.5327	0.6879	0.7284
27	2.2500E+01	0.5497	0.7069	0.7486
28	2.3500E+01	0.5677	0.7233	0.7588
29	2.4261E+01	0.5864	0.7369	0.7591
30	2.4636E+01	0.6049	0.7431	0.7573
31	2.5017E+01	0.6052	0.7486	0.7670
32	2.5517E+01	0.6198	0.7556	0.7732
33	2.5875E+01	0.6367	0.7609	0.7790
34	2.6566E+01	0.6432	0.7728	0.8011
35	2.7566E+01	0.6660	0.7903	0.8134
36	2.8301E+01	0.6842	0.8038	0.8127
37	2.8801E+01	0.6992	0.8133	0.8137
38	2.9250E+01	0.7064	0.8217	0.8208
39	2.9745E+01	0.7152	0.8303	0.8299
40	3.0256E+01	0.7232	0.8388	0.8393
41	3.0761E+01	0.7323	0.8467	0.8488
42	3.1250E+01	0.7389	0.8542	0.8570
43	3.1608E+01	0.7564	0.8597	0.8629
44	3.2108E+01	0.7448	0.8671	0.8872
45	3.3000E+01	0.7525	0.8802	0.9091

Table 5.7 Continued

J	$\overline{\theta}$	O–CW[b]	1/2–CW[b]	1–CW[b]
46	3.3690E+01	0.7654	0.8918	0.9154
47	3.4440E+01	0.7646	0.9030	0.9337
48	3.5239E+01	0.7799	0.9172	0.9400
49	3.6027E+01	0.7866	0.9273	0.9555
50	3.7288E+01	0.8143	0.9426	0.9726
51	3.8761E+01	0.8540	0.9585	0.9764
52	3.9761E+01	0.8857	0.9648	0.9613
53	4.0236E+01	0.8980	0.9678	0.9623
54	4.0986E+01	0.9064	0.9751	0.9803
55	4.1874E+01	0.9159	0.9809	0.9817
56	4.2510E+01	0.9231	0.9855	0.9833
57	4.3386E+01	0.9186	0.9947	1.0000
58	4.4250E+01	0.9257	0.9982	0.9875
59	4.4725E+01	0.9290	0.9996	0.9757
60	4.4975E+01	1.0000	1.0000	0.9686

[a] Peak values are normalized to unity

[b] Location in the cavity (i.e. 1/2–CW = one-half cavity width = middle of the cavity, etc.)

Table 5.8   Radial Variation of the Total DPA, Flux >1 MeV,
Flux <0.4 eV and Thermal-to-Fast Flux Ratio at
the Axial Core Mid-Plane and Azimuthal Peak

Radius[a]	Total DPA	Fast Flux	Thermal Flux	Ratio[b]
cm	DPA.s^{-1}	n.cm^{-2}.s^{-1}		$\Phi Th/\Phi F$
321.310	2.680E-12	1.749E+09	3.131E+09	1.790
321.790	2.615E-12	1.712E+09	2.180E+09	1.273
322.700	2.445E-12	1.604E+09	1.204E+09	0.751
324.500	2.113E-12	1.355E+09	2.957E+08	0.218
325.888	1.838E-12	1.153E+09	1.289E+08	0.112
326.340	1.749E-12	1.087E+09	7.738E+07	0.071
328.200	1.434E-12	8.585E+08	2.462E+07	0.029
329.990	1.178E-12	6.768E+08	9.329E+07	0.014
331.810	9.610E-13	5.278E+08	5.016E+06	0.010
333.630	7.726E-13	4.064E+08	5.334E+06	0.013
334.080	7.322E-13	3.820E+08	7.024E+06	0.018
335.500	6.049E-13	3.055E+08	1.295E+07	0.042
337.300	4.502E-13	2.189E+08	4.132E+07	0.189
338.182	3.831E-13	1.845E+08	6.312E+07	0.342
340.460	3.695E-13	1.754E+08	6.381E+07	0.364
360.610	2.783E-13	1.344E+08	7.782E+07	0.579
377.000	2.372E-13	1.133E+08	8.328E+07	0.735
387.530	2.227E-13	1.056E+08	8.432E+07	0.798
409.660	2.032E-13	9.477E+07	8.692E+07	0.917
420.550	1.968E-13	9.092E+07	8.808E+07	0.969
436.880	1.721E-13	7.843E+07	1.409E+08	1.797
438.200	1.664E-13	7.576E+07	1.549E+08	2.044
443.200	6.355E-14	3.191E+07	2.669E+08	8.365
448.300	2.416E-14	1.315E+07	2.172E+08	16.515
452.120	1.279E-14	7.130E+06	1.501E+08	21.047
455.900	6.618E-15	3.740E+06	9.169E+07	24.512
461.000	2.820E-15	1.616E+06	4.186E+07	25.899
467.400	1.094E-15	6.360E+05	1.582E+07	24.875
470.000	6.679E-16	3.971E+05	8.738E+06	22.003

[a] Refer to the reactor one-dimensional model figure 3.8
[b] Thermal-to-fast flux ratio

Table 5.9   Radial Variation of the Total DPA, Flux >1 MeV,
            Flux <0.4 eV and Thermal-to-Fast Flux Ratio at
            the Axial and Azimuthal Peaks

Radius[a]	Total DPA	Fast Flux	Thermal Flux	Ratio[b]
cm	$DPA.s^{-1}$	$n.cm^{-2}.s^{-1}$		$\Phi Th/\Phi F$
321.310	2.786E−12	1.819E+09	3.265E+09	1.795
321.790	2.718E−12	1.781E+09	2.273E+09	1.277
322.700	2.542E−12	1.668E+09	1.256E+09	0.753
324.500	2.196E−12	1.409E+09	3.077E+08	0.218
325.888	1.911E−12	1.199E+09	1.344E+08	0.112
326.340	1.817E−12	1.130E+09	8.077E+07	0.071
328.200	1.489E−12	8.924E+08	2.567E+07	0.029
329.990	1.223E−12	7.036E+08	9.655E+07	0.014
331.810	9.967E−13	5.482E+08	5.183E+06	0.009
333.630	8.003E−13	4.217E+08	5.402E+06	0.013
334.080	7.583E−13	3.964E+08	7.097E+06	0.018
335.500	6.259E−13	3.170E+08	1.305E+07	0.041
337.300	4.642E−13	2.263E+08	4.171E+07	0.184
338.182	3.949E−13	1.910E+08	6.377E+07	0.334
340.460	3.797E−13	1.808E+08	6.442E+07	0.356
360.610	2.843E−13	1.376E+08	7.846E+07	0.570
377.000	2.413E−13	1.156E+08	8.407E+07	0.728
387.530	2.259E−13	1.073E+08	8.517E+07	0.793
409.660	2.051E−13	9.583E+07	8.775E+07	0.916
420.550	1.985E−13	9.185E+07	8.889E+07	0.968
436.880	1.735E−13	7.911E+07	1.422E+08	1.797
438.200	1.677E−13	7.642E+07	1.563E+08	2.045
443.200	6.417E−14	3.225E+07	2.692E+08	8.348
448.300	2.447E−14	1.334E+07	2.191E+08	16.431
452.120	1.298E−14	7.243E+06	1.514E+08	20.907
455.900	6.720E−15	3.797E+06	9.256E+07	24.378
461.000	2.859E−15	1.637E+06	4.230E+07	25.843
467.400	1.107E−15	6.442E+05	1.600E+07	24.831
470.000	6.638E−16	3.923E+05	8.839E+06	22.530

[a] Refer to the reactor one-dimensional model figure 3.8
[b] Thermal-to-fast flux ratio

Table 5.10   Radial Variation of the Total DPA, Flux >1 MeV, Flux
<0.4 eV and Thermal-to-Fast Flux Ratio at the Axial
Feed Water Nozzle Elevation and Azimuthal Peak

Radius[a] cm	Total DPA DPa . s^{-1}	Fast Flux	Thermal Flux n . cm^{-2} . s^{-1}	Ratio[b] ØTh/ØF
321.310	1.154E-16	7.259E+04	1.094E+05	1.507
321.790	1.126E-16	7.110E+04	7.575E+04	1.066
322.700	1.048E-16	6.650E+04	4.254E+04	0.640
324.500	9.808E-16	1.429E+05	3.470E+04	0.243
325.888	1.161E-15	1.586E+05	4.150E+04	0.262
326.340	1.217E-15	1.635E+05	4.377E+04	0.268
328.200	1.459E-15	1.944E+05	7.167E+04	0.369
329.990	1.710E-15	2.370E+05	1.222E+05	0.516
331.810	2.000E-15	3.010E+05	2.211E+05	0.736
333.630	2.328E-15	3.936E+05	4.837E+05	1.229
334.080	2.438E-15	4.331E+05	7.165E+05	1.654
335.500	2.795E-15	5.620E+05	1.515E+06	2.695
337.300	3.568E-15	8.808E+05	4.794E+06	5.443
338.182	4.376E-15	1.270E+06	7.799E+06	6.139
340.460	4.324E-15	1.228E+06	7.834E+06	6.378
360.610	5.688E-15	1.745E+06	1.070E+07	6.131
377.000	6.130E-15	1.958E+06	1.219E+07	6.230
387.530	6.505E-15	2.134E+06	1.260E+07	5.904
409.660	7.482E-15	2.604E+06	1.305E+07	5.011
420.550	7.961E-15	2.827E+06	1.315E+07	4.651
436.880	4.880E-15	1.663E+06	1.477E+07	8.880
438.200	4.033E-15	1.339E+06	1.519E+07	11.341
443.200	8.801E-16	2.442E+05	1.751E+07	71.720
448.300	2.693E-16	7.402E+04	1.117E+07	150.916
452.120	1.306E-16	3.507E+04	6.705E+06	191.172
455.900	6.189E-17	1.636E+04	3.575E+06	218.535
461.000	2.311E-17	6.165E+03	1.394E+06	226.129
467.400	7.850E-18	2.219E+03	4.625E+05	208.423
470.000	4.094E-18	1.239E+03	2.300E+05	185.645

[a]Refer to the reactor one-dimensional model figure 3.8

[b]Thermal-to-fast flux ratio

Table 5.11 Determination of RPV Peak Cumulative Fluence
$[n.cm^{-2}]$ and DPA for Grand Gulf BWR/6

Radial Location	Cycle-2[a]		32 EFPY[b]	
	Fluence	DPA	Fluence	DPA
RPV wetted surface	4.406E+16	6.749E-05	1.838E+18	2.815E-03
0-T RPV	4.314E+16	6.584E-05	1.800E+18	2.747E-03
1/4-T "	2.904E+16	4.629E-05	1.212E+18	1.931E-03
1/2-T "	1.704E+16	2.983E-05	7.110E+17	1.236E-03
3/4-T "	9.602E+15	1.837E-05	4.006E+17	7.663E-04
4/4-T "	4.627E+15	9.566E-06	1.930E+17	3.991E-04

[a]Cycle-2 was about 280.37 pull power days = 2.422E+07 seconds

[b]32 EFPY amounts to 11696 full power days = 1.011E+09 seconds

-111-

Table 5.12 Radial Variation in Gamma Heating[a] and Gamma Absorbed Dose[b] Rate at Three Axial Locations

Radius (cm)	Core Mid-plane		Peak		F.W.N[c]	
	γ heating	γ dose	γ heating	γ dose	γ heating	γ dose
321.790	2.463E-3	8.866E+5	2.544E-3	9.158E+5	9.639E-6	3.470E+3
325.888	7.905E-4	2.846E+5	8.163E-4	2.939E+5	3.037E-6	1.093E+6
329.990	2.722E-4	9.799E+4	2.818E-4	1.015E+5	1.030E-6	3.709E+2
334.080	5.894E-5	2.122E+4	6.073E-5	2.186E+4	2.837E-7	1.021E+2
338.182	2.769E-5	9.968E+3	2.840E-5	1.022E+4	2.457E-7	8.847E+1
360.610	2.174E-5	7.827E+3	2.214E-5	7.970E+3	3.519E-7	1.267E+2
387.530	2.000E-5	7.210E+3	2.030E-5	7.310E+3	3.900E-7	1.390E+2
420.500	1.840E-5	6.620E+3	1.874E-5	6.620E+3	4.400E-7	1.590E+2
436.880	1.695E-5	6.102E+3	1.700E-5	6.094E+3	3.089E-7	1.112E+2
452.120	2.601E-6	9.364E+2	2.605E-6	9.378E+3	4.409E-8	1.587E+1
467.400	3.000E-7	1.080E+2	3.028E-6	1.090E+3	4.985E-9	1.795E+0

---

[a] Gamma heating [w/gm-SS 304]

[b] Gamma absorbed dose rate [rad/hr]

[c] Feed water nozzle elevation (517.0 cm above the mid-plane)
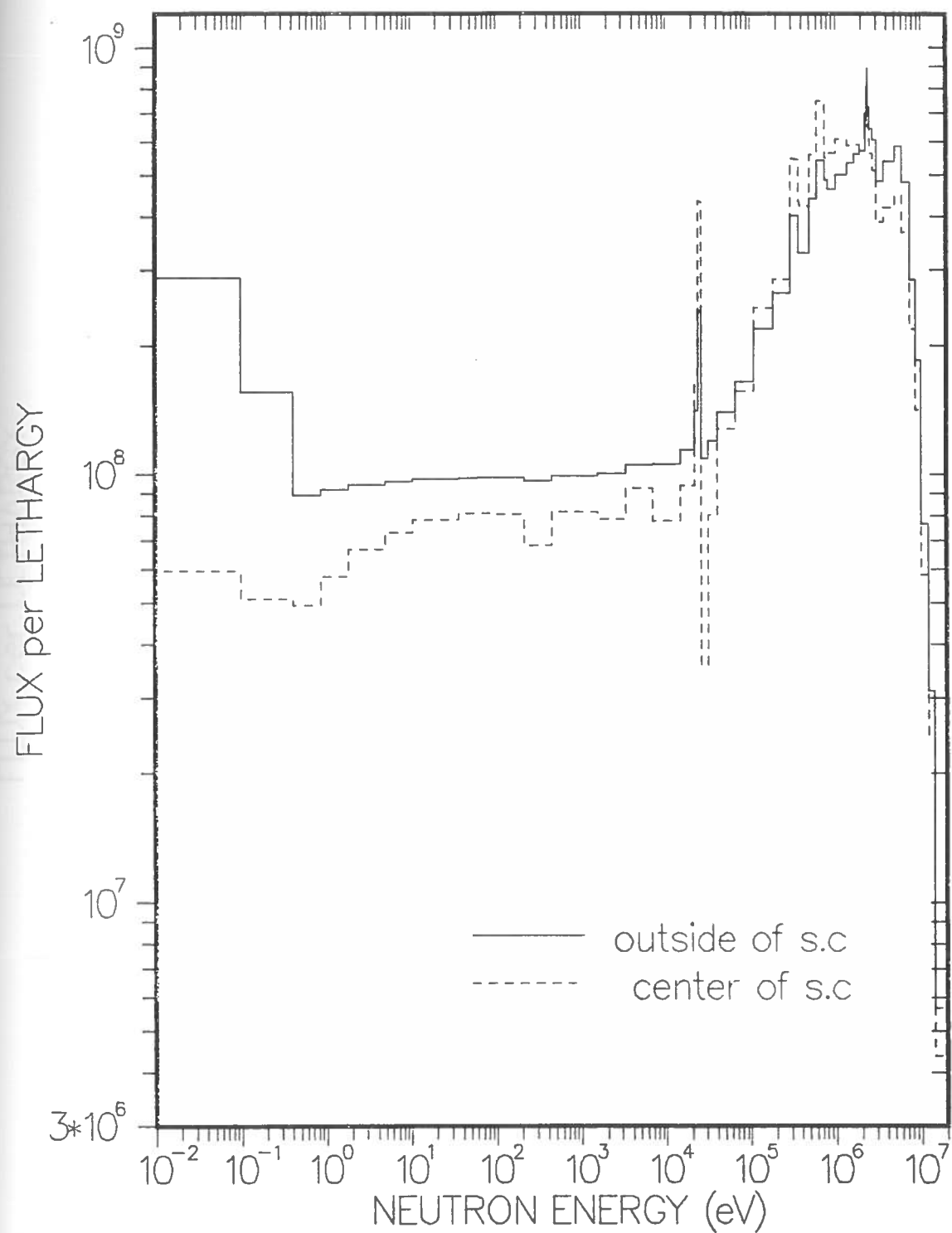
Fig. 5.12 Neutron energy spectra [n.cm^{-2}.s^{-1}.Δu^{-1}] outside and center
of the 3^0 surveillance capsule (SC) at the axial peak
location
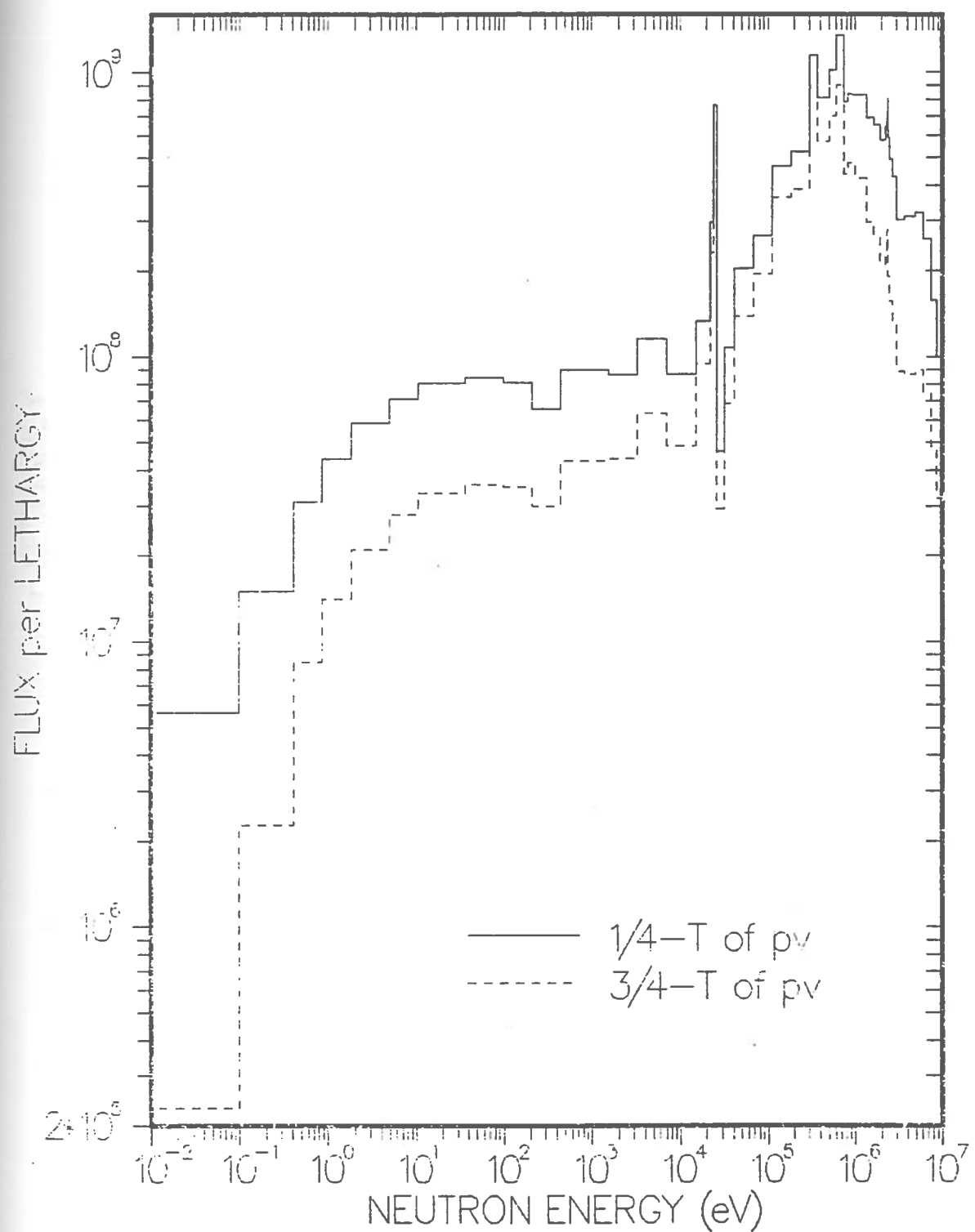
Fig. 5.13 Neutron energy spectra [n.cm^{-2}.s^{-1}.Δu^{-1}] at two radial locations in the RPV at the axial core mid-plane
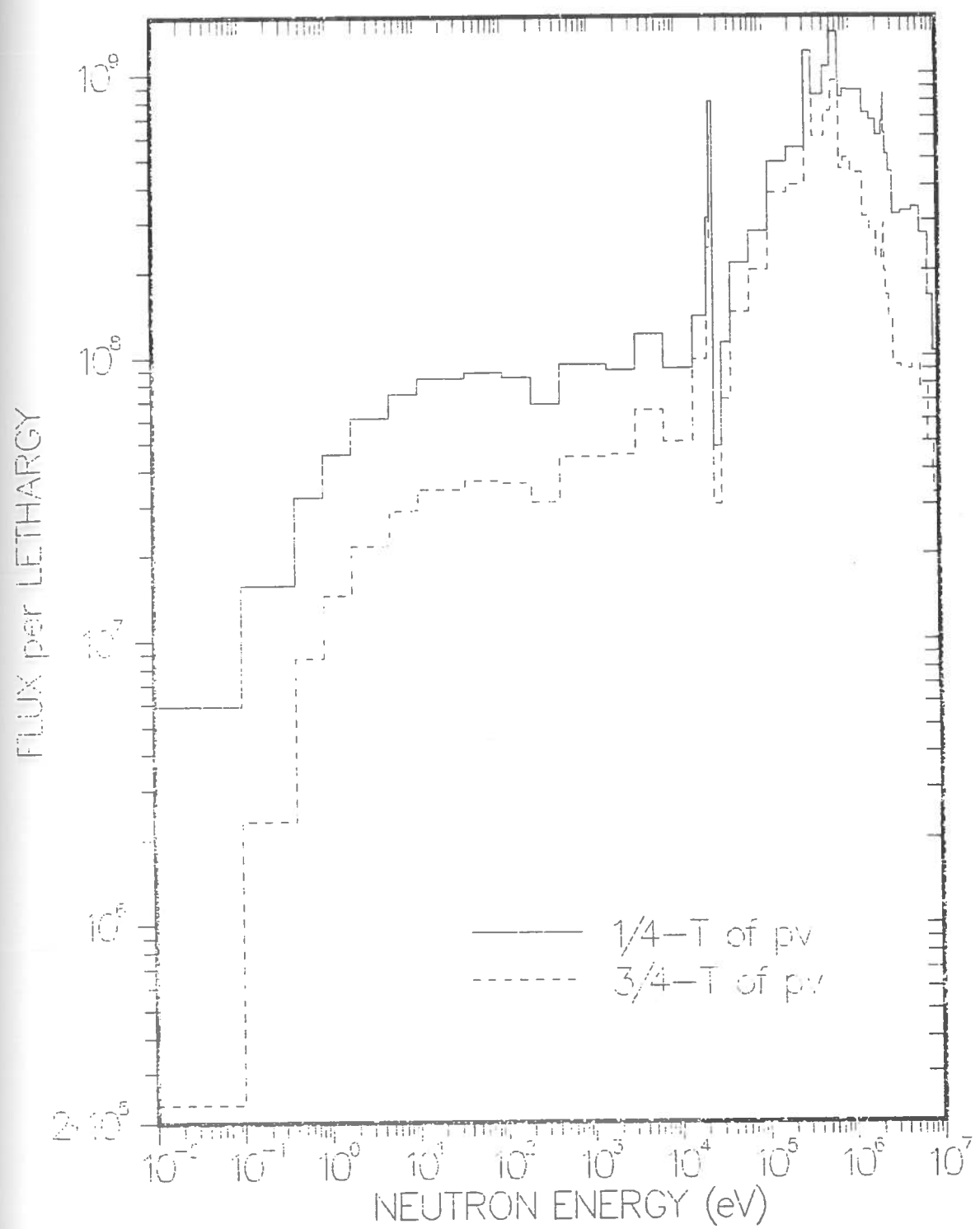
Fig. 5.14 Neutron energy spectra [n.cm^{-2}.s^{-1}.Δu^{-1}] at two radial
locations in the RPV at the axial peak
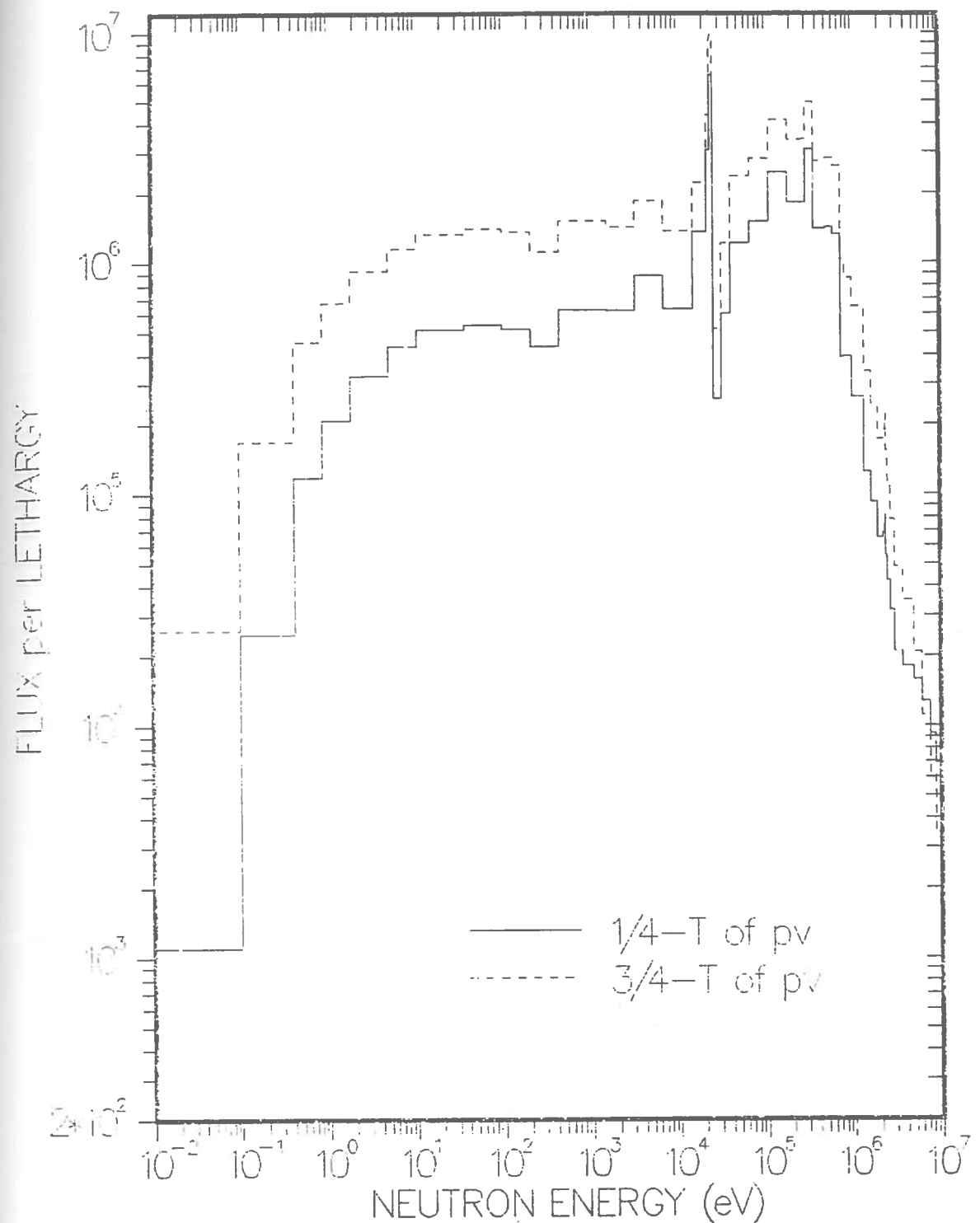
Fig. 5.15 Neutron energy spectra [n.cm^{-2}.s^{-1}.Δu^{-1}] at two radial locations in the RPV at the feed water nozzle elevation
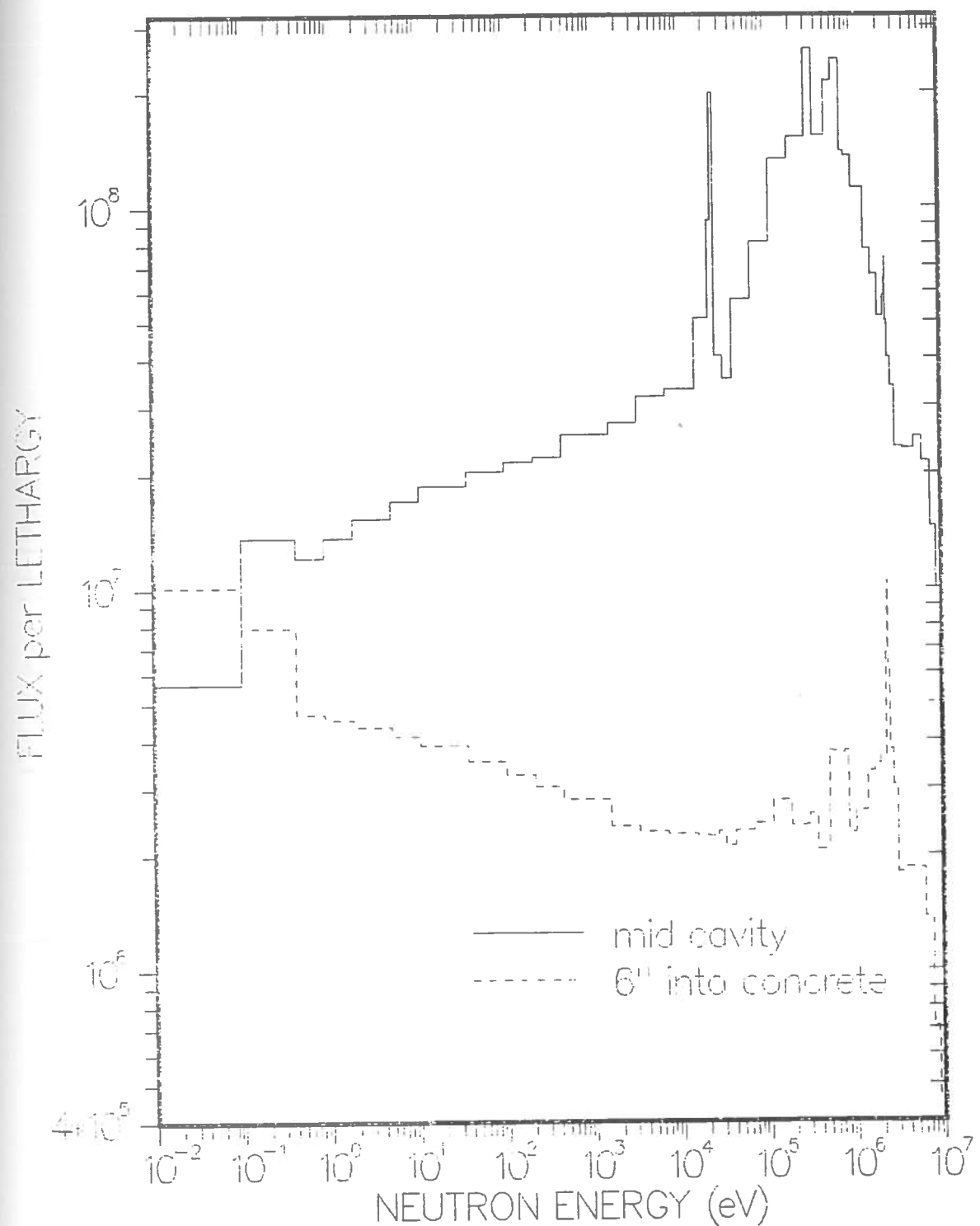
Fig. 5.16 Neutron energy spectra [n.cm^{-2}.s^{-1}.Δu^{-1}] at mid-cavity and 6" into the concrete shield wall at the axial core mid-plane
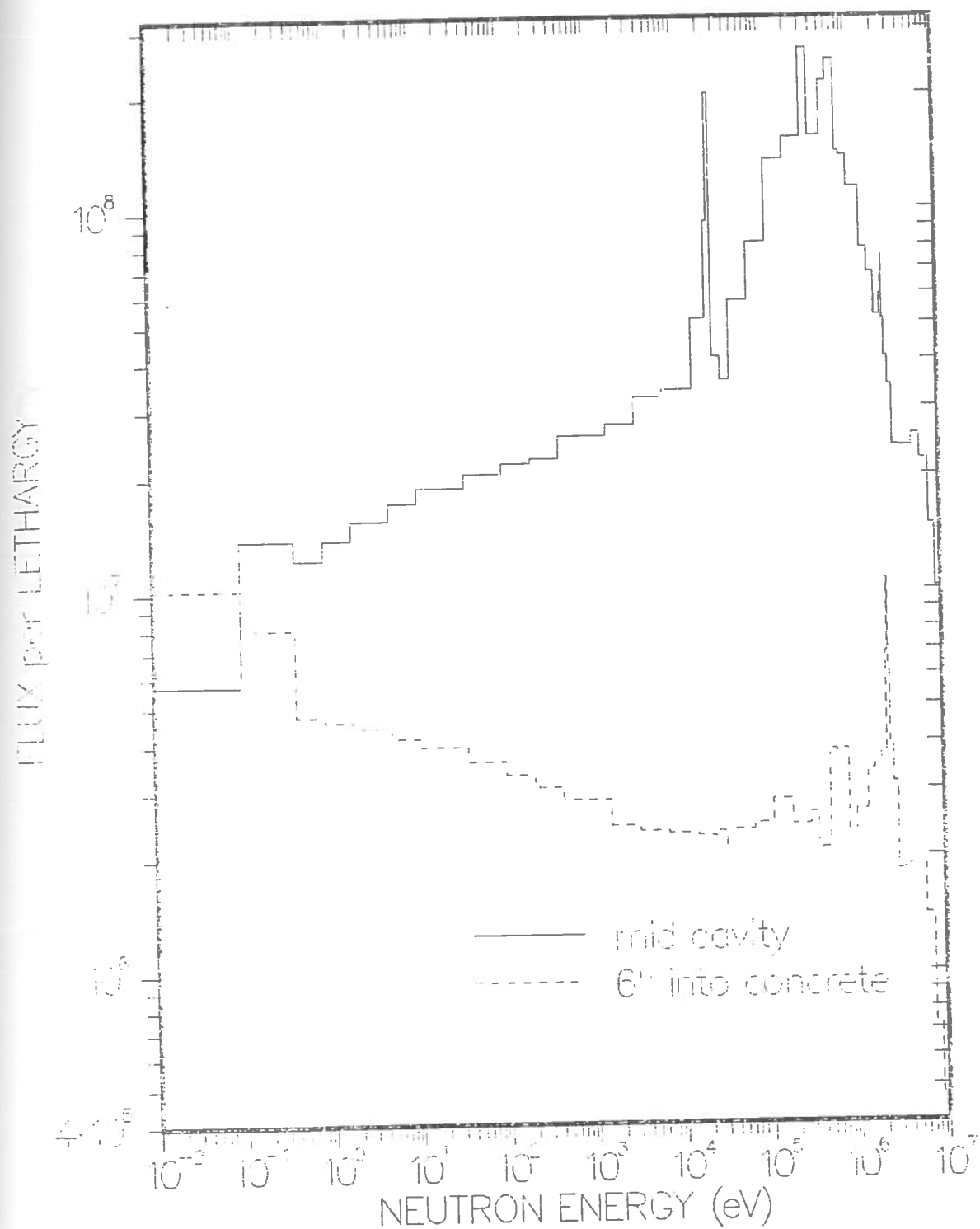
Fig. 5.17 Neutron energy spectra [n.cm^{-2}.s^{-1}.Δu^{-1}] at mid-cavity and 6" into the concrete shield wall at the axial peak
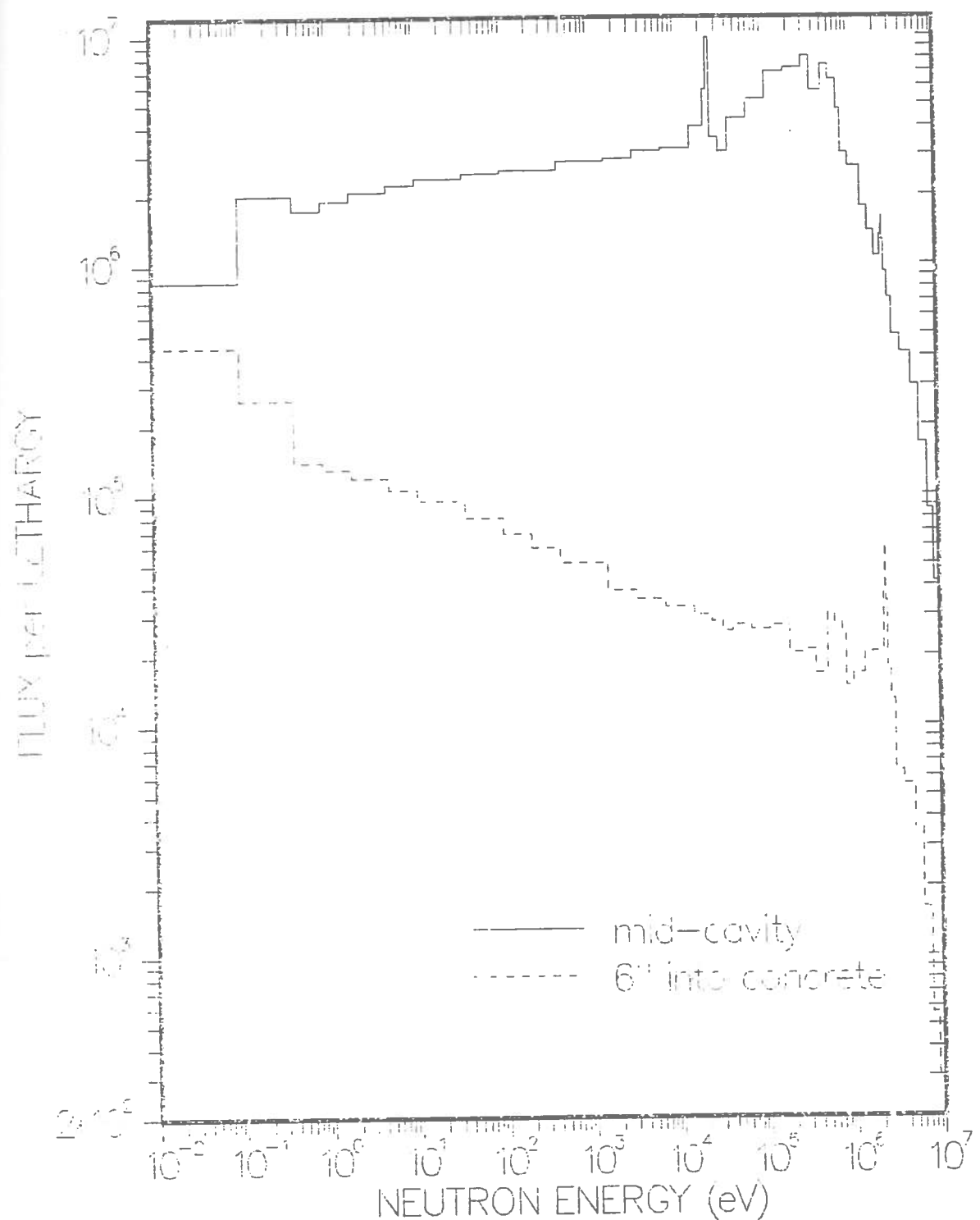
Fig. 5.18 Neutron energy spectra [n.cm^{-2}.s^{-1}.Δu^{-1}] at mid-cavity
and 6" into the concrete shield wall at the feed water
nozzle elevation
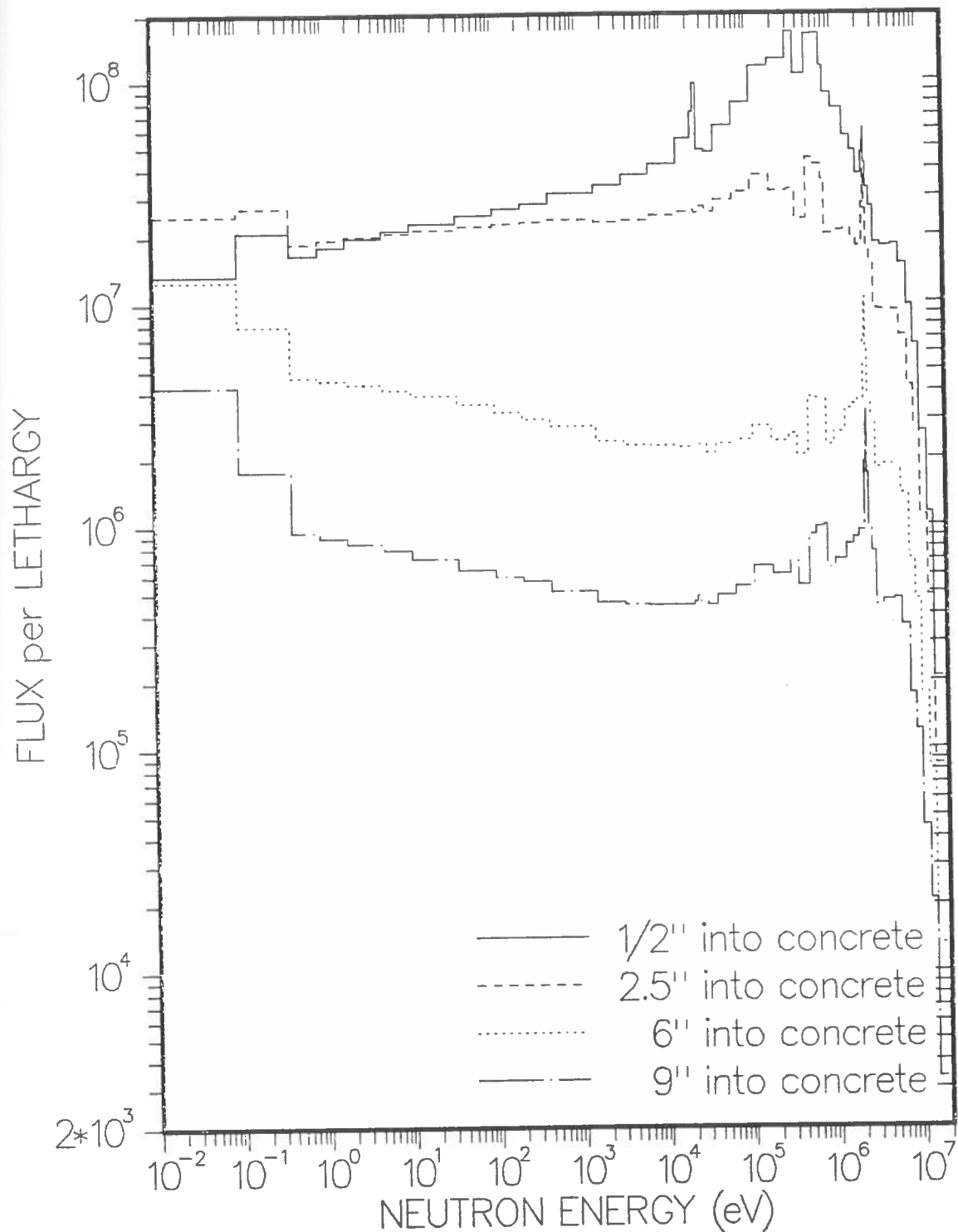
Fig. 5.19 Radial variation of neutron energy spectra [n.cm^{-2}.s^{-1}.Δu^{-1}]
through the concrete shield wall at the axial core mid-plane
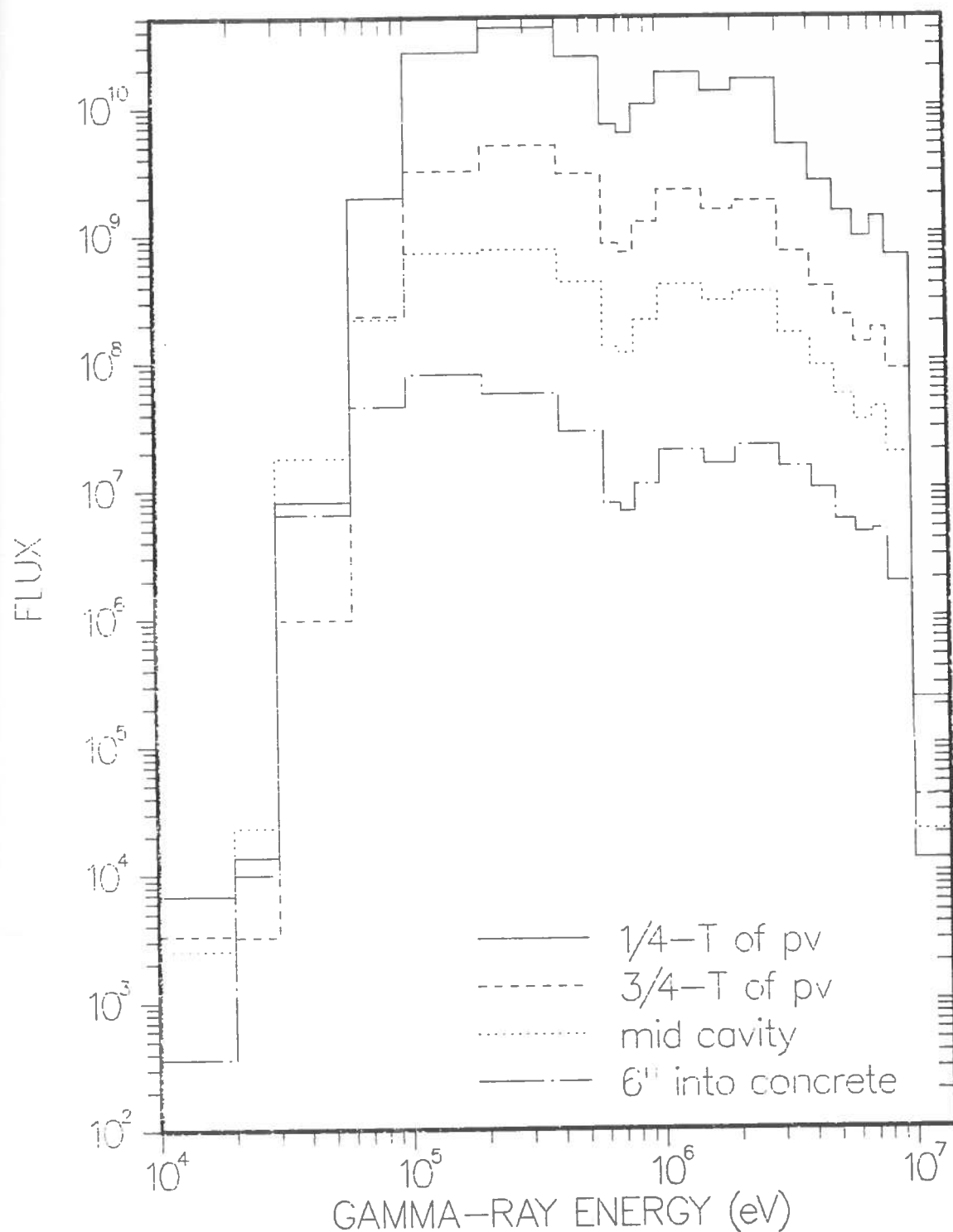
Fig. 5.20 Gamma energy spectra [$\gamma.cm^{-2}.s^{-1}$] at four radial locations throughout the RPV and the concrete shield wall at the axial core mid-plane
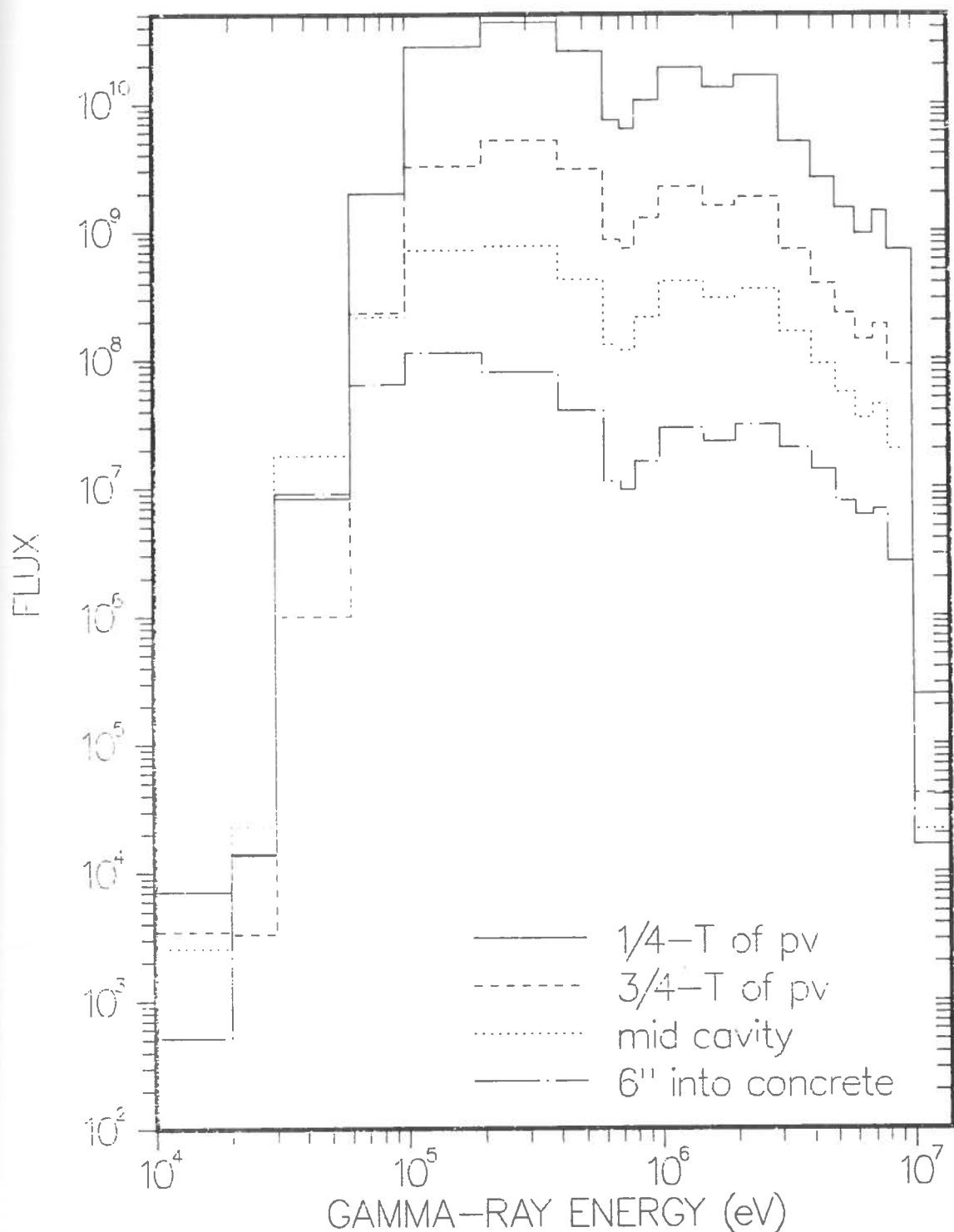
Fig. 5.21 Gamma energy spectra $[\gamma.cm^{-2}.s^{-1}]$ at four radial locations throughout the RPV and the concrete shield wall at the axial peak
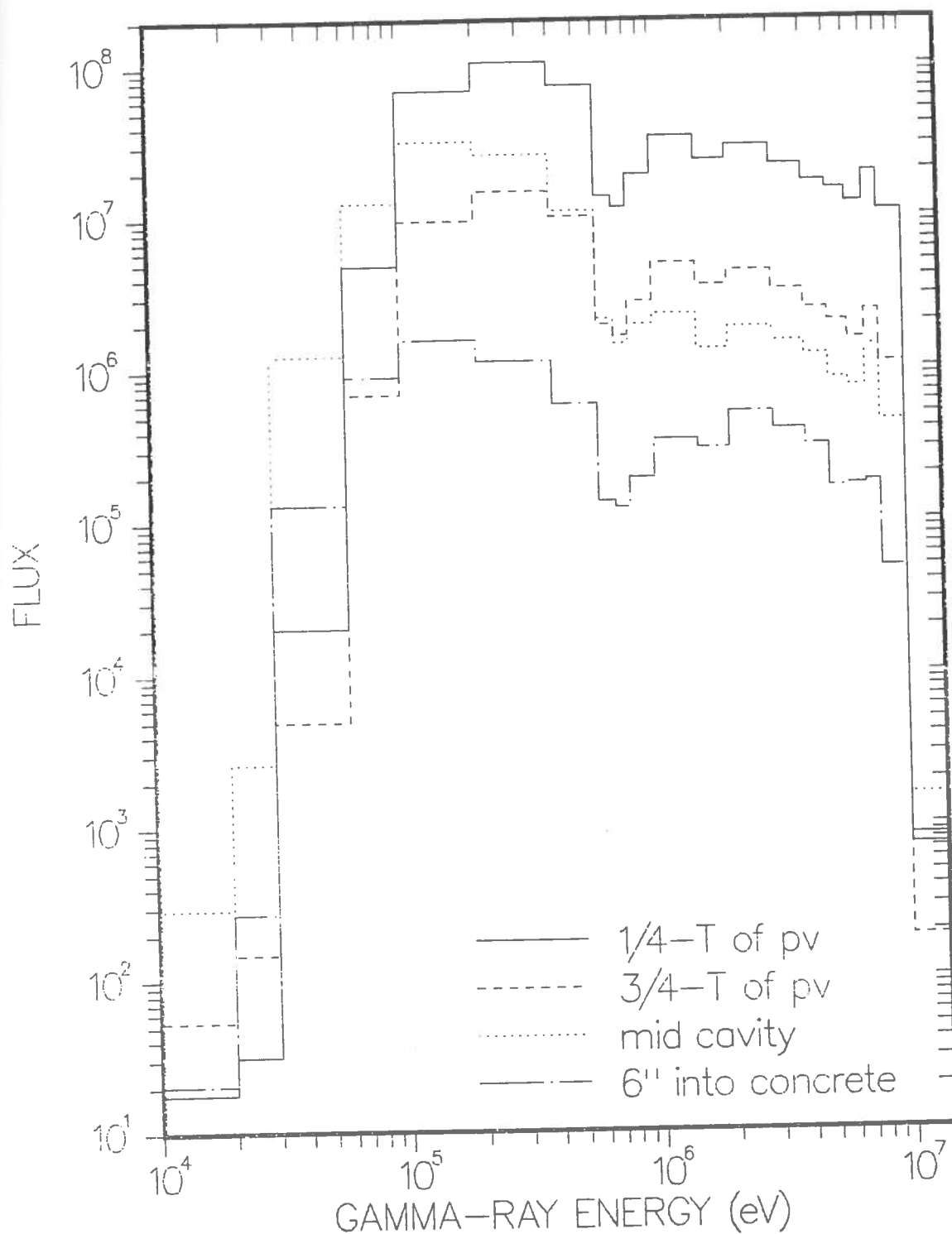
Fig. 5.22 Gamma energy spectra [$\gamma \cdot cm^{-2} \cdot s^{-1}$] at four radial locations throughout the RPV and the concrete shield wall at the feed water nozzle elevation
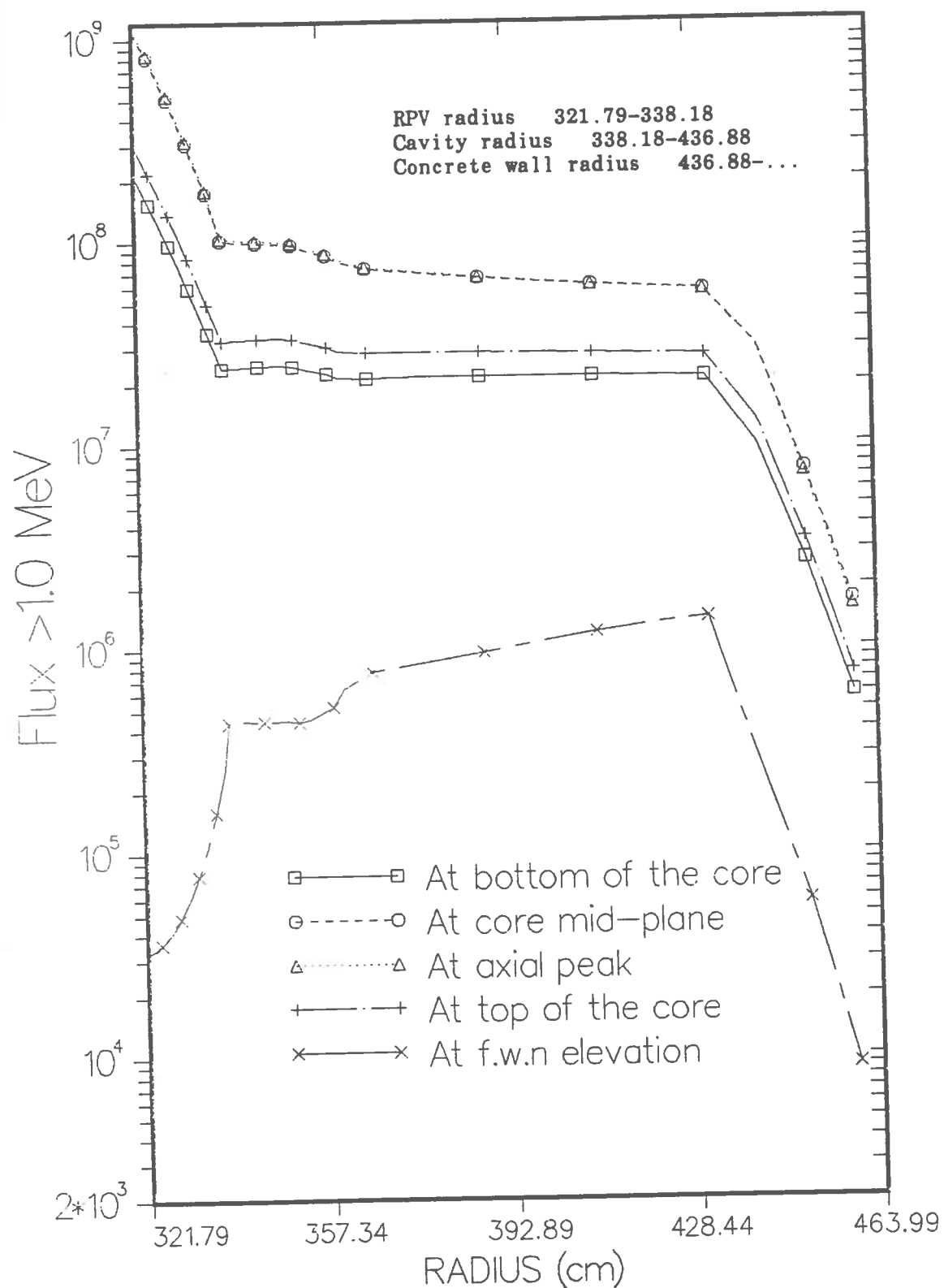
Fig. 5.23 Radial variation of the flux above 1.0 MeV [n.cm^{-2}.s^{-1}] at five axial locations
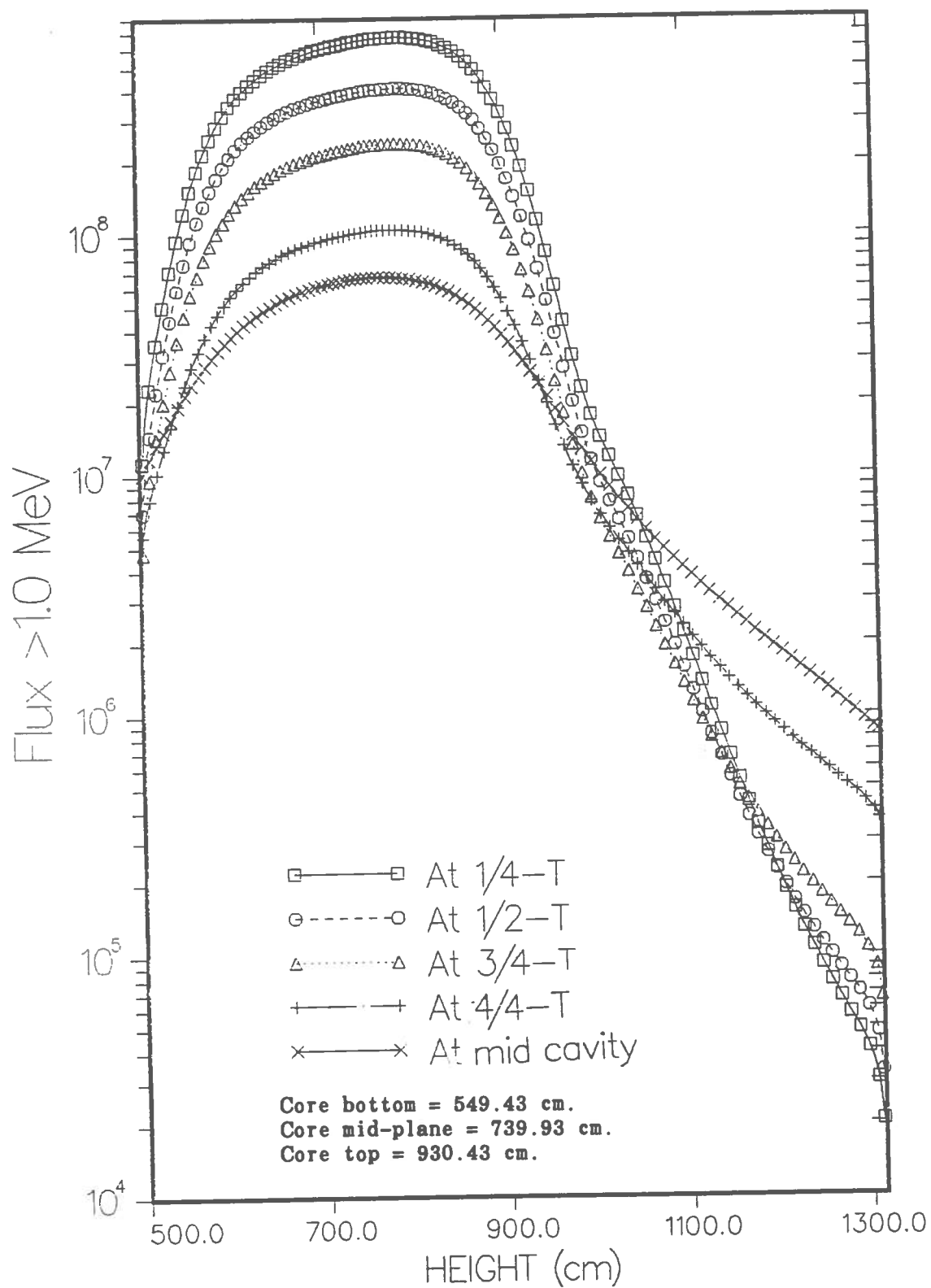
Fig. 5.24 Axial variation of the flux above 1.0 MeV [n.cm^{-2}.s^{-1}] at five radial locations

the vessel, reactor cavity and concrete shield wall. The gamma heating

source values can be used in determining the temperature of the

structural components if a thermal analysis is performed. The peak

gamma heating at three radial locations of O-T, 3/4-T RPV and the front

of the concrete shield wall has values of 2.544E-03, 6.073E-05, and

1.700E-05 w/gm-SS 304, respectively as shown in table 5.12. The gamma

absorbed dose data can be used in the quantative determination of the

radiation exposure to any instrumentation and wiring located in the

cavity or concrete shield wall. Table 5.12 shows that the gamma

absorbed dose rate at the mid-cavity is about 7.310E+03 rad/hr during

full power operation.

5.3 Comparison of calculated and experimental results

As discussed earlier, the experimental analysis of the activated

wires revealed an abnormal behavior in the axial distribution of the

activity of the wires. The experimental data indicats the presence of

relatively high activity in all wires far below the bottom of the active

core, and little activity for elevations corresponding to the upper half

of the active core.

Figures 5.25 through 5.27 compare the measured relative axial

distribution of the activated wires with that calculated at three

azimuthal locations of 15°, 40°, and 45°, respectively. The calculated

results are the synthesized values of the activity obtained in the

transport calculations. In these figures, both calculated and

experimental axial distribution of each wire at each location is

normalized to its own peak value. As seen in these figures, the

experimental distribution appears shifted axially from the calculated

results. Based on these results, it appears that the location of the wires relative to the core mid-plane reported in figure 4.3 is displaced by about 5 feet. Table 5.13 shows the comparison of the calculated and experimental absolute activity of the dosimeter foils.

If all the experimental results are displaced by 5 feet, then the calculated and experimental axial distribution of the activated wires agree quite well, as shown in figures 5.28 through 5.30. Also, as seen in table 5.14, the agreement between experimental and calculated activity of the dosimeter foils is much improved by the axial displacement. It should be noted that if the assumed five foot shift is real, then the actual axial locations of all but one of the dosimeters are far above the active core height (contrary to what was intended in the original experiment design). For example, instead of being located at the mid-plane, 11 feet, and 17 feet above the mid-plane respectivly, the three dosimeter packets would be located 5, 16, and 22 feet above the mid-plane. At such extreme axial elevations, the agreement between the calculated and experimental results is relatively poor due to the streaming effect and inadequate performance of the synthesis calculation under these circumstances. The absence of activity in Cu foils and insufficient activity in Fe foils at the highest elevations is due to the low fast neutron flux at these locations. Furthermore The statistical error in the measured activity of the Fe foils at the highest elevation is very large and the comparison with the calculated values is meaningless.

Since all of the dosimeters were presumably shifted, there were no dosimeter foils located at the peak flux elevation, which is located

near the core mid-plane. Therefore several pieces of the Ni wire near the peak location were cut to be used as dosimeters. The Ni wire was the only pure wire used in this experiment. Table 5.15 shows the comparison of the calculated and measured nickel activity before and after an assumed 5 feet axial shift, respectively. As seen in this table, the agreement between the calculated and measured activity nearby the core mid-plane is also significantly improved by the assumed displacement, providing further evidence of a discrepancy in the quoted location of the experiment wires. The C/E values were found to be 1.01, 1.29, and 1.11 at the azimuthal locations of 15^0, 40^0, and 45^0, respectively, after the 5 foot shift in the axial location.
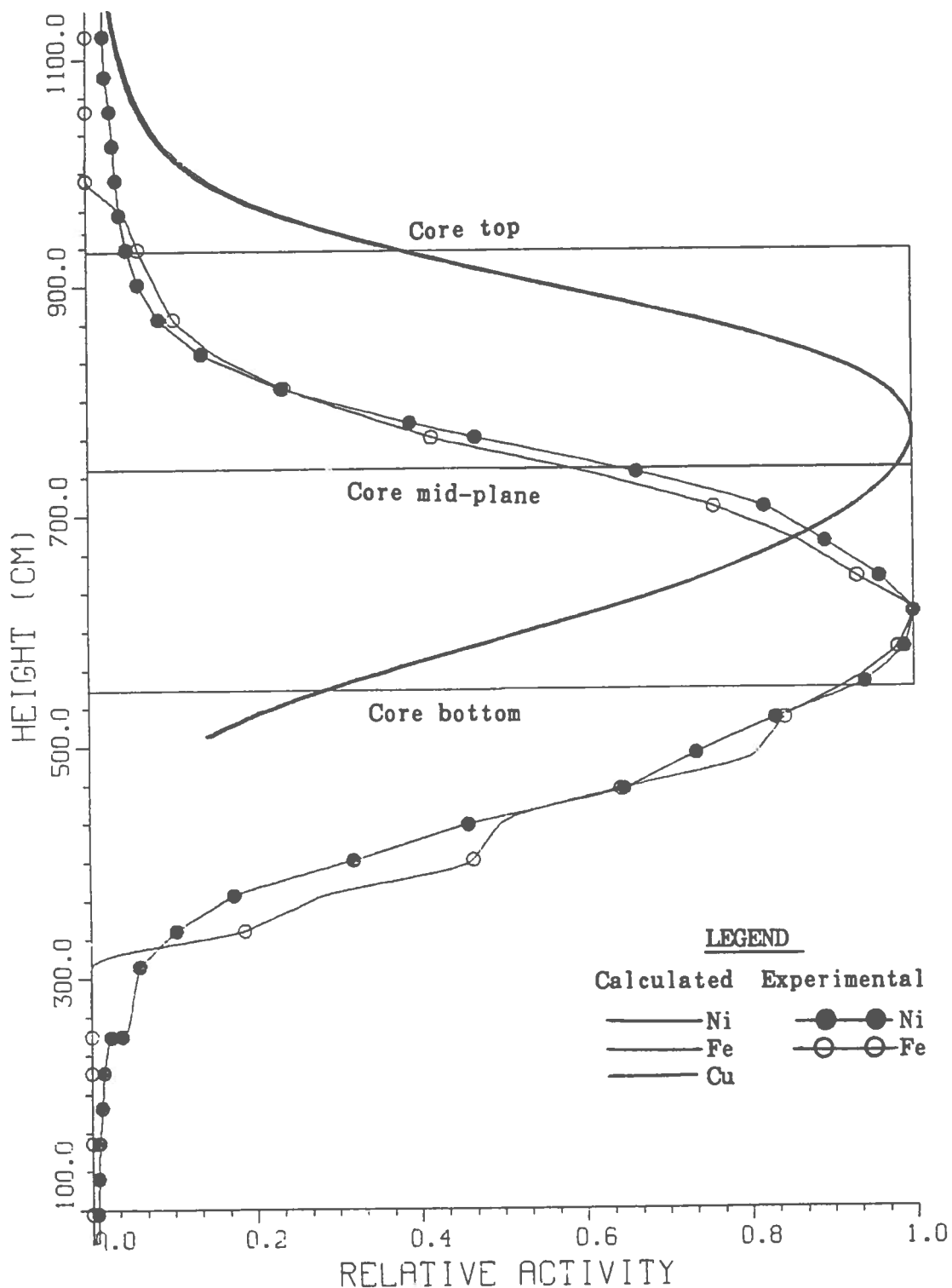
Fig. 5.25 Comparison of the experimental and calculated relative axial activity distribution of Ni and Fe wires at the 15^0 azimuth location
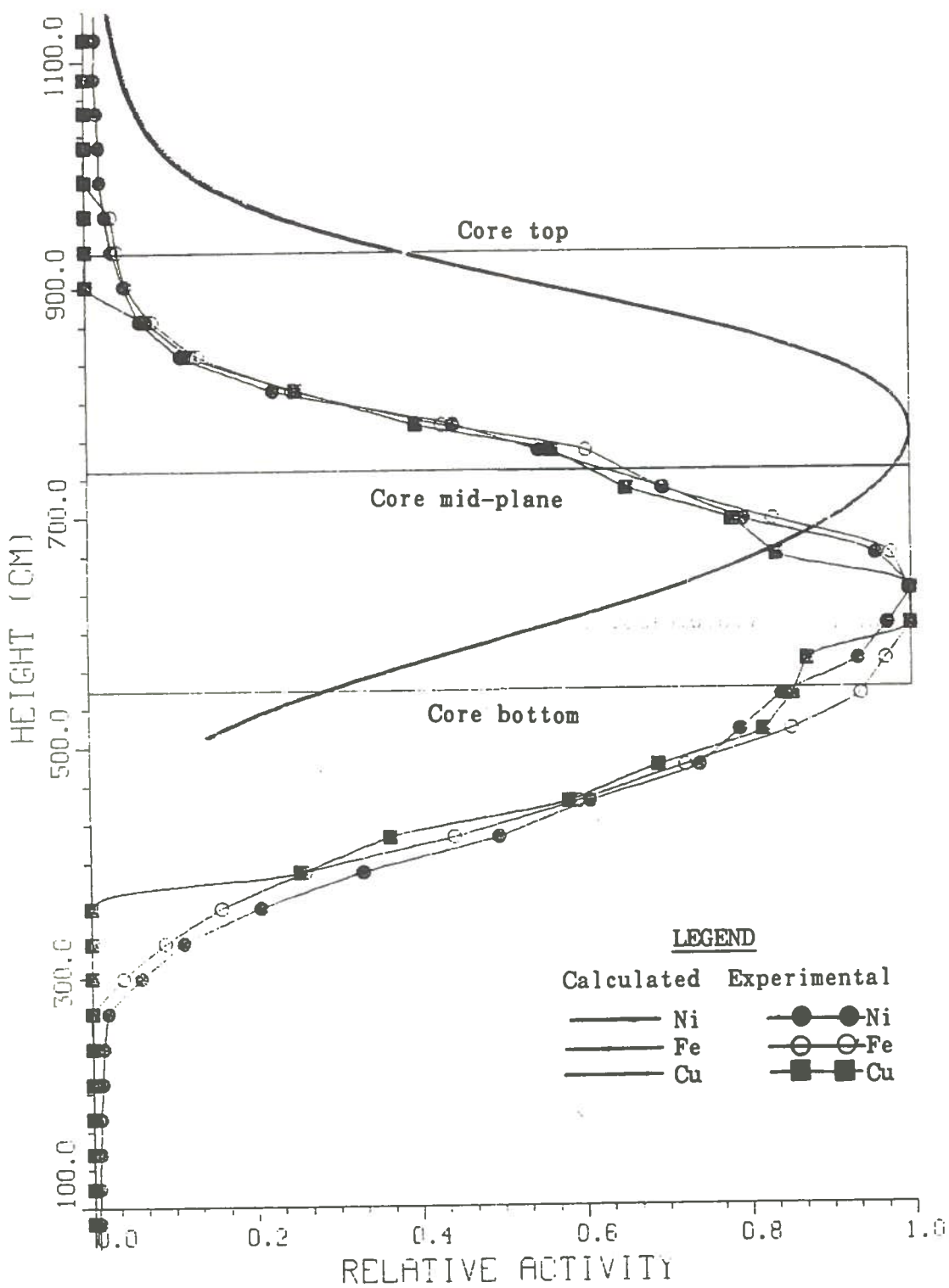
Fig. 5.26 Comparison of the experimental and calculated relative axial activity distribution of Ni, Fe and Cu wires at the 40^0 azimuth location
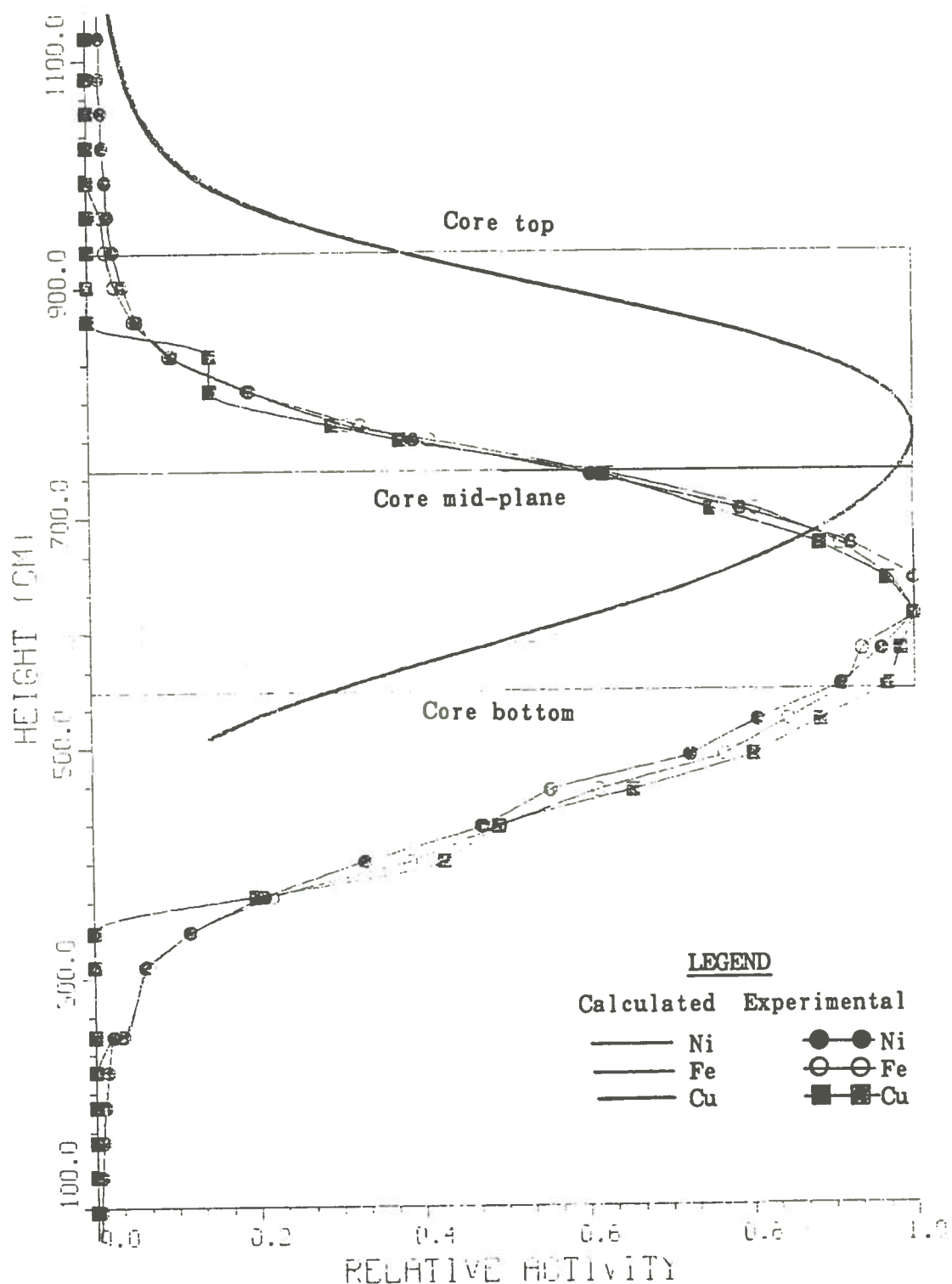
Fig. 5.27 Comparison of the experimental and calculated relative axial activity distribution of Ni, Fe and Cu wires at the 45° azimuth location

Table 5.13 Comparison of the Experimental and Calculated Absolute
Activity of the Dosimeter Foils at Several Axial and
Azimuthal Locations

15^0 Azimuth

Height[a]	Foils and reactions	Ac[b]	Ae[c] ± % SD[d]	C/E[e]
779.78	$^{58}Ni(n,p)^{58}Co$	5.60E+4	2.15E+4±1.00%	2.60
	$^{54}Fe(n,p)^{54}Mn$	2.03E+3	7.83E+2±5.75%	2.59
	$^{63}Cu(n,\alpha)^{60}Co$	8.54E+1	2.38E+1±4.15%	3.59
	$^{181}Ta(n,\gamma)^{182}Ta$	4.17E+7	2.54E+7±0.51%	1.63
1115.06	$^{58}Ni(n,p)^{58}Co$	2.13E+3	5.35E+2±3.80%	3.98
	$^{54}Fe(n,p)^{54}Mn$	7.16E+1	1.20E+1±16.1%	5.97
	$^{63}Cu(n,\alpha)^{60}Co$	1.57E+0	No Activity	-----
1297.94	$^{58}Ni(n,p)^{58}Co$	5.30E+2	1.07E+2±8.10%	4.95
	$^{54}Fe(n,p)^{54}Mn$	1.80E+1	1.33E+1±29.0%	1.35
	$^{63}Cu(n,\alpha)^{60}Co$	3.42E-1	No Activity	-----
	$^{181}Ta(n,\gamma)^{182}Ta$	2.05E+6	4.17E+5±0.68%	4.91

40^0 Azimuth

Height[a]	Foils and reactions	Ac[b]	Ae[c] ± % SD[d]	C/E[e]
1115.06	$^{58}Ni(n,p)^{58}Co$	3.36E+3	7.15E+2±3.20%	4.70
	$^{54}Fe(n,p)^{54}Mn$	1.13E+2	1.58E+1±27.0%	7.15
	$^{63}Cu(n,\alpha)^{60}Co$	2.42E+0	No Activity	-----
1297.94	$^{58}Ni(n,p)^{58}Co$	8.45E+2	2.25E+2±5.80%	3.76
	$^{54}Fe(n,p)^{54}Mn$	2.87E+1	1.07E+1±18.0%	2.68
	$^{63}Cu(n,\alpha)^{60}Co$	5.32E-1	No Activity	-----
	$^{181}Ta(n,\gamma)^{182}Ta$	3.38E+6	6.93E+5±0.80%	4.88

Table 5.13 Continued

45^0 Azimuth

Height[a]	Foils and reactions	Ac[b]	Ae[c] ± % SD[d]	C/E[e]
840.74	^{58}Ni(n,p)^{58}Co	8.15E+4	8.76E+3±1.60%	9.30
	^{54}Fe(n,p)^{54}Mn	2.95E+3	3.30E+2±8.20%	8.94
	^{63}Cu(n,α)^{60}Co	1.19E+2	9.20E+0±5.00%	12.9
	^{181}Ta(n,γ)^{182}Ta	4.55E+7	2.28E+7±0.50%	2.00
1115.06	^{58}Ni(n,p)^{58}Co	3.51E+3	4.62E+2±2.75%	7.60
	^{54}Fe(n,p)^{54}Mn	1.19E+2	1.37E+1±16.0%	8.69
	^{63}Cu(n,α)^{60}Co	2.55E+0	No Activity	----
1297.94	^{58}Ni(n,p)^{58}Co	8.75E+2	1.98E+2±5.80%	4.42
	^{54}Fe(n,p)^{54}Mn	2.97E+1	6.90E+0±25.3%	4.30
	^{63}Cu(n,α)^{60}Co	5.61E-1	No Activity	----
	^{181}Ta(n,γ)^{182}Ta	3.40E+6	6.26E+6±0.64%	5.43

[a]The height corresponds to the original axial locations of the dosimeters

[b]Calculated activity (Bq/g)

[c]Experimental measured activity (Bq/g)

[d]% Standard Deviation

[e]Calculated-to-measured activity ratio
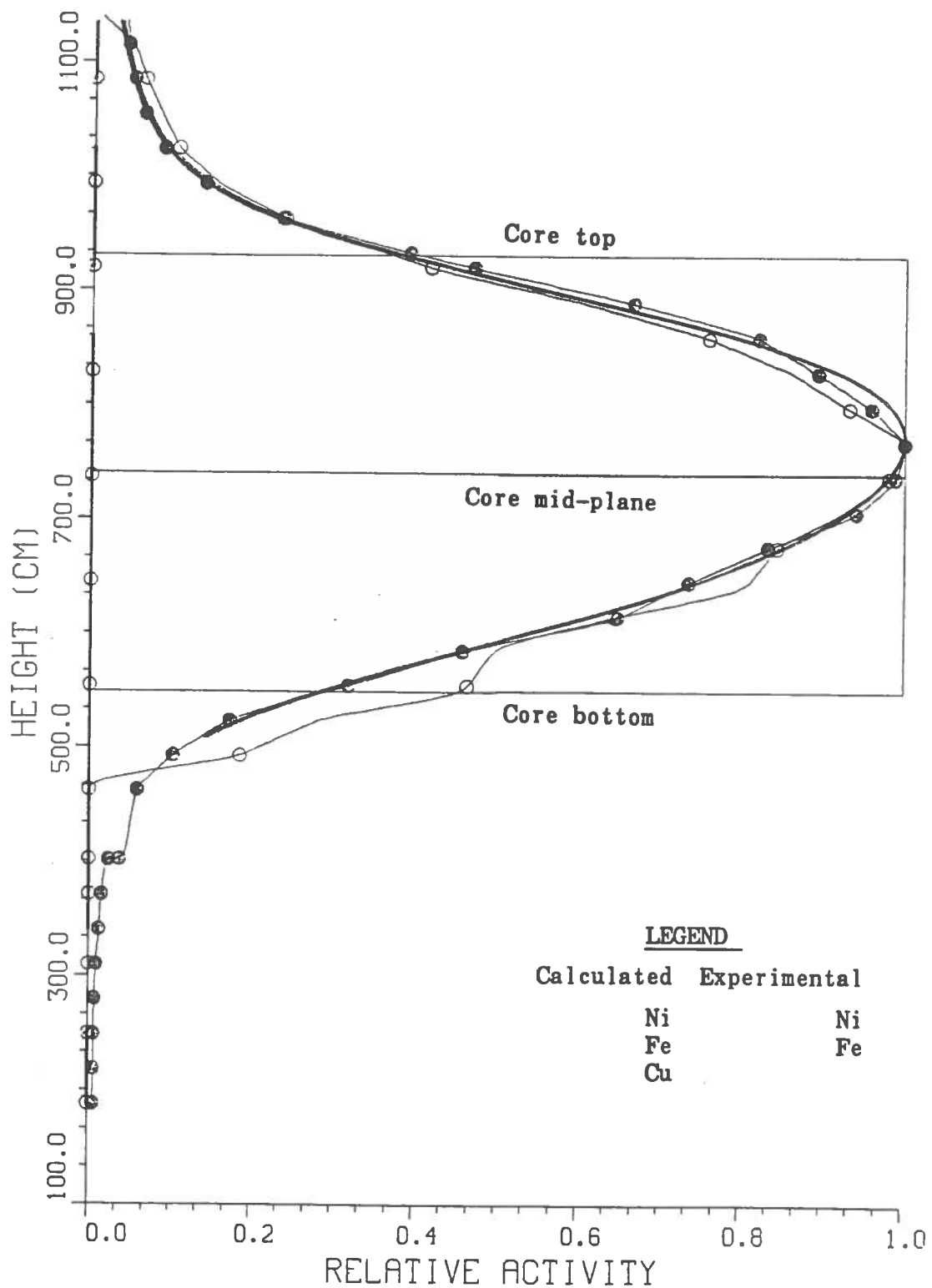
Fig. 5.28 Comparison of the experimental and calculated relative axial activity distribution of Ni and Fe wires at the 15^0 azimuth location after a 5' shift in experimental values
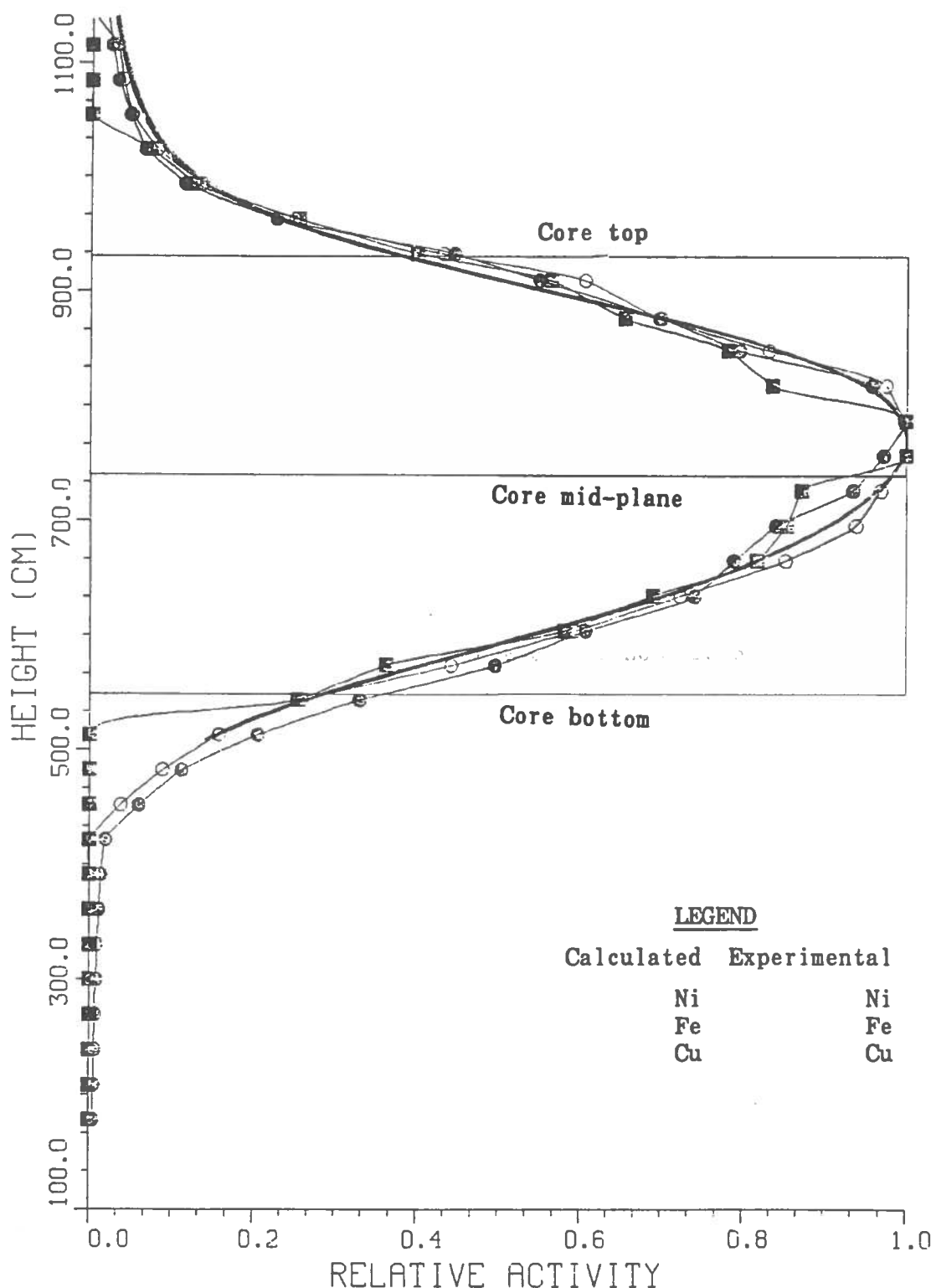
Fig. 5.29 Comparison of the experimental and calculated relative axial
activity distribution of Ni, Fe and Cu wires at the 40^0
azimuth location after a 5' shift in experimental values
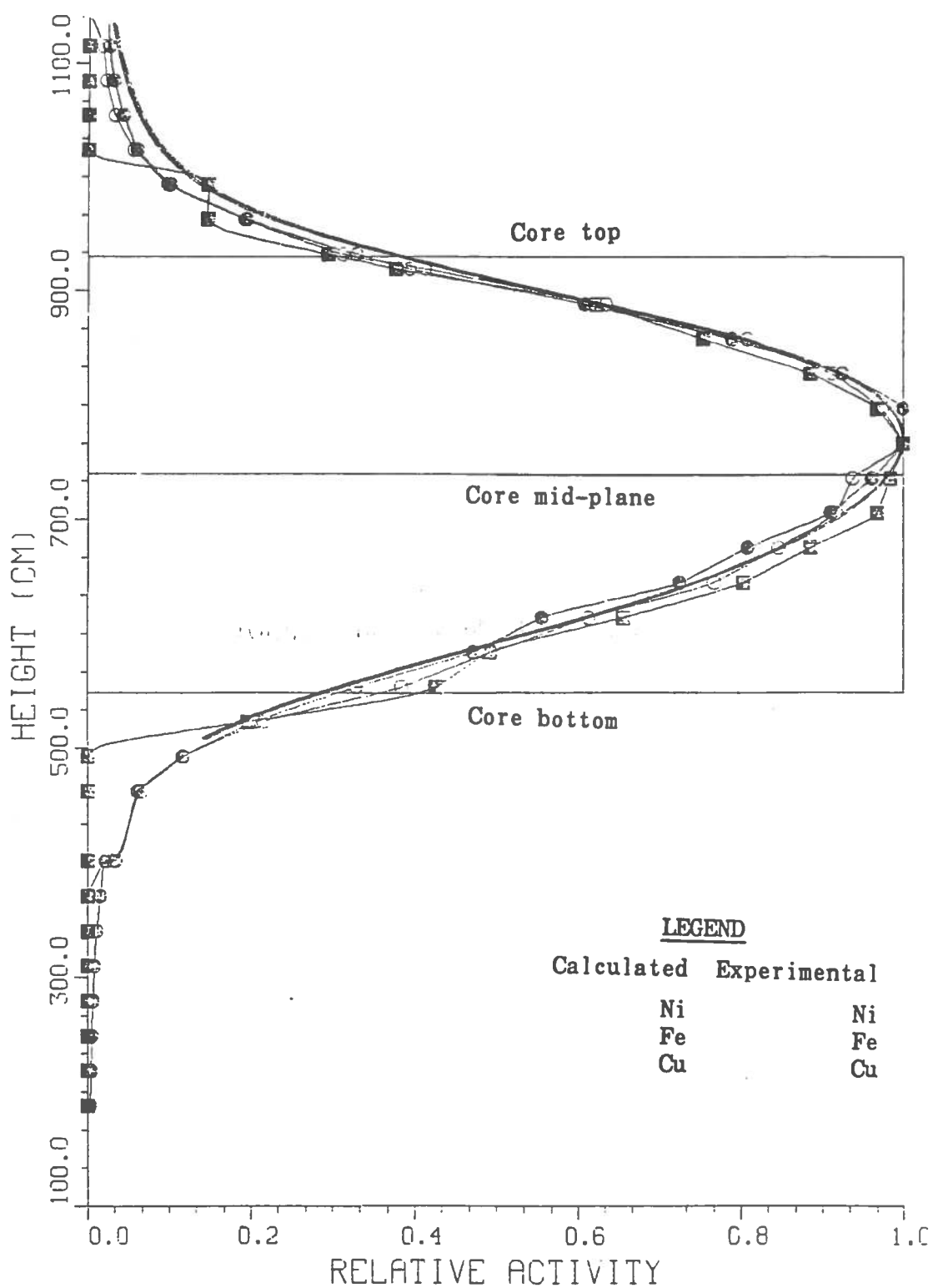
Fig. 5.30   Comparison of the experimental and calculated relative axial
activity distribution of Ni, Fe and Cu wires at the 45^0
azimuth location after a 5' shift in experimental values

Table 5.14 Comparison of the Experimental and Calculated Absolute
Activity of the Dosimeter Foils After a Five Foot
Axial Shift in the Experimental Results

15^0 Azimuth

Height[a]	Foils and reactions	Ac[b]	Ae[c] $\pm$ % SD[d]	C/E[e]
932.18	$^{58}Ni(n,p)^{58}Co$	2.11E+4	2.15E+4$\pm$1.00%	0.98
	$^{54}Fe(n,p)^{54}Mn$	7.54E+2	7.83E+2$\pm$5.75%	0.96
	$^{63}Cu(n,\alpha)^{60}Co$	2.96E+1	2.38E+1$\pm$4.15%	1.24
	$^{181}Ta(n,\gamma)^{182}Ta$	2.39E+7	2.54E+7$\pm$0.51%	0.94
1267.5	$^{58}Ni(n,p)^{58}Co$	6.67E+2	5.35E+2$\pm$3.80%	1.25
	$^{54}Fe(n,p)^{54}Mn$	2.23E+1	1.20E+1$\pm$16.1%	1.85
	$^{63}Cu(n,\alpha)^{60}Co$	4.27E-1	No Activity	----
1450.34	$^{58}Ni(n,p)^{58}Co$	2.39E+2	1.07E+2$\pm$8.10%	2.23
	$^{54}Fe(n,p)^{54}Mn$	8.05E+0	1.33E+1$\pm$29.0%	0.60
	$^{63}Cu(n,\alpha)^{60}Co$	1.54E-1	No Activity	----
	$^{181}Ta(n,\gamma)^{182}Ta$	1.42E+6	4.17E+5$\pm$0.68%	3.41

40^0 Azimuth

Height[a]	Foils and reactions	Ac[b]	Ae[c] $\pm$ % SD[d]	C/E[e]
1267.50	$^{58}Ni(n,p)^{58}Co$	1.06E+3	7.15E+2$\pm$3.20%	1.48
	$^{54}Fe(n,p)^{54}Mn$	3.53E+1	1.58E+1$\pm$27.0%	2.23
	$^{63}Cu(n,\alpha)^{60}Co$	6.62E-1	No Activity	----
1450.34	$^{58}Ni(n,p)^{58}Co$	3.77E+2	2.25E+2$\pm$5.80%	1.68
	$^{54}Fe(n,p)^{54}Mn$	1.27E+1	1.07E+1$\pm$18.0%	1.19
	$^{63}Cu(n,\alpha)^{60}Co$	2.29E-1	No Activity	----
	$^{181}Ta(n,\gamma)^{182}Ta$	1.83E+6	6.93E+5$\pm$0.80%	2.64

Table 5.14   Continued

45^0 Azimuth

Height[a]	Foils and reactions	Ac[b]	Ae[c] ± % SD[d]	C/E[e]
993.14	$^{58}Ni(n,p)^{58}Co$	1.33E+4	8.76E+3±1.60%	1.52
	$^{54}Fe(n,p)^{54}Mn$	4.66E+2	3.30E+2±8.20%	1.41
	$^{63}Cu(n,\alpha)^{60}Co$	1.48E+1	9.20E+0±5.00%	1.60
	$^{181}Ta(n,\gamma)^{182}Ta$	2.02E+7	2.28E+7±0.50%	0.89
1267.50	$^{58}Ni(n,p)^{58}Co$	1.11E+3	4.62E+2±2.75%	2.40
	$^{54}Fe(n,p)^{54}Mn$	3.69E+1	1.37E+1±16.0%	2.69
	$^{63}Cu(n,\alpha)^{60}Co$	6.97E-1	No Activity	-----
1450.34	$^{58}Ni(n,p)^{58}Co$	3.95E+2	1.98E+2±5.80%	1.76
	$^{54}Fe(n,p)^{54}Mn$	1.32E+1	6.90E+0±25.3%	1.91
	$^{63}Cu(n,\alpha)^{60}Co$	2.42E-1	No Activity	-----
	$^{181}Ta(n,\gamma)^{182}Ta$	1.84E+6	6.26E+5±0.64%	2.94

[a] The height orresponds to the 5' shifted axial locations of the dosimeters

[b] Calculated activity (Bq/g)

[c] Experimental measured activity (Bq/g)

[d] % Standard Deviation

[e] Calculated-to-measured activity ratio

Table 5.15 Comparison of the Experimental and Calculated Absolute
Activity of the Ni Wire[a] Before and After a Five Foot
Axial Shift in the Experimental Results

Before 5' axial shift

Axial location[b]	Azimuthal location	A_c[d]	A_e[e] ± % SD[f]	C/E[g]
584.20	45^0	4.20E+4	8.13E+4±1.00%	0.52
604.52	40^0	4.98E+4	6.86E+4±1.37%	0.73
614.68	45^0	5.70E+4	8.42E+4±1.26%	0.68
645.16	15^0	4.18E+4	5.48E+4±1.05%	0.76

After 5' axial shift

Axial location[c]	Azimuthal location	A_c[d]	A_e[e] ± % SD[f]	C/E[g]
736.60	45^0	9.07E+4	8.13E+4±1.00%	1.12
756.92	40^0	8.82E+4	6.86E+4±1.37%	1.29
767.08	45^0	9.27E+4	8.42E+4±1.26%	1.10
897.56	15^0	5.53E+4	5.48E+4±1.05%	1.01

[a] Several pieces of the Ni wires were cut to be used as dosimeters for an absolute activity measurement.

[b] The axial location corresponds to the original axial locations of the dosimeters

[c] The axial location corresponds to the 5' shifted axial locations of the dosimeters

[d] Calculated activity (Bq/g)

[e] Experimental measured activity (Bq/g)

[f] % Standard Deviation

[g] Calculated-to-measured activity ratio

CHAPTER 6

CONCLUSION

Based upon the transport calculation results, the flux above 1 MeV peaks near the axial mid-plane and at an azimuthal angle between 40° and 45°, depending upon the radial locations. There is a factor of 1.76 and 1.67 variation in the azimuthal dependence of the fast flux (E>1 MeV) at RPV O-T and mid-cavity, respectively. The fast flux (E>1 MeV) at mid-cavity and at elevations corresponding to the top of the active core and inlet feed water nozzle are factors of 2.74 and 4.95 lower than core mid-plane values, respectively.

At the peak location, the fast flux (E>1 MeV) incident on the vessel has a value of 1.819E9 $n.cm^{-2}.s^{-1}$. Based on this flux, the fluence accumulated after 280.37 full power days of operation during cycle-2 is about 4.406E16 $n.cm^{-2}$. The fluence after 32 effective full power years is estimated to be 1.838E18 $n.cm^{-2}$ based on the fluence rate calculated for cycle-2. The cumulative displacement per atom (DPA) after 32 EFPY is estimated to be 2.815E--03, 1.931E--03, and 7.663E--04 for RPV wetted surface, 1/4-T and 3/4-T, respectively.

The results obtained from the cavity R-Z transport calculations clearly illustrate the axial streaming of the fast flux in the cavity. At an axial location above the active core height, the neutron flux above 1 MeV increases radially throughout the vessel wall due to the neutrons entering the RPV wall from the cavity. Also the results indicate that the fast neutron leaking from the vessel wall are thermalized upon entering the concrete wall thus creating a large thermal neutron source within the concrete wall. The thermal neutrons

emerging from the concrete travel across the cavity and re-enter the RPV wall, causing a peak in the thermal flux at the outer surface of the RPV wall. Based on these calculations, it is important to include the cavity region in the reactor modeling for transport calculations of the thermal flux.

The results obtained from the gamma calculations show that the peak gamma heating at O-T and 3/4-T RPV had values of 2.544E-03 and 6.073E-05 w/gm-SS 304, respectively. The peak gamma absorbed dose rate at the mid-cavity is about 7.310E+03 rad/hr at full power operation.

Three sets of Ni, Cu, and Fe wires and dosimeter foils were installed in the cavity of Grand Gulf by a team assigned by Grand Gulf to be in charge of the experiment. The neutron dosimeters were activated during cycle-2 of Grand Gulf for approximately 10 months. These dosimeters were analyzed at the LSU Nuclear Science Center after removal.

The results obtained from the analysis of the activated wires and dosimeters revealed a large discrepancy with the calculated results. The comparison of the calculated and measured relative axial distribution of the wires shows a 5 foot discrepancy in the axial location of the peak activation. The measurements indicate the presence of relatively high activity far below the bottom of the active core and almost no activity within the upper half of the core. This behavior appears to be improbable because of the presence of a significant neutron source within the upper half of the core; therefore it is believed that there is a discrepancy in the axial installation locations of the wires.

The experimental results were shifted axially by about 5 feet and then were compared with the calculated results. The comparison of the experimental and calculated relative axial distribution after the axial shift are more consistent. At an axial location five feet from the mid-plane (after the assumed shift), the C/E values for the Ni, Fe, and Cu dosimeters at 15^0 were 0.98, 0.96, and 1.24, respectively. These factors for the location 17 feet above the mid-plane were 1.52, 1.41, and 1.60, respectively. At the highest dosimeter location (ie, 23 feet above mid-plane) , the agreement tends to be poor due to the combined effect of insufficient activity in some foils such as Fe and Cu, and inadequate performance of the discrete ordinates calculation in treating the streaming in the cavity. But still the agreement between the calculated and the measured activity for Ni wire at the higher elevations is reasonable. The best agreement is obtained when a piece of the Ni wire was cut near the mid-plane from each set and is counted for the absolute activity. The average disagreement was within 14% for the mid-plane nickel activity.

Despite the complication with the experimental part of this study, the cavity dosimetry is adequate methodology in determining the intensity of the neutron flux bombarding the RPV wall at any time during the lifetime of the reactor operation. This methodology could become more valuable during the latter years of the reactor's lifetime when there are no more in-vessel dosimetry available. While the dosimetry provides information at selected points in the reactor, the discrete ordinates transport calculation provides a detailed knowledge of the neutron flux and spectrum at any points in the reactor.

Future studies are needed for a better understanding of the cavity streaming effect in the theoretical determination of the RPV fluence. The results of this study could be compared with in-vessel discrete ordinates calculations in conjunction with ex-vessel Monte Carlo methodology. Performing additional and more detailed cavity neutron dosimetry could provide necessary data to benchmark the calculated results. Finally, studies are needed in the development of automated computer codes for modeling the reactor configuration for transport calculation and performing standardized analysis on the obtained results.

REFERENCES

1. "Browns Ferry Unit-3 Cavity Neutron Spectral Analysis." Final
Report, NP-1997. Electric Power Research Institute, Palo Alto, CA,
August 1981.

2. "Calculation of Neutron Energy Spectra in the Core and Cavity of
a PWR (ANO-1)". Topical Report, NP-3776. Electric Power Research
Institute, Palo Alto, CA, December 1984.

3. A. F. Henry, Nuclear Reactor Analysis, the MIT Press, Cambridge,
MA and London, England, 1975.

4. R. D. O'Dell and R. E. Alcouffe, "Transport Calculations for
Nuclear Analyses: Theory and Guidelines for Effective use of Transport
Codes." LA-10983-MS, UC-32, Los Alamos National Laboratory, September
1987 (this report is a revision of the chapter titled "Transport
Calculations for Nuclear Reactors," written by the authors for vol. 1
of the three-volume CRC Handbook of Nuclear Reactor Calculations, Y.
Ronen editor, published by the CRC Press, Boca Raton, FL, 1986)

5. E. E. Lewis and W. F. Miller, Jr., Computational Methods of
Neutron Transport. John Wiley and Sons, Inc., New York, 1984.

6. W. A. Rhoades, D. B. Simpson, R. L. Childs and W. W. Engle, Jr.,
"The DOT-IV Two-Dimensional Ordinates Transport Code with
Space-Dependent Mesh and Quadrature." August 15, 1978.

7. G. L. Simmons and R. Roussin. "RSIC Data Library Collection
(DLC-76) - SAILOR - Coupled, Self-shielded, 47 Neutron, 20 Gamma-Ray,
P_3, Cross Section Library for Light Water Reactors." Radiation
Shielding Information Center, Oak Ridge, TN, 1985.

8. "The ELXSIR Cross-Section Library for LWR Pressure Vessel

Irradiation Studies: Part of the LEPRICON Computer Code System."
Interim Report, NP-3654. Electric Power Research Institute, Palo
Alto, CA, Spetember 1984.

9. M. L. Williams, P. Chowdhury, and B. L. Broadhead, "DOTSYN:
LEPRICON Module for Synthesizing 3-D R-θ-Z Flux Distribution."
Electric Power Research Institute, Palo Alto, CA, (to be published).

10. BWR/6 General Description of a Boiling Water Reactor. General
Electric Company, Nuclear Energy Group, San Jose, CA, September 1980.

11. R. E. Maerker, M. L. Williams and B. L. Broadhead, "Summary
Documentation of Workshop on LWR Pressure Vessel Fluence Calculations
with LEPRICON Code System." Meeting, held at Palo Alto, CA, April
18-19, 1983.

12. M. L. Williams, "DOTSOR: A Module in the LEPRICON Computer Code
System for Representing the Neutron Source Distribution in LWR Cores."
(to be published)

13. R. Paterson, personal communication, 1988.

14. C. Y. Fu and D. T. Ingersoll, "VELM61 and VELM22: Multigroup
Cross Section Libraries for Sodium-Cooled Reactor Shield Analysis."
ORNL/TM-10302, Oak Ridge National Laboratory, April 1987.

15. "Standard Guide for Selection of Neutron Activation Detector
Materials." ASTM Designation: E 419 - 73. Annual Book of ASTM
Standards, December 1973.

16. Documented diagram of the neutron dosimeters obtained from Grand
Gulf Nuclear Power Plant.

17. Glenn F. Knoll, Radiation Detection and Measurement. John Wiley
& Sons, New York, 1979.

APPENDIX A

Absolute calculated neutron flux spectra and DPA rate

The definitions used in the following tables are:

G = energy group

Energy = upper energy in MeV for corresponding group

Group flux = flux in $n.cm^{-2}.s^{-1}$ for corresponding energy group

(Φ_g)

Cumulative flux = summed over the group flux,

in $n.cm^{-2}.s^{-1}$ $(\Sigma\Phi_g)$

$$\Sigma\Phi_G = \sum_{g=1}^{G} \Phi_g$$

Group DPA rate = displacement per atom per second, $DPA.s^{-1}$, for

corresponding group $[(DPA)_g]$

Cumulative DPA rate = summed over the group DPA, in $DPA.s^{-1}$,

$[\Sigma(DPA)_G]$

$$[\Sigma(DPA)_G] = \sum_{g=1}^{G} [(DPA)_g]$$

DPA fraction = the ratio of cumulative DPA rate to total DPA

rate

$$\frac{[\Sigma(DPA)_G]}{\sum\limits_{g=1}^{47} [(DPA)_g]}$$

Table A.1-a Absolute Calculated Neutron Flux Spectra and DPA Rate
at the Center of 3°Surveillance Capsule and Core Axial
Mid-Plane of Grand Gulf Cycle-2

G	Energy (MeV)	Group Flux	Cumulative Flux	Group DPA Rate	Cumulative DPA Rate	DPA Fraction
1	1.733E+01	8.550E+05	8.550E+05	2.498E-15	2.498E-15	1.590E-03
2	1.419E+01	3.545E+06	4.400E+06	9.379E-15	1.188E-14	7.558E-03
3	1.221E+01	1.129E+07	1.569E+07	2.719E-14	3.907E-14	2.486E-02
4	1.000E+01	2.052E+07	3.621E+07	4.554E-14	8.461E-14	5.384E-02
5	8.607E+00	3.166E+07	6.787E+07	6.607E-14	1.507E-13	9.588E-02
6	7.408E+00	7.078E+07	1.386E+08	1.375E-13	2.882E-13	1.834E-01
7	6.065E+00	8.608E+07	2.247E+08	1.536E-13	4.418E-13	2.811E-01
8	4.966E+00	1.209E+08	3.456E+08	1.899E-13	6.317E-13	4.020E-01
9	3.679E+00	7.468E+07	4.203E+08	1.023E-13	7.340E-13	4.671E-01
10	3.012E+00	4.934E+07	4.696E+08	6.271E-14	7.967E-13	5.070E-01
11	2.725E+00	5.386E+07	5.235E+08	6.867E-14	8.654E-13	5.507E-01
12	2.466E+00	2.594E+07	5.494E+08	3.040E-14	8.958E-13	5.700E-01
13	2.365E+00	6.350E+06	5.558E+08	6.960E-15	9.028E-13	5.744E-01
14	2.346E+00	3.160E+07	5.874E+08	3.290E-14	9.357E-13	5.954E-01
15	2.231E+00	8.189E+07	6.693E+08	8.467E-14	1.020E-12	6.492E-01
16	1.920E+00	8.466E+07	7.539E+08	6.886E-14	1.089E-12	6.931E-01
17	1.653E+00	1.129E+08	8.669E+08	9.148E-14	1.181E-12	7.513E-01
18	1.353E+00	1.742E+08	1.041E+09	9.761E-14	1.278E-12	8.134E-01
19	1.003E+00	1.080E+08	1.149E+09	3.957E-14	1.318E-12	8.386E-01
20	8.208E-01	5.251E+07	1.202E+09	2.945E-14	1.347E-12	8.573E-01
21	7.427E-01	1.436E+08	1.345E+09	5.189E-14	1.399E-12	8.903E-01
22	6.081E-01	1.070E+08	1.452E+09	3.148E-14	1.431E-12	9.103E-01
23	4.979E-01	1.219E+08	1.574E+09	4.831E-14	1.479E-12	9.411E-01
24	3.688E-01	1.130E+08	1.687E+09	2.335E-14	1.502E-12	9.559E-01
25	2.972E-01	1.327E+08	1.820E+09	2.661E-14	1.529E-12	9.729E-01
26	1.832E-01	1.172E+08	1.937E+09	1.652E-14	1.545E-12	9.834E-01
27	1.111E-01	7.506E+07	2.012E+09	9.706E-15	1.555E-12	9.896E-01
28	6.738E-02	6.140E+07	2.073E+09	3.977E-15	1.559E-12	9.921E-01
29	4.087E-02	1.926E+07	2.092E+09	1.559E-15	1.561E-12	9.931E-01
30	3.183E-02	6.918E+06	2.099E+09	1.967E-15	1.563E-12	9.943E-01
31	2.606E-02	3.126E+07	2.131E+09	6.302E-16	1.563E-12	9.947E-01
32	2.418E-02	1.582E+07	2.146E+09	6.929E-17	1.563E-12	9.948E-01
33	2.188E-02	3.394E+07	2.180E+09	2.780E-16	1.564E-12	9.949E-01
34	1.503E-02	5.610E+07	2.237E+09	1.052E-15	1.565E-12	9.956E-01
35	7.102E-03	6.681E+07	2.303E+09	5.943E-16	1.565E-12	9.960E-01
36	3.355E-03	5.667E+07	2.360E+09	1.995E-16	1.565E-12	9.961E-01
37	1.585E-03	9.795E+07	2.458E+09	1.647E-16	1.566E-12	9.962E-01
38	4.540E-04	4.904E+07	2.507E+09	4.835E-18	1.566E-12	9.962E-01
39	2.144E-04	5.799E+07	2.565E+09	8.316E-18	1.566E-12	9.962E-01
40	1.013E-04	7.762E+07	2.643E+09	1.732E-17	1.566E-12	9.962E-01
41	3.727E-05	9.402E+07	2.737E+09	3.703E-17	1.566E-12	9.963E-01
42	1.068E-05	5.270E+07	2.789E+09	3.387E-17	1.566E-12	9.963E-01
43	5.043E-06	6.412E+07	2.853E+09	6.412E-17	1.566E-12	9.963E-01
44	1.855E-06	4.158E+07	2.895E+09	6.391E-17	1.566E-12	9.964E-01
45	8.764E-07	3.558E+07	2.931E+09	7.984E-17	1.566E-12	9.964E-01
46	4.140E-07	6.985E+07	3.000E+09	2.866E-16	1.566E-12	9.966E-01
47	1.000E-07	5.249E+08	3.525E+09	5.338E-15	1.572E-12	1.000E+00

Table A.1-b Absolute Calculated Neutron Flux Spectra and DPA Rate
at the Center of 3°Surveillance Capsule and Core Axial
Peak of Grand Gulf Cycle-2

G	Energy (MeV)	Group Flux	Cumulative Flux	Group DPA Rate	Cumulative DPA Rate	DPA Fraction
1	1.733E+01	8.768E+05	8.768E+05	2.562E-15	2.562E-15	1.568E-03
2	1.419E+01	3.640E+06	4.517E+06	9.632E-15	1.219E-14	7.462E-03
3	1.221E+01	1.163E+07	1.615E+07	2.802E-14	4.022E-14	2.461E-02
4	1.000E+01	2.120E+07	3.735E+07	4.704E-14	8.726E-14	5.339E-02
5	8.607E+00	3.277E+07	7.012E+07	6.839E-14	1.556E-13	9.524E-02
6	7.408E+00	7.342E+07	1.435E+08	1.427E-13	2.983E-13	1.825E-01
7	6.065E+00	8.945E+07	2.330E+08	1.596E-13	4.579E-13	2.802E-01
8	4.966E+00	1.258E+08	3.588E+08	1.976E-13	6.555E-13	4.011E-01
9	3.679E+00	7.769E+07	4.364E+08	1.064E-13	7.619E-13	4.662E-01
10	3.012E+00	5.137E+07	4.878E+08	6.529E-14	8.272E-13	5.062E-01
11	2.725E+00	5.609E+07	5.439E+08	7.152E-14	8.987E-13	5.499E-01
12	2.466E+00	2.703E+07	5.709E+08	3.168E-14	9.304E-13	5.693E-01
13	2.365E+00	6.625E+06	5.776E+08	7.261E-15	9.376E-13	5.738E-01
14	2.346E+00	3.294E+07	6.105E+08	3.429E-14	9.719E-13	5.947E-01
15	2.231E+00	8.532E+07	6.958E+08	8.822E-14	1.060E-12	6.487E-01
16	1.920E+00	8.820E+07	7.840E+08	7.173E-14	1.132E-12	6.926E-01
17	1.653E+00	1.176E+08	9.016E+08	9.530E-14	1.227E-12	7.509E-01
18	1.353E+00	1.814E+08	1.083E+09	1.016E-13	1.329E-12	8.131E-01
19	1.003E+00	1.124E+08	1.195E+09	4.120E-14	1.370E-12	8.383E-01
20	8.208E-01	5.468E+07	1.250E+09	3.067E-14	1.401E-12	8.571E-01
21	7.427E-01	1.495E+08	1.400E+09	5.402E-14	1.455E-12	8.902E-01
22	6.081E-01	1.114E+08	1.511E+09	3.277E-14	1.487E-12	9.102E-01
23	4.979E-01	1.269E+08	1.638E+09	5.030E-14	1.538E-12	9.410E-01
24	3.688E-01	1.176E+08	1.755E+09	2.430E-14	1.562E-12	9.559E-01
25	2.972E-01	1.382E+08	1.894E+09	2.770E-14	1.590E-12	9.728E-01
26	1.832E-01	1.220E+08	2.016E+09	1.720E-14	1.607E-12	9.834E-01
27	1.111E-01	7.816E+07	2.094E+09	1.011E-14	1.617E-12	9.895E-01
28	6.738E-02	6.393E+07	2.158E+09	4.141E-15	1.621E-12	9.921E-01
29	4.087E-02	2.005E+07	2.178E+09	1.623E-15	1.623E-12	9.931E-01
30	3.183E-02	7.204E+06	2.185E+09	2.048E-15	1.625E-12	9.943E-01
31	2.606E-02	3.248E+07	2.217E+09	6.547E-16	1.626E-12	9.947E-01
32	2.418E-02	1.647E+07	2.234E+09	7.214E-17	1.626E-12	9.948E-01
33	2.188E-02	3.534E+07	2.269E+09	2.895E-16	1.626E-12	9.949E-01
34	1.503E-02	5.841E+07	2.328E+09	1.096E-15	1.627E-12	9.956E-01
35	7.102E-03	6.957E+07	2.397E+09	6.189E-16	1.628E-12	9.960E-01
36	3.355E-03	5.902E+07	2.456E+09	2.077E-16	1.628E-12	9.961E-01
37	1.585E-03	1.020E+08	2.558E+09	1.716E-16	1.628E-12	9.962E-01
38	4.540E-04	5.108E+07	2.609E+09	5.036E-18	1.628E-12	9.962E-01
39	2.144E-04	6.040E+07	2.670E+09	8.662E-18	1.628E-12	9.962E-01
40	1.013E-04	8.085E+07	2.751E+09	1.804E-17	1.628E-12	9.962E-01
41	3.727E-05	9.794E+07	2.849E+09	3.858E-17	1.628E-12	9.963E-01
42	1.068E-05	5.491E+07	2.903E+09	3.529E-17	1.628E-12	9.963E-01
43	5.043E-06	6.680E+07	2.970E+09	6.680E-17	1.628E-12	9.963E-01
44	1.855E-06	4.332E+07	3.014E+09	6.659E-17	1.628E-12	9.964E-01
45	8.764E-07	3.707E+07	3.051E+09	8.319E-17	1.628E-12	9.964E-01
46	4.140E-07	7.278E+07	3.123E+09	2.986E-16	1.629E-12	9.966E-01
47	1.000E-07	5.476E+08	3.671E+09	5.569E-15	1.634E-12	1.000E+00

Table A.2-a Absolute Calculated Neutron Flux Spectra and DPA Rate
            at the Axial Mid-Plane, Azimuthal Peak and RPV Wetted
            Surface Wall of Grand Gulf Cycle-2

G	Energy (MeV)	Group Flux	Cumulative Flux	Group DPA Rate	Cumulative DPA Rate	DPA Fraction
1	1.733E+01	1.310E+06	1.310E+06	3.827E-15	3.827E-15	1.428E-03
2	1.419E+01	5.449E+06	6.758E+06	1.442E-14	1.824E-14	6.807E-03
3	1.221E+01	1.855E+07	2.531E+07	4.469E-14	6.293E-14	2.348E-02
4	1.000E+01	3.450E+07	5.980E+07	7.655E-14	1.395E-13	5.204E-02
5	8.607E+00	5.475E+07	1.146E+08	1.143E-13	2.538E-13	9.468E-02
6	7.408E+00	1.245E+08	2.390E+08	2.419E-13	4.956E-13	1.849E-01
7	6.065E+00	1.543E+08	3.933E+08	2.753E-13	7.709E-13	2.876E-01
8	4.966E+00	2.214E+08	6.148E+08	3.479E-13	1.119E-12	4.174E-01
9	3.679E+00	1.351E+08	7.499E+08	1.851E-13	1.304E-12	4.865E-01
10	3.012E+00	8.815E+07	8.380E+08	1.120E-13	1.416E-12	5.283E-01
11	2.725E+00	9.464E+07	9.327E+08	1.207E-13	1.537E-12	5.733E-01
12	2.466E+00	4.552E+07	9.782E+08	5.334E-14	1.590E-12	5.932E-01
13	2.365E+00	1.114E+07	9.893E+08	1.221E-14	1.602E-12	5.978E-01
14	2.346E+00	5.399E+07	1.043E+09	5.621E-14	1.658E-12	6.187E-01
15	2.231E+00	1.338E+08	1.177E+09	1.383E-13	1.797E-12	6.703E-01
16	1.920E+00	1.344E+08	1.312E+09	1.093E-13	1.906E-12	7.111E-01
17	1.653E+00	1.761E+08	1.488E+09	1.427E-13	2.049E-12	7.644E-01
18	1.353E+00	2.614E+08	1.749E+09	1.464E-13	2.195E-12	8.190E-01
19	1.003E+00	1.640E+08	1.913E+09	6.011E-14	2.255E-12	8.414E-01
20	8.208E-01	8.400E+07	1.997E+09	4.712E-14	2.302E-12	8.590E-01
21	7.427E-01	2.096E+08	2.207E+09	7.576E-14	2.378E-12	8.873E-01
22	6.081E-01	1.641E+08	2.371E+09	4.829E-14	2.426E-12	9.053E-01
23	4.979E-01	1.861E+08	2.557E+09	7.376E-14	2.500E-12	9.328E-01
24	3.688E-01	1.691E+08	2.726E+09	3.494E-14	2.535E-12	9.459E-01
25	2.972E-01	2.216E+08	2.948E+09	4.444E-14	2.580E-12	9.624E-01
26	1.832E-01	1.880E+08	3.136E+09	2.650E-14	2.606E-12	9.723E-01
27	1.111E-01	1.356E+08	3.271E+09	1.753E-14	2.624E-12	9.789E-01
28	6.738E-02	1.148E+08	3.386E+09	7.436E-15	2.631E-12	9.816E-01
29	4.087E-02	4.666E+07	3.433E+09	3.776E-15	2.635E-12	9.831E-01
30	3.183E-02	3.210E+07	3.465E+09	9.127E-15	2.644E-12	9.865E-01
31	2.606E-02	3.725E+07	3.502E+09	7.510E-16	2.645E-12	9.867E-01
32	2.418E-02	2.292E+07	3.525E+09	1.004E-16	2.645E-12	9.868E-01
33	2.188E-02	6.198E+07	3.587E+09	5.076E-16	2.645E-12	9.870E-01
34	1.503E-02	1.218E+08	3.709E+09	2.284E-15	2.648E-12	9.878E-01
35	7.102E-03	1.270E+08	3.836E+09	1.130E-15	2.649E-12	9.882E-01
36	3.355E-03	1.206E+08	3.956E+09	4.246E-16	2.649E-12	9.884E-01
37	1.585E-03	1.997E+08	4.156E+09	3.359E-16	2.649E-12	9.885E-01
38	4.540E-04	1.153E+08	4.271E+09	1.137E-17	2.649E-12	9.885E-01
39	2.144E-04	1.194E+08	4.391E+09	1.713E-17	2.649E-12	9.885E-01
40	1.013E-04	1.587E+08	4.549E+09	3.542E-17	2.650E-12	9.885E-01
41	3.727E-05	1.961E+08	4.746E+09	7.723E-17	2.650E-12	9.886E-01
42	1.068E-05	1.151E+08	4.861E+09	7.396E-17	2.650E-12	9.886E-01
43	5.043E-06	1.486E+08	5.009E+09	1.486E-16	2.650E-12	9.887E-01
44	1.855E-06	1.064E+08	5.116E+09	1.635E-16	2.650E-12	9.887E-01
45	8.764E-07	1.013E+08	5.217E+09	2.273E-16	2.650E-12	9.888E-01
46	4.140E-07	3.027E+08	5.520E+09	1.242E-15	2.651E-12	9.893E-01
47	1.000E-07	2.828E+09	8.347E+09	2.876E-14	2.680E-12	1.000E+00

Table A.2-b Absolute Calculated Neutron Flux Spectra and DPA Rate
at the Axial Mid-Plane, Azimuthal Peak and R = O-T RPV
Wall of Grand Gulf Cycle-2

G	Energy (MeV)	Group Flux	Cumulative Flux	Group DPA Rate	Cumulative DPA Rate	DPA Fraction
1	1.733E+01	1.240E+06	1.240E+06	3.624E-15	3.624E-15	1.386E-03
2	1.419E+01	5.164E+06	6.404E+06	1.366E-14	1.729E-14	6.611E-03
3	1.221E+01	1.750E+07	2.390E+07	4.215E-14	5.944E-14	2.273E-02
4	1.000E+01	3.255E+07	5.646E+07	7.223E-14	1.317E-13	5.036E-02
5	8.607E+00	5.164E+07	1.081E+08	1.078E-13	2.394E-13	9.157E-02
6	7.408E+00	1.173E+08	2.254E+08	2.280E-13	4.674E-13	1.788E-01
7	6.065E+00	1.455E+08	3.710E+08	2.596E-13	7.271E-13	2.780E-01
8	4.966E+00	2.095E+08	5.805E+08	3.291E-13	1.056E-12	4.039E-01
9	3.679E+00	1.286E+08	7.091E+08	1.762E-13	1.232E-12	4.713E-01
10	3.012E+00	8.473E+07	7.938E+08	1.077E-13	1.340E-12	5.125E-01
11	2.725E+00	9.157E+07	8.854E+08	1.168E-13	1.457E-12	5.571E-01
12	2.466E+00	4.422E+07	9.296E+08	5.182E-14	1.509E-12	5.770E-01
13	2.365E+00	1.085E+07	9.405E+08	1.189E-14	1.521E-12	5.815E-01
14	2.346E+00	5.294E+07	9.934E+08	5.511E-14	1.576E-12	6.026E-01
15	2.231E+00	1.330E+08	1.126E+09	1.375E-13	1.713E-12	6.552E-01
16	1.920E+00	1.351E+08	1.262E+09	1.099E-13	1.823E-12	6.972E-01
17	1.653E+00	1.789E+08	1.440E+09	1.449E-13	1.968E-12	7.526E-01
18	1.353E+00	2.719E+08	1.712E+09	1.523E-13	2.120E-12	8.109E-01
19	1.003E+00	1.710E+08	1.883E+09	6.266E-14	2.183E-12	8.348E-01
20	8.208E-01	8.601E+07	1.969E+09	4.824E-14	2.231E-12	8.533E-01
21	7.427E-01	2.259E+08	2.195E+09	8.165E-14	2.313E-12	8.845E-01
22	6.081E-01	1.736E+08	2.369E+09	5.108E-14	2.364E-12	9.040E-01
23	4.979E-01	1.981E+08	2.567E+09	7.853E-14	2.443E-12	9.341E-01
24	3.688E-01	1.828E+08	2.750E+09	3.779E-14	2.480E-12	9.485E-01
25	2.972E-01	2.255E+08	2.975E+09	4.522E-14	2.526E-12	9.658E-01
26	1.832E-01	1.928E+08	3.168E+09	2.719E-14	2.553E-12	9.762E-01
27	1.111E-01	1.330E+08	3.301E+09	1.720E-14	2.570E-12	9.828E-01
28	6.738E-02	1.117E+08	3.413E+09	7.234E-15	2.577E-12	9.856E-01
29	4.087E-02	4.265E+07	3.455E+09	3.452E-15	2.581E-12	9.869E-01
30	3.183E-02	2.665E+07	3.482E+09	7.578E-15	2.588E-12	9.898E-01
31	2.606E-02	4.367E+07	3.526E+09	8.804E-16	2.589E-12	9.901E-01
32	2.418E-02	2.356E+07	3.549E+09	1.032E-16	2.589E-12	9.902E-01
33	2.188E-02	5.710E+07	3.606E+09	4.677E-16	2.590E-12	9.903E-01
34	1.503E-02	1.119E+08	3.718E+09	2.100E-15	2.592E-12	9.911E-01
35	7.102E-03	1.219E+08	3.840E+09	1.084E-15	2.593E-12	9.916E-01
36	3.355E-03	1.133E+08	3.954E+09	3.990E-16	2.593E-12	9.917E-01
37	1.585E-03	1.899E+08	4.143E+09	3.193E-16	2.594E-12	9.918E-01
38	4.540E-04	1.067E+08	4.250E+09	1.052E-17	2.594E-12	9.918E-01
39	2.144E-04	1.136E+08	4.364E+09	1.629E-17	2.594E-12	9.918E-01
40	1.013E-04	1.512E+08	4.515E+09	3.374E-17	2.594E-12	9.918E-01
41	3.727E-05	1.859E+08	4.701E+09	7.322E-17	2.594E-12	9.919E-01
42	1.068E-05	1.079E+08	4.809E+09	6.933E-17	2.594E-12	9.919E-01
43	5.043E-06	1.373E+08	4.946E+09	1.373E-16	2.594E-12	9.920E-01
44	1.855E-06	9.620E+07	5.042E+09	1.479E-16	2.594E-12	9.920E-01
45	8.764E-07	8.963E+07	5.132E+09	2.011E-16	2.594E-12	9.921E-01
46	4.140E-07	2.435E+08	5.375E+09	9.989E-16	2.595E-12	9.925E-01
47	1.000E-07	1.936E+09	7.311E+09	1.969E-14	2.615E-12	1.000E+00

Table A.2-c   Absolute Calculated Neutron Flux Spectra and DPA Rate
at the Axial Mid-Plane, Azimuthal Peak and R = 1/4-T RPV
Wall of Grand Gulf Cycle-2

G	Energy (MeV)	Group Flux	Cumulative Flux	Group DPA Rate	Cumulative DPA Rate	DPA Fraction
1	1.733E+01	6.868E+05	6.868E+05	2.007E-15	2.007E-15	1.092E-03
2	1.419E+01	2.865E+06	3.551E+06	7.580E-15	9.587E-15	5.214E-03
3	1.221E+01	9.423E+06	1.297E+07	2.270E-14	3.229E-14	1.756E-02
4	1.000E+01	1.773E+07	3.071E+07	3.935E-14	7.164E-14	3.897E-02
5	8.607E+00	2.787E+07	5.858E+07	5.817E-14	1.298E-13	7.061E-02
6	7.408E+00	6.187E+07	1.205E+08	1.202E-13	2.500E-13	1.360E-01
7	6.065E+00	7.555E+07	1.960E+08	1.348E-13	3.848E-13	2.093E-01
8	4.966E+00	1.081E+08	3.041E+08	1.699E-13	5.547E-13	3.017E-01
9	3.679E+00	6.924E+07	3.734E+08	9.487E-14	6.496E-13	3.533E-01
10	3.012E+00	4.836E+07	4.217E+08	6.147E-14	7.110E-13	3.868E-01
11	2.725E+00	5.502E+07	4.768E+08	7.015E-14	7.812E-13	4.249E-01
12	2.466E+00	2.733E+07	5.041E+08	3.203E-14	8.132E-13	4.423E-01
13	2.365E+00	7.102E+06	5.112E+08	7.783E-15	8.210E-13	4.466E-01
14	2.346E+00	3.532E+07	5.465E+08	3.677E-14	8.578E-13	4.666E-01
15	2.231E+00	9.446E+07	6.410E+08	9.767E-14	9.554E-13	5.197E-01
16	1.920E+00	1.049E+08	7.459E+08	8.534E-14	1.041E-12	5.661E-01
17	1.653E+00	1.475E+08	8.934E+08	1.195E-13	1.160E-12	6.311E-01
18	1.353E+00	2.595E+08	1.153E+09	1.454E-13	1.306E-12	7.102E-01
19	1.003E+00	1.727E+08	1.326E+09	6.330E-14	1.369E-12	7.446E-01
20	8.208E-01	8.155E+07	1.407E+09	4.574E-14	1.415E-12	7.695E-01
21	7.427E-01	2.727E+08	1.680E+09	9.857E-14	1.513E-12	8.231E-01
22	6.081E-01	2.040E+08	1.884E+09	6.004E-14	1.573E-12	8.558E-01
23	4.979E-01	2.431E+08	2.127E+09	9.635E-14	1.670E-12	9.082E-01
24	3.688E-01	2.453E+08	2.372E+09	5.071E-14	1.720E-12	9.358E-01
25	2.972E-01	2.533E+08	2.626E+09	5.078E-14	1.771E-12	9.634E-01
26	1.832E-01	2.318E+08	2.857E+09	3.269E-14	1.804E-12	9.812E-01
27	1.111E-01	1.335E+08	2.991E+09	1.726E-14	1.821E-12	9.906E-01
28	6.738E-02	1.033E+08	3.094E+09	6.691E-15	1.828E-12	9.942E-01
29	4.087E-02	2.766E+07	3.122E+09	2.238E-15	1.830E-12	9.954E-01
30	3.183E-02	9.654E+06	3.132E+09	2.745E-15	1.833E-12	9.969E-01
31	2.606E-02	5.720E+07	3.189E+09	1.153E-15	1.834E-12	9.976E-01
32	2.418E-02	2.941E+07	3.218E+09	1.288E-16	1.834E-12	9.976E-01
33	2.188E-02	5.062E+07	3.269E+09	4.146E-16	1.835E-12	9.979E-01
34	1.503E-02	6.866E+07	3.337E+09	1.288E-15	1.836E-12	9.986E-01
35	7.102E-03	8.967E+07	3.427E+09	7.976E-16	1.837E-12	9.990E-01
36	3.355E-03	6.809E+07	3.495E+09	2.397E-16	1.837E-12	9.991E-01
37	1.585E-03	1.181E+08	3.613E+09	1.986E-16	1.837E-12	9.992E-01
38	4.540E-04	5.241E+07	3.666E+09	5.166E-18	1.837E-12	9.992E-01
39	2.144E-04	6.468E+07	3.730E+09	9.275E-18	1.837E-12	9.992E-01
40	1.013E-04	8.915E+07	3.820E+09	1.989E-17	1.837E-12	9.992E-01
41	3.727E-05	1.067E+08	3.926E+09	4.204E-17	1.837E-12	9.993E-01
42	1.068E-05	5.698E+07	3.983E+09	3.662E-17	1.837E-12	9.993E-01
43	5.043E-06	6.319E+07	4.046E+09	6.319E-17	1.837E-12	9.993E-01
44	1.855E-06	3.596E+07	4.082E+09	5.527E-17	1.837E-12	9.993E-01
45	8.764E-07	2.608E+07	4.108E+09	5.853E-17	1.837E-12	9.994E-01
46	4.140E-07	2.771E+07	4.136E+09	1.137E-16	1.837E-12	9.994E-01
47	1.000E-07	1.012E+08	4.237E+09	1.030E-15	1.838E-12	1.000E+00

Table A.2-d Absolute Calculated Neutron Flux Spectra and DPA Rate
at the Axial Mid-Plane, Azimuthal Peak and R = 3/4-T RPV
Wall of Grand Gulf Cycle-2

G	Energy (MeV)	Group Flux	Cumulative Flux	Group DPA Rate	Cumulative DPA Rate	DPA Fraction
1	1.733E+01	1.913E+05	1.913E+05	5.591E-16	5.591E-16	7.635E-04
2	1.419E+01	7.851E+05	9.764E+05	2.077E-15	2.636E-15	3.600E-03
3	1.221E+01	2.455E+06	3.431E+06	5.914E-15	8.550E-15	1.168E-02
4	1.000E+01	4.593E+06	8.024E+06	1.019E-14	1.874E-14	2.560E-02
5	8.607E+00	6.952E+06	1.498E+07	1.451E-14	3.325E-14	4.541E-02
6	7.408E+00	1.438E+07	2.936E+07	2.795E-14	6.120E-14	8.358E-02
7	6.065E+00	1.710E+07	4.646E+07	3.050E-14	9.170E-14	1.252E-01
8	4.966E+00	2.455E+07	7.101E+07	3.857E-14	1.303E-13	1.779E-01
9	3.679E+00	1.697E+07	8.798E+07	2.325E-14	1.535E-13	2.097E-01
10	3.012E+00	1.236E+07	1.003E+08	1.571E-14	1.692E-13	2.311E-01
11	2.725E+00	1.479E+07	1.151E+08	1.886E-14	1.881E-13	2.569E-01
12	2.466E+00	7.570E+06	1.227E+08	8.873E-15	1.970E-13	2.690E-01
13	2.365E+00	2.125E+06	1.248E+08	2.329E-15	1.993E-13	2.722E-01
14	2.346E+00	1.075E+07	1.356E+08	1.119E-14	2.105E-13	2.875E-01
15	2.231E+00	3.016E+07	1.657E+08	3.118E-14	2.417E-13	3.300E-01
16	1.920E+00	3.775E+07	2.035E+08	3.070E-14	2.724E-13	3.720E-01
17	1.653E+00	5.700E+07	2.605E+08	4.619E-14	3.185E-13	4.350E-01
18	1.353E+00	1.215E+08	3.820E+08	6.810E-14	3.866E-13	5.281E-01
19	1.003E+00	9.228E+07	4.743E+08	3.382E-14	4.205E-13	5.742E-01
20	8.208E-01	4.193E+07	5.162E+08	2.352E-14	4.440E-13	6.064E-01
21	7.427E-01	1.727E+08	6.890E+08	6.243E-14	5.064E-13	6.916E-01
22	6.081E-01	1.346E+08	8.236E+08	3.963E-14	5.460E-13	7.457E-01
23	4.979E-01	1.635E+08	9.871E+08	6.481E-14	6.109E-13	8.343E-01
24	3.688E-01	1.851E+08	1.172E+09	3.826E-14	6.491E-13	8.865E-01
25	2.972E-01	1.810E+08	1.353E+09	3.630E-14	6.854E-13	9.361E-01
26	1.832E-01	1.755E+08	1.529E+09	2.475E-14	7.102E-13	9.699E-01
27	1.111E-01	9.426E+07	1.623E+09	1.219E-14	7.223E-13	9.865E-01
28	6.738E-02	6.657E+07	1.690E+09	4.312E-15	7.267E-13	9.924E-01
29	4.087E-02	1.634E+07	1.706E+09	1.323E-15	7.280E-13	9.942E-01
30	3.183E-02	5.653E+06	1.712E+09	1.607E-15	7.296E-13	9.964E-01
31	2.606E-02	4.174E+07	1.753E+09	8.415E-16	7.304E-13	9.976E-01
32	2.418E-02	2.248E+07	1.776E+09	9.843E-17	7.305E-13	9.977E-01
33	2.188E-02	3.434E+07	1.810E+09	2.812E-16	7.308E-13	9.981E-01
34	1.503E-02	3.558E+07	1.846E+09	6.674E-16	7.315E-13	9.990E-01
35	7.102E-03	4.552E+07	1.891E+09	4.049E-16	7.319E-13	9.995E-01
36	3.355E-03	3.161E+07	1.923E+09	1.113E-16	7.320E-13	9.997E-01
37	1.585E-03	5.132E+07	1.974E+09	8.632E-17	7.321E-13	9.998E-01
38	4.540E-04	2.134E+07	1.996E+09	2.104E-18	7.321E-13	9.998E-01
39	2.144E-04	2.491E+07	2.020E+09	3.573E-18	7.321E-13	9.998E-01
40	1.013E-04	3.357E+07	2.054E+09	7.489E-18	7.321E-13	9.998E-01
41	3.727E-05	3.887E+07	2.093E+09	1.531E-17	7.321E-13	9.998E-01
42	1.068E-05	1.977E+07	2.113E+09	1.271E-17	7.321E-13	9.999E-01
43	5.043E-06	1.977E+07	2.132E+09	1.977E-17	7.321E-13	9.999E-01
44	1.855E-06	9.857E+06	2.142E+09	1.515E-17	7.322E-13	9.999E-01
45	8.764E-07	5.950E+06	2.148E+09	1.335E-17	7.322E-13	9.999E-01
46	4.140E-07	3.437E+06	2.152E+09	1.410E-17	7.322E-13	1.000E+00
47	1.000E-07	3.587E+06	2.155E+09	3.648E-17	7.322E-13	1.000E+00

Table A.2-e Absolute Calculated Neutron Flux Spectra and DPA Rate
at the Axial Mid-Plane, Azimuthal Peak and R = Mid-Cavity
of Grand Gulf Cycle-2

G	Energy (MeV)	Group Flux	Cumulative Flux	Group DPA Rate	Cumulative DPA Rate	DPA Fraction
1	1.733E+01	6.942E+04	6.942E+04	2.028E-16	2.028E-16	9.108E-04
2	1.419E+01	2.720E+05	3.414E+05	7.197E-16	9.226E-16	4.143E-03
3	1.221E+01	8.229E+05	1.164E+06	1.982E-15	2.905E-15	1.304E-02
4	1.000E+01	1.499E+06	2.664E+06	3.327E-15	6.232E-15	2.798E-02
5	8.607E+00	2.180E+06	4.844E+06	4.550E-15	1.078E-14	4.842E-02
6	7.408E+00	4.312E+06	9.156E+06	8.378E-15	1.916E-14	8.603E-02
7	6.065E+00	4.982E+06	1.414E+07	8.889E-15	2.805E-14	1.259E-01
8	4.966E+00	6.965E+06	2.110E+07	1.094E-14	3.899E-14	1.751E-01
9	3.679E+00	4.691E+06	2.579E+07	6.426E-15	4.542E-14	2.039E-01
10	3.012E+00	3.383E+06	2.918E+07	4.299E-15	4.972E-14	2.232E-01
11	2.725E+00	4.008E+06	3.318E+07	5.110E-15	5.483E-14	2.462E-01
12	2.466E+00	2.097E+06	3.528E+07	2.458E-15	5.729E-14	2.572E-01
13	2.365E+00	5.927E+05	3.587E+07	6.496E-16	5.794E-14	2.601E-01
14	2.346E+00	2.930E+06	3.881E+07	3.050E-15	6.099E-14	2.738E-01
15	2.231E+00	7.717E+06	4.652E+07	7.979E-15	6.896E-14	3.097E-01
16	1.920E+00	9.972E+06	5.649E+07	8.110E-15	7.707E-14	3.461E-01
17	1.653E+00	1.553E+07	7.202E+07	1.258E-14	8.966E-14	4.026E-01
18	1.353E+00	3.359E+07	1.056E+08	1.882E-14	1.085E-13	4.871E-01
19	1.003E+00	2.725E+07	1.329E+08	9.987E-15	1.185E-13	5.319E-01
20	8.208E-01	1.393E+07	1.468E+08	7.812E-15	1.263E-13	5.670E-01
21	7.427E-01	4.885E+07	1.956E+08	1.765E-14	1.439E-13	6.463E-01
22	6.081E-01	4.272E+07	2.384E+08	1.257E-14	1.565E-13	7.027E-01
23	4.979E-01	4.611E+07	2.845E+08	1.828E-14	1.748E-13	7.848E-01
24	3.688E-01	5.622E+07	3.407E+08	1.162E-14	1.864E-13	8.370E-01
25	2.972E-01	7.346E+07	4.141E+08	1.473E-14	2.011E-13	9.031E-01
26	1.832E-01	6.641E+07	4.805E+08	9.364E-15	2.105E-13	9.451E-01
27	1.111E-01	4.041E+07	5.210E+08	5.225E-15	2.157E-13	9.686E-01
28	6.738E-02	2.855E+07	5.495E+08	1.849E-15	2.176E-13	9.769E-01
29	4.087E-02	8.831E+06	5.583E+08	7.147E-16	2.183E-13	9.801E-01
30	3.183E-02	8.130E+06	5.665E+08	2.311E-15	2.206E-13	9.905E-01
31	2.606E-02	1.490E+07	5.814E+08	3.004E-16	2.209E-13	9.918E-01
32	2.418E-02	9.187E+06	5.905E+08	4.023E-17	2.209E-13	9.920E-01
33	2.188E-02	1.915E+07	6.097E+08	1.568E-16	2.211E-13	9.927E-01
34	1.503E-02	2.495E+07	6.346E+08	4.680E-16	2.216E-13	9.948E-01
35	7.102E-03	2.392E+07	6.586E+08	2.128E-16	2.218E-13	9.958E-01
36	3.355E-03	2.036E+07	6.789E+08	7.167E-17	2.218E-13	9.961E-01
37	1.585E-03	3.166E+07	7.106E+08	5.326E-17	2.219E-13	9.963E-01
38	4.540E-04	1.660E+07	7.272E+08	1.637E-18	2.219E-13	9.963E-01
39	2.144E-04	1.615E+07	7.433E+08	2.315E-18	2.219E-13	9.963E-01
40	1.013E-04	2.025E+07	7.636E+08	4.517E-18	2.219E-13	9.964E-01
41	3.727E-05	2.321E+07	7.868E+08	9.143E-18	2.219E-13	9.964E-01
42	1.068E-05	1.276E+07	7.995E+08	8.203E-18	2.219E-13	9.964E-01
43	5.043E-06	1.530E+07	8.148E+08	1.530E-17	2.219E-13	9.965E-01
44	1.855E-06	1.020E+07	8.250E+08	1.568E-17	2.219E-13	9.966E-01
45	8.764E-07	9.079E+06	8.341E+08	2.037E-17	2.220E-13	9.967E-01
46	4.140E-07	1.931E+07	8.534E+08	7.921E-17	2.220E-13	9.970E-01
47	1.000E-07	6.501E+07	9.184E+08	6.612E-16	2.227E-13	1.000E+00

Table A.2-f Absolute Calculated Neutron Flux Spectra and DPA Rate
at the Axial Mid-Plane, Azimuthal Peak and R = Front of
the Concrete Shield Wall of Grand Gulf Cycle-2

G	Energy (MeV)	Group Flux	Cumulative Flux	Group DPA Rate	Cumulative DPA Rate	DPA Fraction
1	1.733E+01	4.366E+04	4.366E+04	1.276E-16	1.276E-16	7.413E-04
2	1.419E+01	1.772E+05	2.209E+05	4.689E-16	5.965E-16	3.466E-03
3	1.221E+01	5.485E+05	7.694E+05	1.321E-15	1.918E-15	1.114E-02
4	1.000E+01	1.018E+06	1.787E+06	2.259E-15	4.176E-15	2.427E-02
5	8.607E+00	1.521E+06	3.308E+06	3.174E-15	7.351E-15	4.271E-02
6	7.408E+00	3.111E+06	6.419E+06	6.045E-15	1.340E-14	7.784E-02
7	6.065E+00	3.778E+06	1.020E+07	6.740E-15	2.014E-14	1.170E-01
8	4.966E+00	5.542E+06	1.574E+07	8.707E-15	2.884E-14	1.676E-01
9	3.679E+00	3.801E+06	1.954E+07	5.208E-15	3.405E-14	1.978E-01
10	3.012E+00	2.753E+06	2.229E+07	3.498E-15	3.755E-14	2.182E-01
11	2.725E+00	3.309E+06	2.560E+07	4.220E-15	4.177E-14	2.427E-01
12	2.466E+00	1.781E+06	2.738E+07	2.087E-15	4.386E-14	2.548E-01
13	2.365E+00	4.926E+05	2.788E+07	5.399E-16	4.440E-14	2.580E-01
14	2.346E+00	2.377E+06	3.025E+07	2.474E-15	4.687E-14	2.723E-01
15	2.231E+00	5.784E+06	3.604E+07	5.981E-15	5.285E-14	3.071E-01
16	1.920E+00	7.366E+06	4.340E+07	5.990E-15	5.884E-14	3.419E-01
17	1.653E+00	1.158E+07	5.498E+07	9.379E-15	6.822E-14	3.964E-01
18	1.353E+00	2.346E+07	7.843E+07	1.314E-14	8.136E-14	4.727E-01
19	1.003E+00	1.856E+07	9.699E+07	6.801E-15	8.816E-14	5.123E-01
20	8.208E-01	1.181E+07	1.088E+08	6.627E-15	9.479E-14	5.508E-01
21	7.427E-01	3.399E+07	1.428E+08	1.228E-14	1.071E-13	6.221E-01
22	6.081E-01	3.314E+07	1.759E+08	9.754E-15	1.168E-13	6.788E-01
23	4.979E-01	3.369E+07	2.096E+08	1.335E-14	1.302E-13	7.564E-01
24	3.688E-01	3.827E+07	2.479E+08	7.910E-15	1.381E-13	8.024E-01
25	2.972E-01	6.168E+07	3.096E+08	1.237E-14	1.505E-13	8.742E-01
26	1.832E-01	5.860E+07	3.682E+08	8.263E-15	1.587E-13	9.222E-01
27	1.111E-01	3.955E+07	4.077E+08	5.114E-15	1.638E-13	9.519E-01
28	6.738E-02	3.056E+07	4.383E+08	1.979E-15	1.658E-13	9.634E-01
29	4.087E-02	1.140E+07	4.497E+08	9.226E-16	1.667E-13	9.688E-01
30	3.183E-02	9.432E+06	4.591E+08	2.682E-15	1.694E-13	9.844E-01
31	2.606E-02	8.181E+06	4.673E+08	1.649E-16	1.696E-13	9.853E-01
32	2.418E-02	7.369E+06	4.747E+08	3.227E-17	1.696E-13	9.855E-01
33	2.188E-02	2.023E+07	4.949E+08	1.657E-16	1.698E-13	9.865E-01
34	1.503E-02	3.038E+07	5.253E+08	5.699E-16	1.704E-13	9.898E-01
35	7.102E-03	2.744E+07	5.527E+08	2.441E-16	1.706E-13	9.912E-01
36	3.355E-03	2.449E+07	5.772E+08	8.621E-17	1.707E-13	9.917E-01
37	1.585E-03	3.769E+07	6.149E+08	6.339E-17	1.707E-13	9.921E-01
38	4.540E-04	2.024E+07	6.351E+08	1.995E-18	1.707E-13	9.921E-01
39	2.144E-04	1.922E+07	6.544E+08	2.757E-18	1.708E-13	9.921E-01
40	1.013E-04	2.402E+07	6.784E+08	5.359E-18	1.708E-13	9.922E-01
41	3.727E-05	2.764E+07	7.060E+08	1.089E-17	1.708E-13	9.922E-01
42	1.068E-05	1.541E+07	7.214E+08	9.902E-18	1.708E-13	9.923E-01
43	5.043E-06	1.889E+07	7.403E+08	1.889E-17	1.708E-13	9.924E-01
44	1.855E-06	1.297E+07	7.533E+08	1.994E-17	1.708E-13	9.925E-01
45	8.764E-07	1.189E+07	7.652E+08	2.668E-17	1.708E-13	9.927E-01
46	4.140E-07	2.786E+07	7.930E+08	1.143E-16	1.710E-13	9.933E-01
47	1.000E-07	1.131E+08	9.061E+08	1.150E-15	1.721E-13	1.000E+00

Table A.2-g Absolute Calculated Neutron Flux Spectra and DPA Rate
at the Axial Mid-Plane, Azimuthal Peak and R = 6" in
the Concrete Shield Wall of Grand Gulf Cycle-2

G	Energy (MeV)	Group Flux	Cumulative Flux	Group DPA Rate	Cumulative DPA Rate	DPA Fraction
1	1.733E+01	3.375E+03	3.375E+03	9.863E-18	9.863E-18	7.708E-04
2	1.419E+01	1.531E+04	1.869E+04	4.051E-17	5.038E-17	3.937E-03
3	1.221E+01	4.525E+04	6.394E+04	1.090E-16	1.594E-16	1.246E-02
4	1.000E+01	8.996E+04	1.539E+05	1.996E-16	3.590E-16	2.806E-02
5	8.607E+00	1.373E+05	2.912E+05	2.866E-16	6.456E-16	5.046E-02
6	7.408E+00	3.491E+05	6.403E+05	6.782E-16	1.324E-15	1.035E-01
7	6.065E+00	4.643E+05	1.105E+06	8.283E-16	2.152E-15	1.682E-01
8	4.966E+00	6.929E+05	1.797E+06	1.089E-15	3.241E-15	2.533E-01
9	3.679E+00	4.427E+05	2.240E+06	6.065E-16	3.847E-15	3.007E-01
10	3.012E+00	3.785E+05	2.619E+06	4.811E-16	4.328E-15	3.383E-01
11	2.725E+00	4.662E+05	3.085E+06	5.944E-16	4.923E-15	3.847E-01
12	2.466E+00	3.179E+05	3.403E+06	3.725E-16	5.295E-15	4.139E-01
13	2.365E+00	1.014E+05	3.504E+06	1.111E-16	5.406E-15	4.226E-01
14	2.346E+00	4.127E+05	3.917E+06	4.297E-16	5.836E-15	4.561E-01
15	2.231E+00	6.803E+05	4.597E+06	7.034E-16	6.539E-15	5.111E-01
16	1.920E+00	6.529E+05	5.250E+06	5.310E-16	7.070E-15	5.526E-01
17	1.653E+00	8.438E+05	6.094E+06	6.838E-16	7.754E-15	6.061E-01
18	1.353E+00	1.036E+06	7.130E+06	5.804E-16	8.335E-15	6.514E-01
19	1.003E+00	6.168E+05	7.747E+06	2.261E-16	8.561E-15	6.691E-01
20	8.208E-01	5.043E+05	8.251E+06	2.829E-16	8.844E-15	6.912E-01
21	7.427E-01	1.033E+06	9.284E+06	3.734E-16	9.217E-15	7.204E-01
22	6.081E-01	1.046E+06	1.033E+07	3.078E-16	9.525E-15	7.444E-01
23	4.979E-01	8.786E+05	1.121E+07	3.483E-16	9.873E-15	7.717E-01
24	3.688E-01	7.993E+05	1.201E+07	1.652E-16	1.004E-14	7.846E-01
25	2.972E-01	1.650E+06	1.366E+07	3.308E-16	1.037E-14	8.104E-01
26	1.832E-01	1.971E+06	1.563E+07	2.779E-16	1.065E-14	8.321E-01
27	1.111E-01	1.725E+06	1.735E+07	2.231E-16	1.087E-14	8.496E-01
28	6.738E-02	1.656E+06	1.901E+07	1.072E-16	1.098E-14	8.580E-01
29	4.087E-02	7.480E+05	1.976E+07	6.054E-17	1.104E-14	8.627E-01
30	3.183E-02	6.540E+05	2.041E+07	1.859E-16	1.122E-14	8.772E-01
31	2.606E-02	2.459E+05	2.066E+07	4.957E-18	1.123E-14	8.776E-01
32	2.418E-02	3.215E+05	2.098E+07	1.408E-18	1.123E-14	8.777E-01
33	2.188E-02	1.204E+06	2.218E+07	9.863E-18	1.124E-14	8.785E-01
34	1.503E-02	2.448E+06	2.463E+07	4.592E-17	1.129E-14	8.821E-01
35	7.102E-03	2.491E+06	2.712E+07	2.216E-17	1.131E-14	8.838E-01
36	3.355E-03	2.579E+06	2.970E+07	9.078E-18	1.132E-14	8.845E-01
37	1.585E-03	4.989E+06	3.469E+07	8.391E-18	1.133E-14	8.852E-01
38	4.540E-04	3.213E+06	3.790E+07	3.167E-19	1.133E-14	8.852E-01
39	2.144E-04	3.422E+06	4.132E+07	4.907E-19	1.133E-14	8.852E-01
40	1.013E-04	4.894E+06	4.622E+07	1.092E-18	1.133E-14	8.853E-01
41	3.727E-05	6.605E+06	5.282E+07	2.602E-18	1.133E-14	8.855E-01
42	1.068E-05	4.148E+06	5.697E+07	2.666E-18	1.133E-14	8.857E-01
43	5.043E-06	5.784E+06	6.276E+07	5.784E-18	1.134E-14	8.862E-01
44	1.855E-06	4.462E+06	6.722E+07	6.858E-18	1.135E-14	8.867E-01
45	8.764E-07	4.557E+06	7.177E+07	1.023E-17	1.136E-14	8.875E-01
46	4.140E-07	1.432E+07	8.610E+07	5.877E-17	1.141E-14	8.921E-01
47	1.000E-07	1.357E+08	2.218E+08	1.380E-15	1.279E-14	1.000E+00

Table A.2-h Absolute Calculated Neutron Flux Spectra and DPA Rate
at the Axial Mid-Plane, Azimuthal Peak and R = 1' in
the Concrete Shield Wall of Grand Gulf Cycle-2

G	Energy (MeV)	Group Flux	Cumulative Flux	Group DPA Rate	Cumulative DPA Rate	DPA Fraction
1	1.733E+01	2.206E+02	2.206E+02	6.446E-19	6.446E-19	5.894E-04
2	1.419E+01	1.082E+03	1.303E+03	2.864E-18	3.508E-18	3.208E-03
3	1.221E+01	3.102E+03	4.404E+03	7.472E-18	1.098E-17	1.004E-02
4	1.000E+01	6.540E+03	1.094E+04	1.451E-17	2.549E-17	2.331E-02
5	8.607E+00	9.975E+03	2.092E+04	2.082E-17	4.631E-17	4.234E-02
6	7.408E+00	2.976E+04	5.068E+04	5.783E-17	1.041E-16	9.521E-02
7	6.065E+00	4.030E+04	9.098E+04	7.189E-17	1.760E-16	1.609E-01
8	4.966E+00	5.953E+04	1.505E+05	9.353E-17	2.696E-16	2.465E-01
9	3.679E+00	3.800E+04	1.885E+05	5.206E-17	3.216E-16	2.941E-01
10	3.012E+00	3.356E+04	2.221E+05	4.265E-17	3.643E-16	3.330E-01
11	2.725E+00	4.213E+04	2.642E+05	5.371E-17	4.180E-16	3.822E-01
12	2.466E+00	3.205E+04	2.962E+05	3.756E-17	4.555E-16	4.165E-01
13	2.365E+00	1.170E+04	3.079E+05	1.283E-17	4.684E-16	4.282E-01
14	2.346E+00	4.380E+04	3.518E+05	4.560E-17	5.140E-16	4.699E-01
15	2.231E+00	6.588E+04	4.176E+05	6.812E-17	5.821E-16	5.322E-01
16	1.920E+00	5.992E+04	4.776E+05	4.873E-17	6.308E-16	5.768E-01
17	1.653E+00	7.333E+04	5.509E+05	5.942E-17	6.902E-16	6.311E-01
18	1.353E+00	8.513E+04	6.360E+05	4.770E-17	7.379E-16	6.747E-01
19	1.003E+00	4.988E+04	6.859E+05	1.828E-17	7.562E-16	6.914E-01
20	8.208E-01	3.965E+04	7.255E+05	2.224E-17	7.785E-16	7.118E-01
21	7.427E-01	7.397E+04	7.995E+05	2.673E-17	8.052E-16	7.362E-01
22	6.081E-01	7.156E+04	8.711E+05	2.106E-17	8.263E-16	7.555E-01
23	4.979E-01	5.969E+04	9.308E+05	2.366E-17	8.499E-16	7.771E-01
24	3.688E-01	5.304E+04	9.838E+05	1.096E-17	8.609E-16	7.871E-01
25	2.972E-01	1.075E+05	1.091E+06	2.155E-17	8.824E-16	8.068E-01
26	1.832E-01	1.192E+05	1.210E+06	1.681E-17	8.992E-16	8.222E-01
27	1.111E-01	9.895E+04	1.309E+06	1.279E-17	9.120E-16	8.339E-01
28	6.738E-02	9.121E+04	1.401E+06	5.907E-18	9.179E-16	8.393E-01
29	4.087E-02	4.042E+04	1.441E+06	3.271E-18	9.212E-16	8.423E-01
30	3.183E-02	3.514E+04	1.476E+06	9.991E-18	9.312E-16	8.514E-01
31	2.606E-02	1.281E+04	1.489E+06	2.582E-19	9.314E-16	8.516E-01
32	2.418E-02	1.677E+04	1.506E+06	7.341E-20	9.315E-16	8.517E-01
33	2.188E-02	6.148E+04	1.567E+06	5.035E-19	9.320E-16	8.522E-01
34	1.503E-02	1.218E+05	1.689E+06	2.284E-18	9.343E-16	8.543E-01
35	7.102E-03	1.207E+05	1.810E+06	1.074E-18	9.354E-16	8.552E-01
36	3.355E-03	1.229E+05	1.933E+06	4.327E-19	9.358E-16	8.556E-01
37	1.585E-03	2.287E+05	2.161E+06	3.847E-19	9.362E-16	8.560E-01
38	4.540E-04	1.456E+05	2.307E+06	1.435E-20	9.362E-16	8.560E-01
39	2.144E-04	1.537E+05	2.461E+06	2.204E-20	9.362E-16	8.560E-01
40	1.013E-04	2.206E+05	2.681E+06	4.922E-20	9.363E-16	8.561E-01
41	3.727E-05	3.027E+05	2.984E+06	1.192E-19	9.364E-16	8.562E-01
42	1.068E-05	1.940E+05	3.178E+06	1.247E-19	9.365E-16	8.563E-01
43	5.043E-06	2.782E+05	3.456E+06	2.782E-19	9.368E-16	8.565E-01
44	1.855E-06	2.206E+05	3.677E+06	3.391E-19	9.371E-16	8.568E-01
45	8.764E-07	2.325E+05	3.909E+06	5.217E-19	9.377E-16	8.573E-01
46	4.140E-07	7.995E+05	4.709E+06	3.280E-18	9.409E-16	8.603E-01
47	1.000E-07	1.502E+07	1.973E+07	1.528E-16	1.094E-15	1.000E+00

Table A.3-a Absolute Calculated Neutron Flux Spectra and DPA Rate
at the Axial Peak, Azimuthal Peak and RPV Wetted
Surface Wall of Grand Gulf Cycle-2

G	Energy (MeV)	Group Flux	Cumulative Flux	Group DPA Rate	Cumulative DPA Rate	DPA Fraction
1	1.733E+01	1.343E+06	1.343E+06	3.924E-15	3.924E-15	1.408E-03
2	1.419E+01	5.595E+06	6.938E+06	1.481E-14	1.873E-14	6.722E-03
3	1.221E+01	1.912E+07	2.606E+07	4.605E-14	6.478E-14	2.325E-02
4	1.000E+01	3.563E+07	6.168E+07	7.906E-14	1.438E-13	5.162E-02
5	8.607E+00	5.667E+07	1.184E+08	1.183E-13	2.621E-13	9.407E-02
6	7.408E+00	1.291E+08	2.475E+08	2.509E-13	5.130E-13	1.841E-01
7	6.065E+00	1.603E+08	4.078E+08	2.860E-13	7.990E-13	2.868E-01
8	4.966E+00	2.303E+08	6.381E+08	3.618E-13	1.161E-12	4.166E-01
9	3.679E+00	1.405E+08	7.786E+08	1.925E-13	1.353E-12	4.857E-01
10	3.012E+00	9.175E+07	8.704E+08	1.166E-13	1.470E-12	5.276E-01
11	2.725E+00	9.854E+07	9.689E+08	1.256E-13	1.596E-12	5.726E-01
12	2.466E+00	4.742E+07	1.016E+09	5.558E-14	1.651E-12	5.926E-01
13	2.365E+00	1.162E+07	1.028E+09	1.273E-14	1.664E-12	5.972E-01
14	2.346E+00	5.626E+07	1.084E+09	5.857E-14	1.722E-12	6.182E-01
15	2.231E+00	1.393E+08	1.224E+09	1.441E-13	1.867E-12	6.699E-01
16	1.920E+00	1.400E+08	1.364E+09	1.138E-13	1.980E-12	7.107E-01
17	1.653E+00	1.834E+08	1.547E+09	1.486E-13	2.129E-12	7.641E-01
18	1.353E+00	2.721E+08	1.819E+09	1.524E-13	2.281E-12	8.188E-01
19	1.003E+00	1.707E+08	1.990E+09	6.256E-14	2.344E-12	8.412E-01
20	8.208E-01	8.744E+07	2.077E+09	4.904E-14	2.393E-12	8.588E-01
21	7.427E-01	2.181E+08	2.295E+09	7.883E-14	2.472E-12	8.871E-01
22	6.081E-01	1.708E+08	2.466E+09	5.026E-14	2.522E-12	9.052E-01
23	4.979E-01	1.937E+08	2.660E+09	7.677E-14	2.599E-12	9.327E-01
24	3.688E-01	1.759E+08	2.836E+09	3.635E-14	2.635E-12	9.458E-01
25	2.972E-01	2.307E+08	3.066E+09	4.625E-14	2.681E-12	9.624E-01
26	1.832E-01	1.956E+08	3.262E+09	2.758E-14	2.709E-12	9.723E-01
27	1.111E-01	1.411E+08	3.403E+09	1.825E-14	2.727E-12	9.788E-01
28	6.738E-02	1.195E+08	3.523E+09	7.741E-15	2.735E-12	9.816E-01
29	4.087E-02	4.858E+07	3.571E+09	3.931E-15	2.739E-12	9.830E-01
30	3.183E-02	3.343E+07	3.605E+09	9.504E-15	2.748E-12	9.864E-01
31	2.606E-02	3.877E+07	3.643E+09	7.816E-16	2.749E-12	9.867E-01
32	2.418E-02	2.385E+07	3.667E+09	1.045E-16	2.749E-12	9.867E-01
33	2.188E-02	6.452E+07	3.732E+09	5.284E-16	2.750E-12	9.869E-01
34	1.503E-02	1.268E+08	3.858E+09	2.378E-15	2.752E-12	9.878E-01
35	7.102E-03	1.323E+08	3.991E+09	1.177E-15	2.753E-12	9.882E-01
36	3.355E-03	1.256E+08	4.116E+09	4.422E-16	2.754E-12	9.884E-01
37	1.585E-03	2.080E+08	4.324E+09	3.498E-16	2.754E-12	9.885E-01
38	4.540E-04	1.201E+08	4.444E+09	1.184E-17	2.754E-12	9.885E-01
39	2.144E-04	1.244E+08	4.569E+09	1.784E-17	2.754E-12	9.885E-01
40	1.013E-04	1.653E+08	4.734E+09	3.689E-17	2.754E-12	9.885E-01
41	3.727E-05	2.042E+08	4.938E+09	8.045E-17	2.754E-12	9.885E-01
42	1.068E-05	1.199E+08	5.058E+09	7.704E-17	2.754E-12	9.886E-01
43	5.043E-06	1.548E+08	5.213E+09	1.548E-16	2.755E-12	9.886E-01
44	1.855E-06	1.108E+08	5.324E+09	1.703E-16	2.755E-12	9.887E-01
45	8.764E-07	1.055E+08	5.429E+09	2.368E-16	2.755E-12	9.888E-01
46	4.140E-07	3.154E+08	5.745E+09	1.294E-15	2.756E-12	9.892E-01
47	1.000E-07	2.950E+09	8.695E+09	3.000E-14	2.786E-12	1.000E+00

Table A.3-b Absolute Calculated Neutron Flux Spectra and DPA Rate
at the Axial Peak, Azimuthal Peak and R = 0-T RPV Wall
of Grand Gulf Cycle-2

G	Energy (MeV)	Group Flux	Cumulative Flux	Group DPA Rate	Cumulative DPA Rate	DPA Fraction
1	1.733E+01	1.272E+06	1.272E+06	3.716E-15	3.716E-15	1.367E-03
2	1.419E+01	5.303E+06	6.575E+06	1.403E-14	1.775E-14	6.529E-03
3	1.221E+01	1.803E+07	2.461E+07	4.344E-14	6.119E-14	2.251E-02
4	1.000E+01	3.362E+07	5.823E+07	7.461E-14	1.358E-13	4.995E-02
5	8.607E+00	5.344E+07	1.117E+08	1.115E-13	2.473E-13	9.099E-02
6	7.408E+00	1.217E+08	2.334E+08	2.365E-13	4.838E-13	1.780E-01
7	6.065E+00	1.512E+08	3.846E+08	2.698E-13	7.536E-13	2.772E-01
8	4.966E+00	2.179E+08	6.025E+08	3.423E-13	1.096E-12	4.032E-01
9	3.679E+00	1.338E+08	7.363E+08	1.833E-13	1.279E-12	4.706E-01
10	3.012E+00	8.819E+07	8.245E+08	1.121E-13	1.391E-12	5.118E-01
11	2.725E+00	9.534E+07	9.198E+08	1.216E-13	1.513E-12	5.565E-01
12	2.466E+00	4.606E+07	9.659E+08	5.399E-14	1.567E-12	5.764E-01
13	2.365E+00	1.131E+07	9.772E+08	1.240E-14	1.579E-12	5.809E-01
14	2.346E+00	5.516E+07	1.032E+09	5.742E-14	1.637E-12	6.021E-01
15	2.231E+00	1.385E+08	1.171E+09	1.432E-13	1.780E-12	6.547E-01
16	1.920E+00	1.407E+08	1.312E+09	1.144E-13	1.894E-12	6.968E-01
17	1.653E+00	1.862E+08	1.498E+09	1.509E-13	2.045E-12	7.523E-01
18	1.353E+00	2.830E+08	1.781E+09	1.586E-13	2.204E-12	8.107E-01
19	1.003E+00	1.779E+08	1.959E+09	6.521E-14	2.269E-12	8.347E-01
20	8.208E-01	8.952E+07	2.048E+09	5.021E-14	2.319E-12	8.531E-01
21	7.427E-01	2.351E+08	2.283E+09	8.496E-14	2.404E-12	8.844E-01
22	6.081E-01	1.806E+08	2.464E+09	5.315E-14	2.457E-12	9.039E-01
23	4.979E-01	2.061E+08	2.670E+09	8.171E-14	2.539E-12	9.340E-01
24	3.688E-01	1.902E+08	2.860E+09	3.930E-14	2.578E-12	9.485E-01
25	2.972E-01	2.347E+08	3.095E+09	4.706E-14	2.625E-12	9.658E-01
26	1.832E-01	2.007E+08	3.296E+09	2.829E-14	2.654E-12	9.762E-01
27	1.111E-01	1.384E+08	3.434E+09	1.790E-14	2.672E-12	9.828E-01
28	6.738E-02	1.163E+08	3.550E+09	7.530E-15	2.679E-12	9.855E-01
29	4.087E-02	4.441E+07	3.595E+09	3.594E-15	2.683E-12	9.868E-01
30	3.183E-02	2.775E+07	3.622E+09	7.890E-15	2.691E-12	9.898E-01
31	2.606E-02	4.544E+07	3.668E+09	9.160E-16	2.691E-12	9.901E-01
32	2.418E-02	2.452E+07	3.692E+09	1.074E-16	2.692E-12	9.901E-01
33	2.188E-02	5.944E+07	3.752E+09	4.868E-16	2.692E-12	9.903E-01
34	1.503E-02	1.165E+08	3.868E+09	2.186E-15	2.694E-12	9.911E-01
35	7.102E-03	1.269E+08	3.995E+09	1.129E-15	2.695E-12	9.915E-01
36	3.355E-03	1.180E+08	4.113E+09	4.154E-16	2.696E-12	9.917E-01
37	1.585E-03	1.977E+08	4.311E+09	3.326E-16	2.696E-12	9.918E-01
38	4.540E-04	1.111E+08	4.422E+09	1.095E-17	2.696E-12	9.918E-01
39	2.144E-04	1.183E+08	4.540E+09	1.697E-17	2.696E-12	9.918E-01
40	1.013E-04	1.575E+08	4.698E+09	3.514E-17	2.696E-12	9.918E-01
41	3.727E-05	1.936E+08	4.892E+09	7.627E-17	2.696E-12	9.918E-01
42	1.068E-05	1.124E+08	5.004E+09	7.221E-17	2.696E-12	9.919E-01
43	5.043E-06	1.431E+08	5.147E+09	1.431E-16	2.696E-12	9.919E-01
44	1.855E-06	1.002E+08	5.247E+09	1.540E-16	2.697E-12	9.920E-01
45	8.764E-07	9.338E+07	5.341E+09	2.096E-16	2.697E-12	9.921E-01
46	4.140E-07	2.537E+08	5.594E+09	1.041E-15	2.698E-12	9.924E-01
47	1.000E-07	2.020E+09	7.614E+09	2.054E-14	2.718E-12	1.000E+00

Table A.3-c Absolute Calculated Neutron Flux Spectra and DPA Rate
at the Axial Peak, Azimuthal Peak and R = 1/4-T RPV
Wall of Grand Gulf Cycle-2

G	Energy (MeV)	Group Flux	Cumulative Flux	Group DPA Rate	Cumulative DPA Rate	DPA Fraction
1	1.733E+01	7.048E+05	7.048E+05	2.060E-15	2.060E-15	1.078E-03
2	1.419E+01	2.944E+06	3.649E+06	7.789E-15	9.849E-15	5.155E-03
3	1.221E+01	9.719E+06	1.337E+07	2.341E-14	3.326E-14	1.741E-02
4	1.000E+01	1.833E+07	3.170E+07	4.068E-14	7.394E-14	3.870E-02
5	8.607E+00	2.887E+07	6.057E+07	6.026E-14	1.342E-13	7.024E-02
6	7.408E+00	6.424E+07	1.248E+08	1.248E-13	2.590E-13	1.356E-01
7	6.065E+00	7.856E+07	2.034E+08	1.401E-13	3.992E-13	2.089E-01
8	4.966E+00	1.125E+08	3.159E+08	1.768E-13	5.759E-13	3.014E-01
9	3.679E+00	7.202E+07	3.879E+08	9.866E-14	6.746E-13	3.531E-01
10	3.012E+00	5.034E+07	4.382E+08	6.398E-14	7.386E-13	3.865E-01
11	2.725E+00	5.727E+07	4.955E+08	7.302E-14	8.116E-13	4.248E-01
12	2.466E+00	2.847E+07	5.240E+08	3.336E-14	8.449E-13	4.422E-01
13	2.365E+00	7.401E+06	5.314E+08	8.112E-15	8.530E-13	4.465E-01
14	2.346E+00	3.679E+07	5.682E+08	3.830E-14	8.914E-13	4.665E-01
15	2.231E+00	9.833E+07	6.665E+08	1.017E-13	9.930E-13	5.197E-01
16	1.920E+00	1.092E+08	7.757E+08	8.882E-14	1.082E-12	5.662E-01
17	1.653E+00	1.535E+08	9.292E+08	1.244E-13	1.206E-12	6.313E-01
18	1.353E+00	2.700E+08	1.199E+09	1.513E-13	1.357E-12	7.105E-01
19	1.003E+00	1.796E+08	1.379E+09	6.581E-14	1.423E-12	7.449E-01
20	8.208E-01	8.480E+07	1.464E+09	4.756E-14	1.471E-12	7.698E-01
21	7.427E-01	2.834E+08	1.747E+09	1.024E-13	1.573E-12	8.234E-01
22	6.081E-01	2.119E+08	1.959E+09	6.237E-14	1.636E-12	8.561E-01
23	4.979E-01	2.524E+08	2.211E+09	1.000E-13	1.736E-12	9.084E-01
24	3.688E-01	2.544E+08	2.466E+09	5.259E-14	1.788E-12	9.360E-01
25	2.972E-01	2.626E+08	2.728E+09	5.265E-14	1.841E-12	9.635E-01
26	1.832E-01	2.401E+08	2.968E+09	3.385E-14	1.875E-12	9.812E-01
27	1.111E-01	1.383E+08	3.107E+09	1.788E-14	1.893E-12	9.906E-01
28	6.738E-02	1.071E+08	3.214E+09	6.934E-15	1.900E-12	9.942E-01
29	4.087E-02	2.868E+07	3.242E+09	2.321E-15	1.902E-12	9.954E-01
30	3.183E-02	1.001E+07	3.252E+09	2.846E-15	1.905E-12	9.969E-01
31	2.606E-02	5.919E+07	3.312E+09	1.193E-15	1.906E-12	9.976E-01
32	2.418E-02	3.041E+07	3.342E+09	1.331E-16	1.906E-12	9.976E-01
33	2.188E-02	5.238E+07	3.394E+09	4.290E-16	1.907E-12	9.979E-01
34	1.503E-02	7.121E+07	3.466E+09	1.336E-15	1.908E-12	9.986E-01
35	7.102E-03	9.301E+07	3.559E+09	8.273E-16	1.909E-12	9.990E-01
36	3.355E-03	7.066E+07	3.629E+09	2.487E-16	1.909E-12	9.991E-01
37	1.585E-03	1.226E+08	3.752E+09	2.062E-16	1.909E-12	9.992E-01
38	4.540E-04	5.442E+07	3.806E+09	5.365E-18	1.909E-12	9.992E-01
39	2.144E-04	6.718E+07	3.873E+09	9.634E-18	1.909E-12	9.992E-01
40	1.013E-04	9.261E+07	3.966E+09	2.066E-17	1.909E-12	9.992E-01
41	3.727E-05	1.109E+08	4.077E+09	4.369E-17	1.909E-12	9.993E-01
42	1.068E-05	5.923E+07	4.136E+09	3.806E-17	1.909E-12	9.993E-01
43	5.043E-06	6.571E+07	4.202E+09	6.571E-17	1.909E-12	9.993E-01
44	1.855E-06	3.741E+07	4.239E+09	5.750E-17	1.909E-12	9.993E-01
45	8.764E-07	2.715E+07	4.266E+09	6.092E-17	1.909E-12	9.994E-01
46	4.140E-07	2.885E+07	4.295E+09	1.184E-16	1.910E-12	9.994E-01
47	1.000E-07	1.055E+08	4.401E+09	1.073E-15	1.911E-12	1.000E+00

Table A.3-d Absolute Calculated Neutron Flux Spectra and DPA Rate
at the Axial Peak, Azimuthal Peak and R = 3/4-T RPV
Wall of Grand Gulf Cycle-2

G	Energy (MeV)	Group Flux	Cumulative Flux	Group DPA Rate	Cumulative DPA Rate	DPA Fraction
1	1.733E+01	1.960E+05	1.960E+05	5.728E-16	5.728E-16	7.554E-04
2	1.419E+01	8.055E+05	1.002E+06	2.131E-15	2.704E-15	3.566E-03
3	1.221E+01	2.527E+06	3.529E+06	6.088E-15	8.792E-15	1.159E-02
4	1.000E+01	4.738E+06	8.266E+06	1.051E-14	1.930E-14	2.546E-02
5	8.607E+00	7.186E+06	1.545E+07	1.500E-14	3.430E-14	4.524E-02
6	7.408E+00	1.490E+07	3.035E+07	2.895E-14	6.325E-14	8.342E-02
7	6.065E+00	1.774E+07	4.809E+07	3.165E-14	9.490E-14	1.251E-01
8	4.966E+00	2.549E+07	7.358E+07	4.004E-14	1.349E-13	1.780E-01
9	3.679E+00	1.761E+07	9.119E+07	2.413E-14	1.591E-13	2.098E-01
10	3.012E+00	1.283E+07	1.040E+08	1.631E-14	1.754E-13	2.313E-01
11	2.725E+00	1.536E+07	1.194E+08	1.958E-14	1.950E-13	2.571E-01
12	2.466E+00	7.863E+06	1.272E+08	9.215E-15	2.042E-13	2.693E-01
13	2.365E+00	2.208E+06	1.295E+08	2.420E-15	2.066E-13	2.724E-01
14	2.346E+00	1.117E+07	1.406E+08	1.163E-14	2.182E-13	2.878E-01
15	2.231E+00	3.132E+07	1.719E+08	3.239E-14	2.506E-13	3.305E-01
16	1.920E+00	3.920E+07	2.111E+08	3.188E-14	2.825E-13	3.725E-01
17	1.653E+00	5.917E+07	2.703E+08	4.795E-14	3.304E-13	4.358E-01
18	1.353E+00	1.261E+08	3.964E+08	7.066E-14	4.011E-13	5.290E-01
19	1.003E+00	9.569E+07	4.921E+08	3.507E-14	4.362E-13	5.752E-01
20	8.208E-01	4.345E+07	5.356E+08	2.437E-14	4.605E-13	6.073E-01
21	7.427E-01	1.789E+08	7.145E+08	6.467E-14	5.252E-13	6.926E-01
22	6.081E-01	1.393E+08	8.538E+08	4.100E-14	5.662E-13	7.467E-01
23	4.979E-01	1.691E+08	1.023E+09	6.702E-14	6.332E-13	8.351E-01
24	3.688E-01	1.912E+08	1.214E+09	3.953E-14	6.728E-13	8.872E-01
25	2.972E-01	1.866E+08	1.401E+09	3.741E-14	7.102E-13	9.365E-01
26	1.832E-01	1.806E+08	1.581E+09	2.547E-14	7.356E-13	9.701E-01
27	1.111E-01	9.688E+07	1.678E+09	1.253E-14	7.482E-13	9.866E-01
28	6.738E-02	6.837E+07	1.747E+09	4.429E-15	7.526E-13	9.925E-01
29	4.087E-02	1.678E+07	1.763E+09	1.358E-15	7.539E-13	9.943E-01
30	3.183E-02	5.805E+06	1.769E+09	1.650E-15	7.556E-13	9.964E-01
31	2.606E-02	4.293E+07	1.812E+09	8.655E-16	7.565E-13	9.976E-01
32	2.418E-02	2.311E+07	1.835E+09	1.012E-16	7.566E-13	9.977E-01
33	2.188E-02	3.522E+07	1.870E+09	2.884E-16	7.568E-13	9.981E-01
34	1.503E-02	3.643E+07	1.907E+09	6.833E-16	7.575E-13	9.990E-01
35	7.102E-03	4.662E+07	1.953E+09	4.147E-16	7.579E-13	9.995E-01
36	3.355E-03	3.236E+07	1.986E+09	1.139E-16	7.581E-13	9.997E-01
37	1.585E-03	5.252E+07	2.038E+09	8.834E-17	7.581E-13	9.998E-01
38	4.540E-04	2.183E+07	2.060E+09	2.152E-18	7.582E-13	9.998E-01
39	2.144E-04	2.549E+07	2.086E+09	3.655E-18	7.582E-13	9.998E-01
40	1.013E-04	3.437E+07	2.120E+09	7.668E-18	7.582E-13	9.998E-01
41	3.727E-05	3.983E+07	2.160E+09	1.569E-17	7.582E-13	9.999E-01
42	1.068E-05	2.026E+07	2.180E+09	1.302E-17	7.582E-13	9.999E-01
43	5.043E-06	2.025E+07	2.200E+09	2.025E-17	7.582E-13	9.999E-01
44	1.855E-06	1.009E+07	2.210E+09	1.551E-17	7.582E-13	9.999E-01
45	8.764E-07	6.084E+06	2.217E+09	1.365E-17	7.582E-13	9.999E-01
46	4.140E-07	3.490E+06	2.220E+09	1.432E-17	7.583E-13	1.000E+00
47	1.000E-07	3.607E+06	2.224E+09	3.668E-17	7.583E-13	1.000E+00

Table A.3-e   Absolute Calculated Neutron Flux Spectra and DPA Rate
at the Axial Peak, Azimuthal Peak and R = Mid–Cavity
of Grand Gulf Cycle-2

G	Energy (MeV)	Group Flux	Cumulative Flux	Group DPA Rate	Cumulative DPA Rate	DPA Fraction
1	1.733E+01	7.024E+04	7.024E+04	2.052E-16	2.052E-16	9.087E-04
2	1.419E+01	2.754E+05	3.457E+05	7.288E-16	9.340E-16	4.135E-03
3	1.221E+01	8.356E+05	1.181E+06	2.013E-15	2.947E-15	1.305E-02
4	1.000E+01	1.524E+06	2.706E+06	3.383E-15	6.330E-15	2.803E-02
5	8.607E+00	2.219E+06	4.925E+06	4.631E-15	1.096E-14	4.853E-02
6	7.408E+00	4.395E+06	9.320E+06	8.540E-15	1.950E-14	8.634E-02
7	6.065E+00	5.079E+06	1.440E+07	9.060E-15	2.856E-14	1.265E-01
8	4.966E+00	7.090E+06	2.149E+07	1.114E-14	3.970E-14	1.758E-01
9	3.679E+00	4.768E+06	2.626E+07	6.532E-15	4.623E-14	2.047E-01
10	3.012E+00	3.439E+06	2.970E+07	4.371E-15	5.060E-14	2.241E-01
11	2.725E+00	4.072E+06	3.377E+07	5.192E-15	5.580E-14	2.470E-01
12	2.466E+00	2.131E+06	3.590E+07	2.498E-15	5.829E-14	2.581E-01
13	2.365E+00	6.035E+05	3.650E+07	6.614E-16	5.895E-14	2.610E-01
14	2.346E+00	2.981E+06	3.948E+07	3.103E-15	6.206E-14	2.748E-01
15	2.231E+00	7.849E+06	4.733E+07	8.115E-15	7.017E-14	3.107E-01
16	1.920E+00	1.014E+07	5.747E+07	8.246E-15	7.842E-14	3.472E-01
17	1.653E+00	1.577E+07	7.324E+07	1.278E-14	9.120E-14	4.038E-01
18	1.353E+00	3.410E+07	1.073E+08	1.911E-14	1.103E-13	4.884E-01
19	1.003E+00	2.766E+07	1.350E+08	1.014E-14	1.204E-13	5.333E-01
20	8.208E-01	1.409E+07	1.491E+08	7.905E-15	1.283E-13	5.683E-01
21	7.427E-01	4.952E+07	1.986E+08	1.790E-14	1.462E-13	6.475E-01
22	6.081E-01	4.324E+07	2.418E+08	1.273E-14	1.590E-13	7.038E-01
23	4.979E-01	4.666E+07	2.885E+08	1.850E-14	1.775E-13	7.857E-01
24	3.688E-01	5.689E+07	3.454E+08	1.176E-14	1.892E-13	8.378E-01
25	2.972E-01	7.416E+07	4.196E+08	1.487E-14	2.041E-13	9.036E-01
26	1.832E-01	6.704E+07	4.866E+08	9.452E-15	2.135E-13	9.455E-01
27	1.111E-01	4.074E+07	5.273E+08	5.268E-15	2.188E-13	9.688E-01
28	6.738E-02	2.877E+07	5.561E+08	1.863E-15	2.207E-13	9.771E-01
29	4.087E-02	8.884E+06	5.650E+08	7.190E-16	2.214E-13	9.802E-01
30	3.183E-02	8.175E+06	5.732E+08	2.324E-15	2.237E-13	9.905E-01
31	2.606E-02	1.506E+07	5.882E+08	3.037E-16	2.240E-13	9.919E-01
32	2.418E-02	9.278E+06	5.975E+08	4.063E-17	2.241E-13	9.921E-01
33	2.188E-02	1.930E+07	6.168E+08	1.581E-16	2.242E-13	9.928E-01
34	1.503E-02	2.511E+07	6.419E+08	4.711E-16	2.247E-13	9.948E-01
35	7.102E-03	2.409E+07	6.660E+08	2.143E-16	2.249E-13	9.958E-01
36	3.355E-03	2.051E+07	6.865E+08	7.219E-17	2.250E-13	9.961E-01
37	1.585E-03	3.190E+07	7.184E+08	5.366E-17	2.250E-13	9.963E-01
38	4.540E-04	1.673E+07	7.351E+08	1.649E-18	2.250E-13	9.964E-01
39	2.144E-04	1.628E+07	7.514E+08	2.334E-18	2.250E-13	9.964E-01
40	1.013E-04	2.042E+07	7.718E+08	4.556E-18	2.250E-13	9.964E-01
41	3.727E-05	2.342E+07	7.953E+08	9.226E-18	2.250E-13	9.964E-01
42	1.068E-05	1.288E+07	8.081E+08	8.280E-18	2.251E-13	9.965E-01
43	5.043E-06	1.544E+07	8.236E+08	1.544E-17	2.251E-13	9.965E-01
44	1.855E-06	1.030E+07	8.339E+08	1.583E-17	2.251E-13	9.966E-01
45	8.764E-07	9.166E+06	8.431E+08	2.057E-17	2.251E-13	9.967E-01
46	4.140E-07	1.949E+07	8.626E+08	7.998E-17	2.252E-13	9.970E-01
47	1.000E-07	6.568E+07	9.282E+08	6.680E-16	2.259E-13	1.000E+00

Table A.3-f   Absolute Calculated Neutron Flux Spectra and DPA Rate
at the Axial Peak, Azimuthal Peak and R = Front of the
Concrete Shield Wall of Grand Gulf Cycle-2

G	Energy (MeV)	Group Flux	Cumulative Flux	Group DPA Rate	Cumulative DPA Rate	DPA Fraction
1	1.733E+01	4.360E+04	4.360E+04	1.274E-16	1.274E-16	7.344E-04
2	1.419E+01	1.772E+05	2.208E+05	4.688E-16	5.962E-16	3.437E-03
3	1.221E+01	5.497E+05	7.705E+05	1.324E-15	1.921E-15	1.107E-02
4	1.000E+01	1.022E+06	1.792E+06	2.267E-15	4.188E-15	2.414E-02
5	8.607E+00	1.529E+06	3.322E+06	3.192E-15	7.380E-15	4.254E-02
6	7.408E+00	3.134E+06	6.456E+06	6.090E-15	1.347E-14	7.764E-02
7	6.065E+00	3.813E+06	1.027E+07	6.802E-15	2.027E-14	1.169E-01
8	4.966E+00	5.598E+06	1.587E+07	8.794E-15	2.907E-14	1.675E-01
9	3.679E+00	3.838E+06	1.970E+07	5.258E-15	3.432E-14	1.979E-01
10	3.012E+00	2.778E+06	2.248E+07	3.531E-15	3.785E-14	2.182E-01
11	2.725E+00	3.340E+06	2.582E+07	4.259E-15	4.211E-14	2.428E-01
12	2.466E+00	1.797E+06	2.762E+07	2.106E-15	4.422E-14	2.549E-01
13	2.365E+00	4.975E+05	2.812E+07	5.452E-16	4.476E-14	2.580E-01
14	2.346E+00	2.399E+06	3.052E+07	2.497E-15	4.726E-14	2.724E-01
15	2.231E+00	5.837E+06	3.635E+07	6.036E-15	5.330E-14	3.072E-01
16	1.920E+00	7.432E+06	4.379E+07	6.045E-15	5.934E-14	3.421E-01
17	1.653E+00	1.168E+07	5.546E+07	9.463E-15	6.880E-14	3.966E-01
18	1.353E+00	2.365E+07	7.911E+07	1.325E-14	8.206E-14	4.730E-01
19	1.003E+00	1.871E+07	9.782E+07	6.857E-15	8.891E-14	5.125E-01
20	8.208E-01	1.191E+07	1.097E+08	6.680E-15	9.559E-14	5.510E-01
21	7.427E-01	3.425E+07	1.440E+08	1.238E-14	1.080E-13	6.224E-01
22	6.081E-01	3.339E+07	1.774E+08	9.827E-15	1.178E-13	6.790E-01
23	4.979E-01	3.394E+07	2.113E+08	1.346E-14	1.313E-13	7.566E-01
24	3.688E-01	3.855E+07	2.499E+08	7.968E-15	1.392E-13	8.025E-01
25	2.972E-01	6.212E+07	3.120E+08	1.246E-14	1.517E-13	8.743E-01
26	1.832E-01	5.902E+07	3.710E+08	8.321E-15	1.600E-13	9.223E-01
27	1.111E-01	3.982E+07	4.108E+08	5.149E-15	1.651E-13	9.520E-01
28	6.738E-02	3.078E+07	4.416E+08	1.994E-15	1.671E-13	9.635E-01
29	4.087E-02	1.148E+07	4.531E+08	9.292E-16	1.681E-13	9.688E-01
30	3.183E-02	9.497E+06	4.626E+08	2.700E-15	1.708E-13	9.844E-01
31	2.606E-02	8.253E+06	4.708E+08	1.664E-16	1.709E-13	9.853E-01
32	2.418E-02	7.423E+06	4.783E+08	3.251E-17	1.710E-13	9.855E-01
33	2.188E-02	2.038E+07	4.986E+08	1.669E-16	1.711E-13	9.865E-01
34	1.503E-02	3.060E+07	5.292E+08	5.740E-16	1.717E-13	9.898E-01
35	7.102E-03	2.765E+07	5.569E+08	2.459E-16	1.720E-13	9.912E-01
36	3.355E-03	2.468E+07	5.816E+08	8.686E-17	1.720E-13	9.917E-01
37	1.585E-03	3.798E+07	6.195E+08	6.387E-17	1.721E-13	9.921E-01
38	4.540E-04	2.039E+07	6.399E+08	2.010E-18	1.721E-13	9.921E-01
39	2.144E-04	1.938E+07	6.593E+08	2.779E-18	1.721E-13	9.921E-01
40	1.013E-04	2.421E+07	6.835E+08	5.402E-18	1.721E-13	9.921E-01
41	3.727E-05	2.787E+07	7.114E+08	1.098E-17	1.721E-13	9.922E-01
42	1.068E-05	1.554E+07	7.269E+08	9.986E-18	1.721E-13	9.923E-01
43	5.043E-06	1.905E+07	7.460E+08	1.905E-17	1.722E-13	9.924E-01
44	1.855E-06	1.309E+07	7.591E+08	2.011E-17	1.722E-13	9.925E-01
45	8.764E-07	1.199E+07	7.711E+08	2.691E-17	1.722E-13	9.926E-01
46	4.140E-07	2.811E+07	7.992E+08	1.153E-16	1.723E-13	9.933E-01
47	1.000E-07	1.141E+08	9.133E+08	1.160E-15	1.735E-13	1.000E+00

Table A.3-g   Absolute Calculated Neutron Flux Spectra and DPA Rate
at the Axial Peak, Azimuthal Peak and R = 6" in the
Concrete Shield Wall of Grand Gulf Cycle-2

G	Energy (MeV)	Group Flux	Cumulative Flux	Group DPA Rate	Cumulative DPA Rate	DPA Fraction
1	1.733E+01	3.411E+03	3.411E+03	9.968E-18	9.968E-18	7.677E-04
2	1.419E+01	1.548E+04	1.889E+04	4.096E-17	5.093E-17	3.923E-03
3	1.221E+01	4.590E+04	6.479E+04	1.106E-16	1.615E-16	1.244E-02
4	1.000E+01	9.133E+04	1.561E+05	2.027E-16	3.642E-16	2.805E-02
5	8.607E+00	1.395E+05	2.957E+05	2.912E-16	6.554E-16	5.047E-02
6	7.408E+00	3.548E+05	6.505E+05	6.894E-16	1.345E-15	1.036E-01
7	6.065E+00	4.722E+05	1.123E+06	8.425E-16	2.187E-15	1.685E-01
8	4.966E+00	7.048E+05	1.828E+06	1.107E-15	3.294E-15	2.537E-01
9	3.679E+00	4.503E+05	2.278E+06	6.169E-16	3.911E-15	3.012E-01
10	3.012E+00	3.849E+05	2.663E+06	4.892E-16	4.401E-15	3.389E-01
11	2.725E+00	4.739E+05	3.137E+06	6.042E-16	5.005E-15	3.855E-01
12	2.466E+00	3.228E+05	3.459E+06	3.784E-16	5.383E-15	4.146E-01
13	2.365E+00	1.029E+05	3.562E+06	1.128E-16	5.496E-15	4.233E-01
14	2.346E+00	4.190E+05	3.981E+06	4.362E-16	5.932E-15	4.569E-01
15	2.231E+00	6.910E+05	4.672E+06	7.145E-16	6.647E-15	5.119E-01
16	1.920E+00	6.630E+05	5.335E+06	5.392E-16	7.186E-15	5.534E-01
17	1.653E+00	8.566E+05	6.192E+06	6.941E-16	7.880E-15	6.069E-01
18	1.353E+00	1.051E+06	7.243E+06	5.891E-16	8.469E-15	6.523E-01
19	1.003E+00	6.260E+05	7.869E+06	2.294E-16	8.698E-15	6.699E-01
20	8.208E-01	5.117E+05	8.381E+06	2.870E-16	8.986E-15	6.920E-01
21	7.427E-01	1.048E+06	9.429E+06	3.788E-16	9.364E-15	7.212E-01
22	6.081E-01	1.061E+06	1.049E+07	3.122E-16	9.677E-15	7.452E-01
23	4.979E-01	8.912E+05	1.138E+07	3.533E-16	1.003E-14	7.725E-01
24	3.688E-01	8.106E+05	1.219E+07	1.676E-16	1.020E-14	7.854E-01
25	2.972E-01	1.673E+06	1.386E+07	3.354E-16	1.053E-14	8.112E-01
26	1.832E-01	1.998E+06	1.586E+07	2.817E-16	1.081E-14	8.329E-01
27	1.111E-01	1.748E+06	1.761E+07	2.260E-16	1.104E-14	8.503E-01
28	6.738E-02	1.677E+06	1.929E+07	1.086E-16	1.115E-14	8.587E-01
29	4.087E-02	7.576E+05	2.005E+07	6.132E-17	1.121E-14	8.634E-01
30	3.183E-02	6.623E+05	2.071E+07	1.883E-16	1.140E-14	8.779E-01
31	2.606E-02	2.490E+05	2.096E+07	5.020E-18	1.140E-14	8.783E-01
32	2.418E-02	3.256E+05	2.128E+07	1.426E-18	1.141E-14	8.784E-01
33	2.188E-02	1.219E+06	2.250E+07	9.987E-18	1.142E-14	8.791E-01
34	1.503E-02	2.477E+06	2.498E+07	4.648E-17	1.146E-14	8.827E-01
35	7.102E-03	2.521E+06	2.750E+07	2.242E-17	1.148E-14	8.844E-01
36	3.355E-03	2.609E+06	3.011E+07	9.184E-18	1.149E-14	8.852E-01
37	1.585E-03	5.045E+06	3.515E+07	8.486E-18	1.150E-14	8.858E-01
38	4.540E-04	3.248E+06	3.840E+07	3.202E-19	1.150E-14	8.858E-01
39	2.144E-04	3.458E+06	4.186E+07	4.959E-19	1.150E-14	8.859E-01
40	1.013E-04	4.944E+06	4.680E+07	1.103E-18	1.150E-14	8.860E-01
41	3.727E-05	6.671E+06	5.347E+07	2.628E-18	1.151E-14	8.862E-01
42	1.068E-05	4.189E+06	5.766E+07	2.692E-18	1.151E-14	8.864E-01
43	5.043E-06	5.840E+06	6.350E+07	5.840E-18	1.151E-14	8.868E-01
44	1.855E-06	4.505E+06	6.801E+07	6.925E-18	1.152E-14	8.873E-01
45	8.764E-07	4.601E+06	7.261E+07	1.032E-17	1.153E-14	8.881E-01
46	4.140E-07	1.446E+07	8.707E+07	5.933E-17	1.159E-14	8.927E-01
47	1.000E-07	1.370E+08	2.240E+08	1.393E-15	1.298E-14	1.000E+00

Table A.3-h   Absolute Calculated Neutron Flux Spectra and DPA Rate
at the Axial Peak, Azimuthal Peak and R = 1' in the
Concrete Shield Wall of Grand Gulf Cycle-2

G	Energy (MeV)	Group Flux	Cumulative Flux	Group DPA Rate	Cumulative DPA Rate	DPA Fraction
1	1.733E+01	2.222E+02	2.222E+02	6.493E-19	6.493E-19	5.868E-04
2	1.419E+01	1.092E+03	1.314E+03	2.889E-18	3.539E-18	3.198E-03
3	1.221E+01	3.136E+03	4.450E+03	7.555E-18	1.109E-17	1.003E-02
4	1.000E+01	6.636E+03	1.109E+04	1.473E-17	2.582E-17	2.333E-02
5	8.607E+00	1.013E+04	2.121E+04	2.113E-17	4.695E-17	4.243E-02
6	7.408E+00	3.032E+04	5.154E+04	5.892E-17	1.059E-16	9.568E-02
7	6.065E+00	4.093E+04	9.247E+04	7.302E-17	1.789E-16	1.617E-01
8	4.966E+00	5.998E+04	1.525E+05	9.423E-17	2.731E-16	2.468E-01
9	3.679E+00	3.814E+04	1.906E+05	5.226E-17	3.254E-16	2.940E-01
10	3.012E+00	3.378E+04	2.244E+05	4.294E-17	3.683E-16	3.329E-01
11	2.725E+00	4.244E+04	2.668E+05	5.411E-17	4.224E-16	3.818E-01
12	2.466E+00	3.257E+04	2.994E+05	3.817E-17	4.606E-16	4.162E-01
13	2.365E+00	1.196E+04	3.114E+05	1.311E-17	4.737E-16	4.281E-01
14	2.346E+00	4.471E+04	3.561E+05	4.654E-17	5.203E-16	4.702E-01
15	2.231E+00	6.683E+04	4.229E+05	6.911E-17	5.894E-16	5.326E-01
16	1.920E+00	6.076E+04	4.837E+05	4.942E-17	6.388E-16	5.773E-01
17	1.653E+00	7.442E+04	5.581E+05	6.030E-17	6.991E-16	6.318E-01
18	1.353E+00	8.612E+04	6.442E+05	4.825E-17	7.473E-16	6.754E-01
19	1.003E+00	5.034E+04	6.945E+05	1.845E-17	7.658E-16	6.920E-01
20	8.208E-01	4.007E+04	7.346E+05	2.247E-17	7.883E-16	7.123E-01
21	7.427E-01	7.463E+04	8.092E+05	2.697E-17	8.152E-16	7.367E-01
22	6.081E-01	7.217E+04	8.814E+05	2.124E-17	8.365E-16	7.559E-01
23	4.979E-01	6.020E+04	9.416E+05	2.386E-17	8.603E-16	7.775E-01
24	3.688E-01	5.342E+04	9.950E+05	1.104E-17	8.714E-16	7.875E-01
25	2.972E-01	1.083E+05	1.103E+06	2.171E-17	8.931E-16	8.071E-01
26	1.832E-01	1.201E+05	1.223E+06	1.693E-17	9.100E-16	8.224E-01
27	1.111E-01	9.971E+04	1.323E+06	1.289E-17	9.229E-16	8.340E-01
28	6.738E-02	9.197E+04	1.415E+06	5.957E-18	9.289E-16	8.394E-01
29	4.087E-02	4.081E+04	1.456E+06	3.303E-18	9.322E-16	8.424E-01
30	3.183E-02	3.550E+04	1.491E+06	1.009E-17	9.423E-16	8.515E-01
31	2.606E-02	1.292E+04	1.504E+06	2.605E-19	9.425E-16	8.517E-01
32	2.418E-02	1.692E+04	1.521E+06	7.408E-20	9.426E-16	8.518E-01
33	2.188E-02	6.204E+04	1.583E+06	5.081E-19	9.431E-16	8.523E-01
34	1.503E-02	1.230E+05	1.706E+06	2.307E-18	9.454E-16	8.544E-01
35	7.102E-03	1.219E+05	1.828E+06	1.084E-18	9.465E-16	8.553E-01
36	3.355E-03	1.241E+05	1.952E+06	4.370E-19	9.469E-16	8.557E-01
37	1.585E-03	2.313E+05	2.183E+06	3.890E-19	9.473E-16	8.561E-01
38	4.540E-04	1.472E+05	2.331E+06	1.451E-20	9.473E-16	8.561E-01
39	2.144E-04	1.555E+05	2.486E+06	2.229E-20	9.474E-16	8.561E-01
40	1.013E-04	2.232E+05	2.709E+06	4.980E-20	9.474E-16	8.562E-01
41	3.727E-05	3.064E+05	3.016E+06	1.207E-19	9.475E-16	8.563E-01
42	1.068E-05	1.963E+05	3.212E+06	1.262E-19	9.476E-16	8.564E-01
43	5.043E-06	2.816E+05	3.494E+06	2.816E-19	9.479E-16	8.566E-01
44	1.855E-06	2.234E+05	3.717E+06	3.433E-19	9.483E-16	8.569E-01
45	8.764E-07	2.354E+05	3.952E+06	5.283E-19	9.488E-16	8.574E-01
46	4.140E-07	8.093E+05	4.762E+06	3.320E-18	9.521E-16	8.604E-01
47	1.000E-07	1.519E+07	1.995E+07	1.544E-16	1.107E-15	1.000E+00

Table A.4-a   Absolute Calculated Neutron Flux Spectra and DPA Rate
             at the Axial Feed Water Nozzle Elevation, Azimuthal
             Peak and RPV Wetted Surface Wall of Grand Gulf Cycle-2

G	Energy (MeV)	Group Flux	Cumulative Flux	Group DPA Rate	Cumulative DPA Rate	DPA Fraction
1	1.733E+01	1.901E+02	1.901E+02	5.553E-19	5.553E-19	4.812E-03
2	1.419E+01	7.674E+02	9.574E+02	2.030E-18	2.586E-18	2.240E-02
3	1.221E+01	1.711E+03	2.668E+03	4.122E-18	6.708E-18	5.812E-02
4	1.000E+01	2.488E+03	5.156E+03	5.521E-18	1.223E-17	1.060E-01
5	8.607E+00	3.225E+03	8.382E+03	6.731E-18	1.896E-17	1.643E-01
6	7.408E+00	5.923E+03	1.430E+04	1.151E-17	3.047E-17	2.640E-01
7	6.065E+00	6.474E+03	2.078E+04	1.155E-17	4.202E-17	3.641E-01
8	4.966E+00	8.760E+03	2.954E+04	1.376E-17	5.578E-17	4.833E-01
9	3.679E+00	5.360E+03	3.490E+04	7.344E-18	6.312E-17	5.469E-01
10	3.012E+00	3.360E+03	3.826E+04	4.271E-18	6.739E-17	5.839E-01
11	2.725E+00	3.565E+03	4.182E+04	4.546E-18	7.194E-17	6.233E-01
12	2.466E+00	1.664E+03	4.349E+04	1.951E-18	7.389E-17	6.402E-01
13	2.365E+00	3.922E+02	4.388E+04	4.299E-19	7.432E-17	6.439E-01
14	2.346E+00	1.967E+03	4.585E+04	2.048E-18	7.637E-17	6.617E-01
15	2.231E+00	5.000E+03	5.085E+04	5.170E-18	8.154E-17	7.065E-01
16	1.920E+00	5.065E+03	5.591E+04	4.119E-18	8.566E-17	7.422E-01
17	1.653E+00	6.644E+03	6.256E+04	5.384E-18	9.104E-17	7.888E-01
18	1.353E+00	1.003E+04	7.259E+04	5.620E-18	9.666E-17	8.375E-01
19	1.003E+00	6.376E+03	7.896E+04	2.337E-18	9.900E-17	8.578E-01
20	8.208E-01	3.230E+03	8.219E+04	1.812E-18	1.008E-16	8.735E-01
21	7.427E-01	8.198E+03	9.039E+04	2.963E-18	1.038E-16	8.991E-01
22	6.081E-01	6.390E+03	9.678E+04	1.881E-18	1.057E-16	9.154E-01
23	4.979E-01	7.247E+03	1.040E+05	2.873E-18	1.085E-16	9.403E-01
24	3.688E-01	6.739E+03	1.108E+05	1.393E-18	1.099E-16	9.524E-01
25	2.972E-01	8.648E+03	1.194E+05	1.734E-18	1.117E-16	9.674E-01
26	1.832E-01	7.323E+03	1.267E+05	1.033E-18	1.127E-16	9.764E-01
27	1.111E-01	5.208E+03	1.319E+05	6.734E-19	1.134E-16	9.822E-01
28	6.738E-02	4.383E+03	1.363E+05	2.839E-19	1.136E-16	9.846E-01
29	4.087E-02	1.769E+03	1.381E+05	1.432E-19	1.138E-16	9.859E-01
30	3.183E-02	1.212E+03	1.393E+05	3.445E-19	1.141E-16	9.889E-01
31	2.606E-02	1.465E+03	1.408E+05	2.954E-20	1.142E-16	9.891E-01
32	2.418E-02	9.005E+02	1.417E+05	3.943E-21	1.142E-16	9.892E-01
33	2.188E-02	2.377E+03	1.441E+05	1.947E-20	1.142E-16	9.893E-01
34	1.503E-02	4.618E+03	1.487E+05	8.663E-20	1.143E-16	9.901E-01
35	7.102E-03	4.807E+03	1.535E+05	4.276E-20	1.143E-16	9.905E-01
36	3.355E-03	4.546E+03	1.580E+05	1.600E-20	1.143E-16	9.906E-01
37	1.585E-03	7.498E+03	1.655E+05	1.261E-20	1.143E-16	9.907E-01
38	4.540E-04	4.314E+03	1.698E+05	4.253E-22	1.143E-16	9.907E-01
39	2.144E-04	4.456E+03	1.743E+05	6.390E-22	1.143E-16	9.907E-01
40	1.013E-04	5.910E+03	1.802E+05	1.318E-21	1.143E-16	9.907E-01
41	3.727E-05	7.268E+03	1.875E+05	2.863E-21	1.143E-16	9.907E-01
42	1.068E-05	4.254E+03	1.917E+05	2.734E-21	1.143E-16	9.908E-01
43	5.043E-06	5.481E+03	1.972E+05	5.481E-21	1.144E-16	9.908E-01
44	1.855E-06	3.915E+03	2.011E+05	6.017E-21	1.144E-16	9.909E-01
45	8.764E-07	3.716E+03	2.048E+05	8.339E-21	1.144E-16	9.909E-01
46	4.140E-07	1.103E+04	2.159E+05	4.527E-20	1.144E-16	9.913E-01
47	1.000E-07	9.835E+04	3.142E+05	1.000E-18	1.154E-16	1.000E+00

Table A.4-b Absolute Calculated Neutron Flux Spectra and DPA Rate
at the Axial Feed Water Nozzle Elevation, Azimuthal
Peak and R = 0-T RPV Wall of Grand Gulf Cycle-2

G	Energy (MeV)	Group Flux	Cumulative Flux	Group DPA Rate	Cumulative DPA Rate	DPA Fraction
1	1.733E+01	1.794E+02	1.794E+02	5.242E-19	5.242E-19	4.657E-03
2	1.419E+01	7.258E+02	9.052E+02	1.921E-18	2.445E-18	2.172E-02
3	1.221E+01	1.615E+03	2.520E+03	3.890E-18	6.335E-18	5.628E-02
4	1.000E+01	2.352E+03	4.872E+03	5.218E-18	1.155E-17	1.026E-01
5	8.607E+00	3.042E+03	7.914E+03	6.350E-18	1.790E-17	1.590E-01
6	7.408E+00	5.578E+03	1.349E+04	1.084E-17	2.874E-17	2.553E-01
7	6.065E+00	6.100E+03	1.959E+04	1.088E-17	3.962E-17	3.520E-01
8	4.966E+00	8.295E+03	2.789E+04	1.303E-17	5.265E-17	4.678E-01
9	3.679E+00	5.122E+03	3.301E+04	7.017E-18	5.967E-17	5.301E-01
10	3.012E+00	3.245E+03	3.625E+04	4.124E-18	6.380E-17	5.668E-01
11	2.725E+00	3.467E+03	3.972E+04	4.421E-18	6.822E-17	6.060E-01
12	2.466E+00	1.627E+03	4.135E+04	1.907E-18	7.012E-17	6.230E-01
13	2.365E+00	3.850E+02	4.173E+04	4.220E-19	7.055E-17	6.267E-01
14	2.346E+00	1.941E+03	4.367E+04	2.020E-18	7.257E-17	6.447E-01
15	2.231E+00	5.001E+03	4.867E+04	5.171E-18	7.774E-17	6.906E-01
16	1.920E+00	5.124E+03	5.380E+04	4.167E-18	8.190E-17	7.276E-01
17	1.653E+00	6.788E+03	6.059E+04	5.500E-18	8.740E-17	7.765E-01
18	1.353E+00	1.050E+04	7.109E+04	5.885E-18	9.329E-17	8.288E-01
19	1.003E+00	6.692E+03	7.778E+04	2.452E-18	9.574E-17	8.506E-01
20	8.208E-01	3.329E+03	8.111E+04	1.867E-18	9.761E-17	8.672E-01
21	7.427E-01	8.887E+03	9.000E+04	3.212E-18	1.008E-16	8.957E-01
22	6.081E-01	6.801E+03	9.680E+04	2.001E-18	1.028E-16	9.135E-01
23	4.979E-01	7.766E+03	1.046E+05	3.079E-18	1.059E-16	9.408E-01
24	3.688E-01	7.334E+03	1.119E+05	1.516E-18	1.074E-16	9.543E-01
25	2.972E-01	8.858E+03	1.208E+05	1.776E-18	1.092E-16	9.701E-01
26	1.832E-01	7.561E+03	1.283E+05	1.066E-18	1.103E-16	9.795E-01
27	1.111E-01	5.130E+03	1.334E+05	6.632E-19	1.109E-16	9.854E-01
28	6.738E-02	4.275E+03	1.377E+05	2.769E-19	1.112E-16	9.879E-01
29	4.087E-02	1.619E+03	1.393E+05	1.310E-19	1.113E-16	9.891E-01
30	3.183E-02	1.005E+03	1.403E+05	2.857E-19	1.116E-16	9.916E-01
31	2.606E-02	1.724E+03	1.421E+05	3.475E-20	1.116E-16	9.919E-01
32	2.418E-02	9.338E+02	1.430E+05	4.089E-21	1.117E-16	9.919E-01
33	2.188E-02	2.200E+03	1.452E+05	1.802E-20	1.117E-16	9.921E-01
34	1.503E-02	4.249E+03	1.495E+05	7.971E-20	1.118E-16	9.928E-01
35	7.102E-03	4.617E+03	1.541E+05	4.107E-20	1.118E-16	9.932E-01
36	3.355E-03	4.273E+03	1.583E+05	1.504E-20	1.118E-16	9.933E-01
37	1.585E-03	7.132E+03	1.655E+05	1.200E-20	1.118E-16	9.934E-01
38	4.540E-04	3.991E+03	1.695E+05	3.934E-22	1.118E-16	9.934E-01
39	2.144E-04	4.241E+03	1.737E+05	6.081E-22	1.118E-16	9.934E-01
40	1.013E-04	5.631E+03	1.793E+05	1.256E-21	1.118E-16	9.934E-01
41	3.727E-05	6.892E+03	1.862E+05	2.715E-21	1.118E-16	9.935E-01
42	1.068E-05	3.988E+03	1.902E+05	2.563E-21	1.118E-16	9.935E-01
43	5.043E-06	5.066E+03	1.953E+05	5.066E-21	1.118E-16	9.935E-01
44	1.855E-06	3.539E+03	1.988E+05	5.439E-21	1.118E-16	9.936E-01
45	8.764E-07	3.286E+03	2.021E+05	7.374E-21	1.118E-16	9.936E-01
46	4.140E-07	8.857E+03	2.110E+05	3.634E-20	1.119E-16	9.940E-01
47	1.000E-07	6.689E+04	2.779E+05	6.803E-19	1.126E-16	1.000E+00

Table A.4-c   Absolute Calculated Neutron Flux Spectra and DPA Rate
at the Axial Feed Water Nozzle Elevation, Azimuthal
Peak and R = 1/4-T RPV Wall of Grand Gulf Cycle-2

G	Energy (MeV)	Group Flux	Cumulative Flux	Group DPA Rate	Cumulative DPA Rate	DPA Fraction
1	1.733E+01	9.118E+01	9.118E+01	2.664E-19	2.664E-19	2.295E-04
2	1.419E+01	3.749E+02	4.661E+02	9.920E-19	1.258E-18	1.084E-03
3	1.221E+01	8.199E+02	1.286E+03	1.975E-18	3.234E-18	2.786E-03
4	1.000E+01	1.226E+03	2.512E+03	2.720E-18	5.953E-18	5.129E-03
5	8.607E+00	1.621E+03	4.133E+03	3.383E-18	9.337E-18	8.044E-03
6	7.408E+00	3.011E+03	7.143E+03	5.849E-18	1.519E-17	1.308E-02
7	6.065E+00	3.608E+03	1.075E+04	6.436E-18	2.162E-17	1.863E-02
8	4.966E+00	5.926E+03	1.668E+04	9.310E-18	3.093E-17	2.665E-02
9	3.679E+00	4.492E+03	2.117E+04	6.154E-18	3.709E-17	3.195E-02
10	3.012E+00	3.321E+03	2.449E+04	4.221E-18	4.131E-17	3.559E-02
11	2.725E+00	4.336E+03	2.883E+04	5.528E-18	4.683E-17	4.035E-02
12	2.466E+00	2.322E+03	3.115E+04	2.721E-18	4.956E-17	4.269E-02
13	2.365E+00	6.504E+02	3.180E+04	7.129E-19	5.027E-17	4.331E-02
14	2.346E+00	3.429E+03	3.523E+04	3.570E-18	5.384E-17	4.638E-02
15	2.231E+00	9.726E+03	4.495E+04	1.006E-17	6.390E-17	5.505E-02
16	1.920E+00	1.367E+04	5.862E+04	1.111E-17	7.501E-17	6.463E-02
17	1.653E+00	2.441E+04	8.303E+04	1.978E-17	9.479E-17	8.166E-02
18	1.353E+00	7.560E+04	1.586E+05	4.236E-17	1.371E-16	1.182E-01
19	1.003E+00	7.541E+04	2.340E+05	2.764E-17	1.648E-16	1.420E-01
20	8.208E-01	3.732E+04	2.714E+05	2.093E-17	1.857E-16	1.600E-01
21	7.427E-01	2.526E+05	5.239E+05	9.128E-17	2.770E-16	2.386E-01
22	6.081E-01	2.708E+05	7.947E+05	7.969E-17	3.567E-16	3.073E-01
23	4.979E-01	3.980E+05	1.193E+06	1.578E-16	5.145E-16	4.432E-01
24	3.688E-01	6.301E+05	1.823E+06	1.302E-16	6.447E-16	5.554E-01
25	2.972E-01	8.301E+05	2.653E+06	1.664E-16	8.111E-16	6.988E-01
26	1.832E-01	1.161E+06	3.814E+06	1.637E-16	9.748E-16	8.398E-01
27	1.111E-01	7.090E+05	4.523E+06	9.167E-17	1.066E-15	9.188E-01
28	6.738E-02	5.687E+05	5.091E+06	3.683E-17	1.103E-15	9.506E-01
29	4.087E-02	1.402E+05	5.232E+06	1.135E-17	1.115E-15	9.603E-01
30	3.183E-02	4.818E+04	5.280E+06	1.370E-17	1.128E-15	9.721E-01
31	2.606E-02	4.583E+05	5.738E+06	9.239E-18	1.138E-15	9.801E-01
32	2.418E-02	2.912E+05	6.029E+06	1.275E-18	1.139E-15	9.812E-01
33	2.188E-02	4.815E+05	6.511E+06	3.944E-18	1.143E-15	9.846E-01
34	1.503E-02	4.395E+05	6.950E+06	8.246E-18	1.151E-15	9.917E-01
35	7.102E-03	6.078E+05	7.558E+06	5.407E-18	1.156E-15	9.964E-01
36	3.355E-03	4.266E+05	7.985E+06	1.501E-18	1.158E-15	9.977E-01
37	1.585E-03	7.148E+05	8.700E+06	1.202E-18	1.159E-15	9.987E-01
38	4.540E-04	2.958E+05	8.995E+06	2.916E-20	1.159E-15	9.987E-01
39	2.144E-04	3.512E+05	9.347E+06	5.037E-20	1.159E-15	9.988E-01
40	1.013E-04	4.883E+05	9.835E+06	1.089E-19	1.159E-15	9.988E-01
41	3.727E-05	5.793E+05	1.041E+07	2.282E-19	1.160E-15	9.990E-01
42	1.068E-05	2.966E+05	1.071E+07	1.906E-19	1.160E-15	9.992E-01
43	5.043E-06	2.908E+05	1.100E+07	2.908E-19	1.160E-15	9.995E-01
44	1.855E-06	1.391E+05	1.114E+07	2.138E-19	1.160E-15	9.996E-01
45	8.764E-07	7.722E+04	1.122E+07	1.733E-19	1.160E-15	9.998E-01
46	4.140E-07	2.986E+04	1.125E+07	1.225E-19	1.161E-15	9.999E-01
47	1.000E-07	1.163E+04	1.126E+07	1.183E-19	1.161E-15	1.000E+00

Table A.4-d Absolute Calculated Neutron Flux Spectra and DPA Rate
at the Axial Feed Water Nozzle Elevation, Azimuthal
Peak and R = 3/4-T RPV Wall of Grand Gulf Cycle-2

G	Energy (MeV)	Group Flux	Cumulative Flux	Group DPA Rate	Cumulative DPA Rate	DPA Fraction
1	1.733E+01	2.285E+01	2.285E+01	6.677E-20	6.677E-20	2.738E-05
2	1.419E+01	1.135E+02	1.364E+02	3.003E-19	3.671E-19	1.506E-04
3	1.221E+01	3.066E+02	4.429E+02	7.385E-19	1.106E-18	4.534E-04
4	1.000E+01	5.720E+02	1.015E+03	1.269E-18	2.375E-18	9.740E-04
5	8.607E+00	1.053E+03	2.068E+03	2.198E-18	4.573E-18	1.875E-03
6	7.408E+00	2.590E+03	4.659E+03	5.033E-18	9.606E-18	3.940E-03
7	6.065E+00	4.917E+03	9.576E+03	8.772E-18	1.838E-17	7.537E-03
8	4.966E+00	1.235E+04	2.193E+04	1.940E-17	3.778E-17	1.549E-02
9	3.679E+00	1.144E+04	3.337E+04	1.567E-17	5.345E-17	2.192E-02
10	3.012E+00	9.002E+03	4.237E+04	1.144E-17	6.489E-17	2.661E-02
11	2.725E+00	1.298E+04	5.534E+04	1.655E-17	8.144E-17	3.340E-02
12	2.466E+00	7.438E+03	6.278E+04	8.717E-18	9.016E-17	3.697E-02
13	2.365E+00	2.016E+03	6.480E+04	2.210E-18	9.237E-17	3.788E-02
14	2.346E+00	1.079E+04	7.559E+04	1.123E-17	1.036E-16	4.249E-02
15	2.231E+00	2.932E+04	1.049E+05	3.032E-17	1.339E-16	5.492E-02
16	1.920E+00	4.115E+04	1.461E+05	3.347E-17	1.674E-16	6.865E-02
17	1.653E+00	7.557E+04	2.216E+05	6.123E-17	2.286E-16	9.376E-02
18	1.353E+00	2.115E+05	4.331E+05	1.185E-16	3.471E-16	1.424E-01
19	1.003E+00	1.848E+05	6.179E+05	6.773E-17	4.148E-16	1.701E-01
20	8.208E-01	1.123E+05	7.302E+05	6.300E-17	4.778E-16	1.960E-01
21	7.427E-01	5.444E+05	1.275E+06	1.967E-16	6.746E-16	2.767E-01
22	6.081E-01	5.883E+05	1.863E+06	1.731E-16	8.477E-16	3.477E-01
23	4.979E-01	8.517E+05	2.715E+06	3.376E-16	1.185E-15	4.861E-01
24	3.688E-01	1.086E+06	3.801E+06	2.246E-16	1.410E-15	5.782E-01
25	2.972E-01	1.699E+06	5.500E+06	3.407E-16	1.751E-15	7.179E-01
26	1.832E-01	2.092E+06	7.593E+06	2.950E-16	2.046E-15	8.389E-01
27	1.111E-01	1.431E+06	9.024E+06	1.851E-16	2.231E-15	9.148E-01
28	6.738E-02	1.212E+06	1.024E+07	7.851E-17	2.309E-15	9.470E-01
29	4.087E-02	3.106E+05	1.055E+07	2.514E-17	2.334E-15	9.573E-01
30	3.183E-02	1.084E+05	1.065E+07	3.082E-17	2.365E-15	9.700E-01
31	2.606E-02	7.342E+05	1.139E+07	1.480E-17	2.380E-15	9.760E-01
32	2.418E-02	4.358E+05	1.182E+07	1.908E-18	2.382E-15	9.768E-01
33	2.188E-02	8.465E+05	1.267E+07	6.933E-18	2.389E-15	9.797E-01
34	1.503E-02	1.064E+06	1.374E+07	1.997E-17	2.409E-15	9.879E-01
35	7.102E-03	1.418E+06	1.515E+07	1.261E-17	2.421E-15	9.930E-01
36	3.355E-03	1.097E+06	1.625E+07	3.860E-18	2.425E-15	9.946E-01
37	1.585E-03	1.937E+06	1.819E+07	3.259E-18	2.428E-15	9.960E-01
38	4.540E-04	8.598E+05	1.905E+07	8.476E-20	2.429E-15	9.960E-01
39	2.144E-04	1.043E+06	2.009E+07	1.496E-19	2.429E-15	9.960E-01
40	1.013E-04	1.429E+06	2.152E+07	3.187E-19	2.429E-15	9.962E-01
41	3.727E-05	1.688E+06	2.321E+07	6.649E-19	2.430E-15	9.965E-01
42	1.068E-05	8.838E+05	2.409E+07	5.680E-19	2.430E-15	9.967E-01
43	5.043E-06	9.477E+05	2.504E+07	9.477E-19	2.431E-15	9.971E-01
44	1.855E-06	5.180E+05	2.556E+07	7.962E-19	2.432E-15	9.974E-01
45	8.764E-07	3.557E+05	2.591E+07	7.982E-19	2.433E-15	9.977E-01
46	4.140E-07	2.869E+05	2.620E+07	1.177E-18	2.434E-15	9.982E-01
47	1.000E-07	4.296E+05	2.663E+07	4.369E-18	2.438E-15	1.000E+00

Table A.4-e   Absolute Calculated Neutron Flux Spectra and DPA Rate
at the Axial Feed Water Nozzle Elevation, Azimuthal
Peak and R = Mid-Cavity of Grand Gulf Cycle-2

G	Energy (MeV)	Group Flux	Cumulative Flux	Group DPA Rate	Cumulative DPA Rate	DPA Fraction
1	1.733E+01	7.846E+01	7.846E+01	2.293E-19	2.293E-19	3.525E-05
2	1.419E+01	6.758E+02	7.543E+02	1.788E-18	2.017E-18	3.102E-04
3	1.221E+01	2.708E+03	3.462E+03	6.523E-18	8.540E-18	1.313E-03
4	1.000E+01	6.201E+03	9.663E+03	1.376E-17	2.230E-17	3.428E-03
5	8.607E+00	1.288E+04	2.254E+04	2.688E-17	4.918E-17	7.561E-03
6	7.408E+00	3.319E+04	5.573E+04	6.449E-17	1.137E-16	1.747E-02
7	6.065E+00	5.931E+04	1.150E+05	1.058E-16	2.195E-16	3.374E-02
8	4.966E+00	1.225E+05	2.375E+05	1.924E-16	4.119E-16	6.332E-02
9	3.679E+00	9.776E+04	3.353E+05	1.339E-16	5.458E-16	8.391E-02
10	3.012E+00	7.058E+04	4.059E+05	8.971E-17	6.355E-16	9.770E-02
11	2.725E+00	9.133E+04	4.972E+05	1.164E-16	7.520E-16	1.156E-01
12	2.466E+00	5.247E+04	5.496E+05	6.150E-17	8.134E-16	1.251E-01
13	2.365E+00	1.287E+04	5.625E+05	1.411E-17	8.276E-16	1.272E-01
14	2.346E+00	6.614E+04	6.287E+05	6.885E-17	8.964E-16	1.378E-01
15	2.231E+00	1.614E+05	7.901E+05	1.669E-16	1.063E-15	1.635E-01
16	1.920E+00	2.067E+05	9.967E+05	1.681E-16	1.231E-15	1.893E-01
17	1.653E+00	3.516E+05	1.348E+06	2.849E-16	1.516E-15	2.331E-01
18	1.353E+00	7.859E+05	2.134E+06	4.404E-16	1.957E-15	3.008E-01
19	1.003E+00	6.016E+05	2.736E+06	2.205E-16	2.177E-15	3.347E-01
20	8.208E-01	4.689E+05	3.205E+06	2.630E-16	2.440E-15	3.751E-01
21	7.427E-01	1.264E+06	4.468E+06	4.566E-16	2.897E-15	4.453E-01
22	6.081E-01	1.470E+06	5.938E+06	4.326E-16	3.329E-15	5.118E-01
23	4.979E-01	1.706E+06	7.645E+06	6.764E-16	4.006E-15	6.158E-01
24	3.688E-01	1.729E+06	9.374E+06	3.575E-16	4.363E-15	6.708E-01
25	2.972E-01	3.449E+06	1.282E+07	6.914E-16	5.055E-15	7.771E-01
26	1.832E-01	3.438E+06	1.626E+07	4.848E-16	5.540E-15	8.516E-01
27	1.111E-01	2.593E+06	1.885E+07	3.353E-16	5.875E-15	9.032E-01
28	6.738E-02	2.136E+06	2.099E+07	1.384E-16	6.013E-15	9.244E-01
29	4.087E-02	7.672E+05	2.176E+07	6.209E-17	6.075E-15	9.340E-01
30	3.183E-02	7.045E+05	2.246E+07	2.003E-16	6.276E-15	9.648E-01
31	2.606E-02	7.273E+05	2.319E+07	1.466E-17	6.290E-15	9.670E-01
32	2.418E-02	5.691E+05	2.376E+07	2.492E-18	6.293E-15	9.674E-01
33	2.188E-02	1.478E+06	2.524E+07	1.211E-17	6.305E-15	9.693E-01
34	1.503E-02	2.379E+06	2.762E+07	4.462E-17	6.350E-15	9.761E-01
35	7.102E-03	2.309E+06	2.992E+07	2.054E-17	6.370E-15	9.793E-01
36	3.355E-03	2.149E+06	3.207E+07	7.566E-18	6.378E-15	9.804E-01
37	1.585E-03	3.491E+06	3.556E+07	5.872E-18	6.383E-15	9.813E-01
38	4.540E-04	1.917E+06	3.748E+07	1.890E-19	6.384E-15	9.814E-01
39	2.144E-04	1.917E+06	3.940E+07	2.749E-19	6.384E-15	9.814E-01
40	1.013E-04	2.476E+06	4.188E+07	5.525E-19	6.385E-15	9.815E-01
41	3.727E-05	2.943E+06	4.482E+07	1.159E-18	6.386E-15	9.817E-01
42	1.068E-05	1.668E+06	4.649E+07	1.072E-18	6.387E-15	9.818E-01
43	5.043E-06	2.068E+06	4.855E+07	2.068E-18	6.389E-15	9.822E-01
44	1.855E-06	1.421E+06	4.998E+07	2.183E-18	6.391E-15	9.825E-01
45	8.764E-07	1.294E+06	5.127E+07	2.904E-18	6.394E-15	9.829E-01
46	4.140E-07	2.841E+06	5.411E+07	1.166E-17	6.406E-15	9.847E-01
47	1.000E-07	9.761E+06	6.387E+07	9.927E-17	6.505E-15	1.000E+00

Table A.4-f Absolute Calculated Neutron Flux Spectra and DPA Rate at
the Axial Feed Water Nozzle Elevation, Azimuthal Peak and
R = Front of the Concrete Shield Wall of Grand Gulf Cycle-2

G	Energy (MeV)	Group Flux	Cumulative Flux	Group DPA Rate	Cumulative DPA Rate	DPA Fraction
1	1.733E+01	1.192E+02	1.192E+02	3.483E-19	3.483E-19	7.139E-05
2	1.419E+01	7.333E+02	8.525E+02	1.940E-18	2.289E-18	4.691E-04
3	1.221E+01	2.544E+03	3.397E+03	6.129E-18	8.418E-18	1.725E-03
4	1.000E+01	5.848E+03	9.245E+03	1.298E-17	2.140E-17	4.385E-03
5	8.607E+00	1.141E+04	2.066E+04	2.381E-17	4.521E-17	9.266E-03
6	7.408E+00	2.961E+04	5.026E+04	5.753E-17	1.027E-16	2.106E-02
7	6.065E+00	4.968E+04	9.994E+04	8.862E-17	1.914E-16	3.922E-02
8	4.966E+00	9.763E+04	1.976E+05	1.534E-16	3.447E-16	7.066E-02
9	3.679E+00	7.523E+04	2.728E+05	1.031E-16	4.478E-16	9.178E-02
10	3.012E+00	5.994E+04	3.327E+05	7.618E-17	5.240E-16	1.074E-01
11	2.725E+00	7.729E+04	4.100E+05	9.854E-17	6.225E-16	1.276E-01
12	2.466E+00	4.553E+04	4.556E+05	5.336E-17	6.759E-16	1.385E-01
13	2.365E+00	1.145E+04	4.670E+05	1.255E-17	6.884E-16	1.411E-01
14	2.346E+00	5.710E+04	5.241E+05	5.944E-17	7.479E-16	1.533E-01
15	2.231E+00	1.345E+05	6.586E+05	1.390E-16	8.869E-16	1.818E-01
16	1.920E+00	1.642E+05	8.228E+05	1.335E-16	1.020E-15	2.091E-01
17	1.653E+00	2.748E+05	1.098E+06	2.226E-16	1.243E-15	2.548E-01
18	1.353E+00	5.658E+05	1.663E+06	3.170E-16	1.560E-15	3.198E-01
19	1.003E+00	4.336E+05	2.097E+06	1.589E-16	1.719E-15	3.523E-01
20	8.208E-01	3.414E+05	2.438E+06	1.915E-16	1.911E-15	3.916E-01
21	7.427E-01	9.230E+05	3.361E+06	3.336E-16	2.244E-15	4.599E-01
22	6.081E-01	1.029E+06	4.390E+06	3.027E-16	2.547E-15	5.220E-01
23	4.979E-01	1.095E+06	5.485E+06	4.340E-16	2.981E-15	6.109E-01
24	3.688E-01	1.198E+06	6.682E+06	2.475E-16	3.228E-15	6.617E-01
25	2.972E-01	2.423E+06	9.106E+06	4.859E-16	3.714E-15	7.612E-01
26	1.832E-01	2.565E+06	1.167E+07	3.616E-16	4.076E-15	8.354E-01
27	1.111E-01	1.977E+06	1.365E+07	2.556E-16	4.331E-15	8.877E-01
28	6.738E-02	1.659E+06	1.531E+07	1.074E-16	4.439E-15	9.097E-01
29	4.087E-02	6.396E+05	1.594E+07	5.176E-17	4.491E-15	9.204E-01
30	3.183E-02	5.694E+05	1.651E+07	1.619E-16	4.652E-15	9.535E-01
31	2.606E-02	4.313E+05	1.695E+07	8.696E-18	4.661E-15	9.553E-01
32	2.418E-02	3.941E+05	1.734E+07	1.726E-18	4.663E-15	9.557E-01
33	2.188E-02	1.158E+06	1.850E+07	9.487E-18	4.672E-15	9.576E-01
34	1.503E-02	1.959E+06	2.046E+07	3.675E-17	4.709E-15	9.651E-01
35	7.102E-03	1.888E+06	2.235E+07	1.679E-17	4.726E-15	9.686E-01
36	3.355E-03	1.798E+06	2.414E+07	6.329E-18	4.732E-15	9.699E-01
37	1.585E-03	2.985E+06	2.713E+07	5.022E-18	4.737E-15	9.709E-01
38	4.540E-04	1.690E+06	2.882E+07	1.666E-19	4.737E-15	9.709E-01
39	2.144E-04	1.678E+06	3.050E+07	2.406E-19	4.738E-15	9.710E-01
40	1.013E-04	2.186E+06	3.268E+07	4.877E-19	4.738E-15	9.711E-01
41	3.727E-05	2.633E+06	3.531E+07	1.037E-18	4.739E-15	9.713E-01
42	1.068E-05	1.514E+06	3.683E+07	9.728E-19	4.740E-15	9.715E-01
43	5.043E-06	1.911E+06	3.874E+07	1.911E-18	4.742E-15	9.719E-01
44	1.855E-06	1.342E+06	4.008E+07	2.063E-18	4.744E-15	9.723E-01
45	8.764E-07	1.251E+06	4.133E+07	2.807E-18	4.747E-15	9.729E-01
46	4.140E-07	2.960E+06	4.429E+07	1.214E-17	4.759E-15	9.754E-01
47	1.000E-07	1.181E+07	5.610E+07	1.201E-16	4.879E-15	1.000E+00

Table A.4-g Absolute Calculated Neutron Flux Spectra and DPA Rate at
the Axial Feed Water Nozzle Elevation, Azimuthal Peak and
R = 6" in the Concrete Shield Wall of Grand Gulf Cycle-2

G	Energy (MeV)	Group Flux	Cumulative Flux	Group DPA Rate	Cumulative DPA Rate	DPA Fraction
1	1.733E+01	1.615E+00	1.615E+00	4.720E-21	4.720E-21	3.613E-05
2	1.419E+01	9.114E+00	1.073E+01	2.411E-20	2.883E-20	2.207E-04
3	1.221E+01	2.689E+01	3.762E+01	6.478E-20	9.362E-20	7.167E-04
4	1.000E+01	5.984E+01	9.746E+01	1.328E-19	2.264E-19	1.733E-03
5	8.607E+00	1.183E+02	2.157E+02	2.468E-19	4.732E-19	3.622E-03
6	7.408E+00	4.374E+02	6.531E+02	8.499E-19	1.323E-18	1.013E-02
7	6.065E+00	9.375E+02	1.591E+03	1.672E-18	2.995E-18	2.293E-02
8	4.966E+00	2.182E+03	3.773E+03	3.428E-18	6.423E-18	4.917E-02
9	3.679E+00	1.662E+03	5.434E+03	2.277E-18	8.700E-18	6.660E-02
10	3.012E+00	1.681E+03	7.116E+03	2.137E-18	1.084E-17	8.296E-02
11	2.725E+00	2.314E+03	9.430E+03	2.951E-18	1.379E-17	1.056E-01
12	2.466E+00	1.829E+03	1.126E+04	2.143E-18	1.593E-17	1.220E-01
13	2.365E+00	6.054E+02	1.186E+04	6.635E-19	1.659E-17	1.270E-01
14	2.346E+00	2.484E+03	1.435E+04	2.586E-18	1.918E-17	1.468E-01
15	2.231E+00	4.101E+03	1.845E+04	4.241E-18	2.342E-17	1.793E-01
16	1.920E+00	4.057E+03	2.251E+04	3.300E-18	2.672E-17	2.046E-01
17	1.653E+00	5.500E+03	2.801E+04	4.457E-18	3.118E-17	2.387E-01
18	1.353E+00	7.065E+03	3.507E+04	3.958E-18	3.514E-17	2.690E-01
19	1.003E+00	4.256E+03	3.933E+04	1.560E-18	3.670E-17	2.809E-01
20	8.208E-01	3.693E+03	4.302E+04	2.072E-18	3.877E-17	2.968E-01
21	7.427E-01	8.345E+03	5.137E+04	3.016E-18	4.178E-17	3.199E-01
22	6.081E-01	9.196E+03	6.056E+04	2.706E-18	4.449E-17	3.406E-01
23	4.979E-01	7.696E+03	6.826E+04	3.051E-18	4.754E-17	3.639E-01
24	3.688E-01	7.230E+03	7.549E+04	1.494E-18	4.903E-17	3.754E-01
25	2.972E-01	1.567E+04	9.116E+04	3.142E-18	5.218E-17	3.994E-01
26	1.832E-01	2.172E+04	1.129E+05	3.062E-18	5.524E-17	4.229E-01
27	1.111E-01	2.115E+04	1.340E+05	2.734E-18	5.797E-17	4.438E-01
28	6.738E-02	2.214E+04	1.562E+05	1.434E-18	5.941E-17	4.548E-01
29	4.087E-02	1.030E+04	1.665E+05	8.337E-19	6.024E-17	4.612E-01
30	3.183E-02	9.344E+03	1.758E+05	2.656E-18	6.290E-17	4.815E-01
31	2.606E-02	3.604E+03	1.794E+05	7.266E-20	6.297E-17	4.821E-01
32	2.418E-02	4.744E+03	1.842E+05	2.077E-20	6.299E-17	4.822E-01
33	2.188E-02	1.845E+04	2.026E+05	1.511E-19	6.314E-17	4.834E-01
34	1.503E-02	4.017E+04	2.428E+05	7.536E-19	6.390E-17	4.891E-01
35	7.102E-03	4.372E+04	2.865E+05	3.889E-19	6.428E-17	4.921E-01
36	3.355E-03	4.732E+04	3.338E+05	1.666E-19	6.445E-17	4.934E-01
37	1.585E-03	1.024E+05	4.362E+05	1.722E-19	6.462E-17	4.947E-01
38	4.540E-04	7.085E+04	5.070E+05	6.984E-21	6.463E-17	4.948E-01
39	2.144E-04	8.001E+04	5.870E+05	1.147E-20	6.464E-17	4.949E-01
40	1.013E-04	1.224E+05	7.095E+05	2.732E-20	6.467E-17	4.951E-01
41	3.727E-05	1.788E+05	8.883E+05	7.044E-20	6.474E-17	4.956E-01
42	1.068E-05	1.184E+05	1.007E+06	7.609E-20	6.482E-17	4.962E-01
43	5.043E-06	1.741E+05	1.181E+06	1.741E-19	6.499E-17	4.975E-01
44	1.855E-06	1.401E+05	1.321E+06	2.154E-19	6.521E-17	4.992E-01
45	8.764E-07	1.485E+05	1.469E+06	3.333E-19	6.554E-17	5.017E-01
46	4.140E-07	5.103E+05	1.980E+06	2.094E-18	6.763E-17	5.177E-01
47	1.000E-07	6.194E+06	8.174E+06	6.300E-17	1.306E-16	1.000E+00

Table A.4-h Absolute Calculated Neutron Flux Spectra and DPA Rate at
the Axial Feed Water Nozzle Elevation, Azimuthal Peak and
R = 1' in the Concrete Shield Wall of Grand Gulf Cycle-2

G	Energy (MeV)	Group Flux	Cumulative Flux	Group DPA Rate	Cumulative DPA Rate	DPA Fraction
1	1.733E+01	8.778E-02	8.778E-02	2.565E-22	2.565E-22	3.267E-05
2	1.419E+01	5.232E-01	6.110E-01	1.385E-21	1.641E-21	2.090E-04
3	1.221E+01	1.466E+00	2.077E+00	3.532E-21	5.173E-21	6.589E-04
4	1.000E+01	3.308E+00	5.385E+00	7.340E-21	1.251E-20	1.594E-03
5	8.607E+00	6.434E+00	1.182E+01	1.343E-20	2.594E-20	3.305E-03
6	7.408E+00	2.810E+01	3.992E+01	5.460E-20	8.054E-20	1.026E-02
7	6.065E+00	6.130E+01	1.012E+02	1.094E-19	1.899E-19	2.419E-02
8	4.966E+00	1.290E+02	2.302E+02	2.027E-19	3.926E-19	5.001E-02
9	3.679E+00	9.022E+01	3.204E+02	1.236E-19	5.162E-19	6.575E-02
10	3.012E+00	1.010E+02	4.214E+02	1.284E-19	6.445E-19	8.211E-02
11	2.725E+00	1.409E+02	5.624E+02	1.797E-19	8.242E-19	1.050E-01
12	2.466E+00	1.340E+02	6.963E+02	1.570E-19	9.812E-19	1.250E-01
13	2.365E+00	5.443E+01	7.507E+02	5.965E-20	1.041E-18	1.326E-01
14	2.346E+00	2.010E+02	9.518E+02	2.093E-19	1.250E-18	1.593E-01
15	2.231E+00	2.909E+02	1.243E+03	3.008E-19	1.551E-18	1.976E-01
16	1.920E+00	2.673E+02	1.510E+03	2.174E-19	1.768E-18	2.253E-01
17	1.653E+00	3.302E+02	1.840E+03	2.676E-19	2.036E-18	2.594E-01
18	1.353E+00	3.789E+02	2.219E+03	2.123E-19	2.248E-18	2.864E-01
19	1.003E+00	2.191E+02	2.438E+03	8.029E-20	2.329E-18	2.966E-01
20	8.208E-01	1.774E+02	2.616E+03	9.950E-20	2.428E-18	3.093E-01
21	7.427E-01	3.402E+02	2.956E+03	1.230E-19	2.551E-18	3.250E-01
22	6.081E-01	3.386E+02	3.294E+03	9.965E-20	2.651E-18	3.377E-01
23	4.979E-01	2.804E+02	3.575E+03	1.112E-19	2.762E-18	3.518E-01
24	3.688E-01	2.503E+02	3.825E+03	5.175E-20	2.814E-18	3.584E-01
25	2.972E-01	5.145E+02	4.340E+03	1.032E-19	2.917E-18	3.716E-01
26	1.832E-01	5.953E+02	4.935E+03	8.394E-20	3.001E-18	3.822E-01
27	1.111E-01	5.125E+02	5.447E+03	6.627E-20	3.067E-18	3.907E-01
28	6.738E-02	4.879E+02	5.935E+03	3.160E-20	3.098E-18	3.947E-01
29	4.087E-02	2.188E+02	6.154E+03	1.771E-20	3.116E-18	3.970E-01
30	3.183E-02	1.943E+02	6.348E+03	5.525E-20	3.171E-18	4.040E-01
31	2.606E-02	7.083E+01	6.419E+03	1.428E-21	3.173E-18	4.042E-01
32	2.418E-02	9.363E+01	6.513E+03	4.100E-22	3.173E-18	4.042E-01
33	2.188E-02	3.498E+02	6.863E+03	2.865E-21	3.176E-18	4.046E-01
34	1.503E-02	7.197E+02	7.582E+03	1.350E-20	3.190E-18	4.063E-01
35	7.102E-03	7.418E+02	8.324E+03	6.599E-21	3.196E-18	4.072E-01
36	3.355E-03	7.783E+02	9.103E+03	2.740E-21	3.199E-18	4.075E-01
37	1.585E-03	1.583E+03	1.069E+04	2.663E-21	3.202E-18	4.079E-01
38	4.540E-04	1.069E+03	1.175E+04	1.054E-22	3.202E-18	4.079E-01
39	2.144E-04	1.205E+03	1.296E+04	1.728E-22	3.202E-18	4.079E-01
40	1.013E-04	1.874E+03	1.483E+04	4.181E-22	3.202E-18	4.079E-01
41	3.727E-05	2.852E+03	1.769E+04	1.124E-21	3.203E-18	4.081E-01
42	1.068E-05	1.959E+03	1.965E+04	1.259E-21	3.205E-18	4.082E-01
43	5.043E-06	3.059E+03	2.270E+04	3.059E-21	3.208E-18	4.086E-01
44	1.855E-06	2.593E+03	2.530E+04	3.986E-21	3.212E-18	4.091E-01
45	8.764E-07	2.903E+03	2.820E+04	6.514E-21	3.218E-18	4.100E-01
46	4.140E-07	1.189E+04	4.009E+04	4.880E-20	3.267E-18	4.162E-01
47	1.000E-07	4.506E+05	4.907E+05	4.583E-18	7.850E-18	1.000E+00

VITA

Mehdi Asgari was born on the 22 of March 1960 in Tabriz, Iran. He received his primary and high school education in Tabriz, Iran, where he graduated from high school in 1978. He came to the United States in 1979 to pursue his degree in Mechanical Engineering at Louisiana State University. He graduated with a B. S. degree in 1984. In 1985 he was admitted to the graduate program in Nuclear Engineering in the Nuclear Science Center at Louisiana State University. During the last five months of 1988, he worked as a programmer consultant with his major professor, Dr. Mark L. Williams and since February of 1989 he has been working as a research associate in the Nuclear Science Center. He is presently a candidate for the M. S. degree in Nuclear Engineering.